Search for beyond Standard Model processes in the muon + missing transverse momentum final state with Run 2 data recorded by the CMS experiment

by

Irene Bachiller Perea

Doctoral Dissertation in Physics submitted to
Universidad Autónoma de Madrid

Supervised by

Dr. Begoña de la Cruz Martínez

Centro de Investigaciones Energéticas, Medioambientales y Tecnológicas

Madrid, September 2021

Búsqueda de procesos más allá del Modelo Estándar en el estado final muon + momento transverso faltante con datos del Run 2 recogidos por el experimento CMS

por

Irene Bachiller Perea

Memoria de tesis presentada en la
Universidad Autónoma de Madrid

Supervisada por

Dra. Begoña de la Cruz Martínez

Centro de Investigaciones Energéticas, Medioambientales y Tecnológicas

Madrid, Septiembre 2021

A mis padres y hermana

Abstract

The curiosity that characterises humankind has driven us to a collective effort to understand Nature, from the exploration of the Universe to the study of the inner structure of matter. Our knowledge regarding the most fundamental pieces of matter has been gathered in a theoretical model, the Standard Model (SM), accurately describing the constituents of matter: the particles and their interactions. Despite having an, experimentally proven, predictive power, the SM does not provide a description for all the phenomena observed in Nature. Physicists firmly believe, driven both by theoretical calculations and experimental facts, that a more complete theory must lie beyond our current SM. The SM would thus be an effective theory valid at energies currently under tests. How far in energy reach does the SM validity extends is something not yet clear. In this context, this doctoral thesis presents a work aimed to search for processes Beyond the Standard Model (BSM), predicted in several theoretical models, in an effort to complete the SM.

The LHC is the biggest and most energetic particle accelerator ever built, and therefore, one of the most promising places to search for new particle physics processes. This work is based on the analysis of proton–proton collision data at the center-of-mass energy of 13 TeV, collected with the CMS detector during Run 2 at the LHC, corresponding with a total integrated luminosity of $137\,\text{fb}^{-1}$. The final state with an energetic muon and apparent transverse momentum imbalance, is chosen since it is a general final state in which many hypothetical new signals could end up, thus offering many possibilities and interpretations of the experimental results. The theoretical context and the BSM scenarios considered are presented in Chapter 1, while the experimental setup, the LHC collider and the CMS experiment is explained in Chapter 2.

Muons, and in particular energetic ones, are a very clean signature, relatively easy to be detected and reconstructed, and with a high accuracy and efficiency. Thus final states containing muons are among the best ones to carry out inclusive searches. In this work the search is oriented towards new massive particles, foreseen in many theoretical models of BSM. These new particles are assumed to decay in a light lepton plus an undetected particle, making the high momentum muons one of the most important ingredients of this work. The detailed study of high momentum muons is presented in Chapters 3 and 4.

The strategy followed in this work consists in looking for deviations in the data with respect to the prediction of the different SM processes contributing to the signal definition.

The deviation might show up as a resonance in the reconstructed mass of the muon and the missing transverse momentum, if the collider provides sufficient energy to produce it directly. Or, in case the new particle is above the kinematic limit, the deviation could still be visible in the interference region between the SM particles masses and the new massive ones. The analysis strategy and scientific results and their interpretations are presented in Chapters 5 and 6.

Among the different models that predict the existence of a resonance we explore the following: a heavy analogue of the SM W boson, a W' as predicted by the Sequential Standard Model (SSM), a model including additional spatial dimensions and SM partners, $W_{KK}^{(2)}$ boson as predicted by the Split Universal Extra Dimensions model, or a new supersymmetric particle as predicted by R–Parity Violation Supersymmetry models.

In a more general frame, by studying any possible deviation in the high mass region we measure the W and Y oblique electroweak parameters, indicators of any BSM effect. Finally, if the Higgs boson is a composite particle, it would also manifest as a resonance or a deviation in this final state. Therefore, the compositeness of the Higgs boson is also explored.

All of them have been explored during this doctoral work, with the aim of contributing to the exhaustive task to increase our knowledge of Nature.

Resumen

La curiosidad que caracteriza a la humanidad ha motivado un esfuerzo colectivo para entender la naturaleza, desde la exploración del universo hasta el estudio de la estructura de la materia. Nuestro conociemiento de los fundamentos de la materia se ha recogido en un modelo teórico, el Modelo Estandar (ME), que describe de forma precisa los constituentes de la materia: las particulas y sus interacciones. A pesar de tener un extraordinario poder de predicción que se ha probado experimentalmente, el ME no describe todos los procesos que observamos en la naturaleza. A partir de los cálculos teóricos y de las pruebas experimentales, se cree que debe haber una teoría completa, más allá del ME.

El LHC es el acelerador de partículas más grande y enérgico jamás construido y, por lo tanto, uno de los lugares más prometedores para buscar nuevos procesos de física de partículas. Este trabajo se basa en el análisis de datos de colisiones protón–protón con una energía en el centro de masas de 13 TeV, recogidos con el detector CMS durante el Run 2 en el LHC, correspondiente a una luminosidad integrada de $137\,\mathrm{fb}^{-1}$. Se ha escogido el estado final con un muon energético y aparente desequilibrio de momento transverso, ya que es un estado final general en el que varias nuevas señales hipotéticas podrían terminar, ofreciendo así muchas posibilidades e interpretaciones de los resultados experimentales. El contexto teórico y los escenarios más allá del ME considerados se presentan en el capítulo 1, mientras que la configuración experimental, el colisionador LHC y el experimento CMS se explican en el capítulo 2.

Los muones, y en particular los muones energéticos, dejan una señal muy clara en el detector, es relativamente fácil detectarlos y reconstruirlos, por lo que los estados finales que contienen muones se encuentran entre los mejores para realizar búsquedas inclusivas. En este trabajo la búsqueda se centra en nuevas partículas masivas, predichas en varios modelos teóricos más allá del ME. Se asume que estas nuevas partículas se descomponen en un muon y una partícula no detectada, lo que convierte a los muones de alto momento en uno de los ingredientes más importantes de este trabajo. El estudio detallado de los muones de alto momento se presenta en los capítulos 3 y 4.

La estrategia seguida en este trabajo consiste en buscar desviaciones en los datos con respecto a la predicción de los diferentes procesos del ME que contribuyen a la

definición de la señal. La desviación puede aparecer como una resonancia en la masa reconstruida del muon y la energía faltante, si el colisionador proporciona suficiente energía para producirla directamente. O, en caso de que la nueva partícula esté por encima del límite cinemático, la desviación aún podría ser visible en la región de interferencia entre las masas de las partículas del ME y las nuevas partículas masivas. La estrategia del análisis y los resultados científicos junto con sus interpretaciones se presentan en los capítulos 5 y 6.

Entre los diferentes modelos que predicen la existencia de una resonancia exploramos los siguientes: un análogo pesado del bosón W del ME, el W' como lo predice el Sequential Standard Model (SSM), un modelo que incluye dimensiones espaciales adicionales y bosones adicionales al ME, $W_{KK}^{(2)}$ según lo predicho por el modelo Split Universal Extra Dimensions, o una nueva partícula supersimétrica según lo predicho por los modelos R–Parity Violation Supersymmetry.

En un marco más general, al estudiar cualquier posible desviación del ME en la región de alta masa, medimos los parámetros electrodébiles oblicuos W e Y, indicadores de cualquier efecto más allá del ME. Finalmente, si el bosón de Higgs es una partícula compuesta, también se manifestaría como una resonancia o una desviación en este estado final. Por lo tanto, también se explora la posibilidad de un bosón de Higgs compuesto. Todas éstas posibilidades han sido exploradas durante este trabajo de doctorado, con el objetivo de contribuir a la exhaustiva tarea de incrementar nuestro conocimiento de la naturaleza.

Contents

Chapter 1

Standard Model and beyond

The Standard Model of particles and interactions (SM) is the theory explaining most experimental phenomena at subatomic level as of today, providing very accurate predictions experimentally tested. However, the SM does not explain all the observed fundamental phenomena in the Universe, neither is a theoretical framework consistent with both, Quantum Mechanics and General Relativity. Thus, new models, extensions of SM, look for providing a more general theoretical framework where descriptions of all observed, though not understood, phenomena are given. Such phenomena include dark matter, dark energy, matter–antimatter asymmetry, mass and couplings hierarchy, or quantum gravity, as examples.

One direction of possible SM extension goes along Grand Unified Theories (GUT) that aims to find an unified theory that could explain and unify the spectrum of particles and interactions. The principle of this theory is a larger gauge symmetry than that of the SM, where the SM would be the result of a broken symmetry at low energy scale of the unify theory. Unified theories may manifest through new physics processes, such as additional gauge bosons, R–Parity Violating Supersymetry mediators, or models with additional spatial dimensions.

A brief introduction to the Standard Model is given in Section 1.1. This section does not aim to explain all the theory that can be found in the literature, but to give the tools to understand the extensions to the SM that are presented after. The theory of the BSM models that are explored in this thesis work, are presented in Section 1.2.

1.1 The Standard Model

The SM is the gauge quantum field theory that describes the elementary constituents of matter and their interactions. The SM theory classifies the constituents of matter, fermionic fields with spin 1/2, in three generations of two quarks (up and down, charm and strange, top and bottom) and two leptons (electron and ν_e, muon and ν_μ, tau and ν_τ). This theory describes three of the four fundamental interactions: strong, electromagnetic and weak. Each interaction is mediated by a spin–1 gauge boson field: gluon, photon, Z, and W$^\pm$. The elementary particles described by the

SM are summarized in Figure 1.
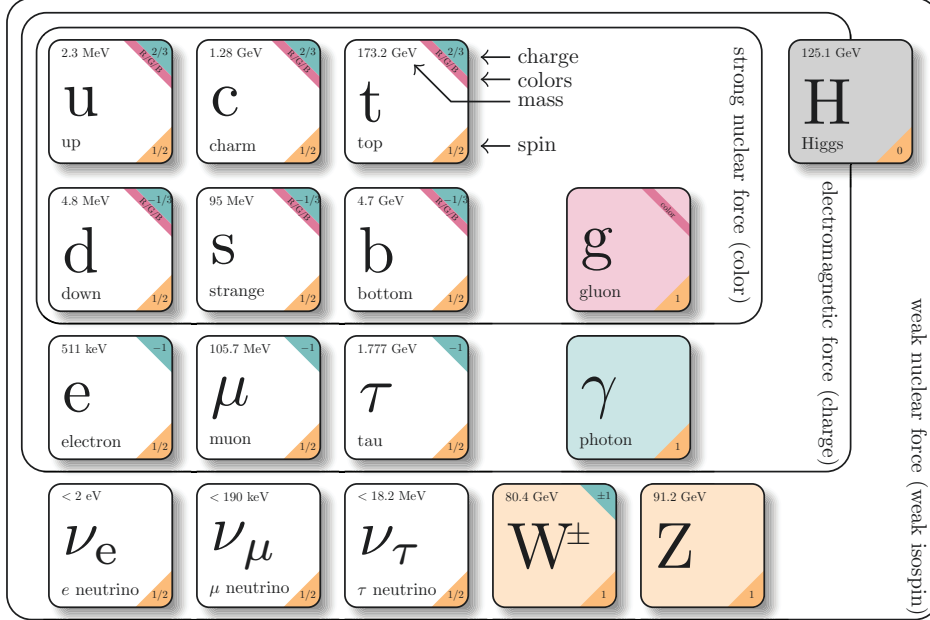
Figure 1: The Standard Model of particles and interactions.

The SM is gauge invariant under transformations of $SU(3)_C \times SU(2)_L \times U(1)_Y$ symmetry group. The $SU(3)_C$ gauge group is the fundamental symmetry group associated with the quantum chromodinamics (QCD), the theory of the strong interaction mediated by the exchange of eight massless gluons. Quarks and gluons carry the quantum charge of the strong interaction: colour. The $SU(2)_L \times U(1)_Y$ gauge group describes the electroweak interactions, a unified picture of electromagnetic and weak forces. It is mediated by four bosons, three related to the $SU(2)_L$ group (Z and $W^{\pm}$) and the other one to the $U(1)_Y$ transformation (photon, denoted as γ).

In addition, the Higgs mechanism is responsible for the spontaneous electroweak symmetry breaking, giving mass to the weak vector bosons, while leaving the photon and gluon massless.

1.1.1 Electroweak interaction

Electromagnetism and the weak interaction were unified as a $SU(2)_L \times U(1)_Y$ local gauge theory [1, 2, 3, 4]. Fermions appear as left–handed doublets and right–handed singlets and they are classified by the quantum numbers of isospin charge I, associated with the SU(2) symmetry group and the left–handed doublets, and the hypercharge Y, associated with the right–handed singlets and the U(1) symmetry group. The third component of the isospin charge, I_3, and the weak hypercharge, Y, are

related to the electric charge, Q, in this way:

$$Y = 2(Q - I_3) \tag{1.1}$$

Therefore, in a field theory for electromagnetic and weak interactions, the Lagrangian must be invariant under gauge transformations of the type SU(2)×U(1).

The Lagrangian describing the electroweak interactions is expressed as a sum of four terms:

$$\mathcal{L}_{EWK} = \mathcal{L}_G + \mathcal{L}_H + \mathcal{L}_F + \mathcal{L}_Y \tag{1.2}$$

where there is a gauge field term, $\mathcal{L}_G$, a Higgs field term describing its interaction with the gauge bosons, $\mathcal{L}_H$, a fermion–gauge boson interaction term, $\mathcal{L}_F$, and a fermion mass term $\mathcal{L}_Y$.

For the gauge term, each isospin operators I_1, I_2, I_3, and the hypercharge, Y, are associated to a vector field. There is a triplet of vector fields W_μ^i for I_i ($i = 1,2,3$) and a singlet field B^μ, for Y. These define the field strength tensors:

$$
\begin{aligned}
W_{\mu\nu}^a &= \partial_\mu W_\nu^a - \partial_\nu W_\mu^a + g_W \epsilon_{abc} W_\mu^b W_\nu^c \\
B_{\mu\nu} &= \partial_\mu B_\nu - \partial_\nu B_\mu,
\end{aligned}
\tag{1.3}
$$

where g_W is the non–Abelian SU(2) gauge coupling constant. Consequently, the gauge field Lagrangian can be written as

$$\mathcal{L}_G = -\frac{1}{4} W_{\mu\nu}^a W_{a,\mu\nu} - \frac{1}{4} B_{\mu\nu} B^{\mu\nu} \tag{1.4}$$

Mathematical formulation of the EW Lagrangian accounts for massless bosons [5]. However it is experimentally known that W and Z bosons have non–zero mass [6][1]:

$$M_W = 80.379 \pm 0.012\,\text{GeV}, \quad M_Z = 91.1876 \pm 0.0021\,\text{GeV}, \quad M_\gamma < 10^{-18}\,\text{eV} \tag{1.5}$$

In order to solve this inconsistency, the Higgs field and the Higgs mechanism are introduced [7, 8, 9, 10, 11]. It is represented by a complex scalar doublet field denoted as $\mathbf{\Phi}$:

$$\Phi = \begin{bmatrix} \Phi^+ \\ \Phi^0 \end{bmatrix} \tag{1.6}$$

It couples with the other gauge fields and with itself through

$$\mathcal{L}_H = (D_\mu \Phi)^\dagger (D^\mu \Phi) - V(\Phi) \ , \tag{1.7}$$

where the gauge invariant covariant derivative, D_μ, and the Higgs self–interaction,

---

[1]This manuscript follows the convention of the natural units, where the speed of light and the reduced Plank's constant are equal to one: $c = 1$. and $\hbar = 1$. This allows us to define mass and momentum in energy units, in this text mostly GeV and TeV.

(**Φ**), are defined as

$$D_\mu = \partial_\mu + i g_{\mathrm{W}} W^a_\mu \frac{\tau^a}{2} + i g' \frac{Y}{2} B_\mu$$

$$(\Phi) = \mu^2 \Phi^\dagger \Phi + \frac{\lambda^2}{2} (\Phi^\dagger \Phi)^2 \ ,$$

$$(1.8)$$

with g' being the Abelian U(1) coupling, λ and μ are constant parameters, τ^a are the Pauli matrices, which constitute a basis for the Lie algebra of SU(2), and g_{W} is the non–Abelian SU(2) gauge coupling constant defined in Eq. 1.3.

The potential in Eq. 1.8 has a vacuum expectation $v/2 = \mu/\lambda$, where $v \approx 246$ GeV, denoted as the Higgs vacuum expectation value, and is determined from the muon lifetime measurement [12]. As a consequence, the bosons associated to the fields in Eq. 1.7 and the Higgs field, acquire the following masses:

$$\mathrm{M_W} = \frac{v g_{\mathrm{W}}}{2} \ , \quad \mathrm{M_Z} = \frac{v}{2}\sqrt{g'^2 + g^2_{\mathrm{W}}}, \quad \text{and} \quad \mathrm{M_H} = v\lambda. \tag{1.9}$$

The Higgs boson was discovered in 2012 by the CMS and ATLAS experiments at LHC [13, 14], with the data collected during the years 2010 to 2012 at $\sqrt{s} = 7$ TeV and 8 TeV, corresponding to an integrated luminosity of 5.1 pb^{-1} and 5.3 pb^{-1}, respectively. The measured Higgs boson mass is 125.25 ± 0.17 GeV [6], extracted from LHC Run 2 data. In this work, the possibility of the Higgs boson of being a composite particle will be explored (explained in Section 1.2.5).

The W and Z boson masses, $\mathrm{M_W}$ and $\mathrm{M_Z}$, are related by the SU(2)$_{\mathrm{L}}$ and U(1)$_{\mathrm{Y}}$ gauge coupling constants, and the ratio between them are associated to the weak mixing angle or Weinberg angle, θ_W, as follows:

$$\cos\theta_W = \frac{\mathrm{M_W}}{\mathrm{M_Z}} = \frac{g_{\mathrm{W}}}{\sqrt{g'^2 + g^2_{\mathrm{W}}}} \tag{1.10}$$

This angle represents the rotation of the original W^3 and B (from Eq. 1.3) vector boson plane, producing as a result the Z boson and the photon:

$$\begin{pmatrix} \gamma \\ Z^0 \end{pmatrix} = \begin{pmatrix} \cos\theta_W & -\sin\theta_W \\ \sin\theta_W & \cos\theta_W \end{pmatrix} \begin{pmatrix} B \\ W^3 \end{pmatrix} \tag{1.11}$$

The fermionic part of the Lagrangian has one term describing the interactions with the boson fields, $\mathcal{L}_F$, and another term where the Yukawa couplings between fermions and the Higgs boson give rise to the fermion masses, $\mathcal{L}_Y$. The fermion

fields, ψ_i, for each of the family, i, are define as follows for the quarks:

$$\psi_1 = \begin{matrix} u \\ d \end{matrix}_L, \quad \psi_2 = u_R, \quad \psi_3 = d_R$$

$$\psi_1 = \begin{matrix} c \\ s \end{matrix}_L, \quad \psi_2 = c_R, \quad \psi_3 = s_R \tag{1.12}$$

$$\psi_1 = \begin{matrix} t \\ b \end{matrix}_L, \quad \psi_2 = t_R, \quad \psi_3 = b_R$$

The same is defined for leptons using ν_e and e instead of u and d, and for the other quark and lepton families:

$$\psi_1 = \begin{matrix} \nu_e \\ e \end{matrix}_L, \quad \psi_2 = e_R, \quad \psi_3 = \nu_{eR}$$

$$\psi_1 = \begin{matrix} \nu_\mu \\ \mu \end{matrix}_L, \quad \psi_2 = \mu_R, \quad \psi_3 = \nu_{\mu R} \tag{1.13}$$

$$\psi_1 = \begin{matrix} \nu_\tau \\ \tau \end{matrix}_L, \quad \psi_2 = \tau_R, \quad \psi_3 = \nu_{\tau R}$$

With this definition, the interaction between gauge boson fields and fermions can be written using the covariant derivative of Eq. 1.8 as:

$$\mathcal{L}_F = \sum_j i\bar{\psi}_j(x)\gamma^\mu D_\mu \psi_j(x) \tag{1.14}$$

And the fermion mass term as:

$$\mathcal{L}_Y = -\sum_f M_f \bar{\psi}_f \psi_f - \sum_f \frac{M_f}{v} \bar{\psi}_f \psi_f H, \tag{1.15}$$

where M_f is the mass of the fermions, which depends on the Yukawa coupling constant g_f: $M_f = g_f v / \sqrt{2}$.

With this Lagrangian the mass eigenstates for fermions are defined, but for quarks they do not correspond with the weak eigenstates. There is a mixing between flavours when there are charged currents involved, which is represented by a unitary matrix, called Cabibbo–Kobayashi–Maskawa (CKM) [15, 16].

1.1.2   Quantum Cromodynamics

The interaction that binds quarks together to form hadrons, like the proton, is the so–called strong interaction, and it is described mathematically by Quantum Cromodynamics (QCD). QCD is a non–Abelian gauge theory represented by the $SU(3)_C$ group, where the charge is called *colour*. Gluons are the QCD mediators, they are spin–1 bosons that carry color charge, and quarks are the fundamental

representation of the SU(3)$_C$ group, constituting a colour triplet.

Since the gluons carry colour charge, there are gluon–gluon interactions in QCD. This causes an antiscreening effect due to gluon pairs in the vacuum, which results in the running coupling constant of QCD, α_s, becoming stronger at higher distances. This leads to *colour confinement*, which implies that quarks cannot be observed freely, and only colourless hadrons made of two or three quarks, denoted as mesons and baryons, respectively, exist in Nature. A quark or a gluon produced in a high energy interaction hadronizes by combination with quark–antiquark pairs spontaneously created from the vacuum, until reaching a colour–neutral state, and producing a cascade of baryons and mesons. This effect is produced when colliding protons, and the experimental signature in the detectors of such cascades are called jets (detail in Section 3.5).

At high energies, however, particles interacting at a short distance or with a high energy transfer behave almost like free particles, due to the low value of α_s. This is known as *asymptotic freedom*, and is the scenario that governs in the proton–proton collisions that we study in this work.

The QCD Lagrangian has two terms: the gauge field propagation and self–interaction, and the quark–gluon interaction. A basis for the Lie algebra of SU(3) is formed by the eight Gell–Mann matrices λ^a, that do not commute with each other. Due to this, QCD is also referred as a non–Abelian theory. The field strength $G_a^{\mu\nu}$ has the following gauge invariant form

$$G_a^{\mu\nu} = \partial^\mu G_a^\nu - \partial^\nu G_a^\mu - g_s f^{abc} G_b^\mu G_c^\nu \,, \tag{1.16}$$

where the last term represents the gluon–gluon interaction, which is proportional to the strong coupling constant g_s, related with the running constand as $\alpha_s = g_s^2/4\pi$, and the structure constants f^{abc} defined by the commutator $[\lambda_a, \lambda_b] = i f^{abc} \lambda_c$. The QCD Lagrangian can be written as:

$$\mathcal{L}_{QCD} = -\frac{1}{4} G_a^{\mu\nu} G_{\mu\nu}^a + \mathcal{L}_F \,, \tag{1.17}$$

where the fermionic Lagrangian $\mathcal{L}_F$ of Eq. 1.14 contains an additional term to preserve the QCD gauge invariance, which is introduced in the covariant derivative:

$$D'_\mu = D_\mu - g_s \sum_f \bar{\psi}_f \gamma_\mu G_a^\mu \frac{\lambda^a}{2} \psi_f \tag{1.18}$$

Putting all together, the final QCD Lagrangian has the following form:

$$\mathcal{L}_{QCD} = -\frac{1}{4} G_a^{\mu\nu} G_{\mu\nu}^a + i \sum_f \bar{\psi}_f (\gamma^\mu \partial_\mu - M_f \bar{\psi}_f) \psi_f - g_s \sum_f \bar{\psi}_f \gamma_\mu G_a^\mu \frac{\lambda^a}{2} \psi_f \tag{1.19}$$

The non–Abelian nature of the generators of the SU(3) matrices gives rise to cubic and quartic self–interactions of the gluon field. The SU(3) symmetry forbids a mass term and the gluons have to be massless.

In the process of building the Standard Model it was introduced 26 free parameters: 3 gauge couplings, 6 mixing angles, 12 masses (6 of the quarks and 6 of the leptons), 2 boson masses, 2 CP–violating phases, and 1 CP–violating angle.

1.2 Beyond the Standard Model

As mentioned in the introduction of this chapter, the SM has been a very successful theory, explaining most fundamental processes mediated by the electroweak and strong interactions. Its formulation has allowed the model to be predictive and thus experimentally tested, up to very high level of accuracy. However, despite the success of incorporating the Higgs mechanism in a rather natural way, this theory is clearly incomplete and can be regarded as an effective theory, valid in a limited range of the energies, or equivalently, masses scale.

The current situation in Particle Physics, closely related to that in Astrophysics and Cosmology fields, is such that several theoretical models are out in the scientific landscape, trying to complete or extend the SM and give answer to some of the still non–understandable processes. There is nowadays no plausible BSM theory, with clear and unique predictions to confront the experimental data. All available at the moment are models or frameworks based on, new particles, or new symmetries or interactions, or new spatial dimensions, which depend on a set of given parameters. Depending on the particular free parameters considered and their values, there can be concrete realization of given models. These scenarios allow for qualitative and quantitative predictions, taking into account the limited validity of the simplified scenario considered.

1.2.1 Sequential Standard Model

The sequential standard model (SSM) [17] has been used as a benchmark in this search. This model predicts the existence of the W' boson, a heavy analog of the SM W boson, with the same left–handed couplings to fermions as the W of the SM described in the previous Section 1.1. The decays are also assumed to be the same as the SM partner. The LO Feynman diagram for the production and decay of a W' boson in the $\mu + \nu$ final state, is shown in Figure 2.

The Lagrangian terms that describe the potential interaction of the W' boson with fermions are given by [18]:

$$\frac{W'_\mu}{2\sqrt{2}} [\bar{u}_i (\ ^R_{qij} P_R + \ _{qij} P \ ) \gamma^\mu d_j + \bar{\nu}_i (\ ^R_{lij} P_R + \ _{lij} P \ ) \gamma^\mu e_j] , \qquad (1.20)$$

where $i = 1, 2, 3$ refers to the three fermion generations, u, d, ν, and e represent the SM fermions in the mass eigenstate basis, $P_R = (1 + \gamma^5)/2$ and $P = (1 - \gamma^5)/2$ the
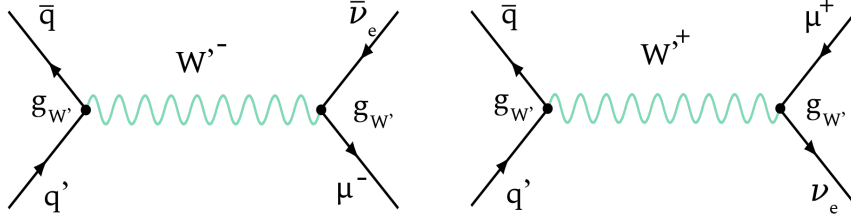
Figure 2: SSM W' LO production Feynman diagrams, decaying into muon and neutrino.

right and left chirality projectors matrices, and and ^{R} are complex dimensionless parameters. Using this notation, the SM W couplings are $= g_W \approx 0.65$, $= g_W$ $_{KM}$, and $^R = {}^R = 0$.

Since the W' mass is larger than the $t\bar{b}$ threshold, $M_{W'} > 180$ GeV, on the contrary than the SM W boson, the $t\bar{b}$ decay channel is available, while diboson decays, WZ and WH, are assumed to be suppressed.

According to the Lagrangian expressed above, the width of the W' boson, Γ, and the mass, $M_{W'}$, depends on its coupling, $g_{W'}$, as follows:

$$\frac{\Gamma}{M_{W'}} = N_c \frac{g_W^4}{48\pi g_{W'}^2},$$

(1.21)

where g_W is the SM weak coupling strength, $g_W \approx 0.65$ [6], and N_c is the number of colors, it is 3 for the di–quark, and 1 for the di–lepton. Therefore, the branching fraction, $\mathcal{B}$, of each leptonic decay is:

$$\mathcal{B}(W' \to \nu) = \frac{N_c(\ )}{N_c(f)} = \frac{1}{3+3+3+1+1+1} \approx 0.083$$

(1.22)

where denotes lepton and f denotes fermion. These assumptions yield a predicted leptonic branching fraction of $\mathcal{B}(W' \to \nu) \approx 8.3\%$, for each of the leptonic channels (e, μ, τ). The corresponding hadronic branching fraction is $\mathcal{B}(W' \to {}^-) \approx 25\%$, for each of the hadronic decay modes $(u\bar{d}, c\bar{s}, t\bar{b})$. Notice that these branching fractions are slightly different from those of the SM W boson. For the SM W boson, the leptonic branching ratio is $\mathcal{B}(W \to \nu) = (10.86 \pm 0.09)\%$ [6].

As can be seen, the phenomenology from this model depends basically on the mass of the new boson and on its coupling to SM particles. The signature of a W' boson is a Jacobian peak in the transverse mass distribution. Constraints on the parton distribution function (PDF) are responsible for a large fraction of off–shell production at low transverse mass for very large W' masses.

Interference between the SM W and the SSM W' is not considered in the study of this model since it is a second order effect in the assumption of a resonance being generated [19, 20, 21]. In the case of a discovery, the study of an interference would

provide information about the W' properties.

Coupling strength variation

The W' boson coupling strength, $g_{W'}$, is usually given in terms of the SM weak coupling strength, g_W. If the W' is a copy of the SM W boson, their coupling ratio is $g_{W'}/g_W = 1$, and the SSM W' theoretical cross sections, signal shapes, and widths apply. However, different couplings are possible.

The width of the W' boson, Γ, relative to the mass, $M_{W'}$, depends on its coupling, $g_{W'}$, as in Equation 1.21, and for the case of the leptonic decay, $N_c = 1$, is as follows:

$$\frac{\Gamma}{M_{W'}} = \frac{g_W^4}{48\pi g_{W'}^2},$$

(1.23)

A variation on the coupling strength ratio, $g_{W'}/g_W$, is also explored, because the dependence of Eq. 1.23 implies modifications in the expected width of the resonance and in its production cross section.

Previous searches

Models proposing the existence of W' also include a Z' vector boson. Searches for these new particles date back to last century, already at LEP experiments. The use of the SSM as a benchmark model used as a reference point for experimental W' boson searches for decades. With a center–of–mass energy of 1.96 TeV, in the Tevatron accelerator, the first searches with proton–antiproton collisions took place. Experiments D0 and CDF established the mass limits of $M_{W'} > 1.0$ TeV [22] with an integrated luminosity of $1\,\text{fb}^{-1}$, and $M_{W'} > 1.1$ TeV [23] with $5\,\text{fb}^{-1}$, respectively, examining the electron + neutrino final state.

The W' boson searches were among the first analyses to be performed at the LHC, exploiting the large center–of–mass energy. First results by CMS were published with Run 1 data, an integrated luminosity of $5.0\,\text{fb}^{-1}$ at $\sqrt{s} = 7$ TeV, and a further $3.7\,\text{fb}^{-1}$ at $\sqrt{s} = 8$ TeV, setting an observed (expected) limit in the W' mass of $M_{W'} > 2.9\,(2.9)$ TeV [24], combining muon and electron channels. With $19.7\,\text{fb}^{-1}$, the full luminosity taken at $\sqrt{s} = 8$ TeV, a new W' search was performed setting an observed (expected) limit in the W' mass of $M_{W'} > 3.3\,(3.3)$ TeV [25]. With the same analysis, limit on the W' coupling strength ratio was set to $g_{W'}/g_W < 0.7$, for a $M_{W'} \sim 3$ TeV.

With the first data collected after increasing the energy at 13 TeV, the search was already more sensitive, even if the integrated luminosity was still $2.3\,\text{fb}^{-1}$, reaching a mass limit of $M_{W'} > 4.1\,(4.0)$ TeV [26], with the CMS experiment.

1.2.2   Split–UED model

Other possible extensions of the SM include additional spatial dimensions, in an effort to incorporate gravitational effects to the quantum world.

Experimental results in astroparticles measurements by the PAMELA exper-

iment, showed an excess on the positron flux over the sum of the electron and positron fluxes with respect to the standard astrophysical expectation [27]. This excess was confirmed by the AMS experiment with more statistics and individual measurements of the positron and electron fluxes [28]. Universal Extra Dimension (UED) [29] models offer a possible explanation of such deviation by introducing an extra parity, called Kaluza Klein (KK)–parity, where the lowest KK–state is stable and is a Dark Matter candidate [30]. However, no excess in antiproton flux has been observed by the same experiments, and thus, the UED model needs to be modified to reduce the hadronic branching fraction and be consistent with the measurements.

The Split–Universal Extra Dimension model [31] solves this problem by introducing an spectrum of quarks in the extra dimension *split* from the other particles. This way, the dark matter particles would annihilate mainly into leptons and the hadronic production would be suppressed by the heavier quarks.

The leptonic final states under study in this work may also be interpreted in the framework of Split–UED with fermions propagating in the extra dimension (or bulk) [32, 33]. The Split–UED model is parametrized by the radius of the additional compact fourth spatial dimension, R, and the bulk mass parameter of the fermion field in five dimensions, μ. In this model all SM particles have corresponding KK–partners, $W_{KK}^{(n)}$ would be the KK–partner of the W boson, where the superscript denotes the nth KK–excitation mode. Only KK–even modes of $W_{KK}^{(n)}$ couple to SM fermions, owing to KK–parity conservation.

In the Split–UED model the parameter μ is assumed to be non–zero, and the mass of the $W_{KK}^{(n)}$ is determined by

$$M_{W_{KK}^{(n)}}^2 = M_W^2 + (n/R)^2, \qquad (1.24)$$

a larger radius (R) corresponds to smaller KK–masses. The mass of KK–fermions, $M_{W_{KK}^{(n)}}^2$, depends on the bulk mass parameter μ through its coupling, g_n, as follows:

$$g_n = g_W \mathcal{F}_n(\pi\mu R) \qquad (1.25)$$

where $\mathcal{F}_n$ is the wave function of the overlap between the nth KK–gauge boson and the SM fermions:

$$\mathcal{F}_n(x) = \begin{cases} 0 & \text{if } n = 2\ell+1 \\ \dfrac{x^2(-1+(-1)^\ell e^{2x})(\coth x - 1)}{\sqrt{2(1+\delta_{\ell 0})}(x^2+\ell^2\pi^2/4)} & \text{if } n = 2\ell \end{cases} \qquad (1.26)$$

The product of the cross section of the $W_{KK}^{(n)}$ production and the branching fraction to standard model fermions goes to zero as μ goes to zero.

The mode $n = 2$ is particularly interesting in this analysis. Because KK–odd

10

modes of W_n are not allowed to couple with SM fermions due to the KK–parity conservation, and $W_{KK}^{(2)}$ is the lowest mode which couples with SM fermions. The $n \geq 4$ modes have no sensitivity at current center of mass energy and luminosity. Since the $W_{KK}^{(2)}$ has even KK–parity it can be produced singly. Furthermore, the decay of $W_{KK}^{(2)}$ to leptons is kinematically identical to the SSM W' boson decay, and the observed limits obtained from the W'$\rightarrow \mu\nu$ search can be reinterpreted directly in terms of the $W_{KK}^{(2)}$ boson mass. The Feynman diagram in Figure 3 shows this process.
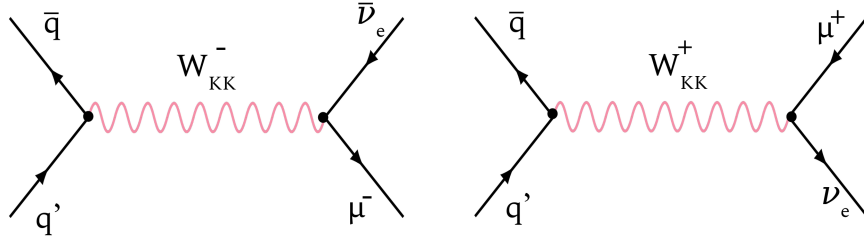
Figure 3: LO Feynman diagrams for $W_{KK}^{(2)}$ production in Split–UED model.

Previous searches

In a general extra dimension scenario, a gauge boson KK–excitation could be searched through its decay to SM gauge bosons. Analyses from CMS [34] and AT-LAS [35] have set a lower limit on the mass of this KK–boson of ~ 2.5 TeV. More specifically, in the UED scenario, using Run 1 data collected from the LHC experiments, the combination of several final states allowed to set a lower bound on $1/R$ of 1.5 TeV [36, 37].

Finally, in the model explored by this work, the Split–UED model, the $W_{KK}^{(2)}$ boson was searched with the CMS experiment in the lepton (electron or muon) and missing energy final state, with $19.7\,\mathrm{fb}^{-1}$ at $\sqrt{s} = 8$ TeV, and the observed limit of the $W_{KK}^{(2)}$ mass was set to $M_{W_{KK}^{(2)}} > 1.75$ TeV assuming a bulk mass parameter $\mu = 0.05$ TeV, or to $M_{W_{KK}^{(2)}} > 3.71$ TeV for $\mu = 10$ TeV [25].

1.2.3 RPV SUSY with a scalar lepton mediator

A more complete model from the theoretical point of view is Supersymmetry (SUSY) theory [38, 39]. This model is based in a new fermion–boson symmetry which predicts that each spin–1 gauge bosons of the SM have spin–1/2 superpartners, and all the spin–1/2 fermions of the SM have spin–0 superpartners. Based on this new fermion–boson symmetry, matter particles appear all as bosons, while interaction particles are fermions. These supersymmetric particles lie at a higher mass values once the symmetry has been broken.

In SUSY extensions of the SM, particles are assigned the R–Parity (R_P) quantum number. The SM particles are defined to have even R_P, and their corresponding superpartners have odd R_P.

The supersymmetric partner of the SM τ lepton is the scalar $\tilde{\tau}$, with subsequent R–Parity and lepton flavor violating decay to a charged lepton (electron or muon) and a neutrino [40, 41, 42]. The decay of the slepton $\tilde{\tau}$ to SM muon and neutrino has the same signature studied in this analysis, as shown on the diagrams in Figure 4.
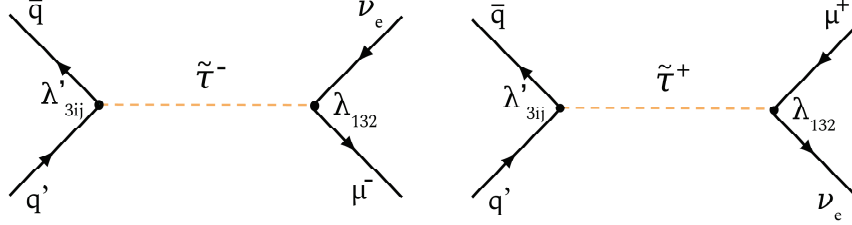
Figure 4: Feynman diagrams for τ slepton mediator in RPV SUSY model in the muon decay channel.

The production coupling is a version of the hadronic–leptonic RPV coupling λ'_{3ij}, which is the coupling to the third generation, the τ slepton. The decay is governed by the leptonic RPV coupling λ_{132} for the $\mu + \nu_e$ decay channel.

Previous searches

In models that conserve R–Parity supersymmetric particles are always produced in pairs. The $\tilde{\tau}$ supersymmetric particle is searched in its decay channel to a SM tau lepton and a massless lightest neutralino that leaves no signature in the detector. In the final state of two τ leptons and missing transverse energy, $\tilde{\tau}$ masses in the range $M_{\tilde{\tau}} = (120\text{–}390)$ GeV [43] are excluded with Run 2 data.

Previous searches on sleptons in R–Parity violating model, the one explored in this work, were carried oute by LEP experiments. The lower limit on the $\tilde{\tau}$ mass was set to $M_{\tilde{\tau}} > 96$ GeV [44, 45].

1.2.4   Oblique electroweak parameters

In the models previously described there is always the assumption of a resonance being produced. The experimental analysis is thus prepared accordingly, to observe a "peak" in the tail of the mass distribution reconstructed from the decay products, resembling the resonance mass, with a given width, assuming a width as large as $\sim 10\,\%$ of the resonance mass. In this scenario, the benchmark presented so far works reasonably well and their predictions are taken as valid. Outside the resonance mass region the simplified model treatment is not necessarily correct, as other effects may come into action. Among such effects there might be interference with the known SM particles (bosons), or the presence of a large tail in the mass distribution towards lower values, due to the kinematic limit imposed by the proton PDFs, or the existence of contact interactions coming from new particles at even higher masses.

The case of a potential resonance outside the kinematic reach of the LHC collider is thus not addressable with a resonance search. But that does not mean we

are totally blind to its existence, especially if the resonance lies "not far away" from the kinematic limit. We still have sensitivity to its presence by means of EWK precision variables such as *S*, *T*, *W*, *Y* [46, 47]. These variables are $S = T = W = Y = 0$ in the SM, they encode any deviation of experimental measurements from their SM prediction, and a different value from 0 means a signal for new physics. These variables, also called oblique parameters, are severely constrained by experimental data, mainly coming from LEP, especially *S* and *T* [6, 47]. The other two parameters, *W* and *Y*, on the other hand, grow with the energy of the process, $\sqrt{s}$, and their constraints are much weaker. Not only that, current LHC experimental data, even if not as precise as that from LEP regarding EWK variables, reach center of mass energies in partonic processes much above those at LEP, therefore they provide a larger capability to measure them.

Quantitatively and with a general spirit, one can write a Lagrangian incorporating up to dimension six operators involving only *H*, *W* and *B* fields, where *B* stands for the mixture of photon and Z particles (defined in Eq. 1.3). This corresponds to hypothetical new physics effects related to electroweak symmetry breaking (EWSB), without considering new strong interactions, and nor flavour violation up to the scale one is testing.

In the presence of non–vanishing *W* and *Y* parameters, the propagators of the SM neutral (γ, Z) and charged (W) electroweak gauge bosons should be modified [48] as:

$$
\begin{aligned}
P_W(\hphantom{q}^2, W, Y) &= \frac{1 + ((2t^2 - 1)W + t^2 Y)/(1 - t^2)}{\hphantom{q}^2 - M_W^2} - \frac{W}{M_W^2} \\[6pt]
P_\gamma(\hphantom{q}^2, W, Y) &= \frac{1}{\hphantom{q}^2} - \frac{t^2 W + Y}{M_Z^2} \\[6pt]
P_Z(\hphantom{q}^2, W, Y) &= \frac{1 - W - t^2 Y}{\hphantom{q}^2 - M_Z^2} - \frac{t^2 Y + W}{M_Z^2} \\[6pt]
P_{\gamma Z}(\hphantom{q}^2, W, Y) &= \frac{t(c^2 Y + s^2 W)}{(c^2 - s^2)(\hphantom{q}^2 - M_Z^2)} + \frac{t(Y - W)}{M_Z^2}
\end{aligned}
\tag{1.27}
$$

where $\hphantom{q}^2$ is the energy–squared of the hard collision and $t \equiv \tan\theta_W$, $c \equiv \cos\theta_W$, $s \equiv \sin\theta_W$, are trigonometric functions of the SM weak mixing angle, θ_W. Note that the neutral term $P_{\gamma Z}$, absent in the SM, accounts for a γ–Z mixing effect induced by new physics. A simple physical example is the presence of a new Z' boson which mixes with both the photon and the Z boson.

W oblique parameter determination from the charged current

In the case of a final state of a charged lepton plus a neutrino, the interpretation of the dilepton mass spectra is done in terms of the measurement on the *W* and *Y* parameters, since the corresponding propagator is P_W from Eq. 1.27. In that

case, the propagator given by the SM is $P_W^{(0)} \equiv 1/(q^2 - M_W^2)$ and that the relative deviations with respect to the SM is given by the ratio $|P_W/P_W^{(0)}|^2$:

$$\left| \frac{P_W}{P_W^{(0)}} \right|^2 = \left(1 + \frac{(2t^2 - 1)W}{1 - t^2} + \frac{t^2 Y}{1 - t^2} - \frac{W(q^2 - M_W^2)}{M_W^2} \right)^2 \tag{1.28}$$

This ratio is used as a weight, applied directly at generator level on a $W \to \mu\nu$ simulation, generated according to the SM predictions. The distribution to be reweighted is the transverse mass, M_T, of the decay products, $\mu + \nu$. The resulting M_T distributions are distributed according to the new physics deviations defined by the parameters W and Y.

As seen in Eq. 1.28 the ratio (weight) only depends on the q^2 of each collision, the invariant mass of the $\mu + \nu$ system (at the hard scattering level) at an event–by–event basis.

Current bounds on W and Y are already rather stringent $(< 10^{-2})$ [49]. This implies that the terms that do not depend on q^2 are negligible in practice, leading to a weight that is effectively independent of Y:

$$\text{Weight}(q^2, W, Y) \xrightarrow[\text{large } q^2]{} \left(1 - \frac{W q^2}{M_W^2} \right)^2 \equiv \text{Weight}(q^2, W) \tag{1.29}$$

which shows explicitly the leading quadratic dependence of the new physics deviations with the hard collision energy. The dependence of the weight with the generated mass (q) of the W ($\mu + \nu$ system) is presented in Figure 5, for the W oblique parameter values of $W = -10^{-3}$ (left) and $W = 10^{-3}$ (right). One can see the largest weights correspond to the highest mass values.
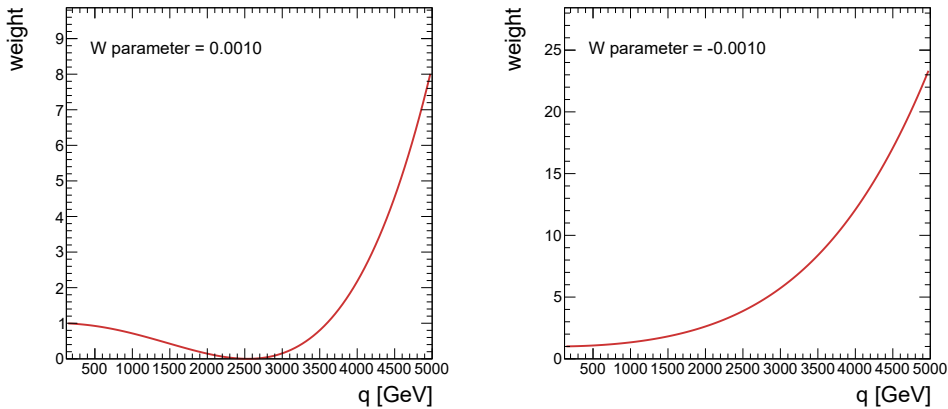
Figure 5: Dependence of the weight with the generated mass (q) of the W ($\mu + \nu$ system) for W oblique parameter values of $W = -10^{-3}$ (left) and $W = 10^{-3}$ (right).

W and Y oblique parameters determination from the neutral current

A similar procedure is adopted for the neutral dimuon final state, using $pp \to Z \to$ events. In this case, the implementation of the reweithing factor, is more compli- cated, but also straight forward.

In order to simplify the notation we re–denote the vector and axial couplings of the photon and the Z to fermions as follows:

$$
\begin{aligned}
v_f^\gamma &= g_W \sin\theta_W Q_f \\
a_f^\gamma &= 0 \\
v_f^Z &= \frac{g_W}{2\cos\theta_W} (\ _3 - 2Q_f \sin^2\theta_W) \\
a_f^Z &= \frac{g_W}{2\cos\theta_W} \ _3
\end{aligned}
\tag{1.30}
$$

where Q_f is the charge of the fermion in positron charge units and $_3$ is the third component (either $+1/2$ or $-1/2$) of its weak isospin. The differential cross section for the $^- \to ^-$ process away from the Z resonance peak, neglecting fermion masses and taking into account all possible propagator contributions is given by [50]:

$$
\frac{d\sigma}{dz}(\ ^2, z, W, Y) = \frac{^2}{32\pi} \ _{i=1}^{4} \ _{j=1}^{4} P_i(\ ^2, W, Y) P_j(\ ^2, W, Y) \left[B_{ij}(1+z^2) + 2\ _{ij} z \right]
\tag{1.31}
$$

where $z \equiv \cos\theta$, being θ the polar angle of the final state lepton with respect to the initial state quark in the $^-$ center–of–mass frame system. We can interpret the full amplitude of the process as the addition of four different terms. Two of them ($i = 3, 4$) are actually absent in the SM; they correspond to a mixing scenario between the photon and the Z, and include photon couplings to one of the fermion pairs and Z couplings to the other fermion pair. Schematically, the four amplitudes could be visualized as:

$$
\begin{aligned}
i = 1: \quad & ^- \to [\gamma^* \to \gamma^*] \to \ ^- \\
i = 2: \quad & ^- \to [Z^* \to Z^*] \to \ ^- \\
i = 3: \quad & ^- \to [\gamma^* \to Z^*] \to \ ^- \\
i = 4: \quad & ^- \to [Z^* \to \gamma^*] \to \ ^-
\end{aligned}
\tag{1.32}
$$

The propagator factors P_i are identified with the propagators that have been intro- duced in Eq. 1.27:

$$
\begin{aligned}
P_1(\ ^2, W, Y) &= P_\gamma(\ ^2, W, Y) \\
P_2(\ ^2, W, Y) &= P_Z(\ ^2, W, Y) \\
P_3(\ ^2, W, Y) &= P_{\gamma Z}(\ ^2, W, Y) \\
P_4(\ ^2, W, Y) &= P_{\gamma Z}(\ ^2, W, Y)
\end{aligned}
\tag{1.33}
$$

Finally, the coefficients B_{ij} and $_{ij}$ are simple functions of the SM vector and axial couplings to the photon and the Z:

$$B_{ij} = (v_\ell^i v_\ell^j + a_\ell^i a_\ell^j)(v^i v^j + a^i a^j)$$
$$_{ij} = (v_\ell^i a_\ell^j + a_\ell^i v_\ell^j)(v^i a^j + a^i v^j) \tag{1.34}$$

with the following mapping between v_f^i, a_f^i and the couplings that were introduced at the beginning of this section:

$$v^i \equiv v^\gamma, \ a^i \equiv a^\gamma; \ i = 1, 3$$
$$v^i \equiv v^Z, \ a^i \equiv a^Z; \ i = 2, 4$$
$$v_\ell^i \equiv v_\ell^\gamma, \ a_\ell^i \equiv a_\ell^\gamma; \ i = 1, 4$$
$$v_\ell^i \equiv v_\ell^Z, \ a_\ell^i \equiv a_\ell^Z; \ i = 2, 3 \tag{1.35}$$

The event weight is the ratio between the differential cross section in the presence of deviations from the SM (Equation 1.31) and the differential cross section predicted in the absence of them (SM case):

$$\text{Weight}(^2, z, W, Y) = \frac{\frac{d\sigma}{dz}(^2, z, W, Y)}{\left[\frac{d\sigma^0}{dz}(^2, z)\right]} \tag{1.36}$$

Note that $d\sigma^0/dz(^2, z)$ is just given by the differential cross section of Equation 1.31 evaluated at $W = Y = 0$, explicitly:

$$\frac{d\sigma^0}{dz}(^2, z) = \frac{2}{32\pi} \sum_{i=1}^{2} \sum_{j=1}^{2} P_i^0(^2) P_j^0(^2) \left[B_{ij}(1 + z^2) + 2_{ij} z \right], \tag{1.37}$$

with:

$$P_1^0(^2) = \frac{1}{2}$$
$$P_2^0(^2) = \frac{1}{^2 - M_Z^2} \tag{1.38}$$

The ratio (weight) now depends not only on the ^{2} of each collision and the invariant mass of the $\mu^+\mu$ system, also on the flavor of the incident quarks and the angle of the final state leptons with respect to the initial state quarks.

1.2.5 Higgs Compositeness

Some BSM models predict the Higgs boson to be a composite particle emerging from a strong interacting sector as a pseudo–Goldstone boson [51]. There are 2 parameters characterizing these models: the mass of the new resonances ($_*$) and

their coupling (g_*).

We explore two possible ways to obtain information from the new composite sector using an effective low energy approach at the energy scales of the LHC: indirectly exploring the new gauge force, and being directly sensitive to the spectrum of new resonances that might be generated.

In the first case, indirectly exploring the new gauge force that may lie at very high energy scales, above the currently accessible ones at the LHC, one can use the measurement of the W oblique electroweak parameter, as a way to quantify deviations from SM. In that case the relation that holds for these parameters is [51]:

$$g_*{}^2 = \frac{g_W^2 M_W^2}{W_*{}^2} \tag{1.39}$$

where g_W is the SU(2)$_L$ SM gauge coupling, and M$_W$ the W boson mass.

In the second case, the direct search for production of resonances is directly exploited. That is the case of a potential W' boson as in the SSM, that could be a composite resonance of more fundamental constituents. In that assumption the gauge coupling to the new composite scale is screened by the presence of the resonance and thus seen at low energy in the form g^2/g_*, i.e.

$$g_{W'} = \frac{g_W^2}{g_*} \tag{1.40}$$

being $g_{W'}$ the W' boson coupling strength. We will make use of these relations to set constraints on the g_*-$_*$ plane using the W' search analysis.

In a more general and model independent way the Lagrangian terms expressing deviations relative to the SM one, and corresponding to dimension–6 operators, can be written as

$$\mathcal{L}_{\text{universal}}^{\text{dim}=6} = c_H \frac{g_*^2}{M_W^2} \mathcal{O}_H + \frac{1}{g_*^2{}_*^2} [c_{2W} g_W^2 \mathcal{O}_W + c_{2B} g'^2 \mathcal{O}_{2B}] + \frac{1}{{}_*^2} [c_W \mathcal{O}_W + c_B \mathcal{O}_B] + ... \tag{1.41}$$

where c_H, c_{2W}, c_{2B}, c_W, and c_B are dimensionless parameters of order 1, $\mathcal{O}_H$, $\mathcal{O}_{2W}$, $\mathcal{O}_{2B}$, $\mathcal{O}_W$, and $\mathcal{O}_B$ are dimension–6 operators accounting for effects linked to the Higgs boson, the W boson and a mixture of Z boson and γ. The couplings g_W and g', presented above, are the SM couplings of the W and B (mix of Z and γ) bosons, respectively. The first term is related to the Higgs boson, acting as a global scaling of all Higgs couplings by a common factor. The second and third terms are related to 4–fermion or 2–fermion–2–bosons contact interactions, respectively, and to the effective coupling to the potential W' and Z' resonances.

Using a third complementary approach, additional constraints are placed in the g_*-$_*$ plane when applying current measurements of the Higgs boson cross section from a combination of production mode and decay channels [52]. In this

case, the new interactions would modify the SM predictions for Higgs production and decay, generating an extra contribution to the Higgs kinetic term in the effective Lagrangian [51]. The corresponding modification would scale as

$$\Delta\mu = \frac{g_*^2 v^2}{2_*},$$ (1.42)

where μ is the measured Higgs boson cross section relative to that of the SM one, and v is the EW symmetry breaking scale, $v = 246$ GeV [6].

The analysis of the experimental data presented in this work is interpreted in terms of all the models presented above, in an attempt to extract as much information as possible from the $\mu + p_T^{miss}$ final state.

Chapter 2

Experimental setup

When experimentally looking for new physics effects, various paths can be taken that span astrophysical and cosmological surveys or particle physics experiments with or without colliders. Accelerator facilities offer numerous advantages such as that the energies of the beams are under control and the interactions take place at a specified location where detectors are installed. And, in particular, hadron colliders are ideal to search for exotic processes since both, QED and QCD interactions are involved.

The Large Hadron Collider (LHC) at the CERN laboratory is the largest and most powerful, hadron collider of the world, colliding proton beams at a center of mass energy of 13 TeV, and collecting an immense amount of data. High energy and large data statistics, are both crucial conditions to explore the limits of the SM and search processes beyond the Standard Model, as the one presented in this thesis.

The LHC offers a unique opportunity to explore Particle Physics up to the TeV energy scale. The particles resulting from the collided protons and heavy ions collisions are detected by the Compact Muon Solenoid (CMS) experiment. This chapter describes the essential features of the LHC accelerator and the CMS detector, which are relevant for this work.

2.1   Large Hadron Collider

The Large Hadron Collider (LHC) is the largest and most powerful particle accelerator in the world [53]. It is located at the CERN laboratory near Geneva, in the French–Swiss border. The LHC is composed by two circular rings in a tunnel of 27 km length, built at around 100 m underground. This is the tunnel that used to host the previous Large Electron–Positron (LEP [54, 55]), which took data from 1989 to 2000. Depending on the physics program, the LHC provides collisions of protons or heavy ions such as lead and xenon.

Figure 6 shows the CERN's complex with the full accelerator chain. Initially, hydrogen atoms are ionized and the resulting protons are injected to the injector chain [56] by LINAC2, where they are accelerated passing through a series of circular synchrotrons: BOOSTER, Proton Synchrotron (PS), Super Proton Synchrotron

(SPS) and finally, injected into the LHC.
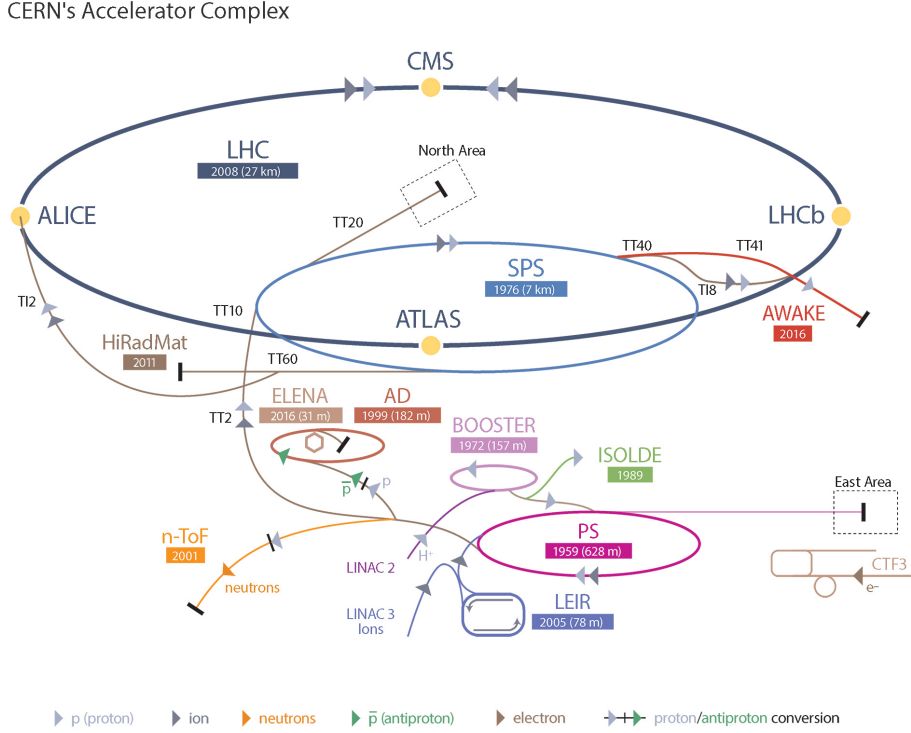
Figure 6: CERN's Accelerator complex [57].

At LHC, the beams circulate along opposite directions on each of the rings, bent by 1232 superconducting magnets cooled down to 1.9 K. Beams of protons and also, in a reduced running time, heavy nuclei such as those of Pb or Xe, were collided in the machine, with the aim of developing a wide scientific program.

The LHC started to operate in 2009 and, after a period of commissioning, provided proton collisions at a centre of mass energy, $\sqrt{s}$, of 7 TeV during 2010 and at $\sqrt{s} = 8$ TeV during 2011 and 2012, in what it is called the Run 1 period. After maintenance and improvement work, the LHC went through a new period, Run 2, of increased $\sqrt{s}$ at 13 TeV, lasting from 2015 to 2018. A new period, Run 3, is foreseen to start next year, in 2022, with a $\sqrt{s}$ between 13 TeV and 14 TeV.

The beams are focused using quadrupole magnets and intersect in four collision points, where the four main detectors, ATLAS [58], CMS [59], ALICE [60] and LHCb [61] are located. The four experiments are designed to detect and reconstruct the proton and heavy ions collisions provided by the LHC. While ATLAS (A Toroidal LHC ApparatuS) and CMS (Compact Muon Solenoid) are general–purpose detectors, ALICE (A Large Ion Collider Experiment) and LHCb (LHC beauty) experiments are focused in the study of Quark Gluon Plasma (QGP) and b quark physics respectively.

Some of the interesting processes where used to look for BSM physics, in par-

ticular those presented in this thesis, happen not only at high energies, but also with low cross section values. To produce enough statistics of such rare processes it is necessary to have a high number of proton–proton collisions, and the magnitude to measure the number of collisions is the *luminosity*.

2.1.1 Luminosity

Protons in the beams travel in groups of n of them called, bunches, in order to maximize the probability of interaction in the collision while having control over the size and position of the beam, and they cross with a frequency, f. The beam shape and dispersion are described by two parameters: the transverse emittance, ϵ, and the amplitude function, β^*. The transverse emittance is the transverse opening of the beam, in the space–momentum phase space, giving an idea of how close are the beam protons in position and momentum. The amplitude function is the distance from where the beam is focused to the point where the beam width is twice as wide.

The instantaneous luminosity, $\mathcal{L}_{ins}$, is the amount of collisions that are produced per unit of time and area, and it is calculated as follows:

$$\mathcal{L}_{ins} = f \frac{n_1 n_2}{4\epsilon\beta^*} \tag{2.1}$$

Typical values for these parameters at LHC during Run 2 data taking were $\epsilon = 3.75\,\mathrm{mm}\,\mu\mathrm{rad}$, $\beta^* = 0.55\,\mathrm{m}$, $f = 40\,\mathrm{MHz}$, and the number of protons in each bunch, $n = 1.2 \times 10^{11}$. With these values, a nominal instantaneous luminosity of $10^{34}\,\mathrm{cm^{-2}\,s^{-1}}$ is obtained, with a maximum obtained during Run 2 of $2.06 \times 10^{34}\,\mathrm{cm^{-2}\,s^{-1}}$. Further description of the beam parameters can be found in [62].

The expected rate of events produced in a given process with a cross section, σ, is given by

$$\frac{dN}{dt} = \sigma \mathcal{L}_{ins} \tag{2.2}$$

and therefore, high luminosity values are needed in order to study physical processes with a low production cross section. The total number of events over a time period is proportional to the integrated luminosity:

$$\mathcal{L}_{int} = \int \mathcal{L}_{ins}\,dt \tag{2.3}$$

The instantaneous luminosity is measured in the hadronic forward calorimeters and calibrated using Van der Meer scans [63]. The scans are performed by varying the separation of the beams, and the resulting profile of luminosity as a function of the separation is fitted in order to determine the beam overlap width, from which the luminosity is calculated. Figure 7 shows the total luminosity delivered by the LHC and the one recorded by the CMS experiment, corresponding to the Run 2 data taking period, spanning the years 2015 to 2018. The CMS recording efficiency is

greater than 90% every year, the small difference between both magnitudes is due to the short periods of time where CMS was not recording the collisions.
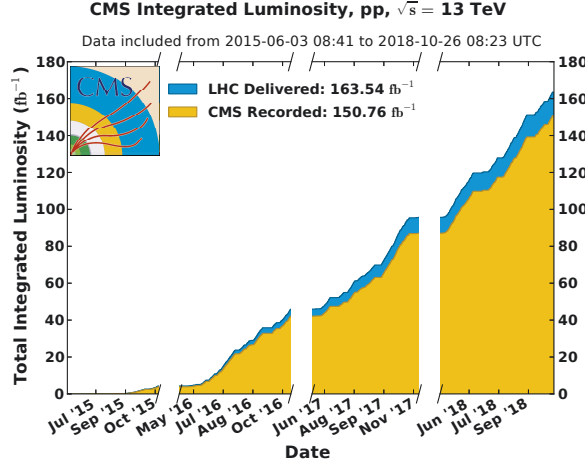
Figure 7: Integrated luminosity delivered by the LHC (blue) and recorded by CMS (yellow) during Run 2 [64].

2.2   Proton–proton collision phenomenology

This section describes the physics of a proton–proton collision and the processes from the beginning of the collision to the measurement of particles in the final state by the detector.

2.2.1   Parton distribution functions

Protons are not elementary particles, but composed of quarks and gluons, usually called partons. These partons are the particles that are actually interacting in the collisions. Thus at the LHC interactions take place among quarks ( ) and gluons (g):   , $^{\bar{}}$, g, gg. The initial energy of each incident parton is described probabilistically by a distribution, the parton distribution function (PDF), that describes the structure of the proton. The PDF, $f_a(x, Q^2)$, is defined as the probability density function of each type of parton, a, with a momentum fraction, x, of the proton's momentum, at a given energy scale, Q^2.

The factorization theorem [65] allows us to compute the cross section of any process in a proton–proton collision (p_1, p_2), $\sigma_{p_1 p_2 \to X}(s, Q^2)$, using a convolution with the PDFs:

$$\sigma_{p_1 p_2 \to X}(s, Q^2) = \sum_{ab} \int_{x_{min}}^{1} dx_1 dx_2 f_a(x_1, Q^2) f_b(x_2, Q^2) \hat{\sigma}_{ab \to X}(x_1 x_2 s, Q^2) \qquad (2.4)$$

where $\hat{\sigma}_{ab \to X}(x_1 x_2 s, Q^2)$ is the partonic cross section and it is evaluated using Feynman rules.

One of the most recent set of PDFs are the MSHT20 [66] determined from global

fits of the available hard scattering data up to date. Figure 8 shows the MSHT20 set of PDFs for different partons at energy scale of $Q^2 = 10^4$ GeV^2.
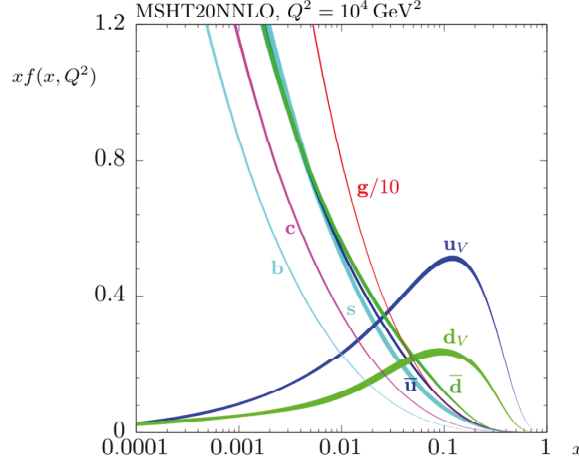
Figure 8: MSHT20 NNLO PDFs for different partons at the energy scale $Q^2 = 10^4$ GeV^2. The bands reflect the uncertainties at the 68 % confidence level [66].

In this work, the PDFs used depend on the dataset: NNPDF 2.3 [67] for 2016 data, NNPDF 3.1 [68] for 2017 and 2018 one. The NNPDF3.1 are more precise and accurate update of the PDF set with respect to the NNPDF 2.3. The improvement is achieved thanks to innovations in terms of methodology and experimental results included in the fits. [68].

2.2.2 The hard interaction

Among the possible interactions between proton beams collisions, the one characterized by the largest momentum exchange, Q^2, is called the *hard interaction*. The hard interaction for a process $ab \rightarrow X$ is characterized by the longitudinal momentum fraction x_1 and x_2 of the partons a and b, respectively. The partonic cross section $\hat{\sigma}_{ab} \rightarrow X(x_1 x_2 s, Q^2)$ is computed as the phase–space integral of the corresponding matrix element squared, $|\mathcal{M}_{ab \rightarrow X}|^2$. The matrix element, $\mathcal{M}_{ab \rightarrow X}$ is expressed as an infinite sum of a power series expansion in the QCD coupling, α_s, in a $ab \rightarrow X$ process:

$$\mathcal{M}_{ab \rightarrow X} = \sum_i^{\infty} \mathcal{F}_{ab \rightarrow X}^{(i)} \tag{2.5}$$

where each term of $\mathcal{F}_{ab \rightarrow X}^{(i)}$ corresponds to one allowed Feynman diagram. The lowest order Feynman diagrams in α_s are called Leading Order (LO) terms and next orders are called Next–to–Leading order (NLO), Next–to–Next–to–Leading order (NNLO), etc. LO calculation is the fastest calculation, but, usually, is not precise enough to predict the measurements, the NLO calculations include hard parton emission, the NNLO are more accurate, and so on. It should be stressed that the improvement in accuracy requires more calculation effort and computational time.

2.2.3 Parton shower and Hadronization

The final products of X in the $ab \to X$ processes are elementary particles: leptons, photons, quarks and gluons. When two quarks are pulled apart the energy content of the system is enough to cause new quark–antiquark pairs to be created and form new color singlet states. The emissions of radiation result in parton showers, where quarks emit gluons and gluons split into quark–antiquark or gluon–gluon pairs. The energy of the products is lower in each emission or pair production, until the production of fundamental particles is no longer energetically favourable and hadron formation becomes the dominant process.

Hadrons are only observed in color singlet states because of color confinement (explained in Section 1.1.2), therefore, in the final state the quarks and gluons cannot be found isolated, they form hadrons, which are neutral in color charge. This process is called hadronization and continues until all outgoing particles are color neutral. A representation of the processes between the initial parton and the final hadrons is shown in Figure 9.
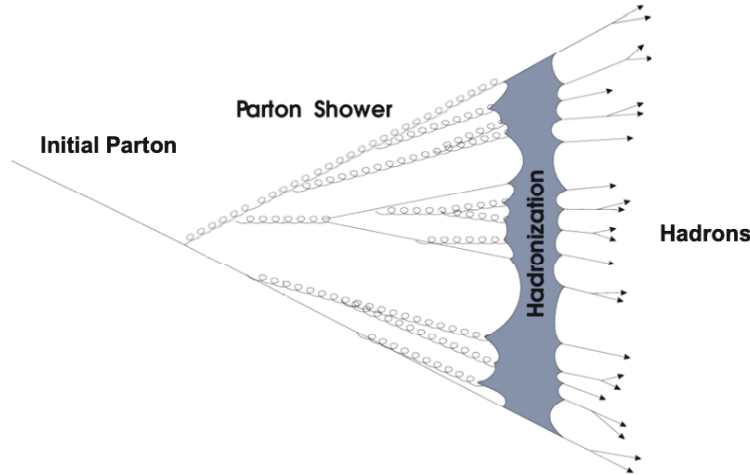
Figure 9: Sketch of the process starting with an initial parton, to parton shower, to hadronization to final detectable hadrons.

2.2.4 Pileup

Since protons travel in bunches of $\sim 10^{11}$ protons at the LHC beams, multiple proton–proton interactions may happen in one bunch–crossing. The number of additional interactions with respect to the collision with the hardest transferred momentum, is called *pileup* (PU). In hadron colliders, QCD processes are produced from parton interactions and the determination of the pileup becomes crucial.

Figure 10 shows the PU profile, and the average number of PU interactions for each year: 13 in 2015, 27 in 2016, and 38 in 2017, and 37 in 2018, and an average PU during Run 2 of 34 additional interactions. This reveals the increasing instantaneous luminosity achieved each year of data taking during Run 2 of the LHC.
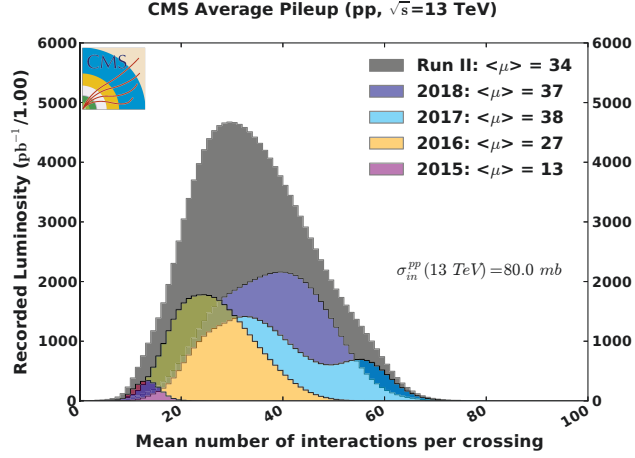
Figure 10: Mean number of interactions per crossing shown per year of data taking and for the whole Run 2 [64].

2.2.5 Underlying event

In parallel to the partons of the hard interaction other partons in the same colliding protons may also interact, with smaller transfer of momentum between them. These are multiple parton interactions, which together with the initial state radiation, final state radiation, and beam remnants, constitute the *underlying event* (UE), which represents the additional activity that is not part of the hard interaction. Figure 11 is a representation of the typical activity in a proton–proton collision, including hard scattering, parton shower, hadronization and the UE.
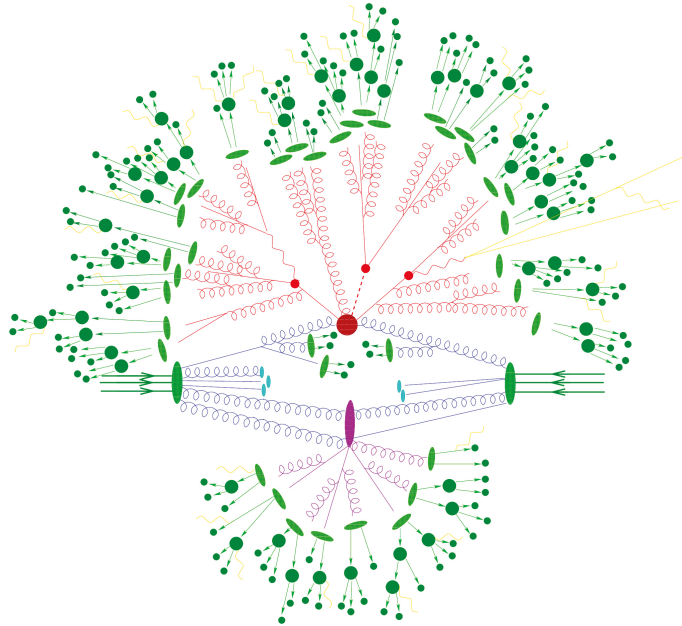
Figure 11: Representation of hard scattering, parton shower, hadronization and the underlying event, from a typical proton–proton collision.

The proton–proton interactions described above take place at each bunch–crossing at the LHC. In a parallel way, we also simulated them using computational programs and generators. From the process of parton interaction, PDF convolution, PU, and hadronization are modeled with the Monte Carlo (MC) generators. Current generators rely on phenomenological models to simulate the UE activity, and constrain their parameters using collision data. The calibration of the UE with data is referred to as the *tuning* of the generator. The UE tunings used in this work are CUETP8M1 [69] and CP5 [70], depending on the year of the data taking. The generation of events is made with the following software–packages: PYTHIA (LO) [71], POWHEG (NLO) [72, 73, 74], and MADGRAPH (NLO) [75, 76, 77].

Once the final state particles are produced, they travel across the CMS detector, interacting with the different subdetectors. In next section the description of the detector is presented.

2.3 Compact Muon Solenoid experiment

The CMS detector [59] layout is organized around a superconducting solenoid of 6 m internal diameter and 12.5 m length, providing a magnetic field of 3.8 T. The overall apparatus is rather compact: 21.6–metre–long, 14.6–metre–wide, 14000–tonne cylinder around the LHC beam axis. The overall layout of the detector is shown in Figure 12.

A right–handed Cartesian coordinate system is used to describe the CMS detector. The origin of the coordinate system is located at the nominal collision point. The z–axis coincides with the proton beam direction, the y–axis points vertically upward, and the x–axis points radially inward towards the centre of the LHC ring. Quantities are often referred to the $(x$–$y)$ plane, or transverse plane, and denoted in the text with a T subscript: X_T. The cylindrical coordinate system (z, ϕ, θ) as shown in Figure 13 is used in this text to refer any variable in the detector.

The variable *rapidity* (y) is defined as

$$y = \frac{1}{2} \ln \left(\frac{E + p_z}{E - p_z} \right) \tag{2.6}$$

for a particle with energy E, and momentum p_z along the beam axis. Differences in rapidity are invariant under Lorentz boosts, making this variable useful in hadronic collision studies. A convenient reformulation of the polar angle is the *pseudorapidity*, η:

$$\eta \equiv -\ln[\tan(\frac{\theta}{2})]. \tag{2.7}$$

The pseudorapidity is an easy variable to measure since the energy and the momentum vector of the particle are not needed, as opposed to the rapidity. The rapidity, one of the most convenient variable in collider physics, can be taken as the pseudorapidity for highly relativistic particles. In Figure 14 some values of θ with
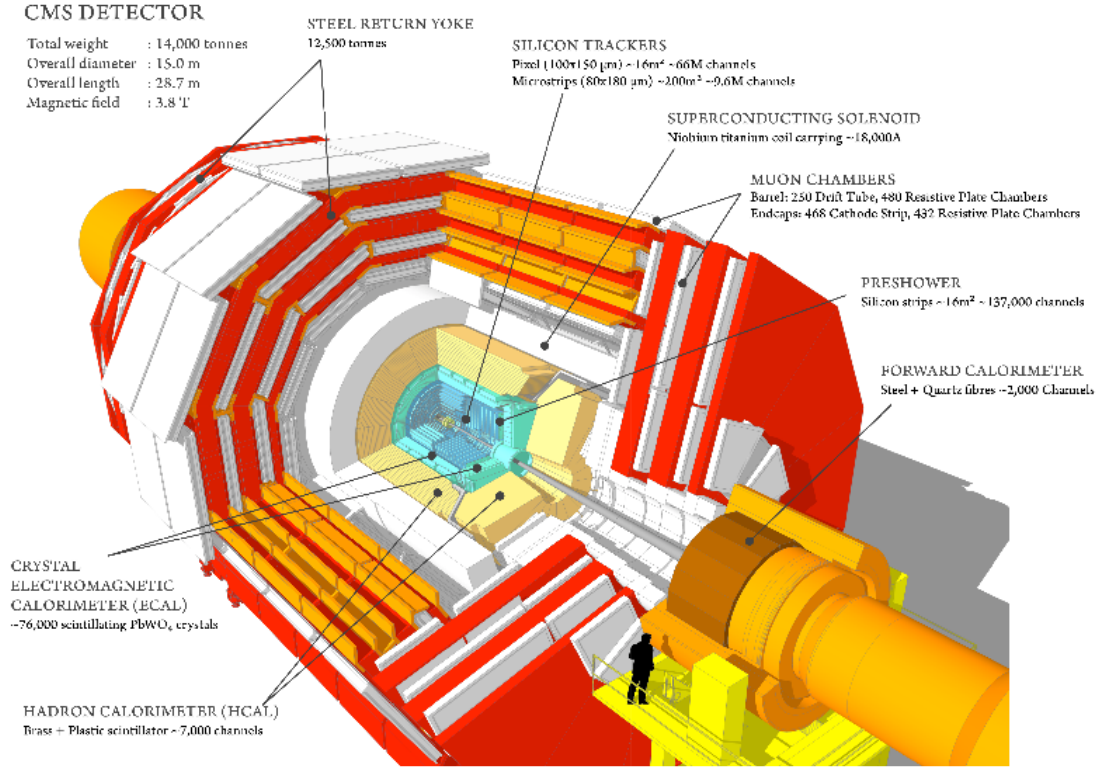
Figure 12: Schematic view of the CMS apparatus and its different subdetectors [78].
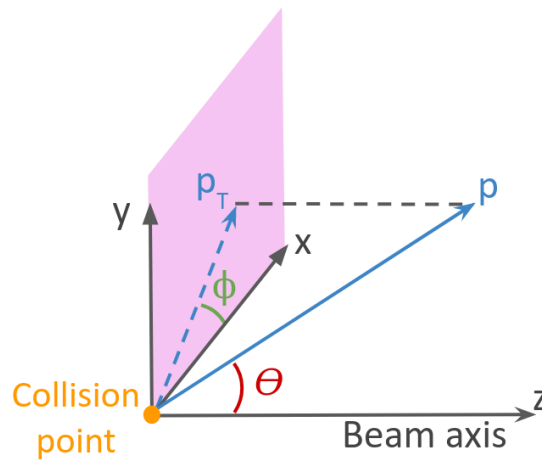
Figure 13: Coordinate system adopted by the CMS detector.

their corresponding η value are shown.

Figure 14: Correspondence between polar angle, θ and pseudo–rapidity, η.

The particle's momentum is determined by measuring the energy, p_T, η, and ϕ. They are related to the usual p_x, p_y and p_z by

$$p_x = p \sin\theta \cos\phi = p \quad \cos\phi \tag{2.8}$$

$$p_y = p \sin\theta \sin\phi = p \quad \sin\phi \tag{2.9}$$

$$p_z = p \cos\theta = p \quad \sinh\eta \tag{2.10}$$

Another useful variable that will be used later in this work, is the angular distance, ΔR, between two objects with coordinates (η_1, ϕ_1) and (η_2, ϕ_2):

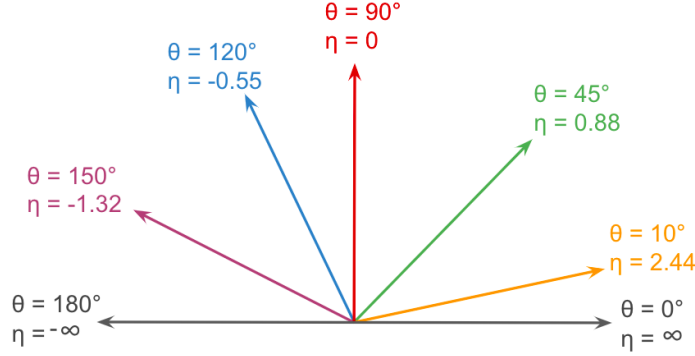$$\Delta R \equiv \sqrt{\Delta\eta^2 + \Delta\phi^2}, \tag{2.11}$$

where $\Delta\eta \equiv \eta_1 - \eta_2$, and $\Delta\phi \equiv \phi_1 - \phi_2$.

CMS is composed of various detectors referred as subdetectors. Within the solenoid volume there are three major subdetectors: a silicon Tracker which measures the trajectories of charged particles, a lead tungstate crystal electromagnetic calorimeter (ECAL) that collects the energies of electrons[1] and photons, and a scintillator hadronic calorimeter (HCAL) which stops the more penetrating hadrons and measures their energy. Extensive forward calorimeters complement the coverage provided by the barrel and endcap detectors. Muons are measured in gas–ionization chambers embedded in the flux–return yoke outside the solenoid. The details of each of the subdetectors are presented in the following sections.

2.3.1   Solenoid Magnet

The central feature of the CMS detector is a superconducting solenoid of $12.5\,\mathrm{m}$ length and $6\,\mathrm{m}$ internal radius, which provides a uniform magnetic field of $3.8\,\mathrm{T}$ [79] for the detectors inside its volume: the Tracker and the calorimeters.

---

[1]In this work, *electrons* refers to both, electrons and positrons, unless the opposite is explicitly said.

The magnet is made of four layers of NbTi superconducting coil and is placed within a vacuum tank cooled down to 4.7 K to maintain the superconducting regime. The return flux of the magnetic field proceeds along the 10k–tons iron yoke, disposed in five wheels and two endcaps, that are interleaved with the muon detectors.

The intense magnetic field enables the measurement of the transverse momentum of charged particles from their curved trajectories in the inner tracking system. The muon momentum is measured in addition in the Muon System, placed outside the solenoid volume, using the outer return flux of the magnetic field.

2.3.2 Tracker

The Tracker system is the innermost detector of the CMS experiment. It occupies a cylindrical volume 5.8 m in length and 2.5 m in diameter, around the interaction point, and with its axis aligned to the LHC beam line. The sensitive part of the Tracker is built with silicon, since it resists well the high radiation levels produced in the collisions, and it provides the needed spatial, and thus momentum, resolution. It consists of two main detectors: a Pixel detector surrounding the beam pipe coping with larger particle densities, and a strip detector surrounding the Pixel detector. The overall layout of this system is shown in Figure 15, and a detailed description can be found in Reference [80].
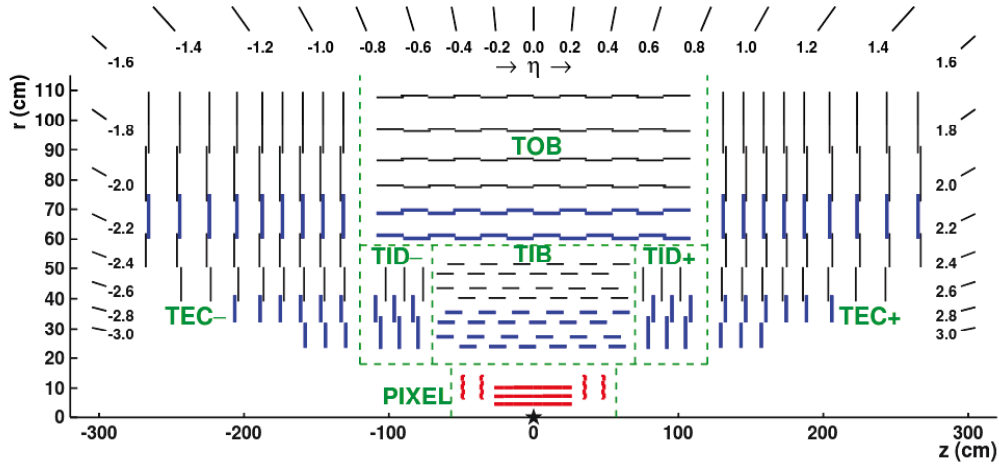
Figure 15: Schematic longitudinal section of the CMS Tracker, showing the inner Pixel detector (in red) with its barrel and endcap modules, and the strip detector with two collections of barrel modules, the Tracker Inner Barrel (TIB) and the Tracker Outer Barrel (TOB), and two collections of endcap modules, the Tracker Inner Disks (TID) and the Tracker EndCaps (TEC) [80].

The amount of material has to be kept to the minimum, in order to limit phenomena such as multiple scattering, bremsstrahlung and photon conversion which complicate particle reconstruction. The silicon detector technology used in the CMS tracking system addresses these needs by providing a large surface of thin, finely segmented, active detectors.

29

Thanks to the uniform magnetic field within its volume, this detector, which provides a precise and efficient measurement of the trajectories of charged particles emerging from the LHC collisions, gives consequently a precise measurement of their momentum. The transverse momentum resolution of muons of $p_T = 1$, 10 and 100 GeV is shown in Figure 16 as a function of the muon η. For 100 GeV momentum tracks, the transverse momentum resolution is ~1% up to $|\eta| \approx 1.6$. Beyond that it degrades due to the reduced lever arm.
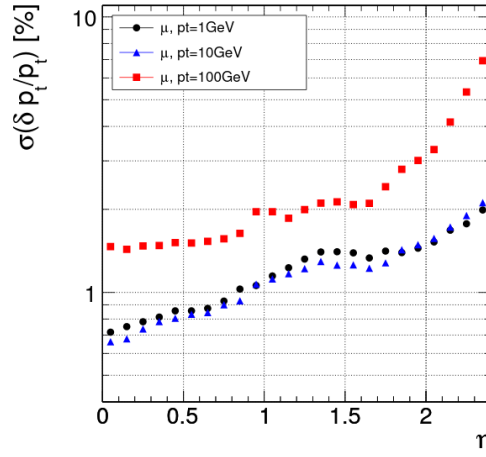
Figure 16: Muon transverse momentum resolution as a function of muon η for muons with transverse momenta of 1 GeV (black circles), 10 GeV (blue triangles), and 100 GeV (red squares), measured in simulation [59].

The tracking detector is finely segmented and equipped with fast readout on–board electronics. The fine spatial and temporal resolution provide efficient operation under high instantaneous luminosities ($\mathcal{L}_{ins} \approx 10^{34}\,\mathrm{cm}^{-2}\mathrm{s}^{-1}$) and bunch–crossing every 25 ns. The spatial measurement provided by the tracking system allows also the determination of the hard scattering interaction point, the primary vertex, and its discrimination against pileup interactions. The position resolution achieved for reconstructed primary vertices is $10 - 12\,\mu$m in each of the three spatial dimensions (details about the primary vertex is presented in Section 3.2). It also allows the reconstruction of in–flight decays and the determination of secondary vertices.

The tracking and vertexing tasks in CMS are performed using the Combinatorial Track Finder (CTF) software [80], an adaptation of the Kalman filter [81] that allows pattern recognition and track fitting to occur in the same framework. The collection of reconstructed tracks is generated by multiple iterations of the CTF track reconstruction sequence.

Pixel detector

The Pixel is the innermost detector. It is distributed concentrically in cylindrical layers surrounding the interaction point. In 2017, the detector was upgraded [82] by

moving the innermost layer closer to the interaction point, from 4.4 to 2.9 cm, and adding a new fourth outer layer at 16 cm and replacing the forward disks with 10 new Pixel disks on each of the forward regions. This new design is referred to as the Phase–1 version and its differences with respect to the previous version, Phase–0, are illustrated in Figure 17.
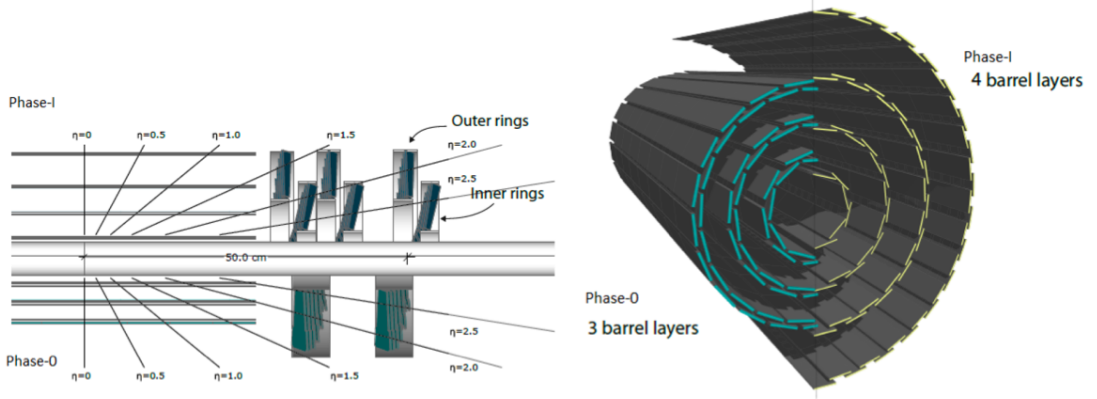
Figure 17: Pixel longitudinal view (left), comparing Phase–1 in the upper part with and Phase–0 in the lower part. Pixel barrel layers in a transverse–oblique view (right), comparing Phase–0 in the left side with Phase–1 in the right side [82].

The layout of the CMS Phase–1 Pixel detector is optimized to have four–hit coverage over the pseudorapidity range $|\eta| < 2.52$. It has an improved pattern recognition and track reconstruction, and added redundancy to cope with hit losses. It is built from 1856 segmented silicon sensor modules, where 1184 modules are used in the Barrel Pixel detector (BPIX) and 672 modules are used for the Forward Pixel (FPIX). Each module consists of a sensor with 160×416 pixels connected to 16 readout chips (ROCs). In total there are 124 million readout channels. Phase–1 is designed to operate at high luminosity, its efficiency at PU of 140 is as good as the Phase–0 efficiency at PU of 50.

The hit position resolution provided by the Pixel detector is $10\,\mu$m and $30\,\mu$m in the transverse and longitudinal position, respectively.

Strip detector

After traversing the Pixel layers, the charged particles enter the silicon strip system. Strip detectors measure the position of a traversing particle. The Strip Tracker consists of ten coaxial barrel layers extending outwards to a radius of 110 cm and three small, plus nine large disks in each of the endcap regions.

The Strip Tracker has 15148 silicon modules, which in total cover an active area of about 198 m^2 and have 9.3 million strips. It is composed of four subsystems as shown in Figure 15: inner barrel, disks, outer barrel, and endcaps. The Tracker Inner Barrel (TIB) and Disks (TID) cover r < 55 cm and $|z|$ < 118 cm, and are composed of four barrel layers, supplemented by three disks at each end. These provide position

measurements in $r\phi$ with a resolution of approximately 13–38 μm, depending on the position in ϕ and η. The Tracker Outer Barrel (TOB) covers r > 55 cm and $|z| < 118$ cm and consists of six barrel layers providing position measurements in $r\phi$ with a resolution of approximately 18–47 μm, depending on the hit position. Tracker EndCaps (TEC) cover the region $124 < |z| < 282$ cm. Each TEC detector is composed of nine disks, each containing up to seven concentric rings of silicon strip modules, yielding a range of resolutions similar to that of the TOB.

2.3.3   Electromagnetic calorimeter

The Electromagnetic Calorimeter (ECAL) is in charge of measuring the energy and position of photons and electrons, as well as contribute to the identification of electrons and pions and measurement of the energy in electromagnetic showers.

The ECAL detector is a hermetic, homogeneous calorimeter made of lead tungstate (PbWO$_4$) crystals. The PbWO$_4$ crystals are characterised for having a high density (8.28 g/cm^3), a short radiation length (0.89 cm), and a small Molière radius (2.2 cm), resulting in a compact calorimeter with a fine granularity.

The different parts of the ECAL cover a pseudorapidity up to $|\eta| = 3$. The ECAL detector is divided in three regions: a central region called barrel (EB) covering $|\eta| < 1.48$, two endcaps section (EE) with a $1.57 < |\eta| < 3$ coverage, and a preshower detector (ES) in front of the endcaps ($1.65 < |\eta| < 2.6$). A schematic layout of the ECAL can be seen in Figure 18 showing the barrel supermodules, the two endcaps and the preshower detectors.
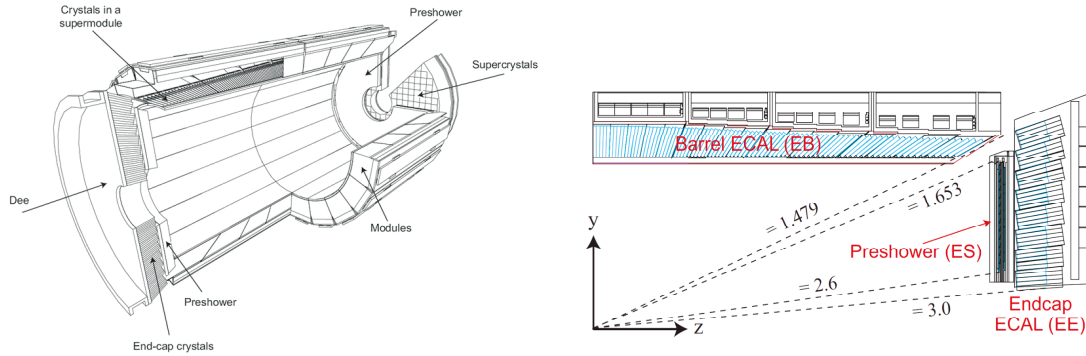
Figure 18: Schematic layout of the CMS ECAL showing the barrel supermodules, the two endcaps and the preshower detectors (left) [83]. Geometric view of one quarter of the ECAL (right) [84].

The EB crystals have a truncated pyramidal shape and are mounted to minimize inter–crystal gaps aligned to particle trajectories. The EB uses 23 cm long crystals with front face cross sections of around 2.2 cm × 2.2 cm, obtaining a crystal cross section of 0.0174 × 0.0174 in $\eta - \phi$, while the EE comprises 22 cm long crystals with front face cross sections of 2.86 cm × 2.86 cm, with a granularity progressively decreasing up to 0.05 × 0.05 in $\eta - \phi$. In the EB the crystals are organized in 36

supermodules, 18 on each side of the beam interaction point, and provide 360–fold granularity in ϕ and 85–fold granularity in each eta direction. The ES contains two active planes of silicon strip sensors and associated mechanics, cooling and front–end electronics. The sensors have an active area of $61\,\text{mm} \times 61\,\text{mm}$, divided into 32 strips. The planes closer to the interaction point have their strips aligned vertically while the farther plane strips are horizontal, to provide accurate position measurement and fine granularity in both coordinates.

The preshower detector, placed in front of the crystals, contains lead converters, followed by detector planes of silicon strips with a pitch of $2\,\text{mm}$. Its main function is to provide $\pi^0 - \gamma$ separation.

As shown in Figure 19, the electron energy resolution ranges $0.9 - 3.5\,\%$ in the central region of the ECAL and $2 - 5\,\%$ in the endcaps.
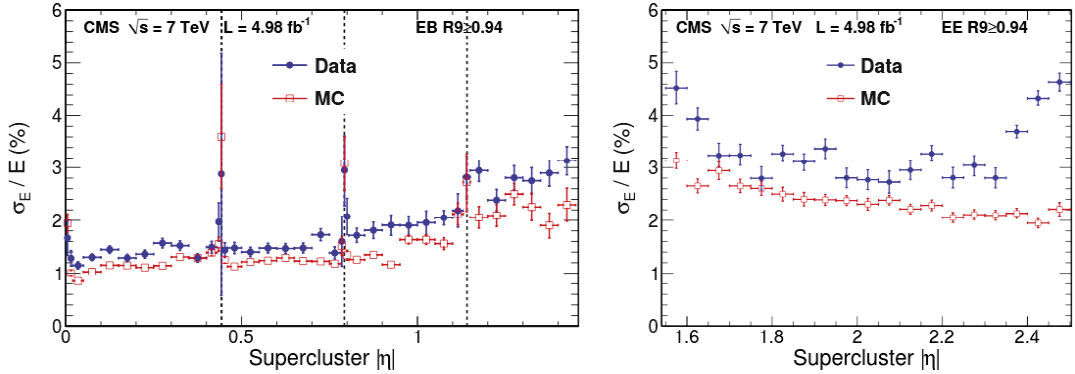
Figure 19: Electron energy resolution in data (blue) and MC simulation (red), as a function of the supercluster η, for the barrel (left) and the endcaps (right) [85].

To accommodate the mismatch in the energy resolution between data and simulation, an additional smearing term is extracted, which is the quadratic difference between the electron resolution in data and MC simulation of Figure 19. This term is added in quadrature as a constant Gaussian smearing to the electron and photon energy in the MC simulation.

A complete description of the ECAL, its calibration and resolution can be found in References [83, 86, 85].

2.3.4 Hadronic calorimeter

The Hadronic Calorimeter (HCAL) completely surrounds the ECAL, and its different subdetector covers pseudorapidity range up to $|\eta| = 5.2$. The energy and position of hadrons showers are measured in this sampling calorimeter. The HCAL is made of layers of a dense brass absorber and tiles of plastic scintillator. In the dense layers of the passive material the hadrons interact and in the plastic scintillator a rapid light pulse is produced when a particle passes through. The total amount of light produced by a shower provides a measurement of the energy of the particle that

initiated that shower. Figure 20 is a schematic layout of the HCAL, showing the different subsystems: barrel (HB), endcap (HE), outer (HO), and forward (HF).
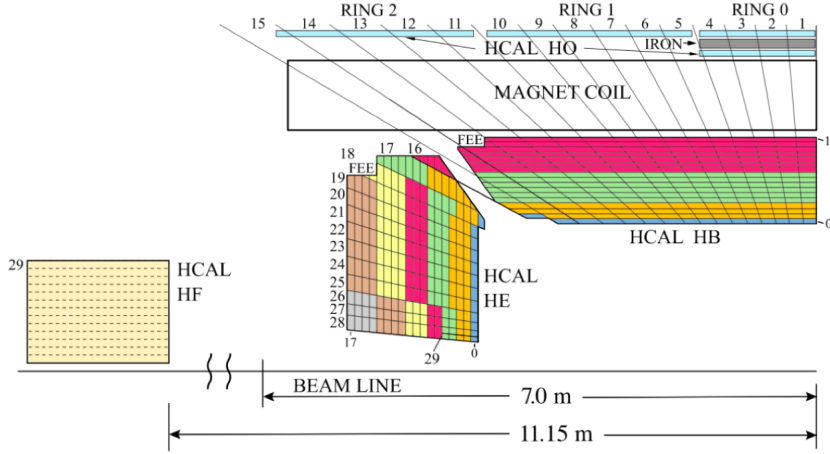
Figure 20: Longitudinal section of a quarter of the hadronic calorimeter, HCAL [87].

The HB is located between radii of 1775 and 2876.5 mm and covers $|\eta| < 1.39$. The HB is divided into two half–barrels in the direction along the beam (z), each assembled from 18 wedges. Each wedge subtends 20° in ϕ and extends to 4330 mm from the CMS detector mid–plane. A wedge contains absorber plates made of brass (an alloy with 70 % copper and 30 % zinc) that are bolted together. The inner and outer plates are made out of stainless steel. There are 17 slots per wedge that house the plastic scintillator tiles. The inner and outer slots are 14 mm thick while the remaining ones are 9.5 mm thick. The HB has about 40000 scintillator tiles.

The HE calorimeter is also made of brass absorber plates with sampling layers of plastic scintillator. The innermost surface of HE is located 4006.5 mm from the interaction point and covers $1.30 < |\eta| < 3.00$. Each endcap has an 18–fold symmetry in ϕ and has 34.5 mm thick sector plates each covering 20° in ϕ.

The HO calorimeter consists of one or two layers of scintillator outside the magnet coil. The entire assembly is divided into 5 rings, each having 12 sectors in ϕ. Six trays of scintillators are assembled on a honeycomb structure, which is then mounted in each of these sectors. The central ring (ring 0) has two layers of 10 mm thick scintillator on either side of a stainless steel block at radial distances of 3850 and 4097 mm, respectively. All other rings have a single layer at a radial distance of 4097 mm. The $\eta - \phi$ segmentation of the HO calorimeter matches closely that of the HB calorimeter. The HO calorimeter covers $|\eta| < 1.26$.

A complete description of the HCAL subdetector and its performance can be found in References [87, 88, 89, 90, 91].

2.3.5 Muon System

One of the main design objectives of the Compact Muon Solenoid was to obtain a high precision muon momentum measurement and trigger capabilities, given the

key role muons have in both, SM measurements, and in new physics searches.

Muons are characterized by their low interactivity with matter at typical LHC energy. When travelling between the collision point and the muon detection system, most particles get absorbed in the large amount of material present in their way, except for muons. They are able to travel outside the magnet since they are minimum ionizing particles.

CMS Muon System [92, 93] has three different kinds of gaseous chambers inserted in the segmented iron return yoke, as shown in Figure 21. The different particle flux and residual magnetic field found in the various angular regions covered by the muon detectors required the use of different technologies to build each subsystem. In the barrel, up to $|\eta| = 1.2$, the low occupancy and residual field led to the construction of the Drift Tubes (DT) stations situated concentrically around the magnet. In the endcaps, up to $|\eta| = 2.4$, the higher particle density and magnetic field require disks of finely segmented Cathode Strip Chambers (CSC), situated perpendicular to the beam. Both, DT and CSC chambers, determine the bending curvature of muons traversing them and thus they measure their transverse momentum and charge. The third kind of chambers, Resistive Plate Chambers (RPC), are situated both in barrel and endcaps. They aid in the triggering of muons up to $|\eta| = 1.6$ and complement the reconstruction of the muon trajectory.
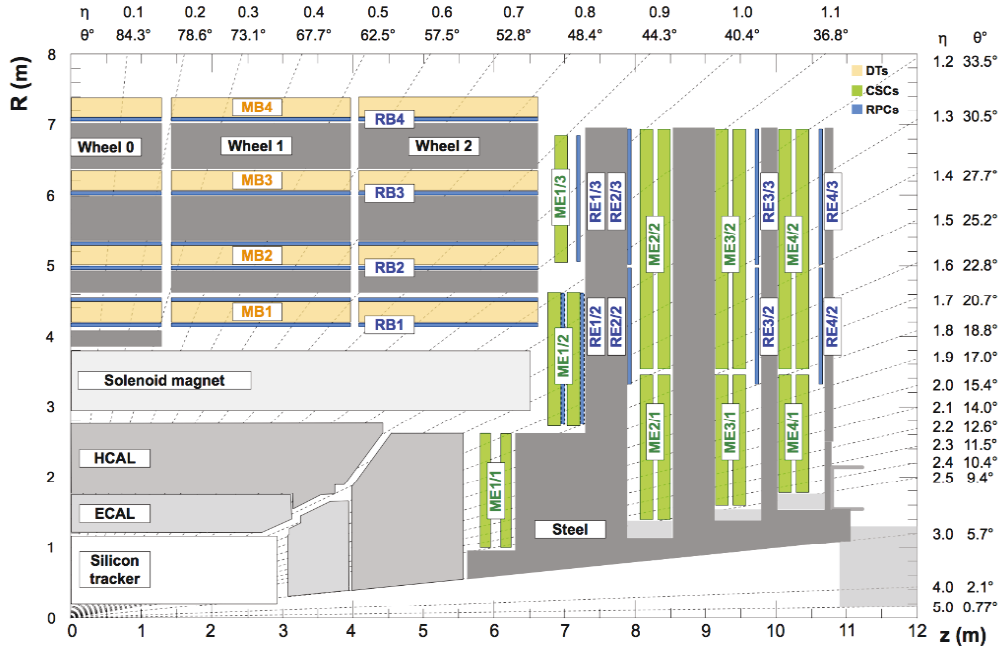
Figure 21: An R–z slice of a quadrant of the CMS detector. The origin of the axes represents the interaction point. The proton beams travel along the *z*–axis and cross at the interaction point. The three CMS muon subdetectors are shown: DT in yellow, labeled MB; CSC in green, labeled ME; and RPC in blue, labeled RB or RE

35

Muons that traverse a muon subdetector ionize the gas in the chambers, which causes electric signals to be produced on the wires and strips. These signals are read out by electronics and are associated with defined locations in the detector called *hits*. While the RPC chambers are single–layer chambers, the CSC and DT chambers are multi–layer detectors where hits are reconstructed in each layer. From the reconstructed hits, straight–line track *segments* are built locally within each CSC or DT chamber.

Tracks in the muon detector are built by combining the hits from the three muon subdetectors, DT, CSC, and RPC, using the Kalman–filter technique [81]. Afterwards, this track will be combined with a track in the Tracker detector to reconstruct the full muon track, as it will be explained in Section 3.3. From the curvature of the track, the muon transverse momentum and charge are determined.

Drift Tubes (DT)

The Drift Tube (DT) [94] system is designed to provide muon track reconstruction and first–level trigger selection. It also provides muon identification and an accurate transverse momentum measurement, in addition to single bunch–crossing identification with good time resolution.

The DT cells, illustrated in Figure 22 (right), have a central wire at a voltage of 3600 V, two electrodes (cathodes) on the sides at -1800 V, and two electrodes above and below the wires at -1800 V. The volume is filled with a $Ar(85\%)/CO_2(15\%)$ gas mixture. When a muon crosses the cell ionizes the gas and creates an electron drift with a velocity of about $55\,\mu$m/ns. This drift current is the experimental signature of the muon in the DT system. Considering the cell size of 42 mm, the maximum drift time is almost 400 ns.
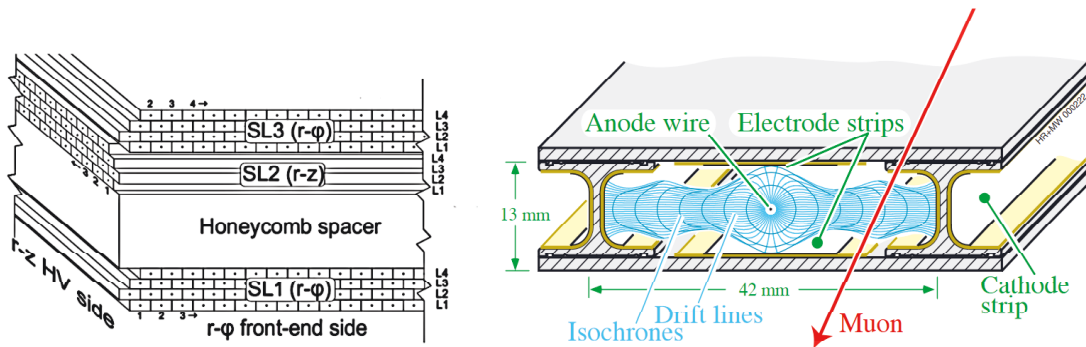
**Figure 22:** DT chamber scheme (left). Section of a drift tube cell showing drift lines (right) [95].

The basic physical module that operates independently, is called "chamber", shown in Figure 22 (left). The chambers are interleaved with the return yoke of the magnet and are composed of three groups, called Super–Layers (SL), of four staggered layers of independent drift cells. Two of the SLs have the wires parallel to the

beam direction and measure the $r\phi$ coordinate, the other SL has wires perpendicular to the beam direction and measures the z–coordinate, providing a 3D measurement of the muon track. The outermost station (MB4) is equipped with chambers containing only the two $r\phi$ Super–Layers. The fine segmented chambers in cells, and the good precision in measuring the drift time, allow the track segments to be reconstructed with a spatial resolution better than $100\,\mu$m along $r\phi$, and $150\,\mu$m along rz.

An assembly of chambers around a fixed value of r is called "station", and across the same ϕ is called "sector". The schematic view of the transverse plane is represented in Figure 23 - left with the stations noted as MB (Muon Barrel) and the sectors with numbers from 1 to 12. Along z, the stations are organized in "wheels". Figure 23 - right represents the longitudinal view of CMS with the wheels labeled from -2 to 2. In total there are 5 wheels, each one made of 3 stations of 12 sectors, and one station of 14 sectors, each sector is made of 4 Super–Layers, reaching a total of 250 DT chambers and 172,000 channels.
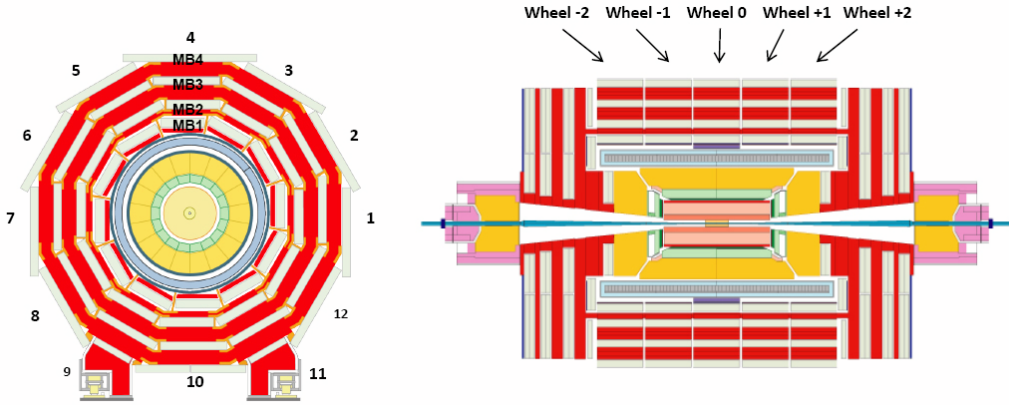
Figure 23: Schematic view of one of the five wheels of the muon barrel system of the CMS experiment, in the x–y plane (left). Longitudinal view of the CMS detector where the five wheels are visible (right) [96].

The CMS–CIEMAT group was responsible for the construction of the DT chambers in the second station, including their readout electronics and part of the alignment system between the Tracker and the Muon System. Validation, qualification and calibration of the chambers was performed at CIEMAT workshops, as well as in the CERN storage rings where they were deposited until final installation. Once in their final location they were once more tested and calibrated. Their operation and maintenance have been since then under CIEMAT's responsibility, among other institutes. Figure 24 shows an image of the DT chamber installation in one of the wheels.

Cathode Strip Chambers (CSC)
The Cathode Strip Chambers (CSC) have shorter drift path and faster time response.
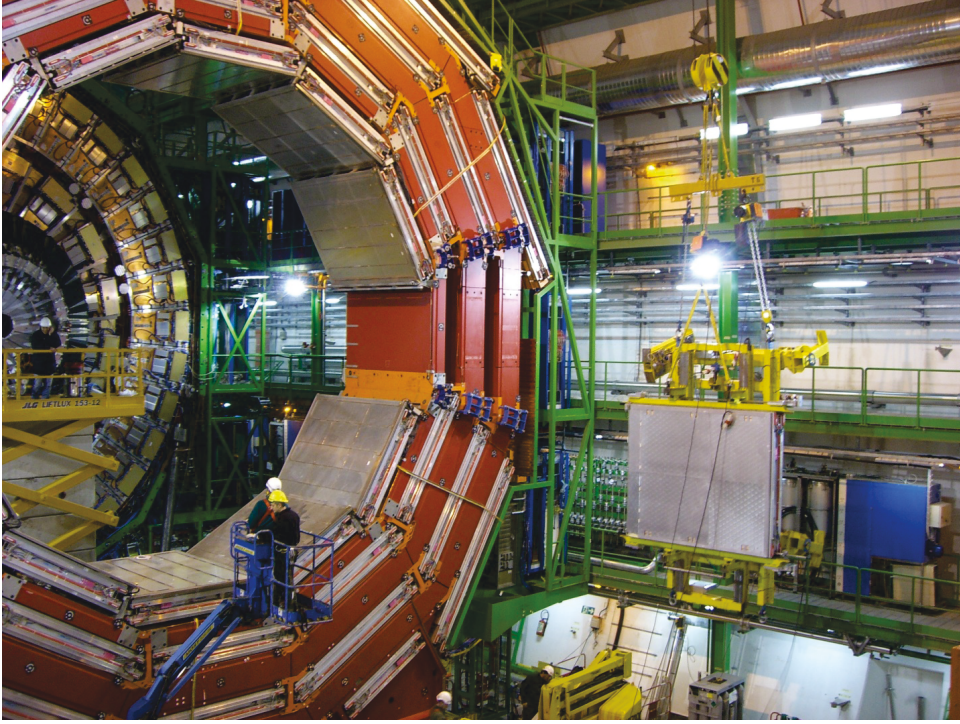
Figure 24: View of the CMS detector during the installation of the DT chambers built at CIEMAT.

For this reason they are located at the endcaps regions of CMS where the muon rates and particle multiplicities are higher.

In order to provide precise space and time information, the CSCs have closely spaced wires. This make the CSC a fast detector suitable for triggering. Each CSC chamber contains 6 layers, sandwiched between cathode panels, which independently measure the muon position in two coordinates, r and ϕ, while the z–coordinate is given by the chamber position. They are organized in 4 stations, with a total of 468 chambers.

Coordinate resolution is in the range of $47\,\mu$m to $243\,\mu$m, depending on the type and position of the chamber. The efficiencies for local charged track triggers, for hit and for segments reconstruction are above $99\,\%$. The timing resolution per layer is approximately $5\,$ns [97].

Resistive Plate Chambers (RPC)

The Resistive Plate Chambers (RPC) are fast gaseous detectors that provide a muon trigger system with a time resolution better than $3\,$s, complementary to those given by the DT and CSC chambers.

The RPC chambers consist of two parallel plates, a positively–charged anode and a negatively charged cathode, both made of a very high resistivity plastic material and separated by a gas volume.

They are distributed in stations attached to the DT and the CSC chambers as

shown in Figure 21. The strips are oriented parallel to the wires of the DT chambers in the barrel and parallel to the CSC strips in the endcaps. Thanks to this design they measure the coordinate in the bending plane $(r\phi)$ at all the detector.

2.3.6 Trigger

Given the high luminosity provided by the LHC collisions, the immense amount of information coming from the total of the detector cells, and the limited bandwith and storage capabilities, not every collision is recorded. The collaboration needs to implement triggering systems that select the most interesting collisions for recording. This extremely important system is called *trigger*.

Events of interest are selected using a two–level trigger system: first a hardware based trigger called Level–1 (L1) and second a software based, High Level Trigger (HLT). A more detailed description of the trigger system can be found in Ref. [98].

Level–1 Trigger (L1)

The Level–1 (L1) trigger [99, 100, 101], is composed of custom hardware processors that uses information from the calorimeters and muon detectors to reduce the readout rate from the 40 MHz bunch–crossing frequency to a maximum of 100 kHz, within a time interval of less than $4\,\mu$s.
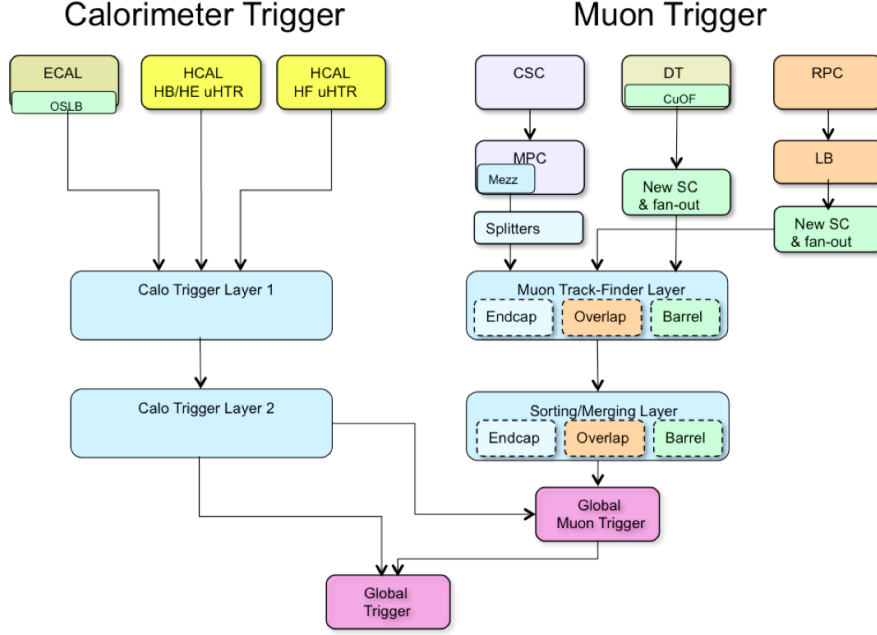
Figure 25 shows the schematic structure of the L1 trigger. In the muon detectors, first segments are formed in the CSC and DT detectors using the hits in the chambers, and RPC chambers provide hit information. Then, the information goes to the track finders that apply the pattern recognition algorithms to reconstruct the path, obtain muon candidates, and measure their transverse momentum from the bending in the transverse plane. The position in a chamber in the outer stations is extrapolated from the information of the inner stations and, if it agrees within a margin with a detected impact on the outer stations, a muon candidate is formed. The number of candidates is sorted and reduced, taking into account duplicated tracks from the same muon.

High Level Trigger (HLT)

Only L1 seeds passing the L1 trigger decision enter into the second step of the chain: the High–Level Trigger (HLT) [102]. The software–based HLT, consists of an array of processors running a version of the full event reconstruction software optimized for fast processing and it reduces the event rate to 1 kHz before data is recorded to storage.

In order to minimize the CPU required by the HLT, a key feature of the algorithms is the reconstruction of the information in the CMS detector only regionally. In many cases, the decision on whether an event should be accepted by the HLT involves the reconstruction of quantities in only a limited region of the detector. As an example, for an event accepted by the Level–1 trigger in the inclusive muon stream,

Figure 25: Schematic structure of the Level–1 trigger.

only the parts of the muon chambers indicated by the Level–1 trigger results, and the corresponding road in the Tracker, need be considered for the validation of the muon.

The criteria of the HLT to select or reject an event is as close as possible to the one used in the final analysis. Each set of selection criteria associated to a L1 seed is called an HLT path.

2.3.7 Computing system

After the trigger filtering of the events, petabytes of data are stored in tape per year. The CMS Collaboration uses an interconnection among computers from 170 computing centers from 42 countries, using the World–Wide LHC Computing Grid [103, 104].

The CMS Offline Grid Computing System [105] is arranged in four different layers or *tiers*. It starts from a single Tier–0, which is connected to the output of the Trigger System and the Online Data Acquisition System of CMS, at CERN, which performs a prompt reconstruction of the raw data to create datasets with the physical objects. Then, the data are distributed to the seven Tier–1 centers, located in different centers, such as PIC in Barcelona (Spain). These centers are in charge of data processing, performing reconstruction, and calibration. They provide the datasets for more than 50 Tier–2 centers, such as CIEMAT in Madrid, providing storage and computing capacity for both, the experimental data, and for the MC simulated samples used by the collaboration, as mentioned at the end of Section 2.2.5. Finally, there are numerous Tier–3 centers with smaller capacity that provide resources for local groups, and for scientific analysis of data.

The analyses in CMS are performed using a software framework that is available to the whole collaboration, called CMS Software (CMSSW). It is an object–oriented structure accessible with C++ and Python code. The CMSSW is constantly evolving according to each data taking period. It contains all the services needed by the simulation, calibration and alignment, and reconstruction. The CMS Event Data Model is centered around the concept of *event*. An event is a C++ object that contains the raw and reconstructed data related to a collision, and used as input for the scientific analysis.

2.3.8 Data samples

The CMS Collaboration uses various data formats depending on the amount of information needed and the level of processing. The RAW format, coming from the Tier–0, is the format with most information about the detector signal, and requires the most storage capacity. Then there are reconstructed (and re–reconstructed) formats with the event information processed by the Tier–1 and Tier–2 centers. Finally, the data format which contains all the information needed for CMS scientific analyses with all the reconstructed objects and a smaller size is the Analysis Object Data (AOD). Similar formats reduced in size such as miniAOD (used in this analysis), and nanoAOD, contain the important physics information of the event while having a reduced size.

The format in which the data are stored and analysed is ROOT [106] files, which contain all the event object information and kinematics. A ROOT file has tree–like structure with the variables as branches, and the events as histogram entries.

The set of data analyzed in this work corresponds to those from LHC Run 2 period. This includes data from 2015 to 2018. The small amount of data collected in 2015 ($2.3\,\mathrm{fb}^{-1}$ of integrated luminosity) was analyzed and published [26]. This analysis focuses only on the data from the years 2016, 2017 and 2018. In this text it will be referred as Run 2 period, even if the 2015 has not been considered.

From the collected data by the CMS detector, a validation process is made in order select the events with optimum detectors conditions, in full operational mode and performance. Figure 26 - left the integrated luminosity delivered by LHC during the 2016 data taking period, shows the CMS recorded luminosity, and the validated luminosity. In Figure 26 - right, the summary of the fraction of validated data by each subdetector is shown for the same time period of 2016. One usual source of non operational time when the data are not validated corresponds to the so–called *warm start*, i.e. the time elapsed between the proton beam being declared stable by LHC operation, and the tracker being fully operational at high voltage. This source is shown apart in the table of Figure 26 - right.

The luminosity validated for data collected in 2016 was $36.30\,\mathrm{fb}^{-1}$, corresponding to a $96\,\%$ of the data recorded. In 2017 $41.48\,\mathrm{fb}^{-1}$, the $92\,\%$. And in 2018 $59.83\,\mathrm{fb}^{-1}$, the $94\,\%$ of the recorded one [107], values summarized in Table 2.1. Integrating over the three years, the full statistics corresponds to $137\,\mathrm{fb}^{-1}$ of proton–
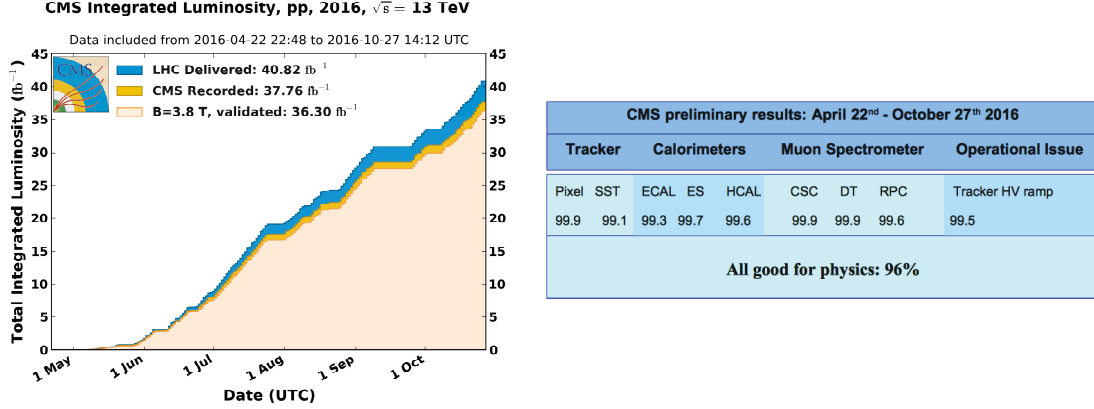
Figure 26: Integrated luminosity delivered by LHC (blue), recorded by CMS (dark orange), and validated (light orange), during 2016 proton–proton collisions (left). The table shows the luminosity fraction (in %) of data validated by the CMS subsystems in 2016. The operational losses related to the warm start of the tracking detector, are accounted separately (right) [107].

proton collision data at $\sqrt{s} = 13$ TeV.

| Year	LHC delivered $\mathcal{L}$	CMS recorded $\mathcal{L}$	CMS validated $\mathcal{L}$
2016	$40.82\,\mathrm{fb}^{-1}$	$37.76\,\mathrm{fb}^{-1}$	$36.30\,\mathrm{fb}^{-1}$
2017	$49.81\,\mathrm{fb}^{-1}$	$44.99\,\mathrm{fb}^{-1}$	$41.48\,\mathrm{fb}^{-1}$
2018	$67.86\,\mathrm{fb}^{-1}$	$63.67\,\mathrm{fb}^{-1}$	$59.83\,\mathrm{fb}^{-1}$

Table 2.1: Summary table of the luminosities ($\mathcal{L}_{\mathrm{int}}$) delivered by LHC, recorded by CMS, and validated, for each year.

In order to give a very first hint on the similarities or differences of these three sets of data, two variables characteristic of the work carried out in this thesis are shown in Figure 27 for data corresponding to each year, scaled to the same luminosity in order to compare the distribution shape, for events containing one muon with $p_T > 53$ GeV (preselection criteria will be explained in Section 5.3).

In Figure 27 - left, the distribution of number of vertices is correlated with the amount of pileup in the set of collisions considered (see Figure 10). Despite this difference, the muon transverse momentum distribution in Figure 27 - right is consistent for the three years, and with the increase of statistics along the years, one can see how the tail of high p_T muons gets more populated.

Apart from the differences in the proton–proton collisions that the LHC provided along the years (e.g. difference in luminosity, in number of interactions per crossing, etc.), the CMS detector has undergone several upgrades and changes during the Run 2 time period. To mention the most relevant ones affecting this work, in 2017, a new pixel detector was installed [82] (see Section 2.3.2), the readout of the Hadron Forward calorimeter and of a 20° sector of HCAL were upgraded [108], and
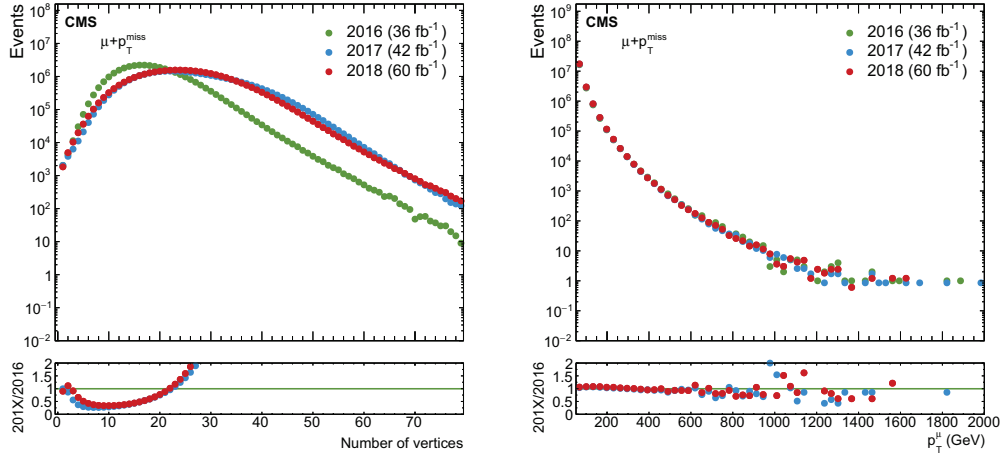
Figure 27: Distribution of number of vertices (left) and muon p_T (right), for events with at least a muon with $p_T > 53$ GeV. Data comparison among years: 2016 (green), 2017 (blue) and 2018 (red). Ratio plot 2017/2016 (blue) and 2018/2016 (red).

five chambers of new GEMs detectors were installed in the negative endcap of the Muon System [109]. In 2018, the DC–DC converters of the pixel were replaced [82], the silicon strip tracker started operating at a lower temperature [110], a new mechanism has been installed in the ECAL DAQ to automatically recover errors induced by particles interactions [111], silicon photomultipliers were installed in the HCAL endcaps [108], and DTs were equipped with micro trigger control and acquisition ROS [112]. All these changes in the collisions and the detector may have introduced changes in the data, therefore, in this analysis all the studies are split by year of data taking.

In the next chapter we will immerse in the identification and reconstruction of particles using the experimental setup that we have presented above.

Chapter 3

Identification and reconstruction of particles

The particles created at the proton-proton collision, their decay products, or the outcome of their hadronization, interact with the detector active material when traversing the CMS detector, creating electric signals along their way. These signals are digitized and stored for their subsequent analysis. Figure 28 shows a scheme of the signatures left by several kinds of particles in the different CMS subdetectors.
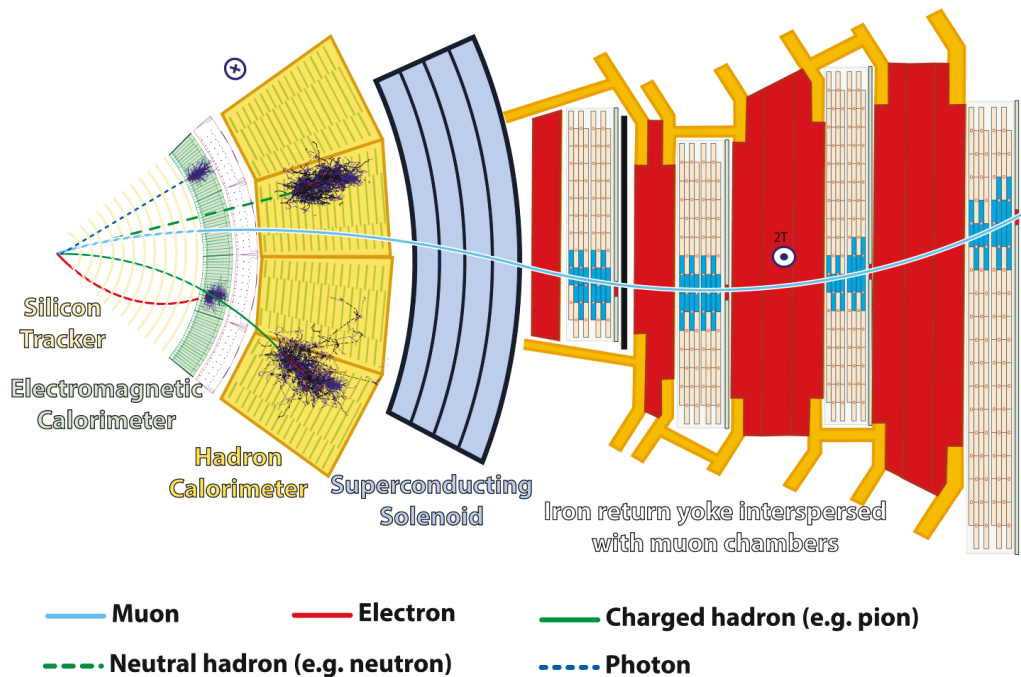
Figure 28: Scheme of the signals left by different kinds of particles inside the CMS detector [113]

This chapter describes the identification and reconstruction of the particles by the CMS experiment using the information from the subdetectors presented in Section 2.3.

As a very general description of what is shown in Figure 28, the trajectory of charged particles is measured in the Silicon Tracker (Tracker). These trajectories are bent due to the presence of the powerful magnetic field created by the Superconducting Solenoid (Section 2.3.1). The calorimeters measure the energy of particles traversing them: photons and electrons are measured in the ECAL, while hadrons are measured using both, ECAL and HCAL calorimeters. Muons are minimum ionizing particles and traverse all CMS detectors reaching the outer Muon System, where their trajectory is once more measured. Neutrinos are other type of particles able to traverse the CMS detectors completely, though they hardly interact with detectors and escape undetected.

The combination of the information from all the subdetectors to reconstruct one by one all the particles and make a global event description, is made by the Particle Flow (PF) algorithm [114]. The sketch in Figure 29 shows how the Particle Flow algorithm converts the detector information into a physical event, with some schematic examples:

- Charged hadrons: combining the Tracker hits and both calorimeters, ECAL and HCAL, energy deposits.
- Neutral hadrons: HCAL deposits with consistent energy deposited in the ECAL, and non compatible Tracker hits.
- Electrons: significant energy deposit in the ECAL linked with a track in the tracker, and hardly no energy deposited in the HCAL.
- Photons: only ECAL deposits, without an associated track in the inner tracker or a shower in HCAL.
- Muons: combining the Tracker hits, the Muon Detector hits, and calorimeters deposits being compatible with a minimum ionizing particle.

By summing up the energy of the particles in the event we infer if neutrinos or other undetected particles were present somewhere in the collision, as will be explained in detail in Section 3.6.

In this work we make use of collision data and Monte Carlo simulation (MC) of such collisions. In order to simulate the response of the detector on the MC and make as similar as possible to data, all generated events are processed through a full simulation of the CMS detector based on the GEANT4 software [115]. This process includes simulation of the detector geometry, its alignment, magnetic field in each part of the detector, and the various types of particle–material interactions. In addition the simulated samples of proton–proton collisions include trigger emulation and event reconstruction, using the Particle Flow algorithm as explained above.
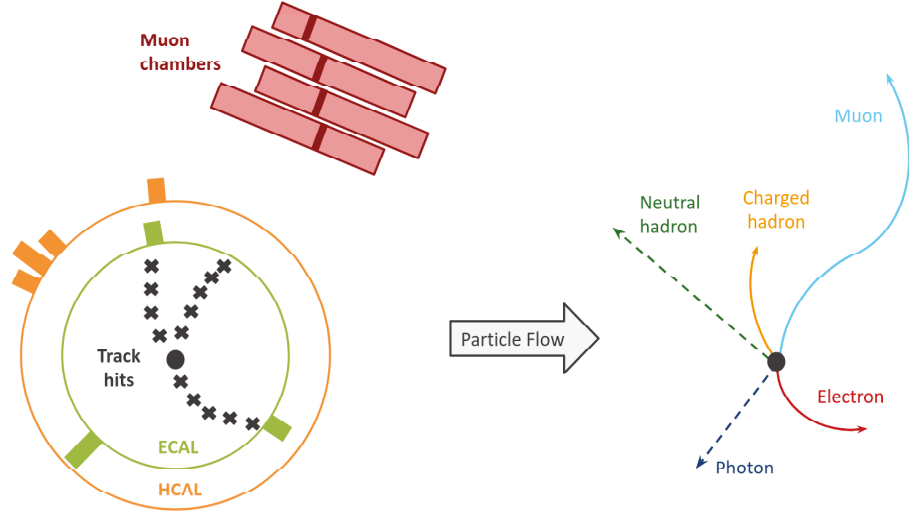
Figure 29: Sketch of how the Particle Flow algorithm translates the detector information (left) into reconstructed particles (right).

3.1 Tracking

The track reconstruction of charged particles in the Tracker detector (Section 2.3.2) gathers the signals above specified thresholds from the Pixel and Strip detectors into hits, which are then used to estimate the cluster positions and their uncertainties [80].

The track finding is done in an iterative way. It starts searching for tracks that are easiest to find (e.g., of relatively large p_T, and produced near the interaction region). After each iteration, hits associated with tracks are removed, simplifying the following iterations in a search for more difficult tracks (e.g., low p_T, or displaced tracks).

After each iteration, Kalman filters [81, 116, 117] are used to extrapolate the trajectory and search for additional hits in the track candidate. With every additional hit, a fit to the trajectory is performed.

To reduce the number of tracks that do not correspond to a charged particle, and to ensure a good p_T measurement, tracks are selected to have certain quality criteria. This criteria is based on the number of layers that have hits, whether their fit yielded a good χ^2/dof, and how compatible they are with originating from a primary interaction vertex (defined in Section 3.2).

3.2 Primary vertex

High values of instantaneous luminosity mean big numbers of proton–proton interactions per bunch–crossing (see pileup Section 2.2.4). Figure 30 shows the maximal instantaneous (peak) luminosity per day for each year of Run 2 data taking. The maximal instantaneous luminosity reached each year is labeled: $5.3\,\mathrm{Hz\,nb^{-1}}$ in 2015,

$14.7\,\mathrm{Hz\,nb^{-1}}$ in 2016, $20.7\,\mathrm{Hz\,nb^{-1}}$ in 2017, and $21.4\,\mathrm{Hz\,nb^{-1}}$ in 2018. This implies that several vertices, each one corresponding to a given proton–proton collision, can take place at each bunch–crossing. The interaction that entails the highest Q^2 value is considered the interaction of interest, and its vertex called the Primary Vertex.
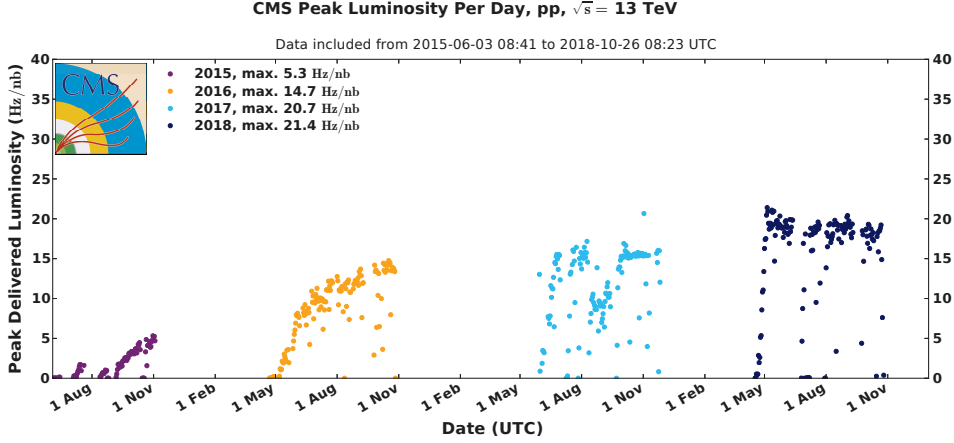

Figure 30: Maximum instantaneous luminosity per day in Run 2 [64].

Vertices are distributed over a luminous region known as the beam spot. To reconstruct a vertex, first, tracks consistent with particles being produced promptly in the interaction region are chosen, by imposing requirements on the maximum value of significance of the transverse impact parameter (<5) relative to the centre of the beam spot, the number of strip and pixel hits associated with a track $(>1$ pixel layers, pixel $+$ strip $> 4)$, and the normalized χ^2 of the trajectory fit (< 20).

The selected tracks are then clustered on the basis of their z–coordinates at their point of closest approach to the centre of the beam spot. Finally, a fit of the position is performed of each vertex using its associated tracks.

The reconstructed vertex with the largest value of p_{T}^2 of the associated tracks, is called Primary Vertex (PV), and all the other reconstructed vertices are called pileup vertices. The primary vertex of the event is of interest since it is the parton collision where the most interesting physics processes has occurred.

Figure 31 shows the reconstruction of an event with a high number of vertices and their associated tracks. This example gives an idea of the fine granularity needed in the Tracker (Section 2.3.2) in order to distinguish the vertices. It is crucial to have such good vertex resolution in order to define variables as the lepton isolation (Section 3.3.2), or the $p_{\mathrm{T}}^{\mathrm{miss}}$ (Section 3.6). In the definition of these variables, among others, it is necessary to take into account only the tracks from the primary vertex and to remove the contribution from tracks from any other vertex.
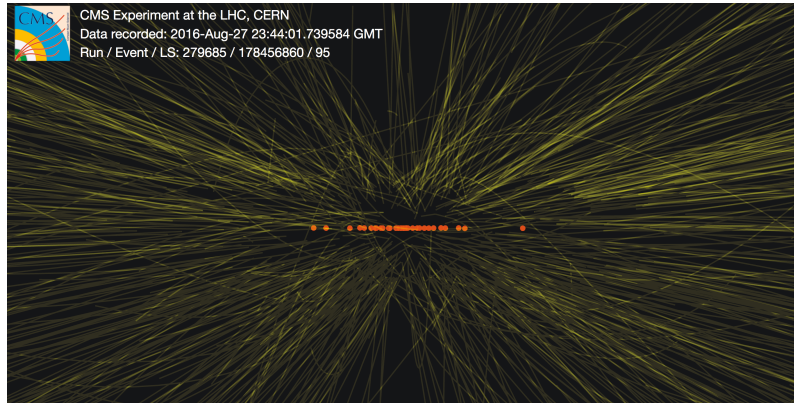
Figure 31: Example of an event display from 2016 with 30 reconstructed vertices, marked as orange circles. Yellow lines represent the tracks with $p_T > 1.5$ GeV [118].

3.3 Muons

Out of all possible particles in the final state, muons, in particular the most energetic ones, are the most determinant particle in this analysis. Therefore, we will especially concentrate on describing their identification and measurement.

As already mentioned in Chapter 1, the range of interest in the values of reconstructed masses lies in the ~ TeV domain, and such high masses are reconstructed from high momentum muons. For this reason one chapter is fully dedicated to them: Chapter 4 gathers all the studies carried out to identify and reconstruct high momentum muons, a key ingredient in the analysis.

Muon trajectories are reconstructed independently in the Tracker, *tracker muon track*, and in the Muon System, *standalone muon track*. Tracker muon tracks are built from tracker tracks with $p_T > 0.5$ GeV and $p > 2.5$ GeV that match at least one segment in the Muon System [93]. Standalone muon tracks are built by gathering the information from the CSC, DT, and RPC detectors using a Kalman-filter technique [81]. Then, both tracks are geometrically matched and combined using, again, a Kalman-filter technique into a common track called *global muon*.

Finally, global muons and muons reconstructed in the tracker are used as input for the Particle Flow (PF) algorithm, together with calorimeters information, to produce the so–called *muon candidate*. Quality requirements on the muon reconstruction parameters define the muon particle. These parameters relate to the goodness of the fit of the muon track, χ^2, the number of hits in the tracker and Muon Systems, and the degree of matching between the tracker and muon tracks.

3.3.1 Muon identification

Since the muon is the only particle escaping from the solenoid and its inner detectors (apart from the undetected neutrino), if a tracker track (Section 3.1) is consistent with a Muon System track, this track is identified corresponding to a muon. Depending on the quality requirements applied to the track and muon variables, and

how tight they are, different types of muon identification (muon ID) are set [93].

The different muon identifications are designed to balance between efficiency and purity. When applying loose requirements, the efficiency of selecting muons is high, while the sample may have contamination from other sources and the purity is reduced. More strict selection reduces the efficiency and ensures a higher purity. Though several types of muon IDs are defined in CMS, we will use here only two: *loose muon* and *high–p_T muon*.

Loose muon is the least restrictive muon ID. It is designed to be highly efficient for prompt[1] muons, as well as for muons from heavy and light quark decays.

This identification has a 99 % efficiency [93], while keeping a relatively low rate of misidentification. The loose muon is reconstructed as PF muon, and also, as tracker or global muon. This ID is used in this analysis to veto events with a second muon as it will be explained in Section 5.3.

High–p_T muon identification is optimised for muons with transverse momentum (p_T) > 200 GeV, and therefore, it is the one used in this analysis to select the muons in the final state.

Firstly, the muon has to be reconstructed as global muon. By considering both, tracker and Muon System information, the detector length is optimised, and the momentum resolution is improved, especially for high momentum muons.

In order to reduce the amount of hadron shower remnants that escape the HCAL (hadronic punch-through), it is required to have segments in at least two muon stations and at least one hit in a muon chamber, as a sign of a more penetrating muon track. This requirement brings also consistency with the muon trigger requirements.

In order to avoid largely miss-measured values of p_T, the p_T relative uncertainty (σ_{p_T}/p_T) is required to be less than 30 %.

To reduce the background from cosmic ray muons, cuts on the impact parameter (d_{xy}) of 0.2 mm, and on the longitudinal distance of the tracker track with respect to the primary vertex (d_z) of 5 mm, are applied.

To ensure enough information for a well reconstructed Tracker track, the muon is required to have at least one hit in the pixel detector and at least six tracker layers with hits.

Finally, a *high purity* (HP) track is required. The HP tag requires values of the track χ^2 and transverse and longitudinal impact parameters (together with their significance) smaller than certain threshold values, varying for each iteration step during the track reconstruction (explained in Section 3.1). This variable is correlated with the quality of the muon track in the tracker.

All the high–p_T ID criteria are summarized in Table 3.1.

High momentum muons may produce bremsstrahlung radiation as a result of their interaction with the iron yoke or the chamber materials, contaminating the detector signals with the so–called, showers. In the presence of showers, the hit

---

[1]Prompt leptons are leptons originating from the main collision taking place in the event.

High–p_T ID definition
Global muon
Muon chamber hits > 0
Muon stations with segments > 1
$\sigma_{p_T}/p_T < 0.3$
$d_{xy} < 0.2\,\text{mm}$
$d_z < 5\,\text{mm}$
Pixel hits > 0
Tracker layers with hits > 5
High purity track

Table 3.1: Definition of the muon high–p_T ID.

multiplicity increases and, when incorporating hits to the trajectory fit, the χ^2 of the reconstruction fit worsen. Therefore, the fit χ^2 is not used as discriminant variable to identify a high–p_T muon.

3.3.2   Muon isolation

To discriminate muons that come from hadron decays in flight, thus appearing surrounded by other particles, in jets, from prompt muons or energetic muons that come from the decay of electroweak bosons, the *isolation* of a muon is evaluated. The isolation of a muon is defined as the scalar sum of the momentum of all the PF particles around it in a cone of $\Delta R < 0.4$ (defined in Eq. 2.11). The contribution from pileup is subtracted to the neutral particles by computing the sum of charged hadron deposits originating from pileup vertices, scaling it by a factor of 0.5. The factor of 0.5 is estimated from simulations to be approximately the ratio of neutral particle to charged hadron production in inelastic proton-proton collisions. The corrected energy sum from neutral particles is limited to be positive or zero [93]. The PF isolation is defined as:

$$\text{PF isolation} = \sum_{char.had.}^{P} p + \max\left(0, \sum_{neut.had.}^{A} E + \sum_{photons}^{A} E - 0.5 \times \sum_{char.had.}^{PU} p\right) \quad (3.1)$$

The muon isolation variable used in this analysis is defined as the scalar sum of transverse momentum of all tracks measured by the Tracker from the primary vertex in the event, in a cone of $\Delta R < 0.3$ around the muon. The relative isolation considers the isolation just defined, divided by the magnitude of the muon $\vec{p}_T$:

$$\text{Relative tracker isolation} = \sum_{tracks} p^{\text{tracker}}/p^{\mu} \quad (3.2)$$

Muons have to fulfill the following isolation criteria: relative tracker isolation < 10 %.

3.4   Electrons

Electrons are not considered in the final state of this analysis, however, they are used to veto the events with electrons besides an energetic muon (see Section 5.5 about selection criteria).

Electrons are reconstructed using a Gaussian Sum Filter (GSF) algorithm [119] which combines a track from the Tracker and a supercluster[2] (SC) in the ECAL, consistent with an electromagnetic cascade. Typically, electrons lose some of their energy due to bremsstrahlung emission in the tracking detector, which is recovered by adding compatible energy deposits to the ECAL cluster. The final clusters are then geometrically associated to tracks to form electron candidates.

The dedicated high-p_T electron identification criteria was developed centrally in CMS and it is defined as follows [83, 120].

High–p_T ID electron candidates correspond to electrons (and positrons) with $p_T > 35$ GeV and $|\eta| < 1.44$ (ECAL barrel region), or $1.57 < |\eta| < 2.50$ (ECAL endcap region), where $|\eta|$ is the ECAL energy cluster pseudorapidity. The transition region $1.44 < |\eta| < 1.57$ is excluded since it leads to lower quality reconstructed clusters, because it corresponds mainly to inactive material of the service areas.

In order to assure the consistency between the tracker track and the energy deposits in the ECAL, the angular difference in terms of η and ϕ is used. The η difference, $|\Delta\eta_{\mathrm{in}}^{\mathrm{seed}}|$, is defined as $|\eta_{\mathrm{seed}} - \eta_{\mathrm{track}}|$, where η_{seed} is the position of the seed cluster in η, and η_{track} is the track η extrapolated from the innermost track position. Similarly, $|\Delta\phi_{\mathrm{in}}| = |\phi_S - \phi_{\mathrm{track}}|$ is the difference in the ϕ coordinate. The quantity $|\Delta\eta_{\mathrm{in}}^{\mathrm{seed}}|$ is required to be less than $0.004\,(0.006)$, and $|\Delta\phi_{\mathrm{in}}|$ less than $0.06\,(0.06)$ in the barrel (endcap) region.

Misreconstructed electrons, and electrons in jets, are reduced by requiring the electron to be isolated. This means requiring the energy in a cone of radius $\Delta R = 0.3$ around the electron direction, and extending in both ECAL and Tracker, to be less than 5 GeV.

When photon conversions take place inside the tracker volume, the first hit of the electron tracks from the converted photons is not likely to be located in the innermost tracker layer, and lost hits are therefore expected in the first tracker layers. The electron is required to have no more than one lost tracker hit.

The impact parameter relative to the interaction point in the transverse plane (d_{xy}) is required to be less than 0.2 mm in the barrel and less than 0.5 mm in the endcap region.

The high–p_T ID electron criteria are summarized in Table 3.2.

The performance of electron reconstruction and identification algorithm in data is studied using $Z \to ee$ events. Figure 32 shows the electron reconstruction efficiency versus η for different p_T ranges. The reconstruction efficiency in data is better than

---

[2]Energy deposits in the calorimeters are in the form of *clusters*. The clusters are then grouped into *superclusters* if they satisfy a low energy threshold requirement.

Variable	Barrel	Endcap
E_T	> 35 GeV	> 35 GeV
ECAL cluster η	$|\eta| < 1.44$	$1.57 < |\eta| < 2.50$
$|\Delta\eta_{\mathrm{in}}^{\mathrm{seed}}|$	< 0.004	< 0.006
$|\Delta\phi_{\mathrm{in}}|$	< 0.06	< 0.06
Track Iso. p_T	< 5 GeV	< 5 GeV
Tracker lost hits	≤ 1	≤ 1
d_{xy}	< 0.2 mm	< 0.5 mm

**Table 3.2:** Definition of the electron high–p_T ID.

95 % in the p_T range from 20 to 500 GeV.
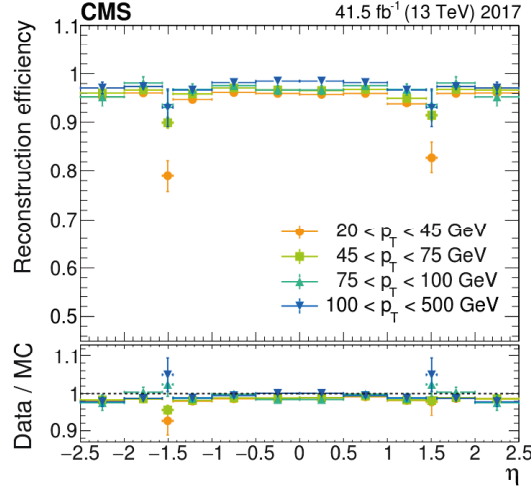
Figure 32: Electron reconstruction efficiency versus η in data (upper panel) and data-to-simulation efficiency ratios (lower panel) for the 2017 data taking period. The region $1.44 < |\eta| < 1.57$ corresponds to the transition between the barrel and endcap regions of ECAL and is not considered in physics analysis [120].

The electron energy resolution is shown in Figure 33 as a function of electron p_T, measured in MC simulation. By combining the information of the ECAL and the Tracker, the electron energy resolution improves with the electron p_T, reaching values of a 0.8 % (2 %) for electrons in the barrel (endcaps), with a p_T of ~ 200 GeV.
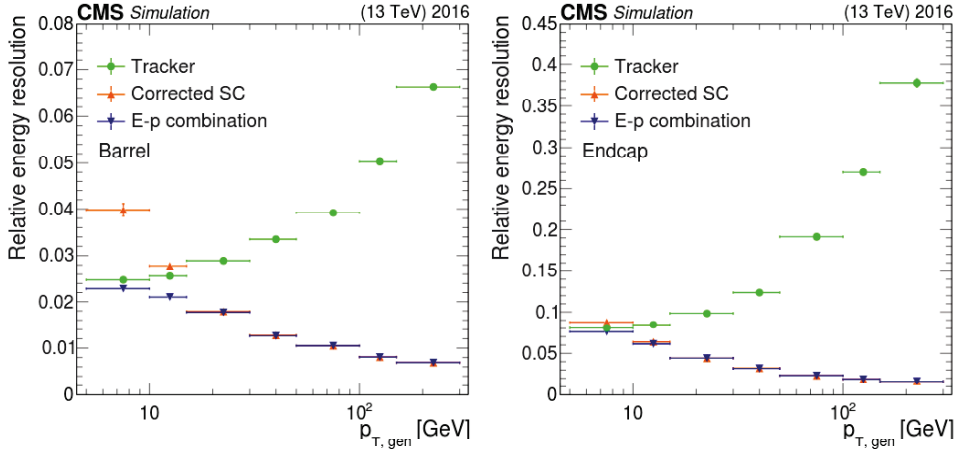
Figure 33: Electron resolution as a function of electron p_T, as measured by the ECAL (orange), by the Tracker (green), and combining both (blue), measured in 2016 MC samples for barrel (left) and endcap (right) electrons [120].

3.5 Jets

Jets are the experimental signatures of the hadronic showers from quarks and gluons. As quarks and gluons have a net colour charge and cannot exist freely due to colour–confinement (explained in Section 1.1.2), they are not directly observed in Nature. Instead, they come together to form colour–neutral hadrons, a process called hadronization (Section 2.2.3) that leads to a collimated spray of hadrons called *jet*, as represented in Figure 34.
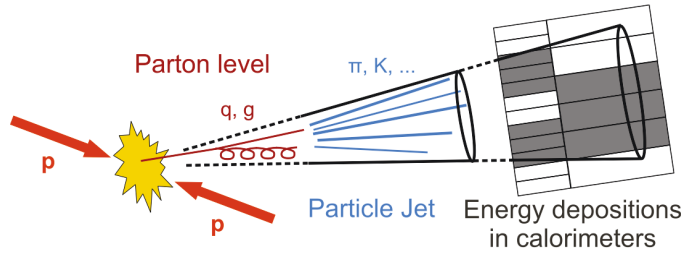
Figure 34: Representation of a jet formation from a proton–proton collision that leads to energy deposits in the calorimeter detectors.

Jets are reconstructed by combining the energy deposits in the tracker and calorimeters using the anti–k algorithm [121] with radius, $\Delta R = 0.4$ (defined in Eq. 2.11). There are different types of jets depending on the way the individual contributions from subdetectors are combined. Those used in this analysis are the Particle Flow jets. The PF jets are reconstructed by clustering the four–momentum vectors of Particle Flow candidates (explained at the beginning of this chapter). The energy of charged hadrons is determined from a combination of the track momentum and the corresponding ECAL and HCAL energy. The energy of neutral hadrons is obtained from the energy deposits in the ECAL and HCAL.

The energy measurements in the ECAL [122] and HCAL [123] are calibrated individually and, subsequently, the reconstructed jet is also calibrated [124]. The purpose of the jet energy calibration is to relate the energy measured for the detector jet, to the energy of the corresponding true particle jet. The jet calibration makes use of the transverse momentum balance in dijet events and $\gamma/Z + \text{jets}$ events.

In this analysis, we will consider the number of jets of the event as the number of jets with $p_T > 25$ GeV, $|\eta| < 2.5$ and the angular distance between the jet and the muon, $\Delta R > 0.5$.

3.5.1 Jet b–tag

Jets originating from decays of heavy–flavour hadrons, b–hadrons, are an important component of the physics program of LHC, they are called *b–quark jets* or *b–jets*.

The characteristics of b–hadrons are exploited to identify b–jets. The long lifetime of hadrons containing a b–quark allow them to travel around $100 - 200 \, \mu\text{m}$ before decaying, and such distances can be measured inside the tracker due to its excellent spatial resolution (see tracker description in Section 15).

The information about secondary vertex and track information is used in the *Deep Combined Secondary Vertex* (DeepCSV) algorithm [125] to discriminate among b–jets and non b–jets. The DeepCSV discriminant assigns each jet a number ranging between 0 and 1, a probability of how likely is the jet to be originated from a b–quark. Figure 35 is an example of the distribution of the DeepCSV discriminator for data and MC simulation for events containing one muon and, at least, two jets. Among the MC simulations there are different jets: b–jets have values close to 1, while light (udsg) jets peak at 0.
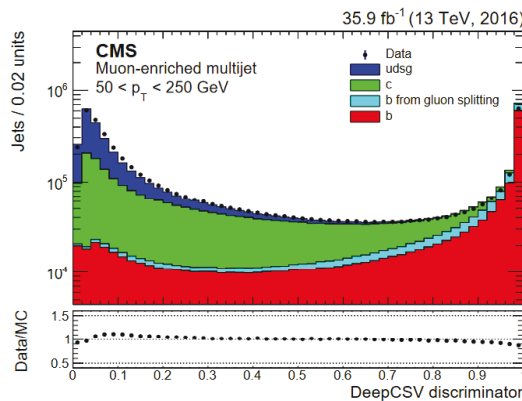
Figure 35: Example of DeepCSV discriminator distribution for 2016 data compared to simulation. The simulated contributions of each jet flavour are shown as histograms of different colours [126].

3.6   Missing transverse momentum

Neutrinos are not detectable by any CMS subdetector due to their low interaction cross section with matter. Therefore, the way to infer their presence is using the energy and momentum conservation in the event. The missing transverse momentum is defined as the negative sum of the transverse momentum of all the reconstructed particles in the event: $\vec{p}_T^{\text{miss}} = -\sum \vec{p}_T$ [127]. Figure 36 shows the sketch of how the $\vec{p}_T^{\text{miss}}$ of an event is reconstructed from the $\vec{p}_T{}^i$ of the five detected particles.
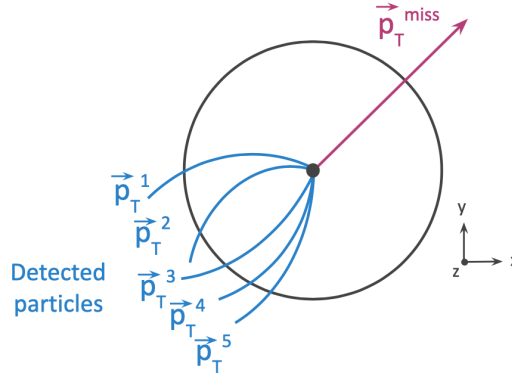
**Figure 36:** Sketch of $\vec{p}_T^{\text{miss}}$ definition by p_T conservation from detected particles.

The modulus of $\vec{p}_T^{\text{miss}}$ is denoted as p_T^{miss}. The sources of p_T^{miss} are particles that are not detected by any subdetector, like the mentioned neutrinos, or unknown particles, as potentially, dark matter particles. But the p_T^{miss} determination is also affected by inefficiencies of the detector, or areas where a particle can escape without being detected due to the detector geometry [128]. Some events could have a large p_T^{miss} due to, for example, calorimeter noise or jets in a non-operational region. These anomalous events with clear sources of instrumental p_T^{miss} are removed using specific filters and prior to any analysis [127]. Figure 37 shows a sketch of the possible sources of p_T^{miss}.
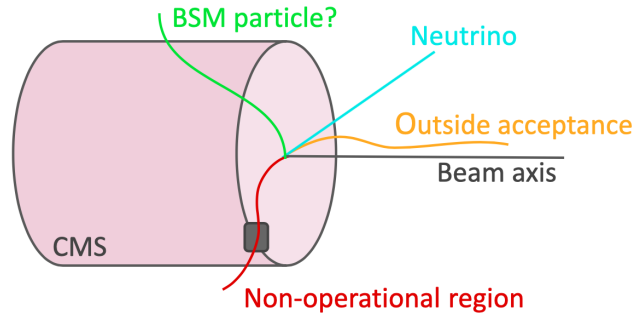
**Figure 37:** Sketch of possible sources of p_T^{miss}.

Events of Z/γ should have little or no genuine p_T^{miss}, therefore, they are used to measure the performance of the p_T^{miss} determination by comparing the momenta of the vector boson to that of the hadronic recoil system. The resolution of the

p_T^{miss} variable is studied in such events, with a Z boson decaying to a pair of electrons or muons, or with an isolated photon. The hadronic recoil system is defined as the vector p_T sum of all PF candidates except for the vector boson. The representation of the transverse momenta of the vector boson, $\vec{}$, and the hadronic recoil, $\vec{u}$, is shown in Figure 38. Momentum conservation in the transverse plane imposes $\vec{}$ $+ \vec{u}$ $+ \vec{p}_T^{miss} = 0$.
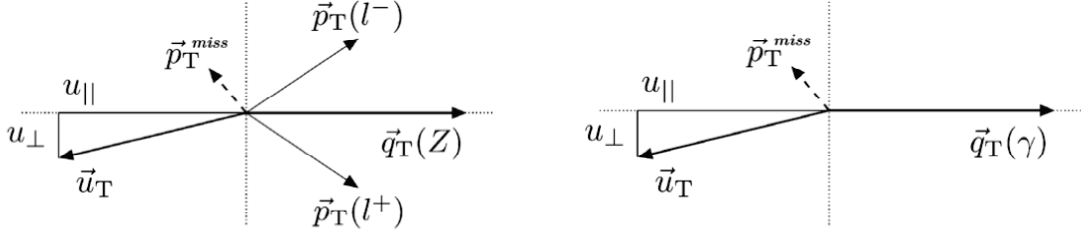
Figure 38: Illustration of the Z boson (left) and photon (right) event kinematics in the transverse plane. The vector $\vec{u}_T$ denotes the vectorial sum of all particles reconstructed in the event except for the two leptons from the Z decay (left) or the photon (right) [127].

The components of the hadronic recoil parallel, $u_\parallel$, and perpendicular, $u_\perp$, are used to study the p_T^{miss} resolution, σ. The resolution is the RMS of the $u_\parallel$ + distribution. Figure 39 shows the resolution of $u_\parallel$ and $u_\perp$ as a function of the scalar p_T sum of all PF candidates ($\sum E_T$). The resolutions measured in different samples, and in data and simulation, are in good agreement, and it varies from 15 GeV to 30 GeV in the $\sum E_T$ range of $400 - 2400$ GeV.
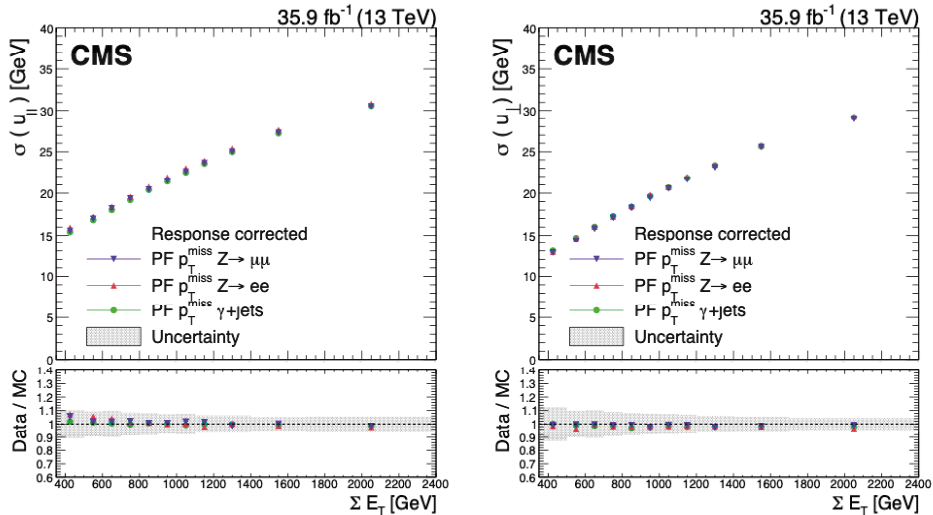
Figure 39: Resolution of the $u_\parallel$ and $u_\perp$ components of the hadronic recoil as a function of the scalar p_T sum of all PF candidates, in $Z \to \mu^+\mu^-$, $Z \to e^+e^-$, and $\gamma +$jets events. The lower panels show the ratio data to MC simulation [127].

Chapter 4

High momentum muons

Good identification and precise measurement of muons, electrons, photons, hadrons (charged and neutral particles), and jets over a large energy range and at high instantaneous luminosities are necessary for rare process searches to be effective. In particular, this search relies on precise reconstruction and measurement of events in the tail of the reconstructed transverse mass distribution, of the muon $+\, p_T^{miss}$ system. At the moment of starting this work, searches for the production of SSM W' had already been ongoing in the leptonic final states by CMS with proton–proton collision at $\sqrt{s} = 13$ TeV with an integrated luminosity of $2.3\,\text{fb}^{-1}$, and the observed limit on the mass of a SSM W' boson was set to $M_{W'} > 4.1$ TeV [26]. To study this mass region and above, we need to reconstruct muons with a transverse momentum in the TeV region. For such high p_T muons the usual techniques of identification and momentum determination used for lower p_T muons are not adequate, therefore, specific studies have been carried out to optimize their measurement.

With the amount of data collected in Run 2, CMS has detected a sufficiently large sample of high energy muons to allow their detailed study. The following features characterize a high p_T muon when traversing the CMS magnetic field:

– **Curvature:** the radius of the curvature of the track generated by the magnetic field in the Tracker, determines the p_T of a charged particle. For high p_T muons, the track in the Tracker is almost a straight line and the Muon System is needed to have a longer lever arm to determine the transverse momentum. The alignment among the subdetectors plays an important role and it is an additional challenge.

– **Statistics:** muons originated in proton–proton collisions, with very high p_T values, of the order of $\sim$ TeV, are statistically limited, as most SM processes yield decreasing distributions with p_T, and it is therefore difficult to perform precision studies of them. The MC simulation and cosmic muons detected by CMS, help to develop and tune the methods and studies, providing an additional source of highly energetic muons.

– **Showers:** the energy loss per distance travelled in a given material, dE/dx,

of charged particles is determined by the Bethe-Bloch formula:

$$-\left\langle \frac{dE}{dx} \right\rangle \propto \frac{1}{\beta^2} \left[\ln \frac{2 m_e c^2 \beta^2}{I(1-\beta^2)} - \beta^2 \right] \tag{4.1}$$

where c is the speed of light, m_e the electron rest mass, I the mean excitation potential of the material, and $\beta = v/c$, the particle speed in speed of light units. In the relativistic regime, $\beta \sim 1$, the energy loss increases logarithmically with the muon energy (momentum). Figure 40 shows the energy loss per distance, dE/dx, for muons in different materials such as hydrogen, uranium and iron, as a function of the muon energy. Since the return yokes in between the muon chambers are made of iron, the energy losses for iron in Figure 40 are representative of a muon passing through the CMS detector. When the radiative energy loss (purple) becomes dominant with respect to the ionization energy (brown), at muon energy ~ 300 GeV, the muons produce cascades of particles called electromagnetic showers or *showers*. The showers lead to extra hits being reconstructed in the muon detectors that contaminate the track fitting procedure, and thus, the p_T determination.
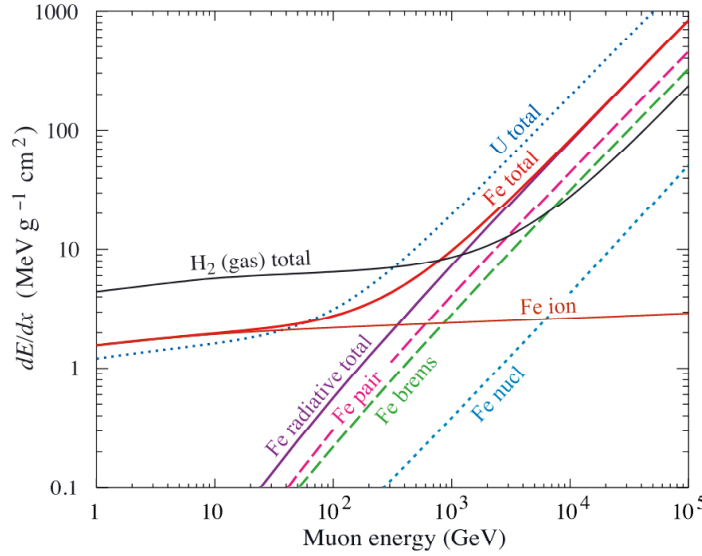
Figure 40: The average energy loss of a muon in hydrogen (black), iron (red), and uranium (dark blue) as a function of muon energy. Contributions to dE/dx in iron from ionization (brown) and pair production (pink), bremsstrahlung (green), and photonuclear (light blue) interactions are also shown [6].

This chapter describes the importance of the detection of high momentum muons and the specific techniques applied to have their precise measurement. Firstly, the description of the momentum assignment from the muon trajectory curvature is presented.

Secondly, the muon momentum related characteristics. The difference between the measured muon curvature (κ_measured) and the real muon curvature, (κ_real) and, therefore the muon p_T measurement, is affected by two effects: the resolution and the scale. This difference in curvature follows a gaussian distribution with a width different from zero due to the resolution effect. If the center of the gaussian distribution is not centered at zero there is also a scale effect. The measured curvature suffers from a combination of both effects as schematically represented in Figure 41. Sections 4.2 and 4.3 explain these two effects in detail, followed by the study of the charge misassignment in Section 4.4.
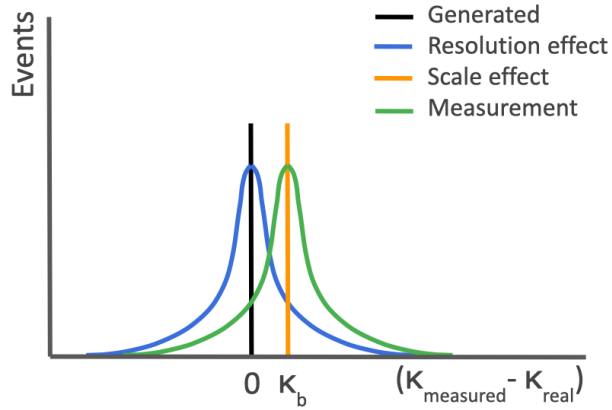
Figure 41: Sketch of the resolution effect (blue), the scale effect (orange), and the combination of both (green), in the distribution of the difference between the measured muon curvature, κ_measured, and the real muon curvature, κ_real.

Finally, the muon efficiencies are presented in Section 4.5. The dedicated studies of efficiencies, momentum assignment, resolution, scale, and showering of very high momentum muons produced at Run 2 were published in a dedicated paper: Ref. [129].

4.1 Transverse momentum assignment

The muon transverse momentum is firstly measured from the curvature of its trajectory when travelling through the magnetic field created by the CMS solenoid. Therefore, the muon p_T depends on the magnitude of the magnetic field, B, and the radius of curvature of the reconstructed track, R, by this equation [18]:

$$p_\mathrm{T}[\mathrm{GeV}] = |0.3 \times B[\mathrm{T}] \times R[\mathrm{m}]| \qquad (4.2)$$

The magnetic field is roughly uniform at $3.8\,\mathrm{T}$ in the volume inside the solenoid (detail in Section 2.3.1), where the Tracker and calorimeters detectors are placed. The measurement of the radius depends on the physical observable sagitta, s, and on the path length of the track, , as defined in Figure 42.
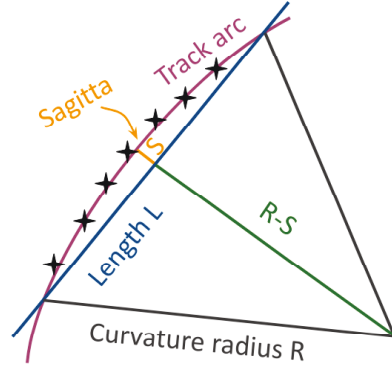
Figure 42: Sketch of the definitions of the muon track variables.

The relation among the sagitta, the radius and the length is the following [129]:

$$R \approx \ell^2/8s \qquad (4.3)$$

where the approximation is valid for $\ell/R \ll 1$. Assigning arithmetic signs consistently to R, s, and the charge, q, (in units of proton charge) yields

$$s \approx (0.3B\ell^2/8) \times (q/p_T) = (0.3B\ell^2/8)\kappa \qquad (4.4)$$

where $\kappa = q/p_T$ referred to as the signed curvature of the muon track. Because s is linearly related to the measurement of hit positions in the detector, which have approximately symmetric uncertainties, the uncertainty in κ from the cumulative effect of hit uncertainties is approximately Gaussian. Hence κ is the natural variable to use in muon transverse momentum resolution and scale studies, as it will be presented in Sections 4.2 and 4.3.

Looking at Equations 4.2, 4.3, and 4.4 we see that, for high p_T muons, the radius is large and the sagitta is small. In other words, high p_T muons have rather straight trajectories (shown in Figure 43) and, therefore, their transverse momentum assignment is harder.

This general description is enlarged to consider not only the hits in the Tracker, but also those in the Muon System. Due to the possible bremsstrahlung energy losses, the measurement of the muon curvature could be distorted, and the reconstructed p_T be different than the real one. A set of muon track refits has been developed to best reconstruct the muon p_T in different scenarios, they are the following:

– **Picky:** this algorithm is designed to avoid miss–reconstruction due to electromagnetic showers. It identifies muon stations containing showers based on large number of hits, and for each of them, it imposes extra requirements on
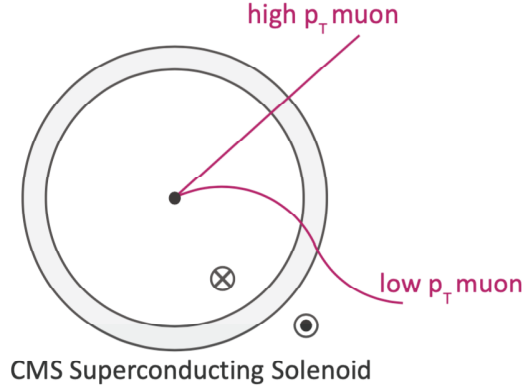
Figure 43: Sketch of the curvature of muons with low and high p_T in the CMS super-conducting solenoid. The magnetic field created by the solenoid bends the charged particles trajectories according to their charge, momentum and their position with respect to the solenoid (inside or outside).

hit compatibility with the muon trajectory. If hits in a muon station with showering fail these requirements, that station is removed from the trajectory fit.

– **Dynamical Truncation (DYT):** the DYT fit approach is based on the observation that in some cases, when a muon loses a large fraction of its energy, its trajectory can change and the segments (or hits) in subsequent stations may no longer be consistent with the initial trajectory. In other cases, where the energy loss is less severe, only hits in one station appear incompatible, while the rest of the trajectory is negligibly changed and can be used in the fit. The DYT algorithm decides to skip chambers or truncate at a certain station in the re–fit based on the estimator, E_i. The estimator E_i is computed in each muon station, i, with the Global Muon track (defined in Section 3.3) segments. The estimator is based on the compatibility of the propagated track from the Tracker to the muon station $i-1$.

– **Tracker Plus First Muon Station (TPFMS):** the TPFMS algorithm re-fits the Global Muon track with only the innermost layer of the muon station. This algorithm is designed to reduce the deviation of the muon momentum due to multiple scattering.

– **Tracker:** this algorithm measures the momentum of the muon using only the information from the Tracker. It is useful for muons with $p_T \lesssim 200$ GeV, that do not need the trajectories far from the interaction point (from the muon chambers) due to their large curvature.

The *TuneP* algorithm [130] chooses the best of the four refits presented, in a muon–by–muon basis. The choice of the TuneP is based in terms of a weighted comparison among the goodness, χ^2, of the different fits.

The combination of information from the Muon System and the Tracker System is specially important when increasing the transverse momentum of the muon. Figure 44 shows the muon p_T resolution as a function of the muon p_T when taking into account the Tracker–only, the Muon System–only, and the combination of both subdetectors as the *full system*. The resolution significantly improves by using the full system for muons with $p_T \gtrsim 200$ GeV. For muons with $p_T < 200$ GeVthe TuneP coincides with the Tracker p_T.The TuneP algorithm is proven to be the algorithm with the best performance, and therefore, from now on in this thesis, the TuneP assignment will be used when we refer to the muon p_T.
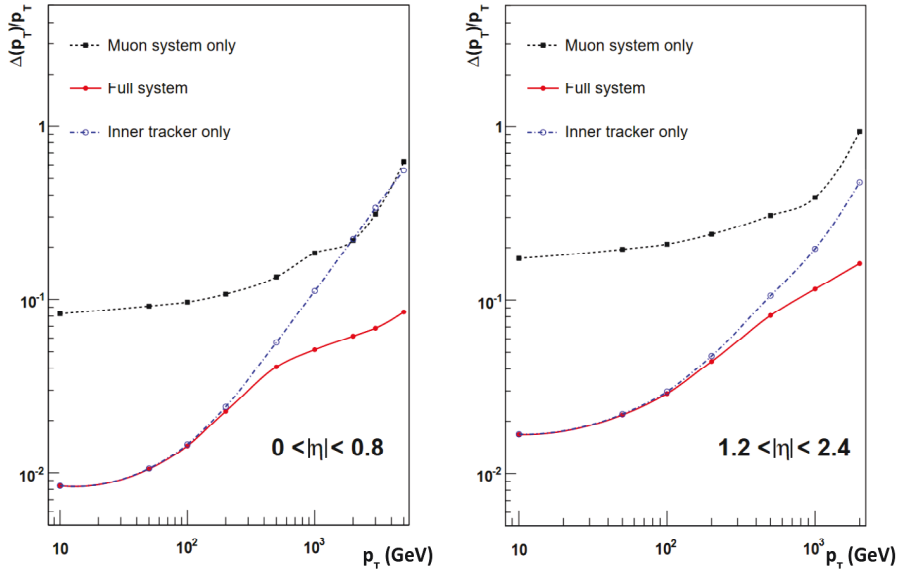
Figure 44: Muon transverse momentum resolution measured in simulation as function of the muon p_T for the Muon System only (black), the Tracker only (blue), and the full system (red), in the barrel ($|\eta| < 0.8$) (left), and the endcaps region ($1.2 < |\eta| < 2.4$) (right) [59].

Figure 44 also shows the better muon transverse momentum resolution in the central region (barrel) of the detector relative to that in the forward regions (endcaps). This is studied in detail in the resolution Section 4.3.

4.2   Momentum scale

The muon p_T measurement can exhibit two correlated features: the scale and resolution. The scale of the muon p_T is sensitive to three effects that may introduce a bias in the muon curvature:

- Magnetic field variations: small differences between the real magnetic field created by the superconducting solenoid and the one assumed in the reconstruction process, can lead to small differences in the curvature measured relative to the one expected. Figure 45 (top–left) shows an example of how a magnetic

field lower than the assumed one would bend less, resulting in a reconstructed p$_T$ larger than the real one.

– Muon energy losses: when a muon suffers energy losses its momentum decreases. If a muon has more energy losses than the assumed ones in simulation, its curvature will not be the expected one, as represented in Figure 45 (top–right).

– Detector misalignment: slight misalignment between detectors or deformations not foreseen in the simulation can give rise to a muon curvature bias. Figure 45 (bottom) shows two examples of misalignment between the subdetectors: a rotation of the Muon System with respect to the Tracker, and a translated geometry. This would introduce a bias in the measurement of the global track, and therefore, in the curvature assignment. Notice that a rotation of the geometry would affect on the same way positive and negative muons, while a translation affects differently depending on the charge.
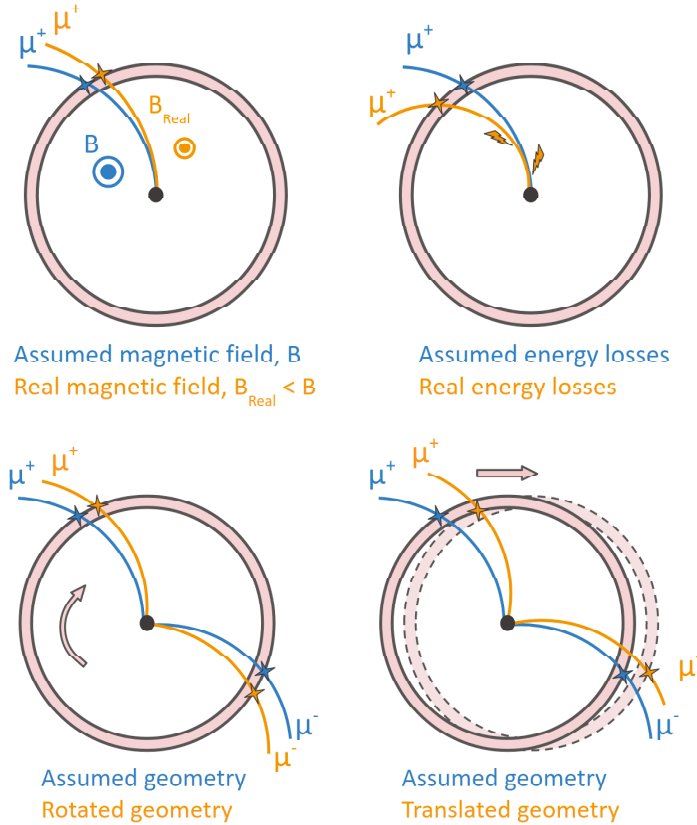
Figure 45: Sketch of different effects that cause curvature bias: magnetic field variation (top–left), energy losses (top–right), and detector misalignment separated in rotated geometry (bottom–left), and translated geometry (bottom–right). The assumed muon track (blue) is modified by the different effects and has a different measured track (orange).

The difference between the reconstructed curvature of the muon, κ_{measured}, and the real curvature, κ_{real}, is called curvature bias or additive bias, κ_b, and may be different for each region of the detector:

$$\kappa_b(\phi, \eta) = \kappa_{\text{measured}}(\phi, \eta) - \kappa_{\text{real}}(\phi, \eta) \tag{4.5}$$

The calibration of the momentum scale is performed with a method that assumes a good measurement in the experiment calibration as a starting point, and it searches for deviations with respect to the simulation in the data. The method used to compute these deviations is based in the Generalized Endpoint (GE) Method [93]. The next Section 4.2.1 explains the GE method, while the results are presented for each year of data taking in Section 4.2.2.

4.2.1 The Generalized Endpoint method

The Generalized Endpoint method [93] quantifies biases in the muon p_T determination by comparing data and MC simulation. It assumes that the simulation contains our best description of the detector (geometry, material, etc.), the passage of muons through it, and their interaction with all the materials they encounter, to find out that possibly data reflect a slightly different condition.

With the purpose of quantifying this difference the distribution of muon curvature, defined as the muon charge, , over the muon p_T, is used as discriminant variable. A χ^2 test is performed between the curvature distribution in data and in simulation, expressed as a function of an injected bias, κ_b:

$$\chi^2(\kappa_b) = \sum_i^{nbins} (n^i_{obs} - n^i_{bkg}(\kappa_b))^2 \tag{4.6}$$

where n^i_{obs} is the number of data events in the ith bin of a total of a number of bins, *nbins*, and $n^i_{bkg}(\kappa_b)$ the number of background expected events as a function of the injected bias, κ_b.

The method artificially injects biases, κ_b, in the SM background prediction as

$$/p \;\rightarrow\; /p \;+\kappa_b \tag{4.7}$$

in the range $\kappa_b = [\text{-}1.0 , 1.0]$ TeV^{-1}, and in steps of 0.01 TeV^{-1}. Notice that a bias κ_b of 1 TeV^{-1} corresponds to a deviation of 0.5 TeV for a p_T value of 1 TeV.

The method is carried out over a selected sample of high mass Z bosons, where the bosons are reconstructed in their dimuon decay channel[1] ($Z \rightarrow \mu^+\mu^-$). This ensures a rather clean and controlled sample enriched in high p_T muons.

The muon targeted by this study are, on one hand, high energy muons, and,

---

[1]This dimuon selection and background estimation will be refered and used later again in this text.

on the other hand, muons with a p_T determined by both, the Tracker and the Muon System. To fulfill both, the muons under study have $p_T > 200$ GeV. The events are selected by having two high p_T ID muons, one with $p_T > 200$ GeV, the second with $p_T > 25$ GeV, opposite charge and relative tracker isolation $< 10\%$. No requirement is set on the dimuon invariant mass in order to consider off–shell Z bosons that provide the type of muons we want to measure. The background is estimated with MC simulation of the main contributing SM processes: $t\bar{t}$ production, and diboson (WW, WZ, and ZZ) where at least one of the bosons decays leptonically. Contribution from events coming from W+jets and QCD multijet production are very much reduced for this muon p_T range.

Several variables have been checked to validate the data–simulation agreement, dimuon p_T and dimuon invariant mass distributions are shown in Figure 46 for the datasets corresponding to each year. A good agreement between data and MC simulation is found and we can proceed to the fit and minimization process of the GE method. The highest dimuon p_T value in the selected events is 1400 GeV, and the highest mass value of the dimuon system is 2500 GeV.

Figure 47 presents the distribution of the muon curvature, discriminant variable in this study, for data and simulation corresponding to each year: 2016, 2017 and 2018.

4.2.2 Muon momentum scale

The χ^2 distribution (Figure 48) resulting from the fit between the curvature distribution in data and in simulation, is first fit to a 6th order polynomial to determine the region of the global minimum. In such region, a 2nd order polynomial is fitted to the χ^2 distribution. The minimum of the 2nd order polynomial yields the measured value of the bias, κ_b.

The result of the χ^2 test, inclusive in η and ϕ, is shown in Figure 48. Computing this bias per each individual year instead of gathering all data together follows from the different beam and detector conditions (pileup, beam spot, detectors alignment, etc.) for each year of data taking, after opening and closing of the CMS experiment (as an example).

The measured κ_b for each year are shown in Table 4.1 inclusive in η and ϕ. The associated uncertainty corresponds to the κ_b values where $\Delta\chi^2 = 1$. The resulting κ_b values are consistent with zero, within the uncertainties.

Year	κ_b (TeV^{-1})
2016	0.02 ± 0.02
2017	0.00 ± 0.02
2018	-0.01 ± 0.02

Table 4.1: Measured scale bias, κ_b, for each year, inclusive in η and ϕ. The uncertainties correspond to the κ_b values where $\Delta\chi^2 = 1$.
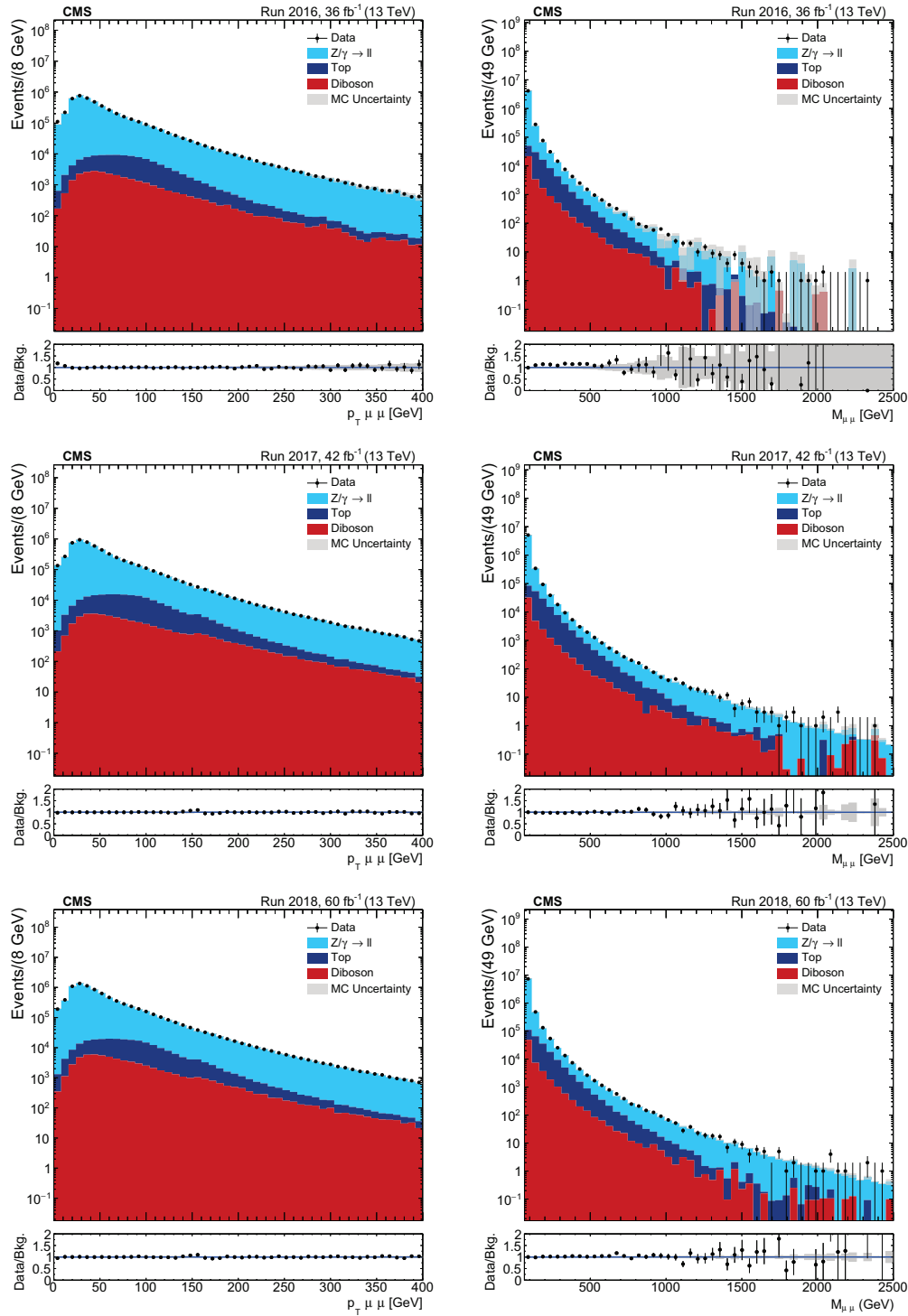
Figure 46: Dimuon pair variables after selection used to validate data to simulation agreement for data taken in 2016 (top), 2017 (middle), and 2018 (bottom). Dimuon p_T (left), and dimuon invariant mass (right) distributions. Data are represented by black dots while the contribution of SM processes are shown by the coloured histograms. Gray bands correspond to statistical uncertainties of simulated samples.
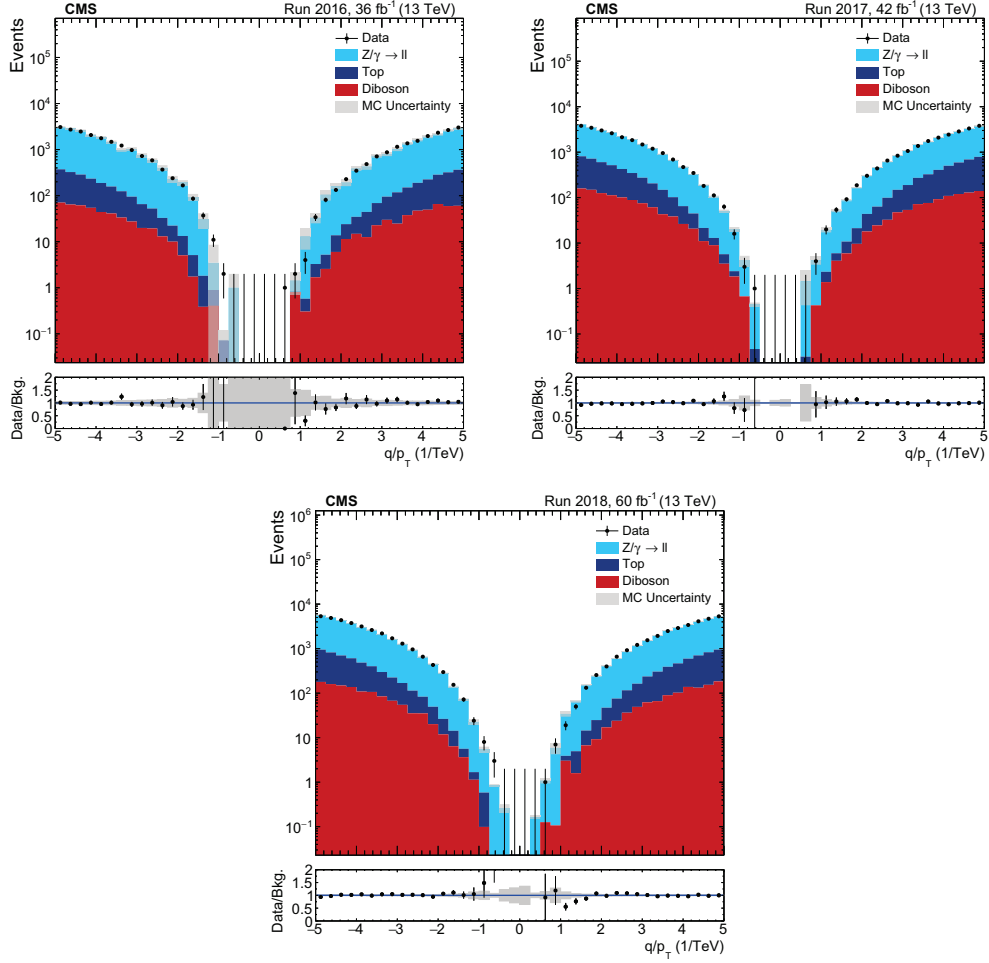
Figure 47: Curvature distribution for data and simulation corresponding to 2016 (left), 2017 (right), and 2018 (bottom) data and simulation, of the dimuon selection. Curvature region showed for muon $p_T > 200$ GeV. Gray bands correspond to statistical uncertainties of simulated samples.
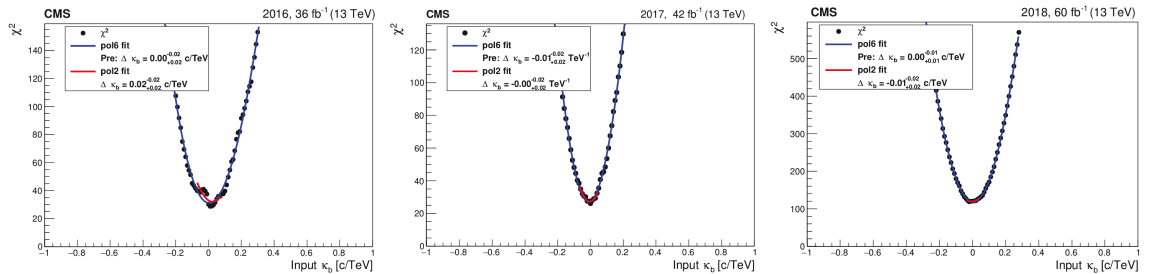
Figure 48: Measurement of scale bias, κ_b, via χ^2 distribution and the 6th and 2nd order polynomials are shown. The minimization is done for muons with $p_T > 200$ GeV, inclusive in muon η and muon ϕ. Obtained 2016 (left), 2017 (middle), and 2018 (right) data and simulation.

This process is studied in regions of muon ϕ and muon η. Figure 49 shows the distribution of muon ϕ and muon η for one year (2018) in the dimuon selected sample. The muon detector is designed with symmetry in the ϕ coordinate (as shown in Figure 23 – left), therefore the muon ϕ variable is uniform. Nevertheless, we split in three arbitrary and wide bins in muon ϕ, to study possible local effects: [-180, -60, 60, 180]. The splitting in muon η allows to study the barrel, endcaps, and "far endcaps" regions independently, and not necessarily assuming symmetry between positive and negative η regions. Measurements in the barrel region are dominated by muons detected in the DT + RPC system, those in the endcap regions by muon in the CSC + RPC system, and the forward endcaps only by the CSC detector (see Muon System distribution in Figure 23 – right). The division in η is done accordingly: [-2.4, -2.1, -1.2, 0, 1.2, 2.1, 2.4].
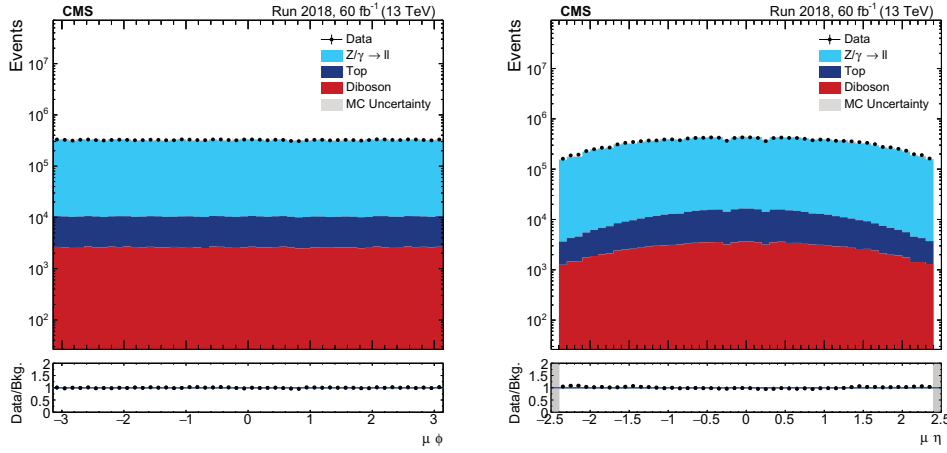

Figure 49: Distribution of muon ϕ (left) and muon η (right) for the dimuon selection for data collected during 2018 and the corresponding SM prediction.

The result for κ_b in the different η and ϕ regions is shown in Figure 50 for 2016, 2017 and 2018 data where the muon p_T corresponds to the value given by the TuneP algorithm. As previously mentioned, the lower muon p_T threshold used is 200 GeV, except for $|\eta| > 2.1$, where the p_T threshold is lowered to 110 GeV in order to increase statistics.

A different graphical way to show the resulting values of κ_b for each region of η and ϕ are presented in Figure 51.

From both Figures 50 and 51, a clear trend in η is found in every year. In the endcaps region ($|\eta| > 1.2$), and especially in the forward endcaps region ($|\eta| > 2.1$), κ_b is of the order of 0.1 TeV^{-1}, while in the barrel region ($|\eta| < 1.2$), κ_b is consistent with 0 TeV^{-1} within the uncertainties. This is understandable since the endcaps detectors (CSC) are harder to align than the barrel detector (DT) [131], they have larger occupancy, and the magnetic field in the forward regions is harder to model.

Regarding the data from different years, 2016 shows larger values of bias κ_b in general, in all η regions. While for 2017 and, especially 2018, the values in the barrel
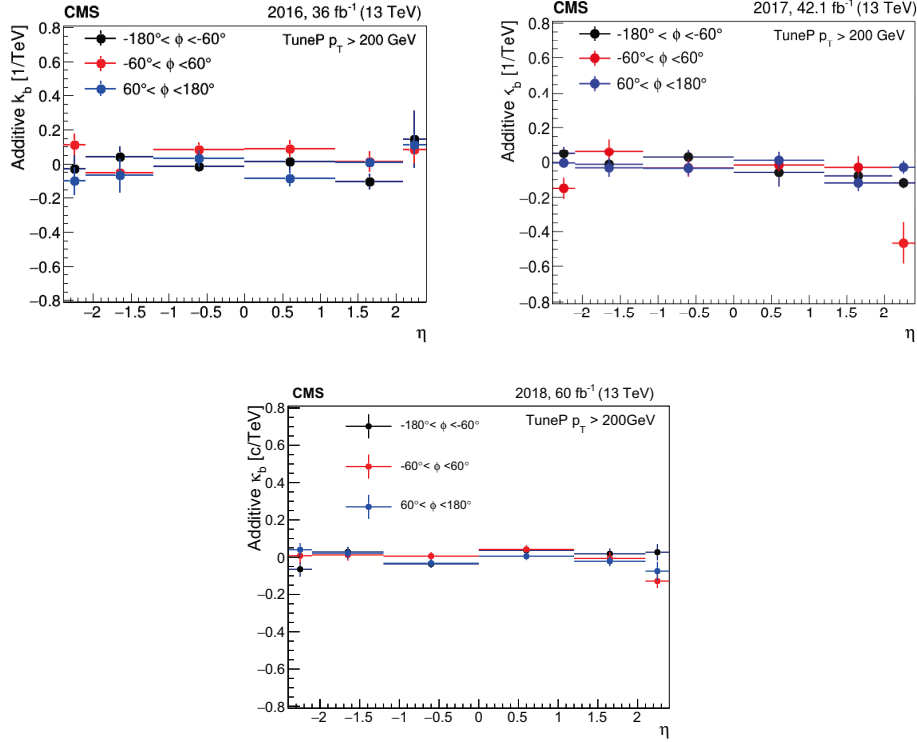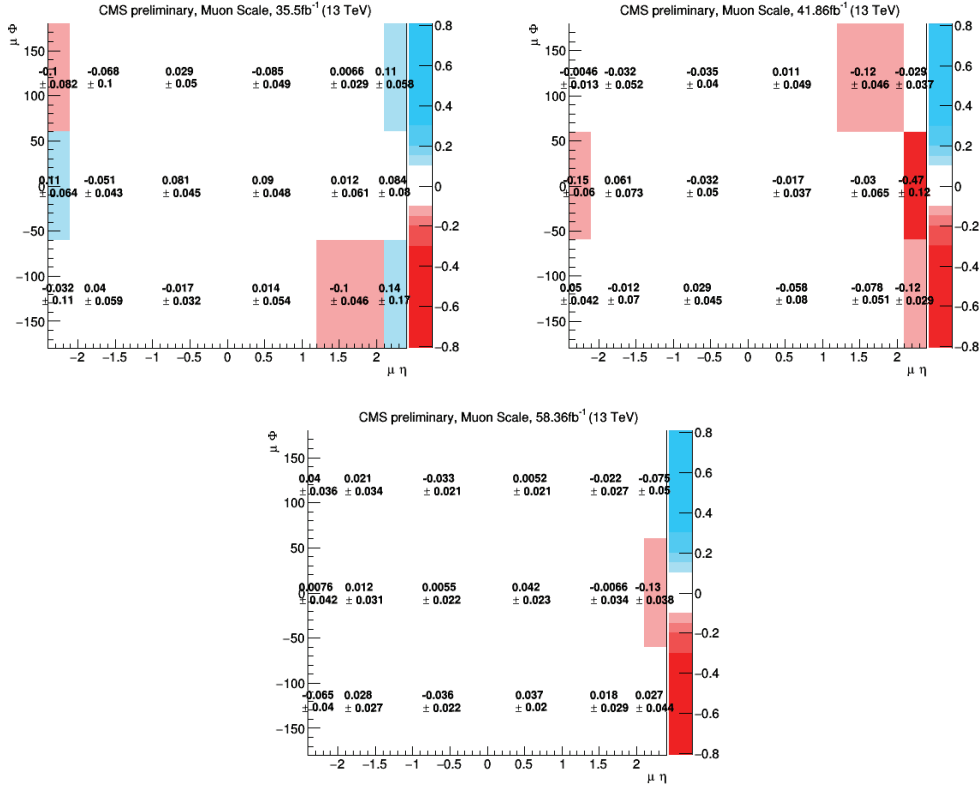
Figure 50: Measurement of scale bias, κ_b, for muons with $p_T > 200$ GeV using 2016 (top-left), 2017 (top-right) and 2018 (bottom), data and MC simulation. The muon p_T is given by the TuneP algorithm. The uncertainties shown correspond to the statistical uncertainty from the fit.

are consistent with zero within the uncertainties. This is due to improvements in the Muon System alignment along the years [132].

Scale bias from Tracker

In order to determine if the bias is coming from the p_T measurement in the Tracker detector, in the Muon System, or from a relative misalignment between both detectors, the GE method was applied using the p_T measurement given by the Tracker only, using muons with $p_T > 200$ GeV. Figure 52 shows the result from applying the GE method to the p_T measured by the Tracker only. The result is compatible with the bias obtained with the p_T TuneP algorithm (Figure 50), which combines information from both, Tracker and Muon System. This points to the p_T scale bias coming from the measurement in the Tracker and not from the Muon System, or the alignment between them.

These measurements of the muon p_T scale bias can be applied to correct the reconstructed muon p_T. But, given they are only relatively significant in the very forward regions, it was convened to introduce them as a source of systematic uncertainty in the measurement of the muon p_T, and thus propagated to all variables using this magnitude. Section 5.6 will explain how to consider the muon scale bias
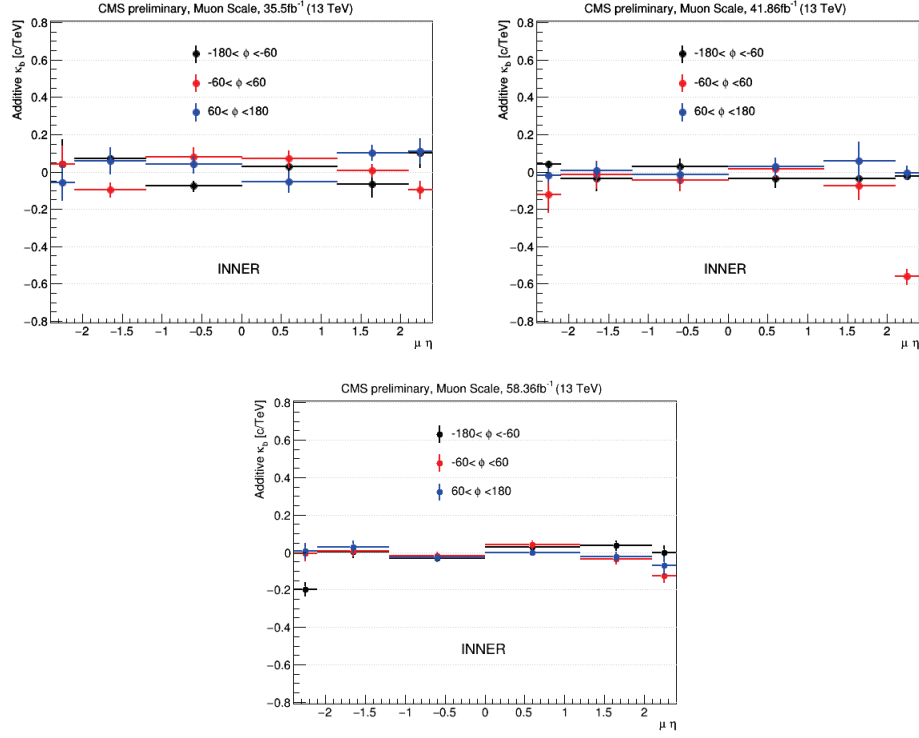
Figure 51: Measurement of scale bias, κ_b, in the $\eta - \phi$ plane, for muons with $p_T > 200$ GeV using 2016 (top-left), 2017 (top-right), and 2018 (bottom) data and MC simulation. Muon p_T corresponds to TuneP p_T. The uncertainties shown represent the statistical uncertainty from the fit.

as a systematic uncertainty.

Scale bias method validation

At low muon p_T, there is another method in CMS that measures the scale bias by looking at the reconstructed invariant mass around the Z boson mass window. This method, developed in CMS by the University of Rochester group, and thus called *Rochester method* [133], derives the p_T scale bias from the mean value of the distribution of the mass of the dimuon system in data and simulation, from Z decays, using the mean of the dimuon invariant mass spectrum.

In order to validate the GE method, it has been applied to the same selection and muon η and ϕ regions as the ones used in the studies with the Rochester method. The events are selected by having two muons, one with $p_T > 25$ GeV, the second with $p_T > 15$ GeV, where the muon p_T corresponds to TuneP p_T, even though for $p_T \lesssim 200$ GeV the TuneP p_T is the same than Tracker p_T. This test is performed with 2017 data and MC simulation. The resulting measurement of scale bias, κ_b, using the GE method is shown in Figure 53. Even if the results from both methods are not directly comparable, the measured scale bias for each η and ϕ region are

Figure 52: Measurement of scale bias, κ_b, for muons with $p_T > 200$ GeV using 2016 (left), 2017 (middle), and 2018 (right) data and MC simulation. Muon p_T is given by the Tracker p_T. The uncertainties shown represent to the statistical uncertainty from the fit.

of the same order, they follow the same trends, and they are compatible within uncertainties [134], validating the GE method.
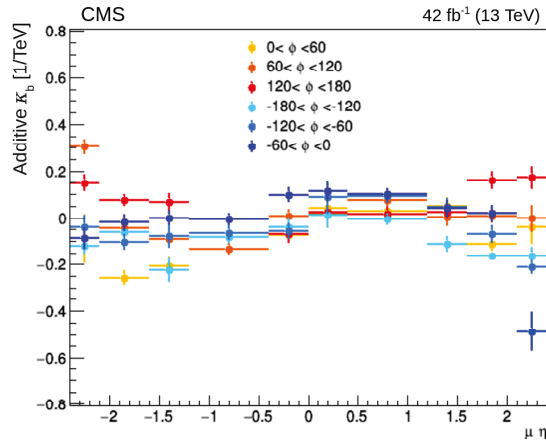
Figure 53: Measurement of scale bias, κ_b, for muons with $p_T > 25$ GeV for 2017 data and MC simulation. Muon p_T is given by the TuneP p_T. The uncertainties shown correspond to the statistical uncertainty from the fit.

4.3 Transverse momentum resolution

The measurement of the muon momentum resolution is an important feature to understand the performance of the detector when detecting muons, to correctly assign a p_T value, and in view of assigning a mass value to any potential new signal observed. In order to determine accurately variables, such as a transverse mass derived from muons, the detector is designed to have the best possible p_T resolution. The standard method to calibrate the muon p_T in CMS is by selecting dimuon events from well known resonances such as $J/\Psi, \Upsilon$ or Z bosons. Since we know with good precision the mass and width of these resonances, the resolution in data and MC simulation is easily calculated and compared. In this method muons in the p_T range up to ~ 100 GeV are used. Unfortunately, there are not resonances at higher mass values that can provide muons with higher p_T. Therefore this method is not totally useful for the high p_T muons that we are discussing in this analysis. The solution adopted lies in releasing the mass constraint for dimuon pairs coming from Z boson decays, accepting off–shell Z bosons, to reproduce the desired high mass (and high p_T) region.

A possible solution to calibrate the high p_T muons is to use also cosmic muons. Cosmic muons are taken by CMS in dedicated data–taking campaigns and they have a large spectrum of momentum reaching values as high as ~ 1 TeV. When they cross vertically the detector they leave one track in the upper part of the detector, and a second track in the lower part of the detector. Using both tracks the resolution is measured for muons with higher p_T than the ones from the previous method (collision data). The limitation of the use of cosmic muons is coming from the geometry. The cosmic muons that arrive to the detector have mostly vertical tracks, or with an angle relatively large with respect to the beam axes. Thus, they are a useful source of high p_T muons to calibrate p_T in the central part of the detector ($|\eta| \lesssim 1.6$). The p_T measured in the detector forward regions cannot be calibrated this way. The p_T resolution measured in data from cosmic muons is presented at the end of this subsection.

Muon p_T resolution in simulation

As an initial evaluation, the transverse momentum resolution of highly energetic muons is measured in simulated events, where the true (generated) muon p_T is known, p_T^{gen}. The resolution is extracted from the distribution of the relative residual between the generated and reconstructed transverse momentum, p_T^{rec},

$$R_{\text{rec–gen}} = \frac{1/p_T^{rec} - 1/p_T^{gen}}{1/p_T^{gen}}, \tag{4.8}$$

that follows a gaussian distribution (as explained in Section 4.1) in the central region. By fitting the middle part of the distribution, fixed according to the mean and the RMS, with a gaussian function, the resolution is defined as the fit width, σ.

Samples containing the production of off–shell W bosons with masses in the range from 100 to 6000 GeV decaying into muon + neutrino, are generated, thus providing a simulated sample of very high p_T muons. The simulation is made for each 2016, 2017, 2018 year. The sample of events used is selected by having a good quality muon, identified with the high–p_T muon ID, with $p_T > 53$ GeV. This muon p_T value is determined by the trigger muon p_T threshold ($p_T > 50$ GeV), and consistent with the steep turn–on curve as it is presented in Section 2.3.6.

The resolution study has been done in bins of the generated muon p_T: (50−100, 100−200, 200−300, 300−550, 550−800, 800−1200, 1200−1600, 1600−2000, and >2000) GeV, divided in the muon barrel region ($|\eta| < 1.2$), negative endcap region ($-2.4 < \eta < -1.2$), and positive endcap region ($1.2 < \eta < 2.4$). Figure 54 shows two examples of two regions, with the residual distribution, the fit and the values of the variables extracted from the fit, mean and σ.
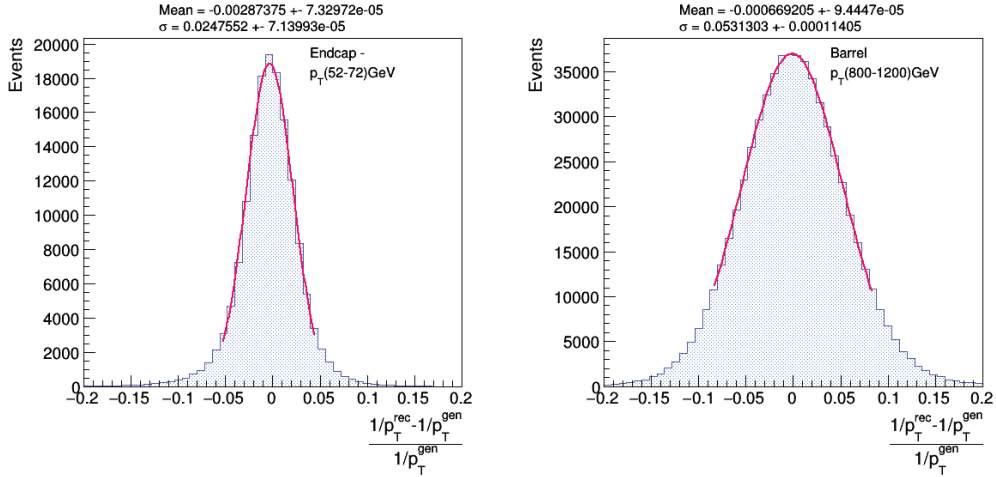
Figure 54: Two examples of residual distributions for two different regions: negative endcap and p_T bin (52–72) GeV (left); and barrel and p_T bin (800–1200) GeV (right). The red curve shows the corresponding gaussian fit from where the resolution is extracted. The mean and σ from the fit are quoted, and the uncertainties refer to statistical uncertainties from the fit.

The transverse momentum resolution (σ from the fit) is shown in Figure 55 as a function of the p_T, and in the $\eta-p_T$ plane in Figure 56. The resolution is about $1\%\,(3\%)$ at $p_T \sim 100$ GeV in the barrel (endcaps) and increases until $7\%\,(8\%)$ for p_T values around ~ 2 TeV. The 2017 and 2018 p_T resolution is slightly better than that in 2016, this is due to improvements in the Muon System alignment [132].

Since the resolution is found to be compatible at positive and negative endcaps, it is more interesting to split the endcaps in two η regions that will be denoted as *endcaps* and *forward endcaps*, corresponding to $1.2 < |\eta| < 2.1$, and $2.1 < |\eta| < 2.4$, respectively. The result of this binning is shown in Figure 57. The p_T resolution in the forward endcaps is significantly higher than in the endcaps and barrel: 4%
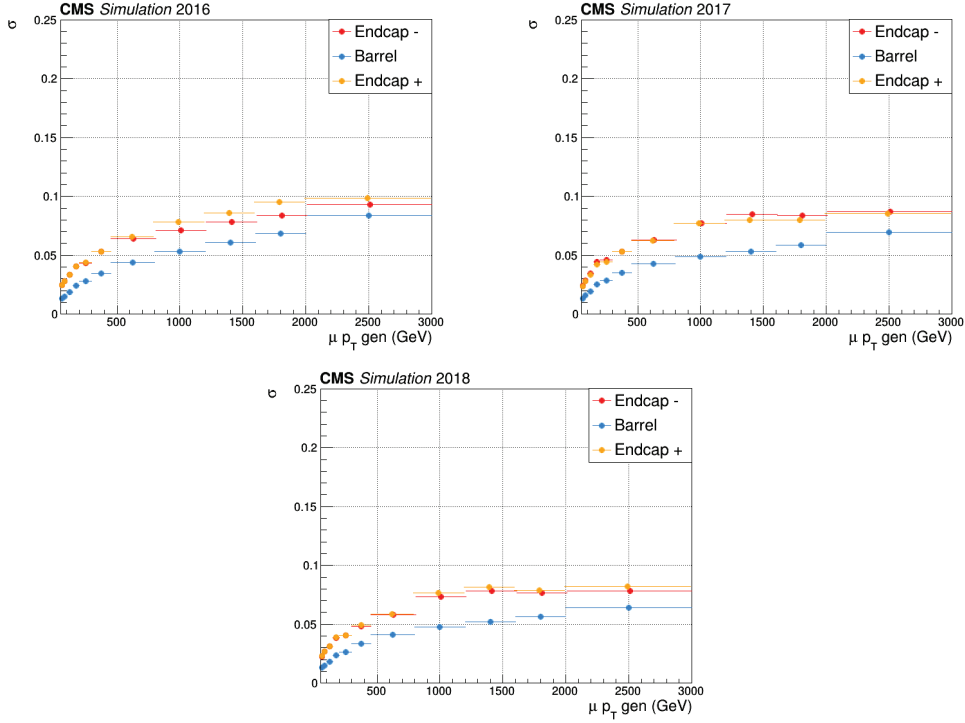
Figure 55: Width of the gaussian fit to the relative $\Delta(1/p_T)$ distribution as a function of generated p_T. Separated for barrel ($|\eta| < 1.2$) (blue) and positive ($1.2 < \eta < 2.4$) (yellow) and negative ($-1.2 < \eta < -2.4$) (red) endcaps. Simulation samples correspond to 2016 (top–left), 2017 (top–right), and 2018 (bottom). Error bars refer to statistical uncertainties from the fit.

at $p_T \sim 100$ GeV, increasing up to 20 % for p_T 1.5 TeV. For geometrical reasons, the particles that pass through the very forward endcaps have large longitudinal momenta, and relatively low transverse momenta. Therefore, the last bin ($p_T > 1600$ GeV) in the forward endcaps distributions has not enough statistics and is not shown in the figure.

Repeating the study splitting according to the muon charge (positive and negative) we find a similar resolution for both charges within statistical uncertainties, as shown in Figure 58.

The error bars in all figures refer only to statistical uncertainties. The resolution measurements are also affected by systematic uncertainties, as, for example, the uncertainty coming from the fit to a gaussian function only in the central part, or the scale effect. No sources of systematic uncertainties have been taken into account in this study.

Muon p_T resolution in cosmic data

The resolution studies presented so far are done with MC simulation. Real muon momentum resolution in data is calculated using cosmic ray muons. As the cosmic muons traverse the CMS detector close to vertically, the detector sees them as having
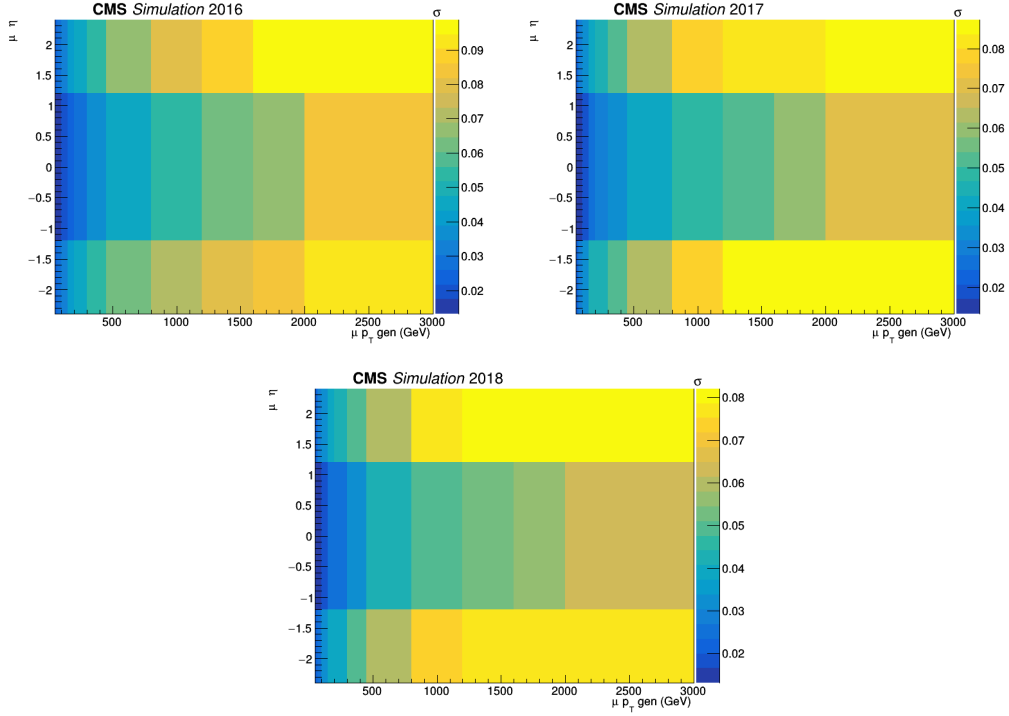
Figure 56: Width of the gaussian fit to the relative $\Delta(1/p_T)$ distribution , in the η vs generated p_T plane. Simulation samples correspond to 2016 (top–left), 2017 (top–right), and 2018 (bottom).

two tracks. One of them looks consistent with coming from the interaction point (if sufficiently close to it) and the other looks reversed in time (they cross the detector outside–in, not inside–out). A specific cosmic reconstruction algorithm in CMS, geometrically fits the track, and assigns a p_T and charge to each of these two tracks.

The two global muon tracks belong to the same cosmic ray muon trajectory and should then have the same (or very similar) momentum. The resolution is calculated using the p_T values of the upper track and the lower track of the cosmic ray are used. Then, the relative q/p_T residual, R_{cosmic}, is calculated as:

$$R_{cosmic} = \frac{(q/p_T)^{upper} - (q/p_T)^{lower}}{\sqrt{2}\,(q/p_T)^{lower}}, \qquad (4.9)$$

where $(q/p_T)^{upper}$ and $(q/p_T)^{lower}$ are the muon charge sign divided by p_T for the upper and the lower muon tracks, respectively. The factor of $\sqrt{2}$ accounts for the fact that the q/p_T measurements of the two tracks are independent.

Figure 59 [129] shows the muon p_T resolution extracted from data using cosmic muons, and from simulation, using off–shell $Z \to \mu\mu$ (DY) generated events, as function of the muon p_T.

The results are shown for 2016 and 2017 years, for the barrel ($|\eta| < 1.2$) (left), and the endcap ($1.2 < |\eta| < 1.6$) (right) regions. The results for muon p_T resolution
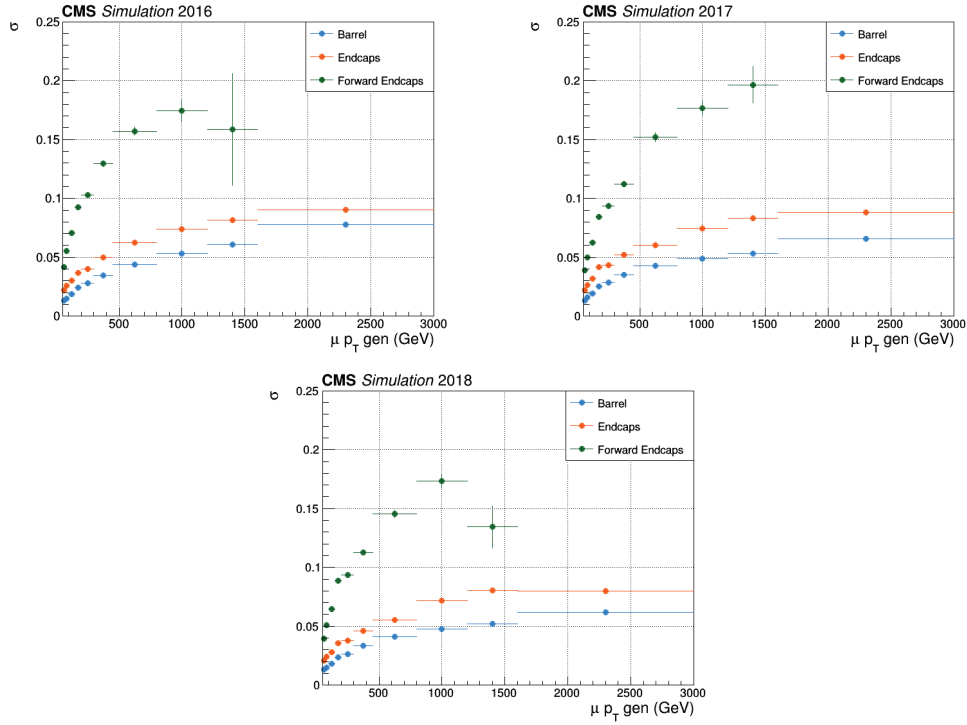
Figure 57: Width of the gaussian fit to the relative $\Delta(1/p_T)$ distribution as a function of generated p_T. Separated for barrel ($|\eta| < 1.2$) (blue), endcaps ($1.2 < |\eta| < 2.1$) (orange), and forward endcaps ($2.1 < |\eta| < 2.4$) (green). Simulation samples correspond to 2016 (top–left), 2017 (top–right), and 2018 (bottom). Error bars refer to statistical uncertainties from the fit.

using $Z \rightarrow \mu\mu$ simulated samples are obtained in the same way as those previously presented with off–shell $W \rightarrow \mu\nu$ samples, and the resolution values are in agreement.
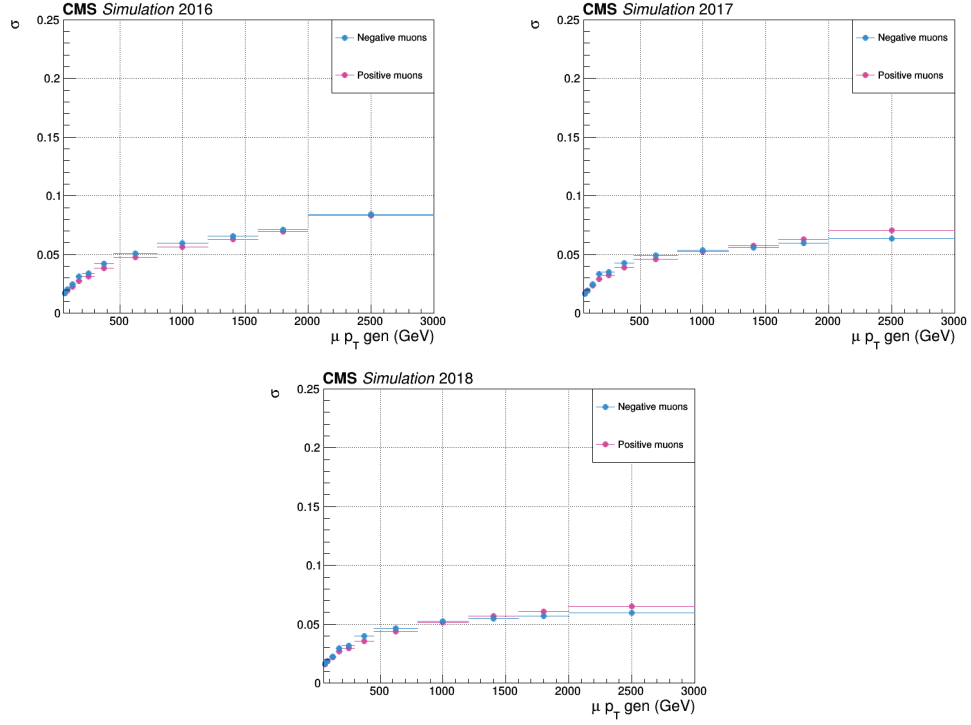
Figure 58: Width of the gaussian fit to the relative $\Delta(1/p_T)$ distribution as a function of generated p_T. Separated for muon charge, negative (blue) and positive (pink). Simulation samples correspond to 2016 (top–left), 2017 (top–right), and 2018 (bottom). Error bars refer to statistical uncertainties from the fit.
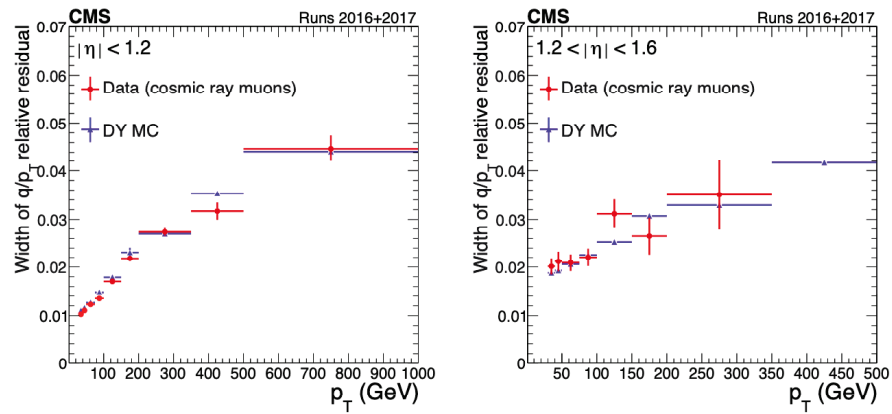
Figure 59: Gaussian σ of fits to q/p_T relative residual distributions of cosmic ray muons collected in 2016 and 2017 in the barrel ($|\eta| < 1.2$) (left), and the endcap ($1.2 < |\eta| < 1.6$) (right) regions, compared to the resolution extracted from DY simulation, as function of the muon p_T [129].

4.4 Charge assignment

The assignment of the muon electric charge is done according to the bending direction of the muon track in the CMS magnetic field. In the transverse plane, with the magnetic field parallel to the z axis, a muon inside the solenoid volume, bends clockwise or anti-clockwise, depending on its charge. Outside the solenoid, the muons bend to the opposite side due to the magnetic return flux as explained in Section 2.3.1.

In the case of ideal alignment conditions among the detectors and magnetic field map knowledge, and for muon energies sufficiently low, the curvature is well determined and the chances to misassign the charge are negligible. As muon energy increases, the trajectory bends less in the magnetic field, becoming a straight line in the limit, and their charge can be mistaken. This effect is represented in Figure 60.
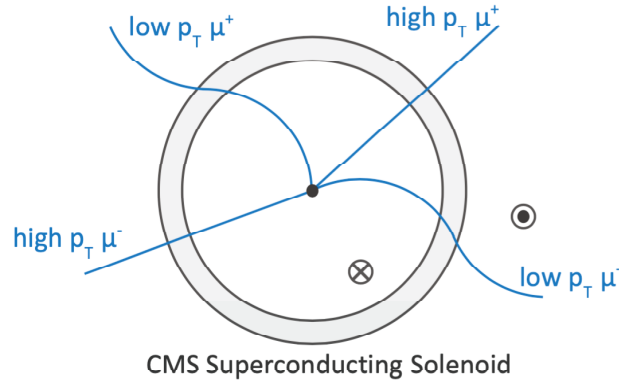
Figure 60: Sketch of curvature of muons tracks with low and high p_T in the CMS superconducting solenoid. The magnetic field created by the solenoid bends the charged particles trajectories according to their charge, and their momentum. The reconstructed charge and transverse momentum is assigned according to its curvature.

In addition, at high p_T values (p_T 200 GeV), muon showering due to bremstrhalung becomes important, creating a high multiplicity of hits in the muon chambers that hinders the track reconstruction and, thus, the charge assignment. At sufficiently high muon energies the probability to misreconstruct the muon charge may become non–negligible. Thus the importance to estimate it.

The variable of interest, denoted as charge mis–ID rate, is defined as the fraction (%) of muons whose reconstructed charge is different from the generated one, and it has been estimated in simulated samples of very energetic muons. Due to the charge symmetry of the reconstruction algorithms, the charge mis–ID rate is expected to be the same for positive and negative muons, i.e. positive muons have the same chances to be reconstructed as negative, than negative muons to positive. Using MC generated samples of muons with a homogeneous (flat) distribution on the muon momentum, p, the charge mis–ID rate is confirmed to be the same for positive and negative muons, as shown in Figure 61.
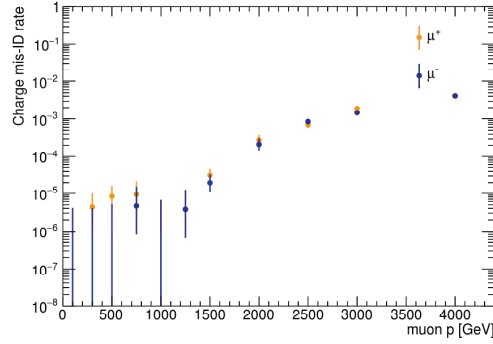
Figure 61: Rate of muon charge misassignment as a function of the muon momentum, in MC generated samples with flat distribution of muon p, separated for muon charge, negative (blue) and positive (orange). Error bars refer to statistical uncertainties.

However, the momentum distribution of the muons coming from a given physics process depends on the process itself, and it may not be flat. In the case of this study, the muons come from the decay of massive W boson decays. Due to the PDFs involved in the production of the W boson, the W^+ and W^- bosons are generated with different kinematic behaviour, and, therefore, the μ^+ and μ^- kinematics from each respective decays is different. The normalized muon η distribution at generated level is shown in Figure 62 - left separately for μ^+ and μ^- for events passing a trigger with muon p_T threshold of 50 GeV in high mass $W \rightarrow \mu\nu$ simulated samples, generated in the mass range from 100 to 6000 GeV.
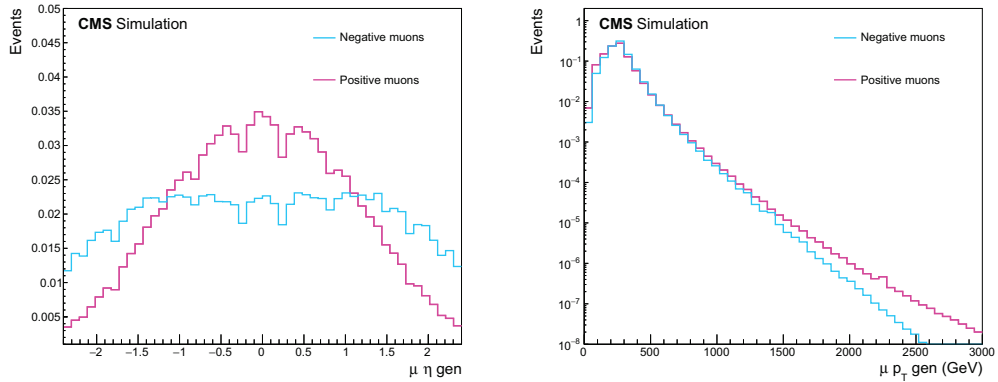
Figure 62: Distribution of muon η (left) and muon p_T (right), for events passing a trigger with muon p_T threshold of 50 GeV, from high mass $W \rightarrow \mu\nu$ simulated samples generated in the mass range from 100 to 6000 GeV.. The distributions are shown split by muon charge: negative (blue) and positive (pink). Distributions are normalized to 1.

The positive muons show a more central distribution peaking at $\eta = 0$, while the negative muons show a rather flat distribution for $|\eta| < 1.5$. The normalized muon

p$_T$ distribution at generated level is shown in Figure 62-right for the same high mass W boson samples. The muon p$_T$ of positive muons is reaches higher values than for negative muons, yielding a harder spectrum.

The differences on the kinematics of W$^+$ and W$^-$ bosons may have an effect on the probability of muon charge misassignment different for positive and negative muons, in the particular case of high mass W bosons reconstructed with the CMS detector. The muon charge mis–ID rate is calculated in high mass W$\rightarrow \mu\nu$ simulated samples, separately for μ^+ and μ^-, as a function of the muon η and the muon p$_T$, and it is shown in Figure 63.
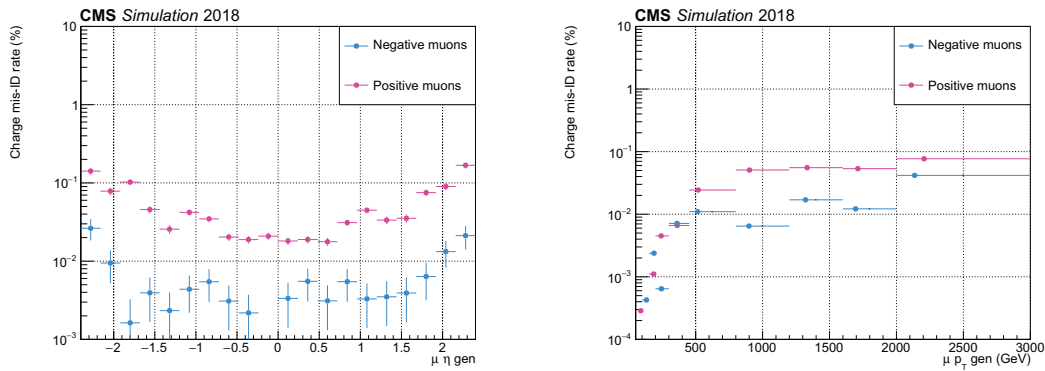
Figure 63: Probability in % for muon charge misassignment as a function of muon η (left) and muon p$_T$ (right), in high mass W$\rightarrow \mu\nu$ simulated samples, separated for muon charge, negative (blue) and positive (pink). The central value in each bin is obtained from the average of the distribution within the bin. Error bars refer to statistical uncertainties.

Both distributions in Figure 63 show very small charge mis–ID values, is below 0.1 % even for p$_T$ in the TeV region. The muon charge mis–ID rate is higher for positive than for negative muons, due, as expected, to their larger p$_T$ distribution. For positive muons with p$_T$ 800 GeV the rate is ~ 0.06 %, while for negative muons is ~ 0.01 %.

Independently of the muon charge, in Figure 63-left is shown that the muon charge mis–ID rate is higher at the forward region than in the central region of the detector. This effect is consistent with the worse p$_T$ resolution and scale bias measured in these regions, as already presented (Section 4.3). The probability for charge confusion as a function of the generated p$_T$, is shown in Figure 64, divided in the muon barrel region ($|\eta| < 1.2$) and endcap regions ($-2.4 < \eta < -1.2$ and $1.2 < \eta < 2.4$), and inclusive in charge, for each year of generated MC simulation.

The simulations of the three years show a consistent charge misassignment rate. The muon charge mis–ID rate is found to be the same in the positive than in the negative endcap region. On the contrary, it is significantly larger in the endcaps than in the barrel region. The value obtained for charge misassignment for muons
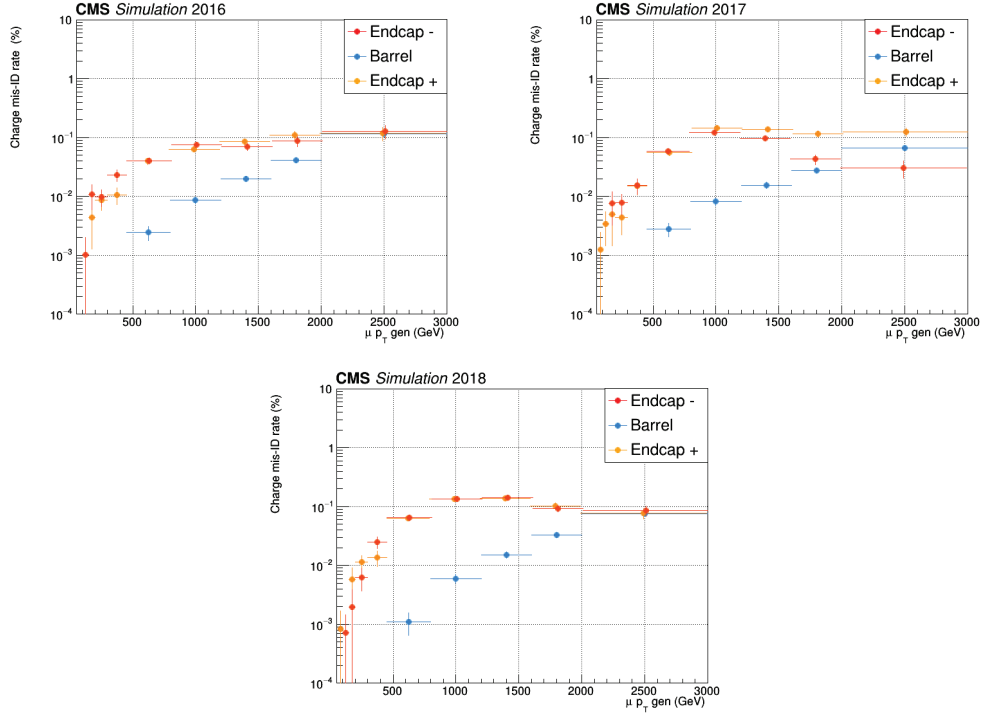
Figure 64: Probability in % for muon charge misassignment in high mass W$\to \mu\nu$ simulated samples, separated for barrel (blue) and positive (yellow) and negative (red) endcaps. For 2016 (top-left), 2017 (top-right), and 2018 (bottom) samples. Error bars refer to statistical uncertainties.

with $p_T \sim 500$ GeV is $\sim 0.002\,\%$ in the barrel and $\sim 0.07\,\%$ in the endcaps, and for muons with $p_T \sim 1$ TeV is $\sim 0.01\,\%$ in the barrel, and $\sim 0.1\,\%$ in the endcaps.

The same way than the muon p_T resolution was measured in cosmic data, by comparing the two reconstructed trajectories (upper and low), the charge misassignment is calculated in cosmic muons. From the 20,000 cosmic muons that were collected during Run 2 by CMS with $p_T > 30$ GeV, only one muon appears to have a wrong charge assignment, with apparent $p_T = 640$ GeV (estimated from the lower CMS hemisphere). [129]. This is a charge misassignment of $0.005\,\%$, consistent within statistical uncertainties with the measured rate in simulation.

4.5 Efficiency

The efficiency to have a well measured muon (ϵ_μ) depends on several factors and steps in its detection, reconstruction, etc. It is factorized in tracking (ϵ_{trk}), reconstruction (ϵ_{reco}), identification (ϵ_{ID}), isolation (ϵ_{iso}), and trigger efficiency ($\epsilon_{\mathrm{trigger}}$):

$$\epsilon_\mu = \epsilon_{\mathrm{trk}} \times \epsilon_{\mathrm{reco}} \times \epsilon_{\mathrm{ID}} \times \epsilon_{\mathrm{iso}} \times \epsilon_{\mathrm{trigger}} \qquad (4.10)$$

The five efficiencies are computed individually using the *Tag and Probe* method [130]. Using this technique it is possible to obtain an unbiased estima-

tion of the efficiencies in data, where the true muon variables cannot be known. This method selects events with strict selection requirements on one muon (the *tag* muon), and with a more relaxed selection on a second muon (the *probe* muon), where the dimuon system is compatible with a Z boson decay. The fraction of probe muons that passes the requirement under study gives an estimate of its efficiency.

This method is applied both in real data and in simulated samples. The data may have a slightly different efficiency than the one assumed in MC simulation. The correction to account for such differences is called Scale Factor (SF). The SF is calculated as the ratio of efficiency in data and MC simulation:

$$\mathrm{SF} = \frac{\epsilon_{\mathrm{Data}}}{\epsilon_{\mathrm{MC}}} \tag{4.11}$$

It is important to study the independent efficiencies, as well as the SFs, and their dependence with certain variables, since they are used as a correction to the simulation as it will be explained in Section 5.4.

Tracking efficiency

Muons are very well reconstructed in the Tracker as they mainly interact with the silicon detector through ionization of the medium and, unlike electrons, their energy loss through bremsstrahlung is negligible. Muons therefore tend to cross the entire volume of the Tracking System, producing detectable hits in several sensitive layers of the detector. The tracking efficiency for muons is $\sim 100\,\%$ [80] as shown in Figure 65, over the full η range of Tracker acceptance, and it does not depend on the muon p_T above a very low p_T threshold of ~ 1 GeV.
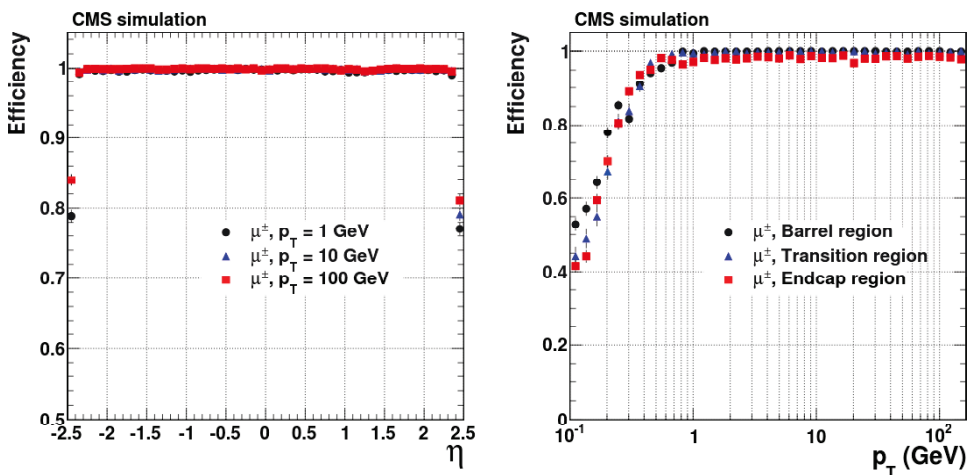
Figure 65: Tracking reconstruction efficiency for muons. Results are shown as a function of η (left), for $p_T = 1$, 10, and 100 GeV; and p_T (right), for the barrel, transition, and endcap regions, which are defined by the η intervals of 0–0.9, 0.9–1.4, and 1.4–2.5, respectively [80].

The efficiency of the Tracker track reconstruction, ϵ_{trk}, appears independent of the muon momentum and does not require dedicated study at high momentum. All other components of ϵ_μ rely on the performance of the Muon System and can potentially be affected by muon showering as well as by the biases in the Muon System alignment relative to the Tracker. Such features would lead to a dependence of efficiency on muon p_T and η.

Reconstruction efficiency

Global muons reconstruction efficiency accounts for the track reconstruction and matching between the Tracker and the Muon System tracks. This efficiency is ~ 1 [129] as shown in Figure 66, in data and MC simulation, for the full momentum spectrum and for 2017 as an example. A slightly decreasing trend is observed for muon $p > 1$ TeV, due to the presence of muon showering, although the global reconstruction efficiency remains larger than 0.99.
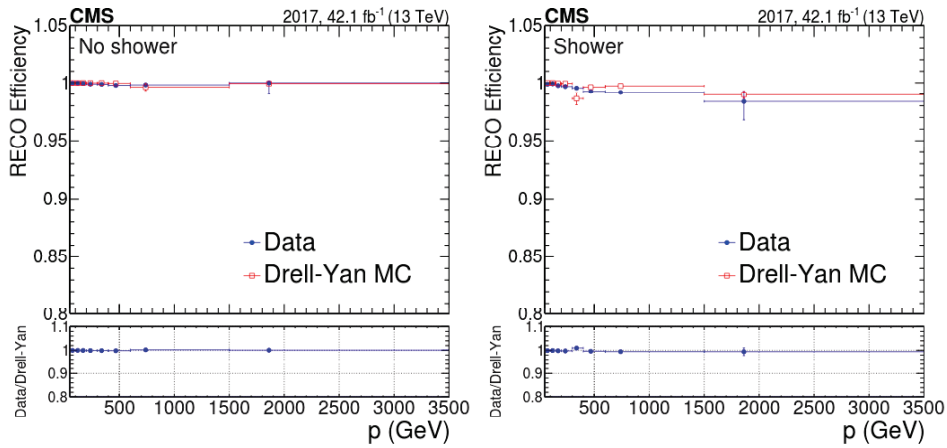
Figure 66: Muon reconstruction efficiency as a function of muon momentum for events without any showers (left), and events with at least one shower (right), for 2017 data and MC simulation. The lower panels show the ratio of efficiencies in data and simulation [129].

Since the same reconstruction efficiency is found for data than for MC simulation, the SF associated to the reconstruction efficiency is 1 for the full range of muon momentum, as shown in the lower panel of Figure 66, where the ratio of efficiencies in data and simulation is presented.

Identification efficiency

Each muon ID criteria explained in Section 3.3.1 has a different efficiency. The looser the ID criteria (e.g. Loose muon ID) the higher the efficiency but, also, the higher the mis–identification rate is, compared with a more restrictive criteria. The efficiency associated to the ID criteria used in this analysis (high–p_T muon ID) is above 0.98 [129] in data, over the full detector acceptance, and non p_T dependence

is found, as shown in Figure 67.
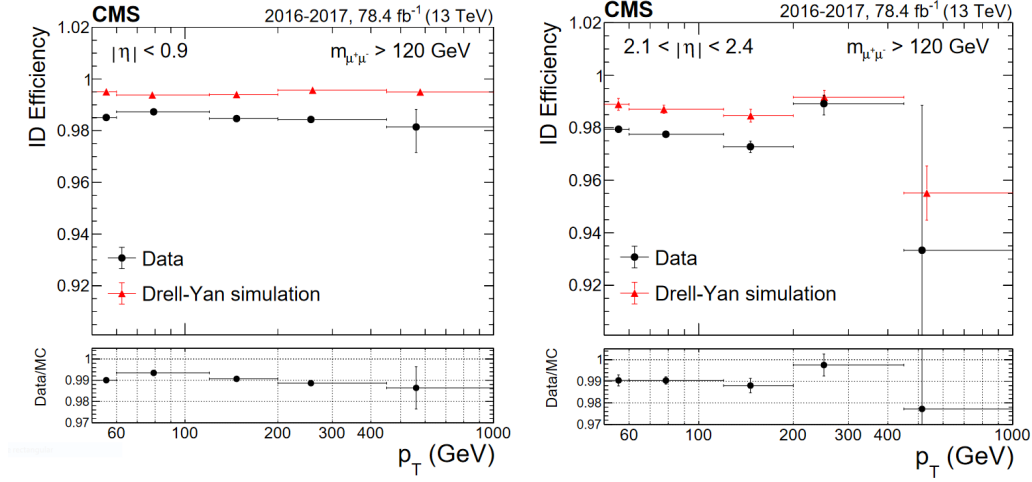
Figure 67: High–p_T muon ID efficiency for 2016 and 2017 data, and corresponding DY simulation, as a function of p_T for $|\eta| < 0.9$ (left) and $2.1 < |\eta| < 2.4$ (right). The lower panels show the ratio of efficiencies in data and simulation [129].

The MC simulation predicts slightly higher efficiency than observed in data, but the data–to–simulation agreement is uniform with increasing p_T. The SFs for the muon identification efficiencies range from 0.97 to 0.99 as a function of the muon pseudorapidity, η.

Isolation efficiency

The efficiency of muon isolation (defined in Section 3.3.2), is studied relative to a probe muon that has passed the high–p_T identification criteria. The muon isolation efficiency for a relative Tracker isolation $< 10\%$ is shown in Figure 68 as a function of the muon p_T for 2017 data and MC simulation.

For the muon p_T region studied in this analysis ($p_T^\mu > 53$ GeV) the muon isolation efficiency is found to be consistent with 1, and independently of the muon p_T. This is found for both, data and MC simulation, therefore, the SF associated to the isolation efficiency is ~ 1 [134, 135].

Trigger efficiency

The HLT trigger path (as described in Section 2.3.6) used to select events with muons, combines Muon System information with Tracker information. This path receives the name of HLT_Mu50. The HLT_Mu50 path triggers only an event if it contains a muon with $p_T > 50$ GeV within the detector acceptance $|\eta| > 2.4$.

The standard technique for measuring efficiencies, the *Tag and Probe* method [130], presented at the beginning of this section, relies in dimuon events coming from Z bosons. But, there are not enough statistics of high p_T muons from the Z boson decays, and given the nature of the efficiency under study (events
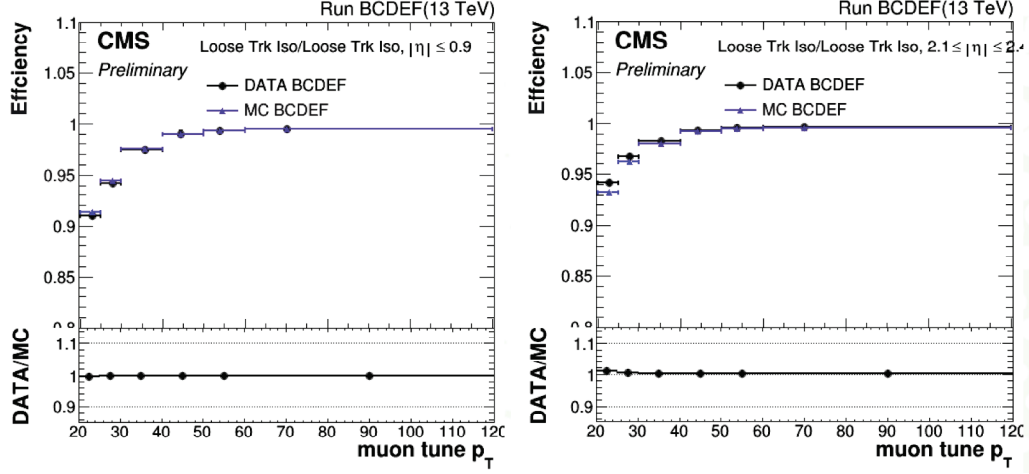
Figure 68: Muon isolation efficiency for high–p_T ID muons with relative Tracker isolation of 10%. Results are shown as a function of the muon p_T, for $|\eta| < 0.9$ (left) and $2.1 < |\eta| < 2.4$ (right), for 2017 data and MC simulation. The lower panels show the ratio of efficiencies in data and simulation [134].

failing the trigger requirement are lost forever), an alternative method is used for high p_T muons trigger efficiency: the orthogonal method. The extraction of the trigger efficiency of the events containing a single high–p_T muon is done by using orthogonal datasets: *SingleElectron* and *MET* datasets. The events selected in these independent datasets have been triggered and collected due to the presence of a high energy electron or high p_T^{miss}, respectively.

We start by selecting events containing isolated muons satisfying the high–p_T ID criteria in these independent datasets, as described in Section 3.3. This constitutes our initial sample. To avoid possible biases, a negligible amount of events with additional muons passing the Loose muon ID requirement are rejected. The efficiency is calculated as the fraction of events (i.e. muons) that fired the trigger path under study over the total number of events in the initial sample of muons.

The efficiency is measured in each year dataset and in the simulated samples where one off–shell W boson is produced and decayed in the $\mu + \nu$ channel. Figure 69 shows the HLT_Mu50 trigger path efficiency as a function of the muon p_T and η for 2016 data and MC simulation, using the orthogonal SingleElectron sample.

The efficiency as a function of p_T shows the turn–on curve at the p_T threshold (50 GeV) of the trigger under study. Given the fast turn–on with p_T, a plateau in efficiency is reached already for $p_T > 53$ GeV. This plateau sits at an efficiency value of ~0.95 in MC simulation and in a slightly smaller value in data, ~0.90. The efficiency as a function of η reproduces the detector geometry. At $|\eta| \sim 0.2$, the efficiency is lower due to the transition region between wheels (see Figure 21). Endcap regions, $|\eta| > 0.9$, have ~10% lower efficiency than the barrel region, $|\eta| < 0.9$.

In order to increase the amount of data available for this study, and since the SingleElectron dataset suffers from the same lack of statistics at the high p_T regime,
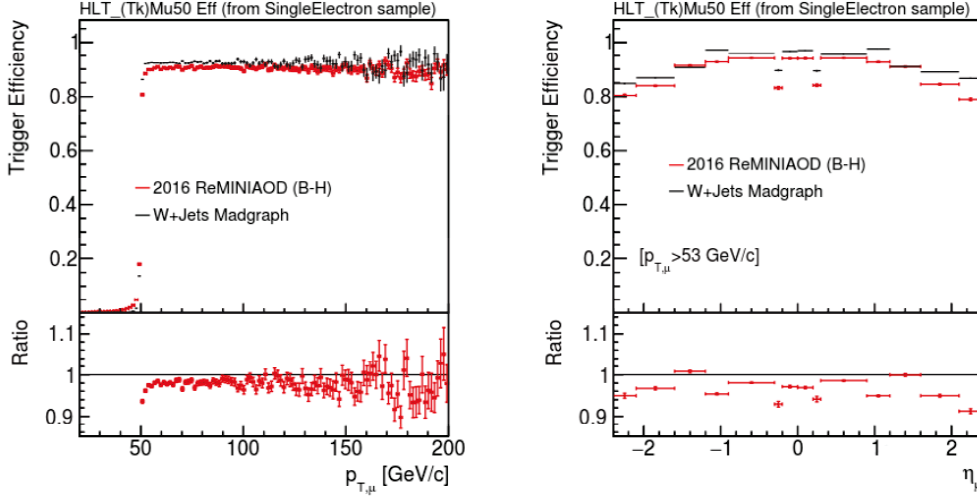
Figure 69: Trigger efficiency as a function of the muon p_T (left) and η (right) for the HLT_Mu50 path. Muons identified in the SingleElectron sample are used to compute the efficiency in 2016 data (red), and W boson MC samples for the simulation efficiency (black). The lower panels represent the ratio of efficiencies, data to simulation. Error bars represent statistical uncertainties.

a dataset based in the presence of large p_T imbalance (p_T^{miss}), MET dataset, is also used. The efficiency and scale factors for 2017 data and MC, obtained from muons in the MET dataset are shown in Figure 70. The MET dataset has higher statistics and allows us to extend the p_T range until higher values. The efficiency tends to decrease at very high p_T, until ~ 0.9 for $p_T > 1$ TeV, for both data and simulation. The scale factors calculated from the SingleElectron dataset are also shown in the ratio plot, even though there are not enough statistics for muon $p_T > 500$ GeV. The efficiencies obtained with both methods are consistent within the uncertainties.

The efficiency and scale factors obtained from muons in the MET dataset of 2018 as a function of muon p_T and η are shown in Figure 71. The efficiency slightly decreases at very high p_T, until ~ 0.9 for $p_T > 1$ TeV, for both data and simulation, in agreement with the previous years. The ratio plots shows as well the scale factors released by the Muon group in CMS Collaboration (Muon POG) and they are found to be compatible withing the uncertainties. Those numbers were computed using the *Tag and Probe* method [130], totally independent of our estimation, as explained at the beginning of this section.

The efficiencies for 2016 (Figure 69), 2017 (Figure 70), and 2018 (Figure 71) data, are consistent with each other.

This chapter has introduced the most important ingredient of the analysis: the high p_T muon. Now we are ready to start the description of the full analysis.
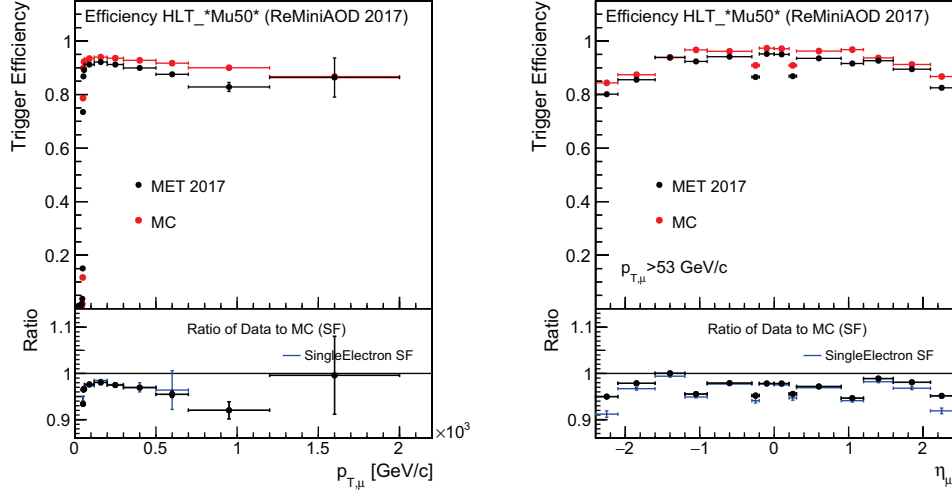
Figure 70: Trigger efficiency as a function of the muon p_T (left) and η (right) for the HLT_Mu50 in 2017 dataset. Muons identified in the MET sample were used to compute the efficiency in data and compare to MC predictions. The lower panels represent the ratio of efficiencies, data to simulation. The scale factor obtained is compared to that computed using the SingleElectron sample (blue). Error bars represent statistical uncertainties.
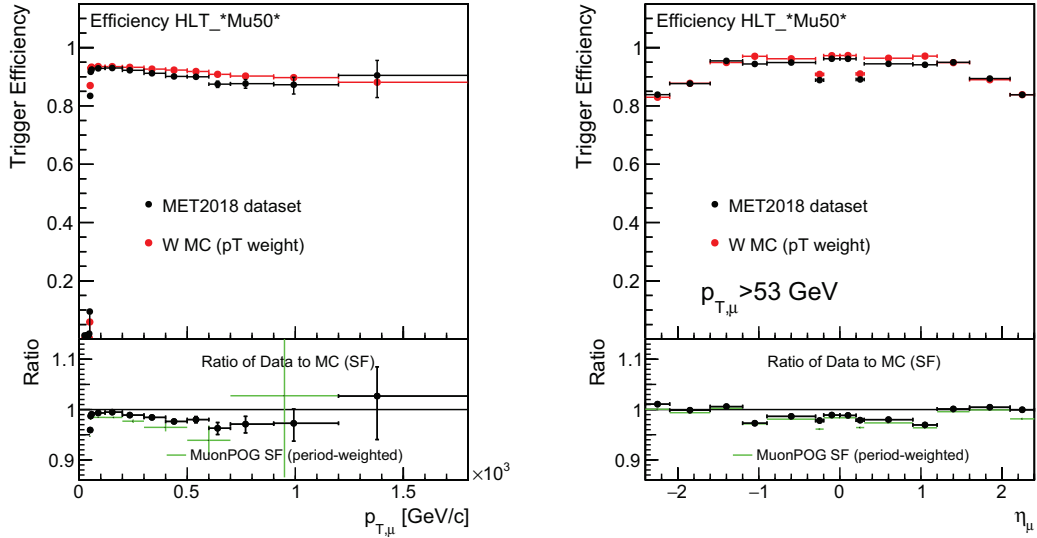
Figure 71: Trigger efficiency and ratio (SF) as a function of the muon p_T (left) and muon η (right). Muons identified in the MET sample were used to compute the efficiency in 2018 data (black) and compared to MC (red). The scale factor obtained (ratio plot) is compared to the one computed officially by the Muon POG (green). Error bars represent statistical uncertainties. The lower panels represent the ratio of efficiencies, data to simulation.

Chapter 5

Analysis strategy

In this analysis, final states containing an energetic muon (μ) and missing transverse momentum ($\vec{p}_T^{\,\text{miss}}$) are studied, looking for deviations from the SM predictions. The discriminant variable used is the transverse mass (M_T) of the $\mu + p_T^{\text{miss}}$ system:

$$M_T = \sqrt{2\, p_T^\mu\, p_T^{\text{miss}}\, (1 - \cos[\Delta\phi(\,\vec{p}_T^{\,\mu}\,,\,\vec{p}_T^{\,\text{miss}}\,)])} \tag{5.1}$$

where p_T^μ is the magnitude of the muon transverse momentum, $\vec{p}_T^{\,\text{miss}}$ is the apparent momentum imbalance in the transverse plane defined in Section 3.6, and $\Delta\phi(p_T^\mu, \vec{p}_T^{\,\text{miss}})$ is the azimuthal angle between the direction of the muon and the $\vec{p}_T^{\,\text{miss}}$ as illustrated in Figure 72.
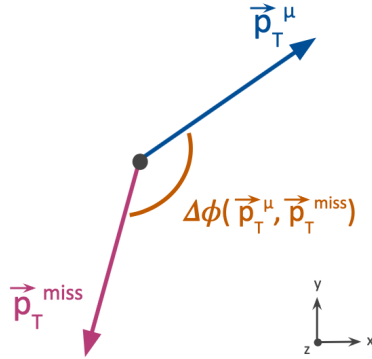
Figure 72: Sketch of the reconstructed variables: $\vec{p}_T^{\,\text{miss}}$ (pink), muon p_T direction (blue) and $\Delta\phi(p_T^\mu, \vec{p}_T^{\,\text{miss}})$ (orange).

The search is performed in a model independent way and also under the framework of given theoretical models. We consider the most general cases: direct production of a resonance, and a non–resonant contact interaction effect, where the resonance is not seen. Also called, direct and indirect searches, respectively.

In the first case we assume the presence of a massive BSM resonance, whose signal stands out from the SM predicted background in the tail of the M_T distribution as represented in Figure 73.
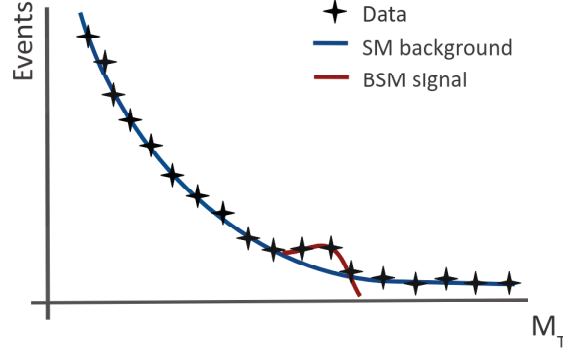
Figure 73: Sketch of the M_T distribution showing experimental data (black dots), SM background (blue), and a resonant signal (red).

In the second case, the BSM signal is assumed to lie above the kinematic limit of the collider and the resonance is not visible in the data. However, a certain deviation may still be observed in the tail of the M_T distribution as illustrated in Figure 74.
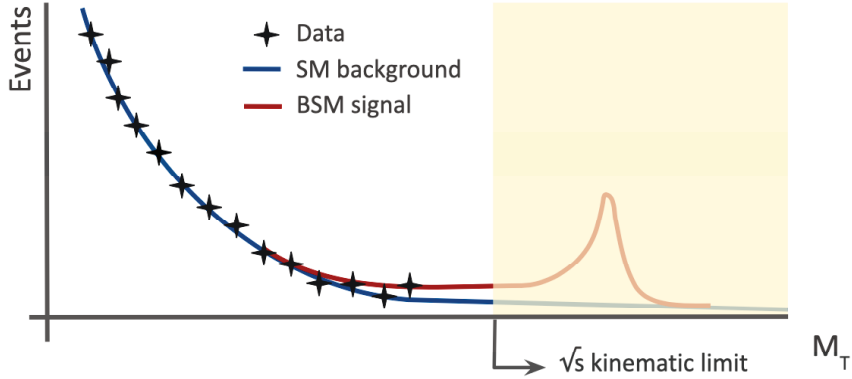
Figure 74: Sketch of the M_T distribution showing a falling background shape (blue) and a hypothetical BSM signal (red) above the accelerator kinematic limit that creates a non–resonant deviation in the M_T accessible region. The experimental data (black dots) may be sensitive enough to the potential deviation in the M_T distribution.

The study of the experimental data has been done in a model independent way, and also interpreted in terms of the BSM models presented in Chapter 1. To design an analysis strategy that maximizes the measurement of a hypothetical signal and minimizes the SM background yields, the processes of signal and background need to be modeled. To implement such modeling, several samples of simulated Monte Carlo (MC) events were generated as it will be explained in the following Section 5.1 for signals, and Section 5.2 for background.

5.1 Signals

Different sets of signals are simulated for this analysis: W' bosons as defined in the Sequential Standard Model (SSM) with SM coupling strength, W' boson varying the coupling strength, Kaluza–Klein bosons ($W_{KK}^{(2)}$) in the Split–UED model, and tau slepton ($\tilde{\tau}$) in a RPV SUSY model. Details of these models were explained in Section 1.2.

5.1.1 SSM model

With the aim of using a guide to explore different BSM models, the SSM has been used as generic (benchmark) model. The SSM model, explained in detail in Section 1.1, assumes the existence of massive bosons as W' and Z', with the same couplings and decay modes as the SM electroweak W and Z bosons, respectively. For this analysis, MC generated samples of SSM W' bosons have been produced.

This model is implemented in several generator programs such as PYTHIA8 [71] or MADGRAPH [75]. The simulation of inclusive $pp \to W' \to \mu\nu$ process in the SSM model is performed at leading order (LO) with PYTHIA8 generator program, using the underlying event tune CUETP8M1 [69] when simulating 2016 samples, and CP5 [70] for the case of 2017 and 2018. The PDF set used is NNPDF 2.3 [67] 2016 and NNPDF 3.1 [68] in 2017 and 2018 (PDF sets and UE were presented in Section 2.2.2).

The set of W' boson masses ranges from 200 to 6400 GeV. The lowest mass matches the beginning of the sensitive region as determined by the efficiency plateau of the trigger above a p_T threshold that translates into this M_T threshold (detail in Section 4.5). The highest generated mass aims to cover the expected sensitivity of Run 2 data. One mass point sample is generated every 200 GeV of W' mass, and each sample contains 2×10^4 events.

The generated mass distributions for three simulated W' boson samples with masses, $M_{W'}$ = 2200, 3800, and 5600 GeV are displayed in Figure 75 - left. The variable relevant in this analysis is the reconstructed M_T of the $\mu + p_T^{miss}$ system, shown in Figure 75 - right. In both distributions we appreciate how the low mass off–shell production becomes more important for higher W' mass samples. This effect is due to the suppression of parton PDFs at very high transferred proton momentum fraction.

The cross sections of production and decay of the SSM W' (inclusive $pp \to W' \to \mu + \nu$), are calculated at NNLO in precision (σ_{NNLO}) using FEWZ [136] simulation code as a function of the W' boson mass. Both, the LO cross section, σ_{LO}, and NNLO cross section, σ_{NNLO}, are shown in Figure 76 as a function of the W' mass. The ratio $\sigma_{NNLO}(\text{FEWZ})/\sigma_{LO}(\text{PYTHIA})$ is defined as a K–factor, depicted in the lower panel of the figure, that is used to correct the MC simulated SSM W' samples to NNLO level.

The K–factors increase with the W' boson mass up to around 3000 GeV, reaching a value of ~1.3. For higher masses, the K–factor decreases and becomes similar
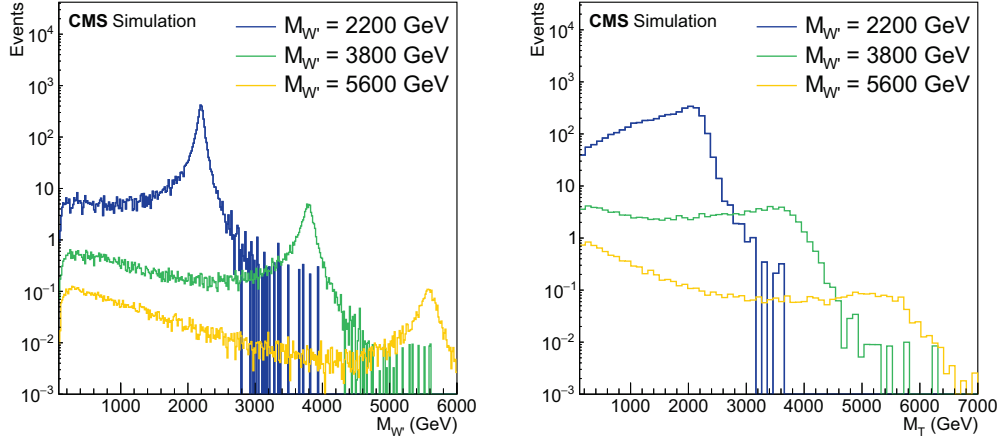
Figure 75: Distribution of W' generated mass (left) and $\mu + p_T^{miss}$ reconstructed transverse mass (right), for three SSM generated signal samples of W' mass, $M_{W'}$ = 2200, 3800, and 5600 GeV.

to the low mass values, because of the increased fraction of off–shell production. The cross sections of the $pp \rightarrow W' \rightarrow \mu + \nu$ process, σ_{NNLO} and σ_{LO}, together with the K–factors are collected in Table 5.1 for the W' mass values corresponding to the generated signal samples.
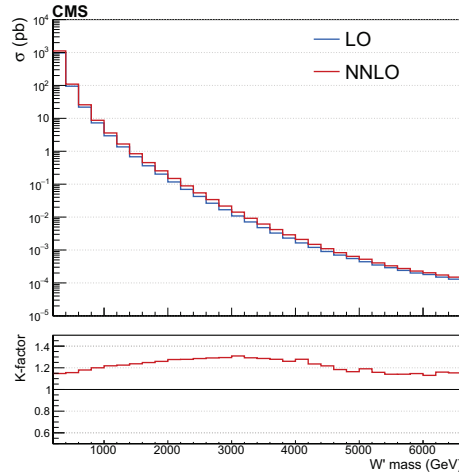
Figure 76: Distributions of LO and NNLO $pp \rightarrow W' \rightarrow \mu + \nu$ cross sections. The lower panel presents the ratio $\sigma_{NNLO}/\sigma_{LO}$ defined as the K–factor.

5.1.2 Coupling strength variation

The SSM benchmark model assumes W' bosons couplings to SM particles to be equal to those from the SM W boson, i.e. $g_{W'} = g_W$ (see Section. 1.2.1). In a more general scenario, this assumption could be released, leading to different coupling values. In that case we can study the possibility of a W' boson that couples weaker

94

W' mass [GeV]	σ_{LO} [pb]	σ_{NNLO} [pb]	K–factor	W' mass [GeV]	σ_{LO} [pb]	σ_{NNLO} [pb]	K–factor
200	975.1	1118.7	1.147	3400	0.0048	0.0061	1.29
400	94.7	109.5	1.156	3600	0.0033	0.0042	1.28
600	21.9	25.8	1.180	3800	0.0023	0.0029	1.26
800	7.3	8.7	1.200	4000	0.0016	0.0021	1.28
1000	2.9	3.6	1.218	4200	0.0012	0.0015	1.23
1200	1.4	1.7	1.225	4400	0.00090	0.0011	1.22
1400	0.68	0.84	1.237	4600	0.00070	0.00083	1.18
1600	0.36	0.45	1.25	4800	0.00055	0.00064	1.16
1800	0.20	0.25	1.26	5000	0.00044	0.00052	1.19
2000	0.12	0.15	1.28	5200	0.00035	0.00040	1.16
2200	0.069	0.089	1.28	5400	0.00029	0.00033	1.14
2400	0.042	0.054	1.28	5600	0.00024	0.00027	1.14
2600	0.026	0.034	1.29	5800	0.00020	0.00023	1.15
2800	0.017	0.022	1.29	6000	0.00018	0.00020	1.13
3000	0.011	0.014	1.31	6200	0.00015	0.00017	1.16
3200	0.0071	0.0092	1.29	6400	0.00013	0.00015	1.15

Table 5.1: The LO and NNLO cross sections for $\mathrm{pp} \to \mathrm{W'} \to \mu + \nu$ process, with the K–factors corresponding to the ratio $\sigma_{\mathrm{NNLO}}/\sigma_{\mathrm{LO}}$.

or stronger to fermions and bosons.

For this coupling strength study, SSM W' signal samples with coupling values ranging, in terms of the ratio $g_{\mathrm{W'}}/g_{\mathrm{W}}$, between 1×10^{-2} and 3, are simulated at LO with the MadGraph generator [75].

These signals samples are only produced at generator level and they are used to weight the generated pythia SSM distributions from where the final M_{T} distributions are obtained.

Because of the relation between the width and the coupling of a resonance, (Equation 1.21) these signals exhibit different resonance widths and cross sections as shown in Figure 77 where the M_{T} distribution for a W' boson signal sample with mass $M_{\mathrm{W'}} = 2000$ GeV is presented, for three different values of the coupling strength ratio, $g_{\mathrm{W'}}/g_{\mathrm{W}} = 1$, 3, and 0.01.

5.1.3   Split–UED model

The simulation of the Split–UED model (presented in Section 1.2.2) is performed at LO with pythia. The mass dependent K–factors from the SSM W' (Table 5.1) interpretation are used. This is possible since the signal shapes of a $W_{\mathrm{KK}}^{(2)}$ and a SSM W' are identical. The signal $W_{\mathrm{KK}}^{(2)}$ samples are generated in the range $1/R = (200 - 3000)$ GeV, and $\mu = (50 - 10000)$ GeV. The $1/R$ range corresponds to the mass of $W_{\mathrm{KK}}^{(2)}$ from approximately 400 to 6000 GeV.

The distributions of generated M_{T} of a $W_{\mathrm{KK}}^{(2)}$ in the Split–UED model, with mass, $M(W_{\mathrm{KK}}^{(2)}) = 1800$, 3800, and 5800 GeV, are shown in Figure 78. Notice that
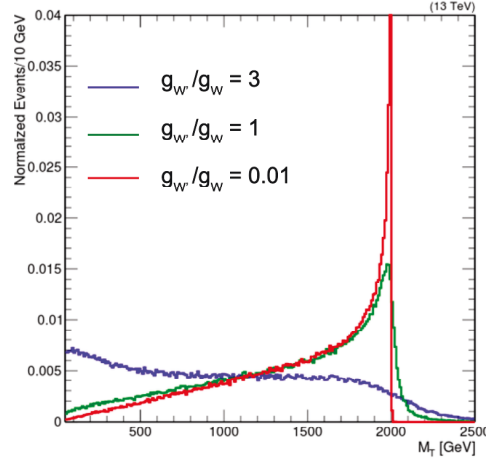
Figure 77: Distribution of M_T for a SSM W' signal sample of mass 2000 GeV, for different coupling ratio ($g_{W'}/g_W$) values: 1 (green), 3 (blue), and 0.01 (red).

this distribution corresponds to the $W_{KK}^{(2)}$ transverse mass at generated level, and the distribution shown in Figure 75 - right instead, is the reconstructed transverse mass from the decay products ($\mu + \nu$) of the SSM W' boson.
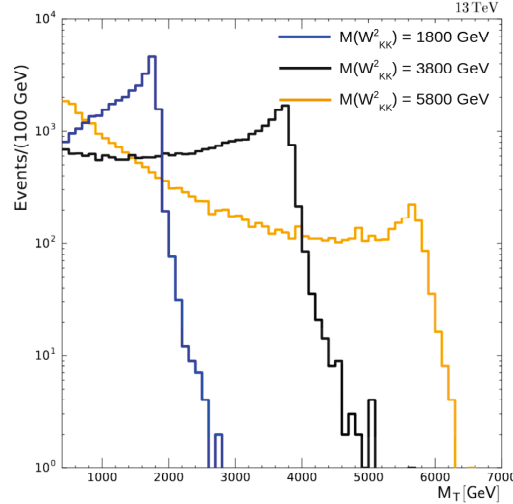
Figure 78: Distribution of generated M_T of a $W_{KK}^{(2)}$ boson in the Split–UED model, with mass, $M(W_{KK}^{(2)}) = 1800$, 3800, and 5800 GeV.

5.1.4   RPV SUSY model

Signal samples for a range of tau slepton masses, $M(\tilde{\tau})$, are simulated with MAD-GRAPH at LO in precision, and no higher order effects are considered. Signals are simulated with the couplings λ_{132} and λ'_{3ij} ranging from 0.05 to 0.5, and $M(\tilde{\tau})$ varying between 400 and 6000 GeV in steps of 200 GeV (model presented in Section 1.2.3).

The distributions of generated M_T of a $\tilde{\tau}$ in the RPV SUSY model, with mass, $M(\tilde{\tau}) = 1800$, 3800, and 5800 GeV, are shown in Figure 79. The model independent

search will be used to explore this RPV SUSY model.
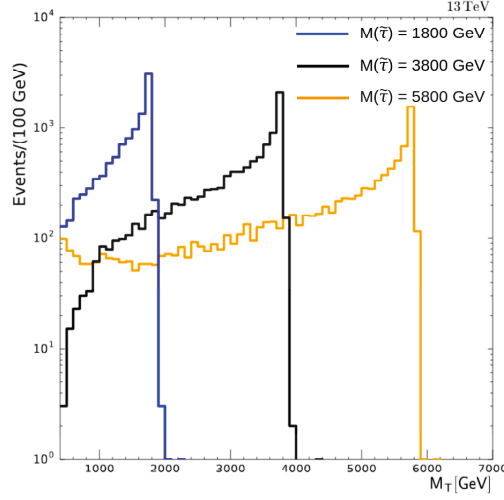
Figure 79: Distribution of generated M_T of a $\tilde{\tau}$ in the RPV SUSY model, with mass, $M(\tilde{\tau}) = 1800$, 3800, and 5800 GeV.

5.1.5 HVT model

In the previous signal models, the resonance (W' boson or other) is assumed to decay leptonically (e, μ, τ), and the decays to bosons (W, Z, H, γ) are suppressed. In a more general scenario where couplings to bosons are possible (HVT model [137]), a reweighting procedure to the SSM signals, has been introduced to account for width and cross section variations. It implements the ratio of Breit–Wigner distributions of corresponding fermionic plus bosonic widths relative to that of only fermionic width, and takes into account the different cross–section values.

The relativistic Breit–Wigner function, G, describing a resonance of a mass, M, with coupling, g, and width, Γ, is given by:

$$G = \frac{g^4}{(s - M^2)^2 + \frac{s^2 \Gamma^2}{M^2}} \tag{5.2}$$

where s is the resonance energy squared. The SSM signal, where W' boson distributions are generated according to fermionic width, Γ_{SSM}, need to be reweithed to signal distributions of fermionic–bosonic width, Γ_{HVT}. The weight is the ratio of two Breit–Wigner distributions, where both, the width and the coupling can be different:

$$\text{weight} = \frac{G_{HVT}}{G_{SSM}} = \frac{g_{W'}^4}{g_W^4} \times \frac{(s - M_{W'}^2)^2 + \frac{s^2 \, \Gamma_{SSM}^2}{M_{W'}^2}}{(s - M_{W'}^2)^2 + \frac{s^2 \, \Gamma_{HVT}^2}{M_{W'}^2}} \tag{5.3}$$

97

where $M_{W'}$ is the nominal mass defined by the sample. In the SSM model, the relation between the width and the coupling of the resonance corresponds only to the fermionic interaction, and is expressed as follow (from Equation 1.21):

$$\Gamma_{\text{SSM}} = \Gamma_{\text{Fermion}} = \frac{M_{W'} g_W^4}{4\pi g_{W'}^2} \tag{5.4}$$

and in the case of the HVT model, the contribution from bosons is added [137]:

$$\Gamma_{\text{HVT}} = \Gamma_{\text{Fermion}} + \Gamma_{\text{Boson}} = \frac{M_{W'} g_W^4}{4\pi g_{W'}^2} + \frac{M_{W'} g_{W'}^2}{96\pi} \tag{5.5}$$

Table 5.2 shows the Γ_{Fermion}, Γ_{Boson}, Γ_{Total} SSM, and Γ_{Total} HVT, relative to the W' mass, for different values of $g_{W'}/g_W$.

$g_{W'}/g_W$	$\Gamma_{\text{Fermion}}/M_{W'}$	$\Gamma_{\text{Boson}}/M_{W'}$	Γ_{Total} SSM $/M_{W'}$	Γ_{Total} HVT $/M_{W'}$
1.0	0.0336	0.0014	0.0336	0.0350
0.7	0.0165	0.0029	0.0165	0.0193
0.5	0.0084	0.0056	0.0084	0.0140
0.3	0.0030	0.0156	0.0030	0.0186
0.2	0.0013	0.0350	0.0013	0.0363
0.1	0.0003	0.1400	0.0003	0.1403

Table 5.2: Width of the W' boson relative to its mass in the SSM and HVT scenarios, for different coupling ratio values, $g_{W'}/g_W$.

When the ratio $g_{W'}/g_W$ decreases the bosonic part of the decays becomes dominant. Figure 80 shows the effect of the reweight to the HVT model for different coupling ratios for two initial SSM samples of W' mass $M_{W'} = 1000$ GeV (left) and 5000 GeV (right). We can see that for lower values of $g_{W'}/g_W$, the width increases, and the cross section gets reduced. Therefore, the sensitivity to such signals is lower.

This model will be taken into account in the Composite Higgs scenario.
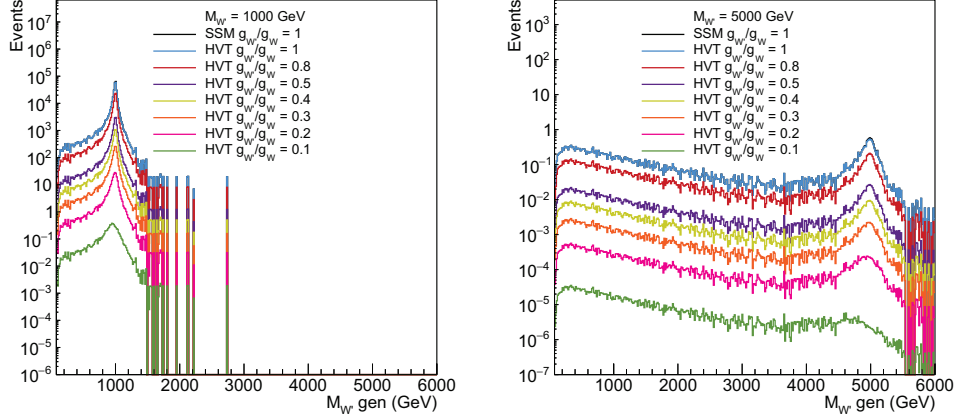
Figure 80: Generated W' mass distribution in the SSM model and reweighted to the HVT model with different coupling ratios for the sample of W' mass $M_{W'} = 1000$ GeV (left) and 5000 GeV (right).

5.2 Background

There are several SM processes whose final state is the same, or can be mistaken as, that of the signal: $\mu + p_T^{miss}$. All these processes are considered as background in our search. Since they correspond to very well known and defined SM processes or detector effects they are estimated using MC simulation samples that reliably reproduce the high mass region under study. The MC simulations are produced centrally at CMS to guarantee that all the collaboration uses a standard production, including the proton PDFs, the detector simulation, and the particle software reconstruction. Figure 81 shows a sketch of the main processes that mimic the signal final state, $\mu + p_T^{miss}$.
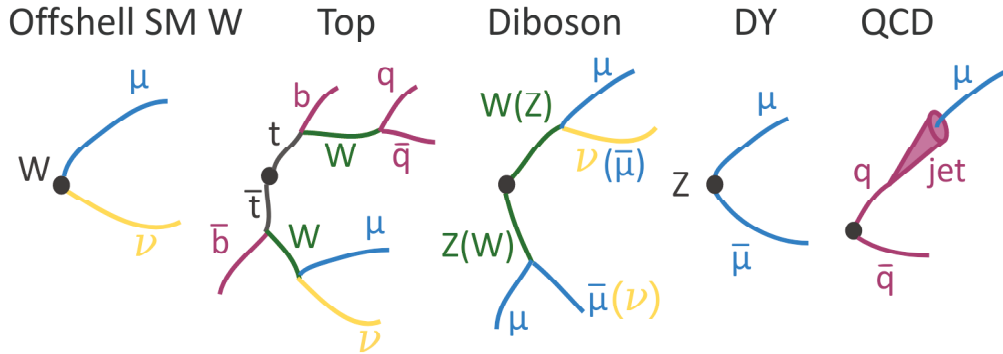
Figure 81: Main contributions to the SM background in the inclusive $\mu + p_T^{miss}$ final state.

Further effects found in data differently from simulations, such as efficiencies, PU distributions, muon p_T assignment (scale and resolution), etc., are implemented in the simulated samples via corrections that will be presented in Section 5.4, or

considered as systematic uncertainties as it will be shown in Section 5.6. This section presents the main background contributions.

5.2.1 W boson background

The dominant and irreducible background is the production of $W \to \mu\nu$. Different contributions have been considered in this process, that generates a high momentum muon and p_T inbalance: the decay of a high W off–shell boson, and W on–shell bosons with high momentum (W boosted). In order to ensure an enough number of simulated W boson events in the complete phase space region, three different kinds of samples have been used:

– **W off–shell:** samples of $W \to \mu\nu$ and $W \to \tau\nu$ decays, have been separately simulated for different mass regions, in order to increase the number of events produced. Thus, samples with masses $M_W > 100, 200, 500, 1000, 2000, 3000, 4000, 5000$, and 6000 GeV, are produced. Since they are generated without upper limit in the W boson mass, they are not orthogonal to each other, and therefore, cuts in the generated W boson mass are applied to avoid overlap in the W boson mass phase space.

These samples were generated, using the PYTHIA8 generator, that provides a NLO accuracy on the W boson variables distributions shape, and a LO for the cross section values [71]. This is expected to be the main background present in this search.

– **W on–shell:** resonant mass region of $W \to \ell\nu + \text{jets}$, with $\ell = e, \mu, \tau$. The W on–shell sample aims to reproduce the W boson mass peak, and the falling mass tail close to the mass peak, therefore, only events with a mass in the range $(50 - 100)$ GeV are generated. This background is not contributing to the high mass region where this analysis is more sensitive, but it is included to describe the background before applying all the selection cuts in the low mass region. This sample was generated with MADGRAPH generator, and the simulated jets are matched to the matrix element and parton shower produced by PYTHIA following the MLM approach [138].

– **W boosted:** samples of $W \to \ell + \nu$ process, with $\ell = e, \mu$, and τ, have been simulated in different regions of the scalar sum of p_T of out–coming hard–process partons, H_T: 100–200, 200–400, 400–600, 600–800, 800–1200, 1200–2500, and > 2500 GeV. This produces on–shell W bosons with a high p_T (boosted). It is reduced by applying some selection criteria that requires the resonance to be produced almost at rest (details in Section 5.5.1), although not necessarily completely rejected. It provides a correct description of the background before applying the complete selection. These samples were generated with MADGRAPH generator.

Since the three types of W boson samples are not orthogonal to each other, cuts in the generated W boson mass and generated H_T are applied, ensuring a soft

and continuous stitching of samples, without discontinuities. The scheme presented in Figure 82 shows the regions in both generated variables, covered by each type of sample.
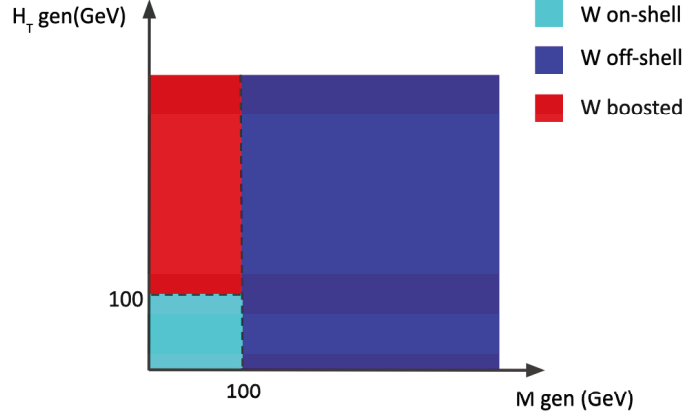
Figure 82: Three types of $W \to \mu\nu$ background samples cover the full phase space: W on–shell with $H_T < 100\,\mathrm{GeV}$ (light blue), W off–shell for any H_T value (dark blue), and W boosted for $H_T > 100\,\mathrm{GeV}$ (red). The three types of $W \to \mu\nu$ background samples are cut in the generated variables H_T and W boson mass to avoid double counting events.

The main generated distributions are presented in Figure 83: the $\mu + \mathrm{p_T^{miss}}$ system invariant mass (W boson mass) spanning two different regions, scalar sum of $\mathrm{p_T}$ of out–coming hard–process partons (H_T), and the $\mu + \mathrm{p_T^{miss}}$ system transverse momentum (W boson $\mathrm{p_T}$).

The generated W boson mass distribution (top–left) reproduces the W boson peak (~ 80.4 GeV [6]) starting at 50 GeV, with the contributions of the on–shell and W boosted samples. For the high mass region (from 100 GeV onwards), only the off–shell W samples contribute. Notice that the continuous W off–shell distribution (dark blue), is not only a sample but composed of 9 samples binned in the W generated mass variable with a smooth stitching. The H_T variable distribution (bottom–left) shows as well a smooth stitching among the samples that compose the W boosted background (in red). The off–shell and on–shell W bosons are produced almost at rest and, therefore, their momentum is low ($\lesssim 100\,\mathrm{GeV}$), as shown in the generated W $\mathrm{p_T}$ variable distribution (bottom–right).

To study the different W boson samples they have been plotted with different colors, but from now on in this text, they will appear together in light blue color to denote the total W boson background.

High order corrections in W boson samples: K–factor

The main background, in particular at very high M_T where new signals are expected, is due to off–shell SM W boson events which exhibit very similar kinematics as the potential signal. Therefore, it is essential to have an accurate description of the tails
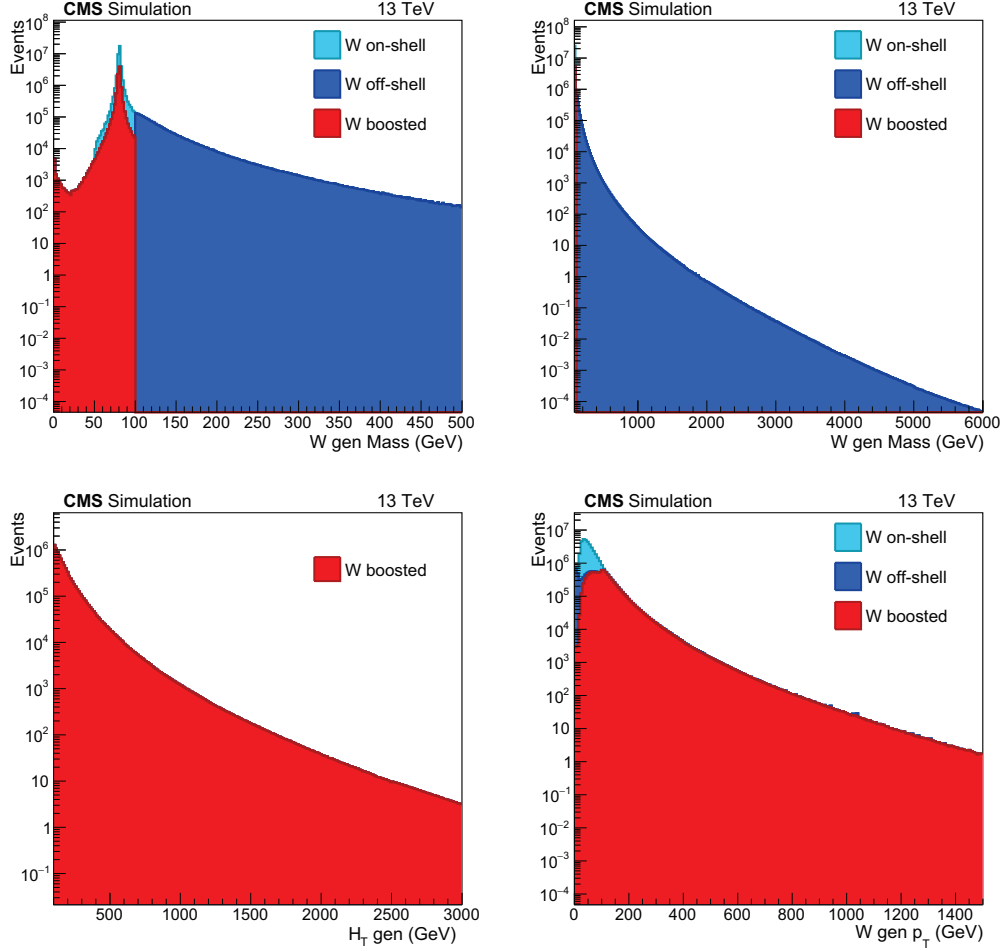
Figure 83: Distributions of generated (gen) variables for W boson background simulated samples: W boson mass from the muon $+ p_T^{miss}$ system at low mass region (0–500) GeV (top–left), and in the extended W mass range (120–6000) GeV (top–right), H_T (bottom–left), and W boson p_T from the muon $+ p_T^{miss}$ system (bottom–right).

of the M_T distributions. The differential cross section of the W boson production is known to NNLO precision in QCD with two jets and NLO in electroweak (EW) calculations. The implementation of these higher order corrections is done in terms of K–factors, evaluated in bins of the W boson mass, M_{inv}:

$$K - factor(M_{inv}) = \frac{\Delta\sigma_{N(NLO)}/\Delta M_{inv}}{\Delta\sigma_{LO}/\Delta M_{inv}} \tag{5.6}$$

The NLO EW corrections at $\sqrt{s} = 13$ TeV, are computed with the MCSANC [139, 140] program, while NNLO QCD corrections are derived with FEWZ [136]. In Figure 84, the high order differential production cross section as a function of the W boson invariant mass, M_{inv}, is shown.
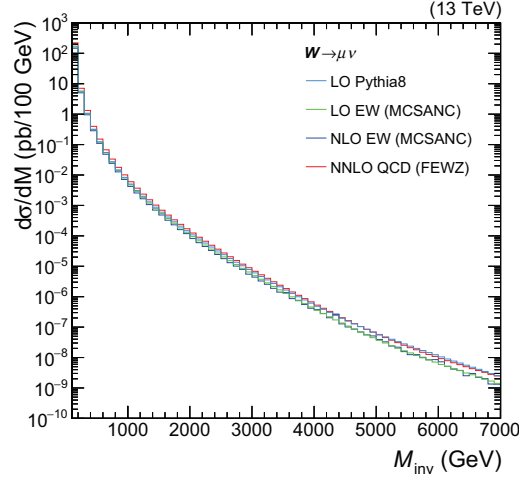
Figure 84: Differential cross section distribution of the $pp \rightarrow W \rightarrow \mu + \nu$ process as a function of the W invariant mass, M_{inv}, calculated at different orders in EW and QCD precision, with different programs: PYTHIA at LO (light blue), MCSANC at LO in EW (green), at NLO in EW (dark blue), and FEWZ at NNLO in QCD (red).

The EW and QCD corrections can be combined with an additive approach:

$$\frac{d\sigma}{d\mathcal{O}}\bigg|_{QCD \oplus EW} = \frac{d\sigma}{d\mathcal{O}}\bigg|_{QCD} + \frac{d\sigma}{d\mathcal{O}}\bigg|_{EW} - \frac{d\sigma}{d\mathcal{O}}\bigg|_{LO}, \tag{5.7}$$

or a factorized approach [141]:

$$\frac{d\sigma}{d\mathcal{O}}\bigg|_{QCD \otimes EW} = \frac{\frac{d\sigma}{d\mathcal{O}}\big|_{QCD}}{\frac{d\sigma}{d\mathcal{O}}\big|_{LO}} \times \frac{d\sigma}{d\mathcal{O}}\bigg|_{EW}. \tag{5.8}$$

The additive approach assumes that the EW corrections, except FSR, have an additive nature, are of the same order, and need to be added for all orders of QCD. Thus the relative fraction of higher order EW corrections for each order of QCD is changing. The factorised approach assumes that the higher order EW corrections are the same for all orders of QCD, and thus can be determined based on LO QCD and then transferred to any order of QCD. Both approaches can be theoretically motivated and the correct combination would lie between these two approaches. The differential cross section of the W boson production as a function of the invariant mass, M_{inv}, is shown in Figure 85 - left, at LO, at (N)NLO on the additive approach, and multiplicative approach. The K–factors as a function of the invariant mass are shown in Figure 85 - right.

The K–factor used in the analysis is based on the additive approach. The K–factor varies from 1.2 ± 0.036 for $M_W = 200$ GeV, to 0.91 ± 0.19 for $M_W = 5500$ GeV.

In order to smooth out the fluctuations of the additive K–factors, they are

parametrized using a 4th–degree polynomial function. The gray uncertainty band in Figure 85 - right is obtained from the statistical fluctuations of the K–factors, to cover the difference with respect to the fit. These fluctuations are very small at low masses, but tend to get larger ($\sim 40\,\%$) at very high masses. These mass dependent values are taken into account for the systematic uncertainty associated to the W off–shell K–factors.
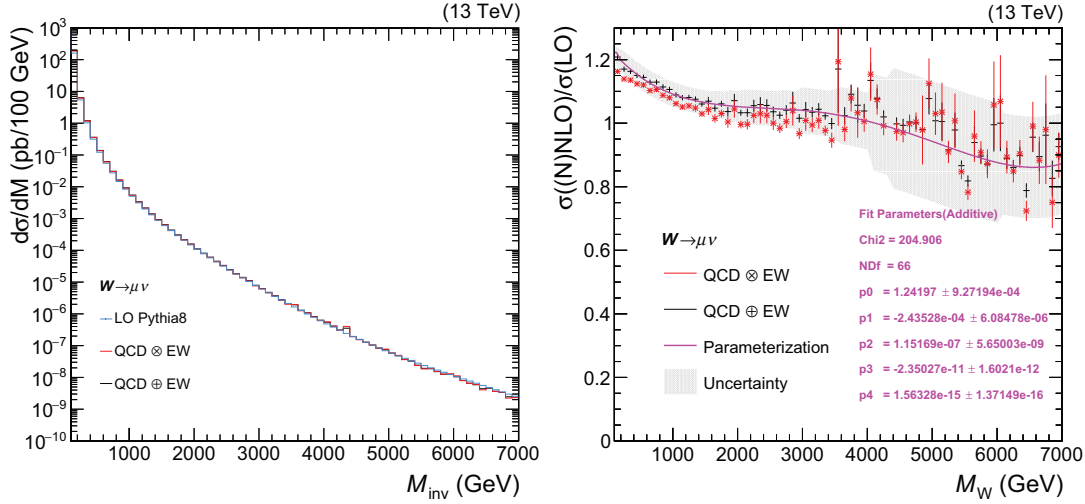
Figure 85: The high order corrected differential cross section (NNLO QCD and NLO EW) for the main background, which is SM off–shell $pp \rightarrow W \rightarrow \mu + \nu$ is presented (left) as a function of the W boson invariant mass. The K–factors (right) are calculated with an additive approach (black). The additive K–factors are parametrized using a 4th–degree polynomial (pink). The gray band is is obtained from the statistical fluctuations of the K–factors, to cover the difference with respect to the fit.

5.2.2 Z boson background

Another process contributing to the background is the Drell–Yan (DY) $Z \rightarrow$ process. This process is a background to our signal when one of the muons is lost or outside the acceptance. To simulate this background, samples were generated with POWHEG [72] generator in the following Z mass regions: 50–120, 120–200, 200–400, 400–800, 800–1400, 1400–2300, 2300–3500, 3500–4500, and 4500–6000 GeV. The $Z \rightarrow$ background will be plotted in red colour in the following plots.

5.2.3 Diboson background

Production of dibosons such as $pp \rightarrow WW$, WZ, ZZ, Wγ, also mimic the signal when one of the bosons decays leptonically, or both but one lepton is lost or outside acceptance, or they decay hadronically but one jet is reconstructed as a muon. Due to the low cross section of the Higgs boson production, its contribution is negligible and is not considered among the simulated background processes.

The POWHEG and PYTHIA generators are used to produce diboson samples with different decay modes. The WW $\to 4$, ν , $\nu\nu$ processes (where stands for lepton, ν of neutrino, and of quark) are simulated with POWHEG. The WZ $\to \nu$, ν, processes are generated with PYTHIA. The ZZ process is generated in an inclusive sample with PYTHIA. And, the Wγ is generated with MAD-GRAPH generator.

The contributions from all diboson processes are grouped together in the main plots that are shown along this chapter, and they are represented in green colour.

5.2.4 Top quark background

Top quarks decay to a bottom quark and a W boson. Therefore, $t\bar{t}$ and single top productions can have a muon and p_T^{miss} in the final state and contribute to the background. Top processes have large number of jets in the final state and the jet from the decay of the bottom quark can be identified with a b–tag discriminator (described in Section 3.5.1). These two features are used to reject as much as possible background coming from top quarks. They will be based in cutting in the number of jets and the b–tag discriminant will reduce the top quark background. The selection procedure will be explained in Section 5.5.

The total contribution from top quark processes is shown in the plots along this chapter in yellow colour.

5.2.5 QCD multijet background

In addition, there is QCD multijet background, where muons can be produced together with p_T^{miss}. The process creating QCD multijets has the largest cross section among all background processes, although it is efficiently reduced with the analysis selection criteria, especially the high p_T threshold coming from the muon trigger and the requirement of muon isolation. The generated muon p_T distribution in the production of QCD multijet peaks at low values of p_T, but, given the high cross section of production, it is necessary to evaluate the tail of the p_T distribution that could affect the analysis.

To obtain the shape of muon p_T distribution, simulated samples enriched in the presence of muons and with a leading jet with $p_T > 15$ GeV, are used. The normalization of this background is obtained from the data as it is explained in Section 5.4.

Table 5.3 summarizes the simulated MC samples of background processes, with the information about the generator used and the cross sections, which in some cases come directly from the generator program, others from theoretical calculations.

Background process		Generator	$\sigma \times \mathcal{B}$ (pb)
W boson	W+jets $\to l\nu$	MADGRAPH (LO)	61527.5 (NNLO)
	W+jets $\to l\nu$, H$_T$: (100–200) GeV	MADGRAPH (LO)	1395 (LO)
	W+jets $\to l\nu$, H$_T$: (200–400) GeV	MADGRAPH (LO)	407.9 (LO)
	W+jets $\to l\nu$, H$_T$: (400–600) GeV	MADGRAPH (LO)	57.48 (LO)
	W+jets $\to l\nu$, H$_T$: (600–800) GeV	MADGRAPH (LO)	12.87 (LO)
	W+jets $\to l\nu$, H$_T$: (800–1200) GeV	MADGRAPH (LO)	5.366 (LO)
	W+jets $\to l\nu$, H$_T$: (1200–2500) GeV	MADGRAPH (LO)	1.074 (LO)
	W+jets $\to l\nu$, H$_T$: (2500–∞) GeV	MADGRAPH (LO)	8.1×10^{-3} (LO)
	W $\to \mu\nu$, W $\to \tau\nu$, M > 200 GeV	PYTHIA (LO)	7.3 (LO)
	W $\to \mu\nu$, W $\to \tau\nu$, M > 500 GeV	PYTHIA (LO)	0.25 (LO)
	W $\to \mu\nu$, W $\to \tau\nu$, M > 1000 GeV	PYTHIA (LO)	0.015 (LO)
	W $\to \mu\nu$, W $\to \tau\nu$, M > 2000 GeV	PYTHIA (LO)	4.4×10^{-4} (LO)
	W $\to \mu\nu$, W $\to \tau\nu$, M > 3000 GeV	PYTHIA (LO)	2.8×10^{-5} (LO)
	W $\to \mu\nu$, W $\to \tau\nu$, M > 4000 GeV	PYTHIA (LO)	2.6×10^{-6} (LO)
	W $\to \mu\nu$, W $\to \tau\nu$, M > 5000 GeV	PYTHIA (LO)	3.8×10^{-7} (LO)
	W $\to \mu\nu$, W $\to \tau\nu$, M > 6000 GeV	PYTHIA (LO)	1.5×10^{-8} (LO)
Top quark	Single top s–channel leptonic	aMC@NLO (NLO)	3.36 (NLO)
	Single top t–channel top	POWHEG (NLO)	136.0 (NLO)
	Single top t–channel antitop	POWHEG (NLO)	80.9 (NLO)
	Single top tW antitop	POWHEG (NLO)	35.8 (NLO)
	Single top tW top	POWHEG (NLO)	35.8 (NLO)
	$t\bar{t}$ dileptonic	POWHEG (NLO)	97.0 (NNLO)
	$t\bar{t}$ semileptonic	POWHEG (NLO)	400.0 (NNLO)
Z boson	Z $\to ll$, M: (50–120) GeV	POWHEG (NLO)	1975 (NLO)
	Z $\to ll$, M: (120–200) GeV	POWHEG (NLO)	19.32 (NLO)
	Z $\to ll$, M: (200–400) GeV	POWHEG (NLO)	2.731 (NLO)
	Z $\to ll$, M: (400–800) GeV	POWHEG (NLO)	0.241 (NLO)
	Z $\to ll$, M: (800–1400) GeV	POWHEG (NLO)	0.01678 (NLO)
	Z $\to ll$, M: (1400–2300) GeV	POWHEG (NLO)	1.39×10^{-3} (NLO)
	Z $\to ll$, M: (2300–3500) GeV	POWHEG (NLO)	8.95×10^{-5} (NLO)
	Z $\to ll$, M: (3500–4500) GeV	POWHEG (NLO)	4.13×10^{-6} (NLO)
	Z $\to ll$, M: (4500–6000) GeV	POWHEG (NLO)	4.56×10^{-7} (NLO)
	Z $\to ll$, M: (6000–∞) GeV	POWHEG (NLO)	2.1×10^{-8} (NLO)
	Z+jets $\to \nu\nu$, H$_T$: (100–200) GeV	POWHEG (NLO)	93.3 (NLO)
	Z+jets $\to \nu\nu$, H$_T$: (200–400) GeV	POWHEG (NLO)	25.8 (NLO)
	Z+jets $\to \nu\nu$, H$_T$: (400–600) GeV	POWHEG (NLO)	3.58 (NLO)
	Z+jets $\to \nu\nu$, H$_T$: (600–800) GeV	POWHEG (NLO)	0.85 (NLO)
W+γ	W$\gamma \to l\nu\gamma$	MADGRAPH MLM (LO)	405.3 (LO)
Diboson	WW $\to l\nu qq$	POWHEG (NLO)	50.0 (NNLO)
	WW $\to 4q$	POWHEG (NLO)	51.7 (NNLO)
	WW $\to ll\nu\nu$	POWHEG (NLO)	12.2 (NNLO)
	WZ $\to l\nu qq$	PYTHIA (LO)	11.6 (NLO)
	WZ $\to lll\nu$	PYTHIA (LO)	5.05 (NLO)
	WZ $\to llqq$	PYTHIA (LO)	6.33 (NLO)
	WZ $\to l\nu\nu\nu$	PYTHIA (LO)	3.05 (NLO)
	ZZ	PYTHIA (LO)	10.3 (NLO)
QCD	QCD μ enriched, p$_T^\mu$: (470–600) GeV	PYTHIA (LO)	56.6 (LO)
	QCD μ enriched, p$_T^\mu$: (600–800) GeV	PYTHIA (LO)	25.1 (LO)
	QCD μ enriched, p$_T^\mu$: (800–1000) GeV	PYTHIA (LO)	4.70 (LO)
	QCD μ enriched, p$_T^\mu$: (1000–∞) GeV	PYTHIA (LO)	1.62 (LO)

Table 5.3: Analyzed simulated samples for several background processes ($= e, \mu, \tau$), generator used and ((N)N)LO $\sigma \times \mathcal{B}$ values.

5.3   Preselection

In this section the preselection of events according to the background processes and the signal is presented. To select single–muon events, they have to fulfill the following criteria.

- **Trigger:** the event must have fired a high p_T muon path, i.e. the presence of an energetic muon in the detector. The trigger applied has a muon p_T threshold of 50 GeV.

- **Identification:** the event has to contain one muon identified as a high–p_T muon ID, as defined in Section 3.3.

- **Isolation:** the muon generated in the W' decay should be isolated (defined in Section 3.3.2). In the case of high momentum muons, and in order to avoid being affected by showers in the return yoke, the isolation is calculated only with the particles detected in the Tracker, the so–called, tracker isolation.

  The tracker isolation of the muon has to be less than 10 % of its p_T. By cutting in this variable, we reject events from background processes where the muon is produced with other particles and jets, such as the QCD multijet background.

- **Acceptance:** due to the coverage of the Muon System, the muon should be reconstructed with $|\eta| < 2.4$. At offline level, the muon must have TuneP $p_T > 53$ GeV to be in the plateau region of the turn on curve of the trigger efficiency (see Figure 69).

  Figure 86 shows the two variables, muon η and p_T, after preselection cuts for data, MC background, and two SSM W' signals. The simulated samples (SM backgrounds and SSM signals) are normalized according to their process cross sections, as presented in previous sections, and the luminosity collected in Run 2 data ($137\,\mathrm{fb}^{-1}$).

- **Second lepton veto:** events containing a second charged lepton (electron or muon), with $p_T > 25$ GeV, and identified as loose ID (defined in Section 3.3), are rejected. This cut reduces significantly the backgrounds with two leptons such as dibosons or $Z \rightarrow$.
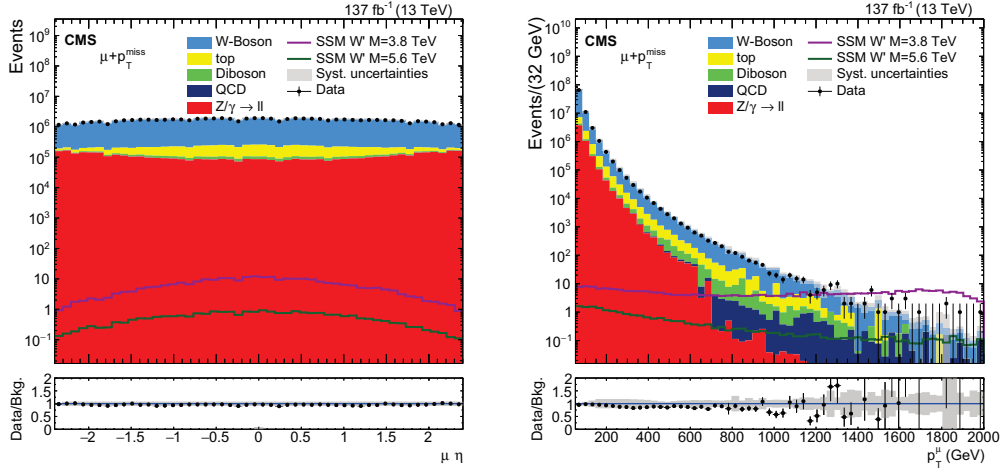
Figure 86: Muon η (left) and muon p_T (right) distributions at preselection level, for data (black dots), MC background (color filled), and two SSM W' signals of mass, $M_{W'}$ = 3.8 TeV (pink) and 5.6 TeV (green).

5.4   MC simulation modeling

As mentioned, all distributions of the simulated samples are normalized to the integrated luminosity of the recorded data using their ((N)N)LO cross sections. Every MC sample is simulated for the three years of data taking to account for possible changes in the detector, and more adequate PDF or UE descriptions. On top of the normalization to the luminosity, the following corrections are applied to the MC samples.

Pileup reweight

The simulation of proton–proton collision data has been done assuming a number of interactions (see pileup Section 2.2.4) at the time of the samples generation. This is prior to the data taking period itself, and this variable depends on the instantaneous luminosity delivered by the LHC, so it may not reflect exactly the eventual PU profile actually happening. Therefore, all MC simulations are corrected in order to match the PU distribution with the one measured in data assuming the inelastic proton–proton cross section of 69.2 mb [142], at a centre–of–mass energy of 13 TeV, shown in Figure 10.

To perform this correction a weight is derived as a function of the number of vertices, and as shown in the lower panel of Figure 87. This figure presents the distribution of the number of vertices in data and in simulated samples, corresponding to 2017, as an example. The same procedure is done for each year of data. The data corresponds to a minimum–bias dataset and not the selected events of the analysis. As observed, the simulated samples reproduce correctly the middle region in number of vertices (10 – 40 vertices), and thus, the weights (Data/Simulation) are close to 1. On the other hand, the simulation was overestimated at high number of vertices

(> 50 vertices), meaning eventually the data did not have as much pileup as initially foreseen, and thus the weights are $\ll 1$.
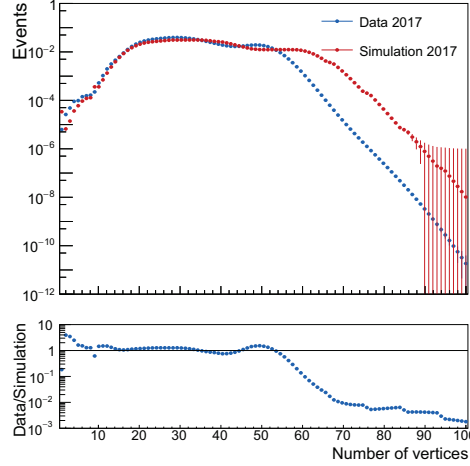
Figure 87: Number of vertices in data (blue) and simulation (red) for 2017 (upper panel). The ratio plot (lower panel) corresponds to the PU weights.

The PU weights from the ratio plot of Figure 87, and the corresponding ones for 2016 and 2018 datasets, are applied to the preselected events, selected by having one quality muon. Figure 88 shows the distribution of number of vertices before applying PU weight (left row) and after applying PU weight (right row) for such selection.

Muon scale factors

The number of events produced in a process, N, is calculated as the product of its cross section, σ, the branching fraction of the decay channel observed, $\mathcal{B}$, the luminosity, $\mathcal{L}$, the efficiency, ϵ, and the acceptance, A:

$$N = \sigma \times \mathcal{B} \times \mathcal{L} \times \epsilon \times A \tag{5.9}$$

All these magnitudes are the same for data and MC simulation, except of the efficiency and acceptance that can be simulated with a different value than the real one. Therefore, the simulated events are corrected by the so–called *Scale Factor* (SF), defined as the ratio of efficiency in data and MC simulation:

$$\text{SF} = \frac{N_{\text{Data}}}{N_{\text{MC}}} = \frac{\epsilon_{\text{Data}}}{\epsilon_{\text{MC}}} \tag{5.10}$$

The total muon efficiency is parametrized in five sources: tracking, identification, isolation, reconstruction, and trigger. Each source introduces a SF that may depend on η and ϕ coordinates, or the p_T range of applicability. The values of the efficiencies in data, MC simulation, and the SFs were presented in Section 4.5.
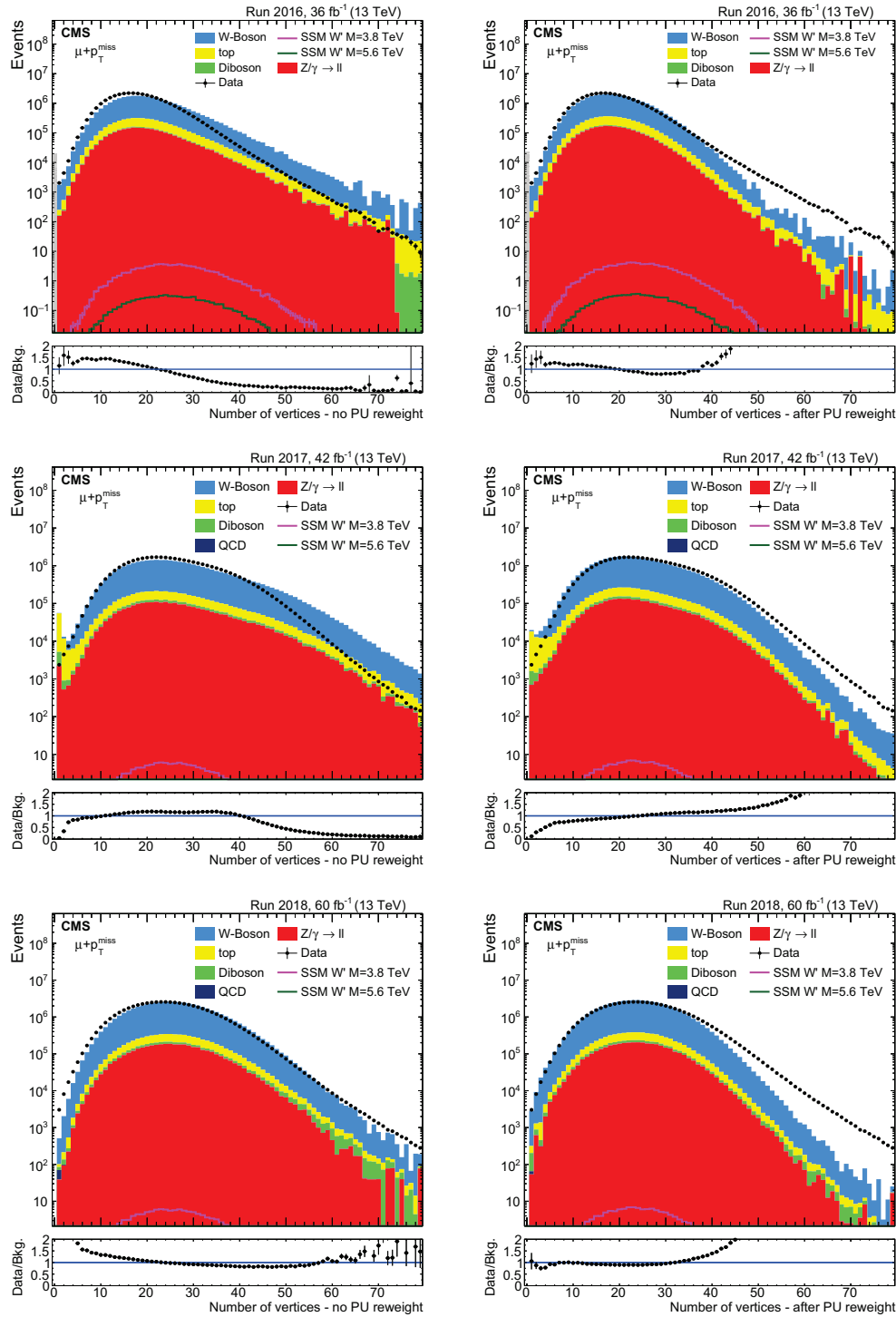
Figure 88: Number of vertices before applying PU weight (left row) and after applying PU weight (right row) for 2016 (top), 2017 (middle), and 2018 (bottom) data and MC samples.

Jet b–tag scale factors

A veto on events containing a b–tagged jet is applied in order to reduce the top quark background (details in Section 5.5.2). Since the simulation of the b–tag discriminant (Section 3.5.1) does not follow exactly the distribution in data, a SF is applied to the MC simulation.

The DeepCSV discriminant is tuned each year, therefore, the SFs are calculated separately for each year. The SFs depend on the jet p_T, and range from 0.92 to 1.10 in 2016, from 0.92 to 1.05 in 2017, and from 0.86 to 0.98 in 2018 [126].

Top–antitop quarks background normalization

In order to check the top–antitop quarks ($t\bar{t}$) background modelling and its normalization, a selected sample called *control region* (CR) is created, enriched in top quark content. Two CRs are designed to select semileptonic and dileptonic $t\bar{t}$ decay modes, represented in Figure 89. These control regions are independent of the sample selected for the analysis.
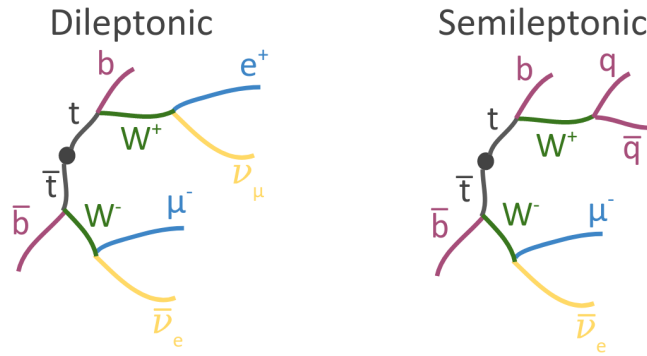
Figure 89: Sketch of $t\bar{t}$ dileptonic (left) and semileptonic (right) decays.

In the dileptonic $t\bar{t}$ decay, both W bosons from the top quarks decay leptonically, thus yielding final states with 2 leptons of opposite sign, 2 b quark jets, and p_T^{miss}. The CR is defined by selecting events containing one muon with $p_T > 53$ GeV, one electron with $p_T > 30$ GeV and, at least, one jet with a DeepCSV discriminant compatible with a b quark jet.

In the semileptonic $t\bar{t}$ decay, one of the W bosons from the top quark decays hadronically, while the other W decays leptonically. The final state contains, at generator LO, 4 jets, 1 lepton, and p_T^{miss}. The CR is defined by selecting events with one muon with $p_T > 53$ GeV, accompanied by more than 3 jets where at least one of them has a DeepCSV discriminant compatible with a b quark jet.

In Figure 90, the distributions of the b–tag discriminant DeepCSV, for 2017 data and MC simulation are shown before applying the b–tag cut for the semileptonic (left), and dileptonic (right) $t\bar{t}$ control regions.

In Figure 91 the distributions of the number of jets for data and MC are shown before cutting in this variable, for the CR selection for the dileptonic (left), and
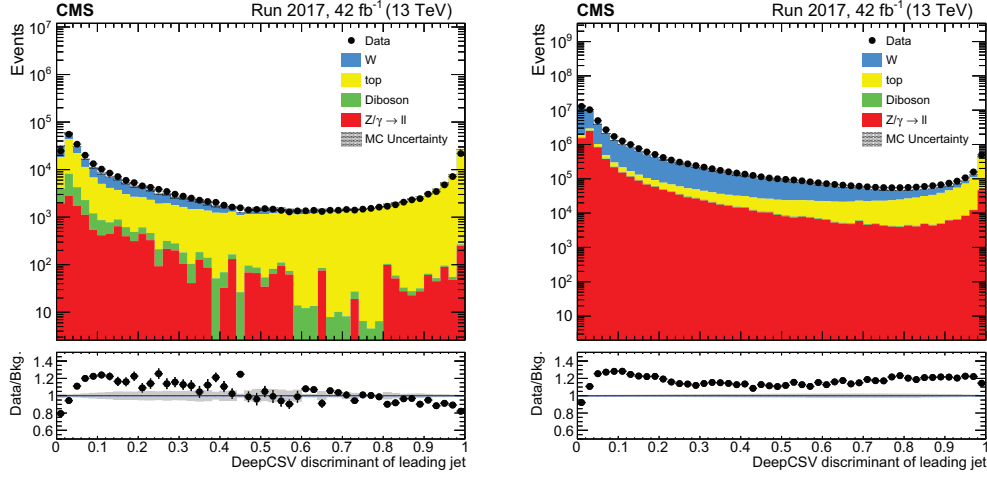
Figure 90: Distribution of DeepCSV b–tag discriminant for the dileptonic (left) and semileptonic (right) t$\bar{\text{t}}$ control region before applying the b–tagging cut, for 2017 data and MC prediction.

semileptonic (right) regions.
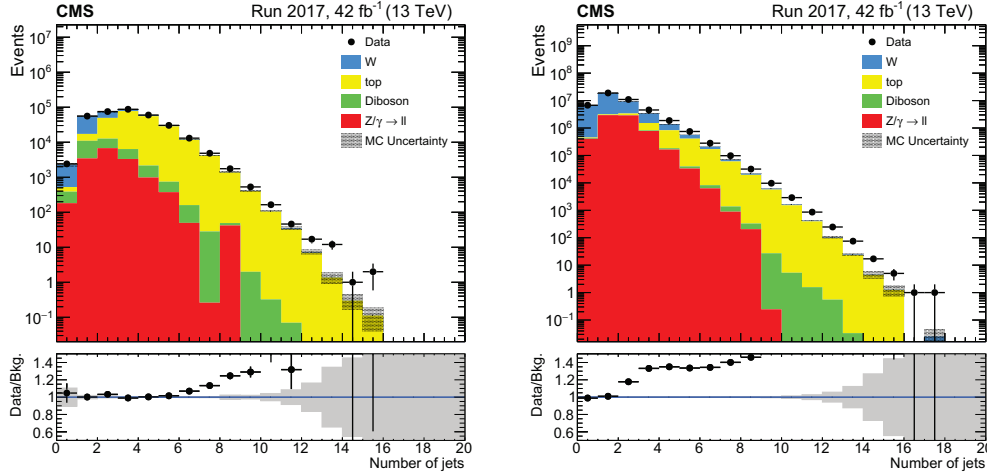
Figure 91: Distribution of number of jets for the dileptonic (left) and semileptonic (right) t$\bar{\text{t}}$ control regions, after applying the b–tag discriminant cut, for 2017 data and MC prediction.

Once selecting the CR, the purity of the t$\bar{\text{t}}$ background in the selected sample is > 90 %, as shown in Table 5.4 for each year of data and MC simulation.

From the ratio of data over MC background in the muon ϕ distribution in Figure 92, which is rather flat, a normalization factor is derived. The dominant source of uncertainty on this factor is the cross section uncertainty of the top simulations that is considered to be 5 %. These factors are 1.076 ± 0.054 and 0.908 ± 0.045 in the semileptonic and dileptonic CR, respectively, in 2017; and 0.815 ± 0.041 and 0.865 ± 0.043 in 2018. In 2016 the t$\bar{\text{t}}$ simulation was made in an inclusive sample,

112

and the corresponding factor is 0.725 ± 0.036. These values are used as a normalization factor to weight each distribution of $t\bar{t}$ simulated samples, and they are summarized in Table 5.4.
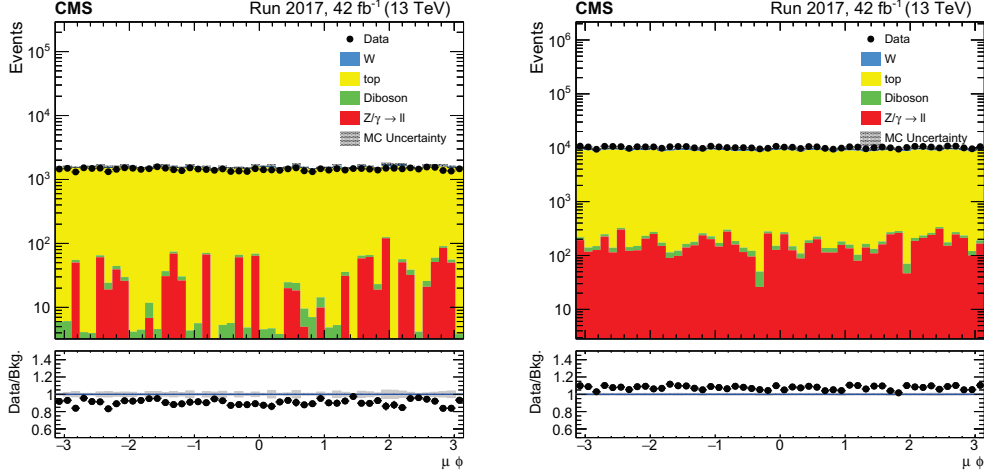
Figure 92: Muon ϕ distribution for the dileptonic (left) and semileptonic (right) $t\bar{t}$ control regions, for 2017 data and SM prediction.

Year	$t\bar{t}$ CR	Purity	Data/MC
2016	Inclusive $t\bar{t}$	90.7 %	0.725 ± 0.036
2017	Dileptonic	94.3 %	0.908 ± 0.045
	Semileptonic	92.1 %	1.076 ± 0.054
2018	Dileptonic	94.3 %	0.865 ± 0.043
	Semileptonic	91.7 %	0.815 ± 0.041

Table 5.4: Purity and normalization factor of data over MC simulation ratio for each $t\bar{t}$ CR, and each year of data and MC simulation. Cross section uncertainty of the $t\bar{t}$ samples are the dominant uncertainty, with a value of 5 %.

QCD multijet background normalization

As presented in Section 5.2 the shape of the p_T distribution for muons coming from QCD multijet production is taken from the QCD simulated samples enriched in the presence of energetic muons. The normalization of this background is obtained from data using the ABCD method. The ABCD method requires that there are two independent variables that form part of the definition of the signal region, region A, which are inverted in order to define three further regions, region B, C, and D, that fail one (or both) of the signal definitions. These control regions should be rich in the events produced from background processes that we are trying to estimate with the method, in this case events containing muons from QCD multijet background.

The independent variables chosen to define the four regions are the relative muon isolation and the M_T. Region A is defined with relative muon isolation less than 0.1 and $M_T > 120$ GeV. The other regions are obtained inverting one or both of these selection cuts: relative muon isolation in the range $[0.1 - 0.5]$ and/or M_T in $[80 - 120]$ GeV. Regions definition are represented in Figure 93.
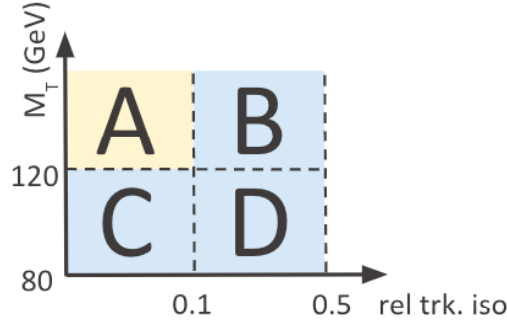
Figure 93: ABCD method applied in the variables M_T and relative muon isolation.

The ABCD method assumes that the following statement is true:

$$\frac{N^{bkg}}{N_D^{bkg}} = \frac{N_A^{bkg}}{N_B^{bkg}} \tag{5.11}$$

where N_i^{bkg} is the number of background events in region i. The goal of the ABCD method is to produce a prediction for the number of non–signal events in the signal region (N_A^{bkg}). Assuming that regions B, C, and D have a negligible number of signal events, from Eq. 5.11 is deduced:

$$N_A^{bkg} = N_B^{bkg} \times \frac{N^{bkg}}{N_D^{bkg}} = N_B \times \frac{N}{N_D} \tag{5.12}$$

The QCD background contribution obtained at high M_T values is found to be very small: $\sim 3\,\%$ of the total SM background. A conservative $50\,\%$ uncertainty in the normalization factor obtained is assumed.

5.5 Selection

The first step in the selection process, called *preselection*, presented in Section 5.3, aims to keep signal events candidates containing only one, and well identified, high momentum muon. Afterwards, the events pass through *kinematic cuts* designed to select the products of a heavy resonance, and finally, the *top veto* is applied to further reduce the top quark background contribution.

5.5.1   Kinematic selection

There are two further cuts designed to exploit the two–body decay kinematics of a massive resonance, referred in this text as *kinematic cuts*. A massive resonance (see scheme in Figure 72) is expected to be produced almost at rest, without boost. In this configuration its decay products must be balanced in p_T and follow opposite directions. In this case the decay products are the muon and the p_T^{miss}, and the variables of interest p_T^μ/p_T^{miss} and $\Delta\phi(\vec{p}_T^\mu, \vec{p}_T^{miss})$ must fulfill:

- Balance in p_T: $0.4 < p_T^\mu / p_T^{miss} < 1.5$.
- Back–to–back topology: $\Delta\phi(\vec{p}_T^\mu, \vec{p}_T^{miss}) > 2.5$.

The values chosen for the interval are wide enough to not be very restrictive in signal efficiency, but still reject a significant part of the background. Figure 94 shows the distributions of the two kinematic variables after the preselection and before applying the cuts on them. In these distributions, the SSM W' signals with masses $M_{W'} = 3.8$ and 5.6 TeV (violet and green lines), are maximal in the regions selected by the kinematic cuts.
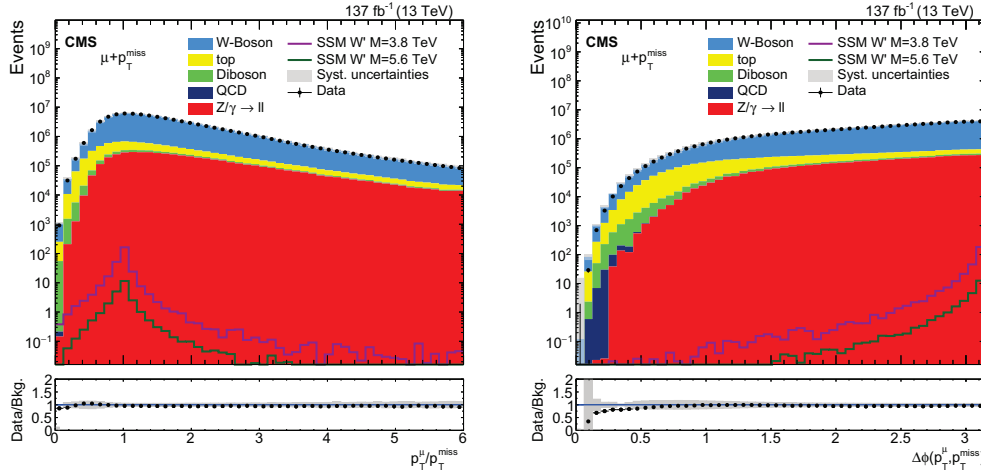
Figure 94: Distribution of p_T^μ / p_T^{miss} (left) and $\Delta\phi(\vec{p}_T^\mu, \vec{p}_T^{miss})$ (right), for preselected events (presence of one and only one, high quality and highly energetic isolated muon).

The data and SM prediction show good agreement in the distributions of the kinematic variables, as shown in the ratio plots of the lower panels. A deviation is found in the $\Delta\phi(\vec{p}_T^\mu, \vec{p}_T^{miss})$ distribution for values close to 0. This region corresponds to events where the muon p_T and the p_T^{miss} are in the same direction. These events usually correspond to QCD multijet production, a process not well modeled as it was mentioned. These events are not in the signal region and they are, in any case, rejected once the two cuts mentioned above are applied.

5.5.2 Top veto

There is a further step in the selection process aimed to reduced the top quark background. When looking at the distribution of the number of jets in the selected events, Figure 95 - left, one sees that the signal–like events are produced with a low number of jets. On the contrary, the events with a large number of jets, jet multiplicity 5, are essentially dominated by top quark background processes, plotted in yellow.

The distribution of the b–tagging discriminant, DeepCSV (Section 3.5.1), for the most energetic (leading) jet in each event, is shown in Figure 95 - right. The top quark background concentrated around DeepCSV discriminant ~ 1, while signal is concentrated at around ~ 0.
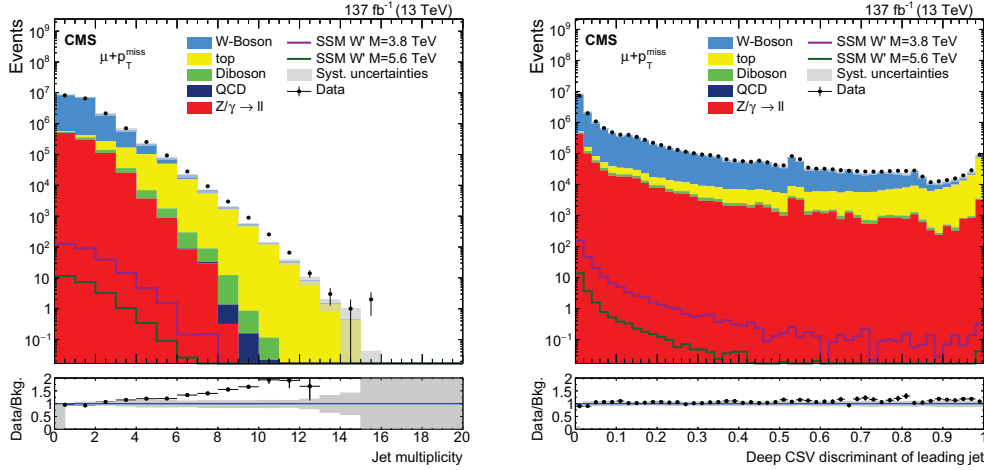
Figure 95: Jet multiplicity (left) and DeepCSV discriminant (right) distributions, for events that pass the preselection, for data (black points), SM predictions (coloured filled histograms), and two SSM W' signals of mass, $M_{W'} = 3.8$ TeV (pink) and 5.6 TeV (green).

To reduce the contamination coming from top quark processes, a top veto is applied in these two variables:

- Number of jets: events are rejected if they contain six or more jets.
- b–tag discriminant: events are rejected if the leading jet is tagged as coming from a b quark according to the DeepCSV discriminant. The cut is placed at the discriminant value corresponding to a misidentification probability less than 0.1 % for light flavoured jets (u, d, s). This value is calculated separately for each year, and implies the discriminant to be less than 0.848 for 2016 conditions, 0.800 for 2017, and 0.753 for 2018 [126].

These two requirements hardly affect the signal efficiency. A massive resonance is expected to be produced almost at rest, with no (or a reduced number of) accompanying jets. The distribution of number of jets of the W' signals peak at 0 jets in

the event, as seen in Figure 95 - left. Regarding jets coming from b quarks, signals are not expected to decay in such quark types and the accompanying jets (if any) do not have a special tendency to be b–jets.

Table 5.5 summarizes the selection cuts applied.

Selection cuts	
Preselection	Trigger (p_T^μ threshold > 50 GeV)
	Muon identified as high–p_T
	Muon $p_T > 53$ GeV
	Muon $|\eta| < 2.4$
	Muon tracker isolation $< 10\,\%\,p_T^\mu$
	Second lepton veto
Kinematic selection	$0.4 < p_T^\mu / p_T^{miss} < 1.5$
	$\Delta\phi(\vec{p}_T^\mu, \vec{p}_T^{miss}) > 2.5$
Top veto	Number of jets < 6
	b–tag discriminant $\lesssim 0.8$

Table 5.5: Selection cuts summary.

The number of events in data, SM background, and one SSM W' signal ($M_{W'} = 5.6$ TeV) for 2017 datasets, are presented in Table 5.6 following the cut flow defined in Table 5.5. The surviving efficiency of each cut and the cumulative efficiency is also presented, with respect to the initial number of events in reduced samples with events containing a muon with $p_T > 50$ GeV. The cuts are sorted in the order that they were applied during the analysis and not necessarily in the order they were presented in the text. The table includes the requirement $M_T > 80$ GeV, applied to remove the lower transverse mass region during the analysis.

	Trigger	2nd lep. veto	High–p$_T$ ID	μ η	μ isolation
Data	107775100	97479018	87783978	87342415	47095931
Cut eff (%)	88.0	90.4	90.0	99.9	53.9
Cumulative (%)	88.0	79.6	71.7	71.3	38.4
Background	59601800	50613100	49662700	49549800	48995800
Cut eff (%)	65.4	84.9	98.1	99.9	98.9
Cumulative (%)	65.4	55.5	54.5	54.3	53.7
SSM M$_{W'}$ = 5.6 TeV	14552	14465	14269	14262	14251
Cut eff (%)	92.0	99.4	98.6	100	99.9
Cumulative (%)	92.0	91.4	90.2	90.2	90.1

	d_{xy}, d_z	p$_T^{\mu}$	M$_T$ > 80 GeV	Kinematic	Top quark veto
Data	46154205	38129313	24864257	5975324	5863765
Cut eff (%)	98.0	82.6	65.2	24.0	98.1
Cumulative (%)	37.7	31.1	20.3	4.9	4.8
Background	48984900	40220100	25920400	6260130	6158090
Cut eff (%)	99.9	82.1	64.4	24.1	98.4
Cumulative (%)	53.7	44.1	28.4	6.9	6.7
SSM M$_{W'}$ = 5.6 TeV	14251	14167	14102	12828	12746
Cut eff (%)	100	99.4	99.5	91.0	99.4
Cumulative (%)	90.1	89.5	89.1	81.1	80.5

Table 5.6: Yields for 2017 data, SM background estimation, and SSM W' signal (M$_{W'}$ = 5.6 TeV), after each selection cut. The surviving efficiency and the cumulative one for the cut workflow is also presented for each type of dataset.

5.6 Systematic uncertainties

The different effects that affect the M$_T$ distribution are called systematic uncertainties. This section presents the systematic uncertainties sources taken into account in this analysis, how they are estimated, and their impact in the final M$_T$ shape and normalization.

K–factor

The uncertainty introduced by K–factors applied to cover missing orders at generation level to the off–shell W distribution (see Section 5.2.1), is based on the statistical fluctuations of the K–factor per mass–bin compared to a smooth fit over all masses.

For low masses these fluctuations are very small and the difference between additive and factorized approach, amounting to 5 % of the K–factor, is taken as uncertainty. At higher masses, these fluctuations increase and go to up $\sim$ 40 % (see Figure 85). These values are taken as uncertainty on the W boson samples K–factors.

PDFs

All MC simulated samples suffer from the uncertainties associated to the PDFs used

for their generation. The uncertainties on the PDFs and on the strong coupling constant, α_S are calculated with a recipe recommended by PDF4LHC group [141], accounting for the NNPDF3.1 set of replicas.

Figure 96 shows the PDF uncertainties for the W' signal, 2016 (left), and 2017 and 2018 (right) simulations, as a function of the W' mass.
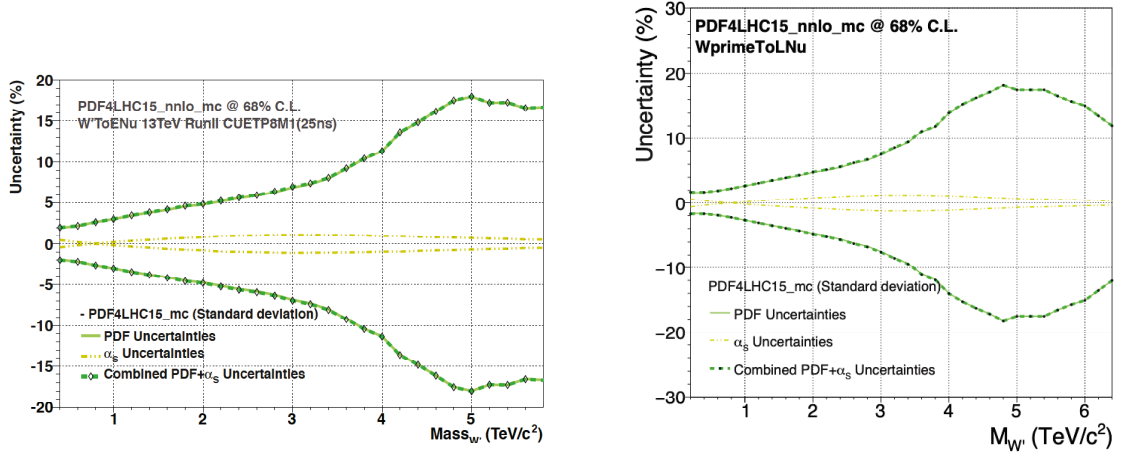
Figure 96: The combined PDF$+\alpha_S$ uncertainties for PDF4LHC15 MC set, as a function of the W' mass, $M_{W'}$, for 2016 (left), 2017 and 2018 (right) simulations.

Since the PDFs involved in the creation of a W' boson and a massive SM W boson are the same, the same systematic uncertainties are taken into account for the SM W background.

The effect of the PDF uncertainties depends strongly on the Q^2 of the hard interaction. Therefore they are moderate at low W mass, they increase up to $\sim 18\%$ for $M_{W'} = 4.8$ TeV, and they are slightly reduced for higher W mass because of the increase of off–shell production.

Cross Sections

The uncertainties on the cross sections used for normalization of the simulated samples are calculated theoretically, experimentally, or from the generators [143, 144, 145, 146, 147, 148, 149, 150], and each of them has its associated uncertainty. These uncertainties are a normalizing factor for each sample, but all together in the final background M_T distribution impact as a shape uncertainty. Each of the cross section uncertainties vary from 3% to 6%.

Pileup

The description in simulation of the number of interactions per bunch–crossing is corrected according to the data as explained in Section 5.4. Figure 88 shows the distribution of PU for data and SM prediction for each year of data taking.

The uncertainty associated to this correction is estimated by varying $\pm 4.6\%$ the nominal value of the minimum bias cross section used to derive the PU weights

(69.2 mb [142]), and redoing the PU reweighting process. Figure 97 shows the distribution for the number of vertices for data and MC, with the nominal minimum bias cross section and $\pm\,4.6\,\%$ of this value for 2017 data taking period. The ratio plot shows the nominal PU weight and the associated $\pm\,1\,\sigma$ (dark and light blue) weights for the systematic study.
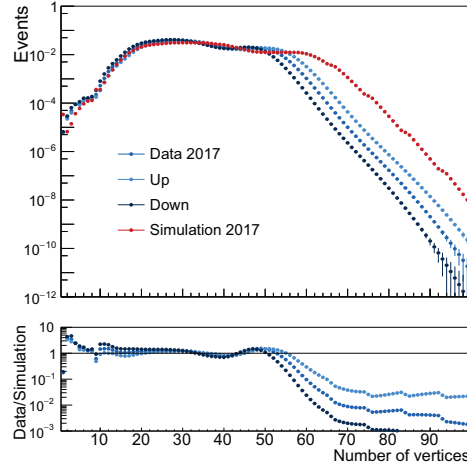
Figure 97: Number of vertices for data (blue) and MC simulation (red), with the nominal minimum bias cross section and $\pm\,5\,\%$ this value, for 2017 data taking period.

Scale Factors

Several scale factors have been used regarding muons and jets. Concerning muons, the tracking and reconstruction ones have a value of 1 with a negligible uncertainty (Section 4.5). The uncertainties on the SF determination for muon identification, isolation and trigger are presented here, as also that for the jet b–tagging veto applied.

The statistical uncertainties of the data and the MC simulation are propagated to the calculation of the muon high–p_T identification SFs (Section 3.3.1). The uncertainties are $0.4\,\%$ for muon $|\eta| < 2.0$ and $2.1\,\%$ for muon $|\eta| > 2.0$, for the three years of data [134].

For the muon isolation, the data and the MC simulation efficiencies are very similar, as shown in Figure 68, and they do not depend on p_T. These small differences of $\pm\,0.08\,\%$ have been considered as uncertainties.

For the trigger scale factors, the differences among the values derived in our analysis, using the orthogonal dataset method on two independent datasets, driven by the presence of an energetic electron or significant p_T imbalance in the event (Section 4.5), and the ones by the Tag & Probe method are used as systematic uncertainties. These three sets of results (SingleElectron dataset, MET dataset and Tag & Probe method) are consistent within $2\,\%$ of the SF values, in all the muon η bins considered, for muon $p_T < 200\,\text{GeV}$ (see Figures 69, 70 and 71). For higher

muon p_T values this difference of SF is within 4% for the whole muon η range, except for the region $2.1 < |\eta| < 2.4$, where differences increase up to 8%. The slight dependence of the scale factor with the muon p_T is included in these values.

Uncertainties introduced by the b–tag SF are calculated centrally at CMS by the b–tagging and vertexing group. The uncertainty depends on the jet p_T and the highest value is $\sim 0.3\%$.

Figure 98 shows the effect of $\pm 1\sigma$ shift of each SF systematic uncertainty on the M_T distribution of the SSM W' $M_{W'} = 4.6$ TeV signal sample. In the lower panel the ratio of the shifted and the nominal distribution shows that the total contribution of SFs uncertainties amounts to $\sim 5\%$ for $p_T > 1$ TeV. In the final figures, all SF contributions will be merged in one single distribution.
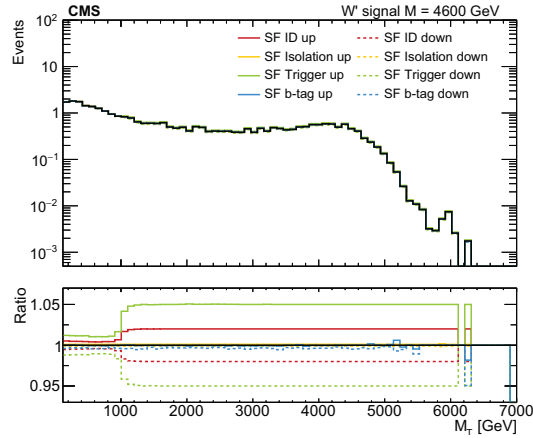
Figure 98: SSM W' ($M_{W'} = 4.6$ TeV) signal M_T distribution with the effect of all SF systematic uncertainties shifted by $\pm 1\sigma$.

Muon momentum scale

The muon p_T scale uncertainty affects the shape of the M_T. The muon p_T scale was calculated with the Generalized Endpoint method presented in Section 4.2 and the result is shown in Figure 50 for each year and each region of η and ϕ .

The procedure to estimate the uncertainty associated to the p_T scale is the following. Firstly, the value for the scale at each η and ϕ region is randomly generated following a gaussian function centered in the bias value calculated with the GE method (Figure 51) and a width corresponding to the uncertainty: gaus(κ_b,σ). This process is repeated fifty times, assuming that fifty is a sufficient large number of trials. In this way fifty maps similar to those in Figure 51 are generated. These maps are calculated for each year of data taking.

Secondly, the calculated biases are applied to muons in a p_T range of (200–3000) GeV, creating a p_T shift following the bias definition from Eq. 4.5. They are applied separately by muon charge, since the scale may affect differently to positive and negative muons (see representation in Figure 45).

Figure 99 - left shows the muon p_T shifts as a function of the muon p_T for each of these maps, for one case as example: positive muons detected in the endcap region and corresponding to 2017 data taking.
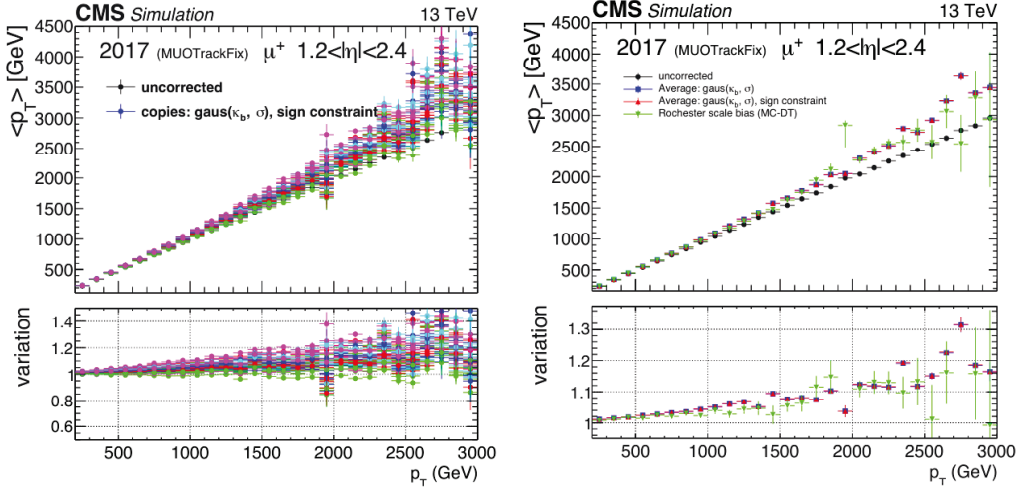
Figure 99: Muon p_T shift as a function of the muon p_T, for 2017 data and MC prediction, for positive muons in the endcap regions, obtained from randomly generated values following a gaussian function $gaus(\kappa_b, \sigma)$ (left). Average of the variation for each bin of muon p_T is shown (right). In addition, results from Rochester method are plotted in green for comparison.

Finally, the average of the fifty variations in each bin of muon p_T, in each year of data taking, each η and ϕ region, and each muon charge is calculated. Such average values are shown for the same example region in Figure 99 - right. These variations are considered as the systematic uncertainties.

Such variations imply a maximum p_T shift of 8, 6, and 2 % at 2 TeV for 2016, 2017, 2018 data respectively, in the barrel, and 10, 10, and 5 % in the endcaps. The uncertainty associated to the muon p_T scale is propagated to the p_T^{miss} and M_T distributions.

Muon momentum resolution

The muon momentum resolution calculated using simulated samples and cosmic muons were presented in Section 4.3.

The uncertainty associated to muon p_T resolution is evaluated as the difference between the resolution derived from real cosmic muons and that obtained in simulated samples. It is found to be negligible in the barrel region, and 1 % for muons in the endcaps, for muons having $p_T > 100$ GeV. These uncertainties are propagated to the p_T^{miss} and M_T distributions.

Missing transverse momentum

Uncertainties affecting the muon p_T, such as the momentum resolution and scale, are propagated to the p_T^{miss}. This is the dominant source of systematic uncertainty

affecting the p_T^{miss}.

In addition, the uncertainty on the jet energy scale directly affects the p_T^{miss} measurement, and this effect is estimated by shifting the jet energy by $\pm 1\sigma$ in the simulation up and down. The uncertainty ranges $2-5\%$, which depends on the jet p_T and η [151].

The overall uncertainty in the determination of p_T^{miss} in each event is derived from the individual uncertainties assigned to the objects (jets, e, μ, τ, γ) obtained from the PF algorithm. The contribution of each object type is varied according to its uncertainty, including a 10% uncertainty in p_T for the unclustered energy[1].

Top quark background normalization

The top quark background normalization method (Section 5.4) introduces a normalization uncertainty of 5%. This contribution to the total systematic uncertainty is, however, negligible since it only affects the reduced top quark background.

Luminosity

Finally, all MC simulated samples are normalized to the recorded luminosity in Run 2 ($137\,\text{fb}^{-1}$) as explained in Section 2.1.1. The uncertainty on this value is evaluated with a Van der Meer scan [63]. It is 1.2% [152], 2.3% [153], and 2.5% [154], for the datasets of 2016, 2017, and 2018, respectively.

Total systematic uncertainty

Each source of uncertainty is shifted by $\pm 1\sigma$ of its nominal value, and the resulting M_T distribution is recalculated. The difference with respect to the nominal distribution is used to estimate the uncertainty in the expected number of events.

Some of these uncertainties only apply to the expected SM background, or the signal, though most of them apply to both, signal and SM background.

The M_T distribution with the effect of each systematic source shifted by $\pm 1\sigma$ is shown in Figure 100 - left, for the SSM W' signal sample with $M_{W'} = 5.6$ TeV, and the total effect of all the contributions in Figure 100 - right.

The SM expected background M_T distribution with the effect of each systematic uncertainties shifted by $\pm 1\sigma$ is shown in Figure 101 - left. The total effect of all the systematic uncertainty sources presented in Figure 101 - right, combined with the simulation statistical uncertainty, will be shown in every background distribution as a gray band.

The systematic uncertainty source with the highest impact in the high mass region ($M_T > 2$ TeV) of the final M_T distribution, is the one associated with the muon p_T scale, followed by the PDFs and K–factors. The effect of the systematic uncertainty has been calculated for each year of data taking.

---

[1]Jets with $p_T < 10$ GeV and PF candidates not within jets are considered as the unclustered energy.
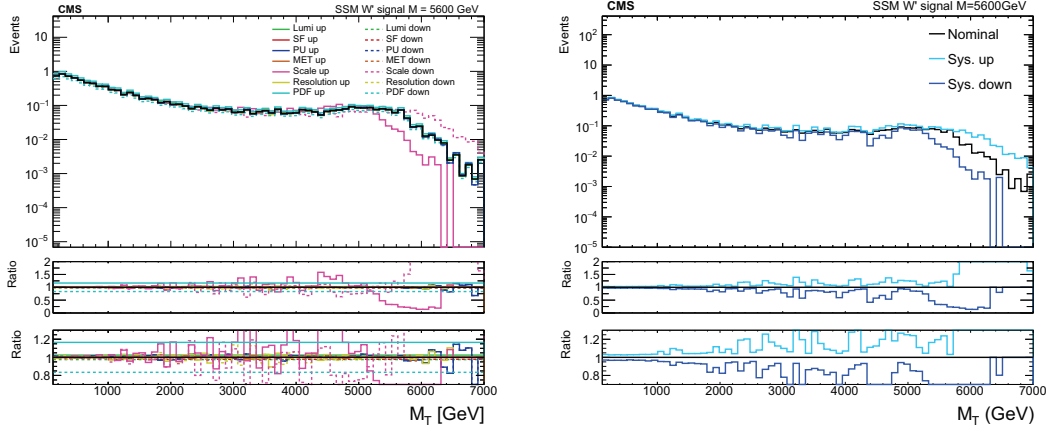
Figure 100: M_T distribution for a signal SSM W' with $M_{W'} = 5.6$ TeV, with the effect of each systematic sources shifted by $\pm 1\sigma$ (left), and the total effect of all the contributions (right). The two ratio plots only differ in the y-axis range.
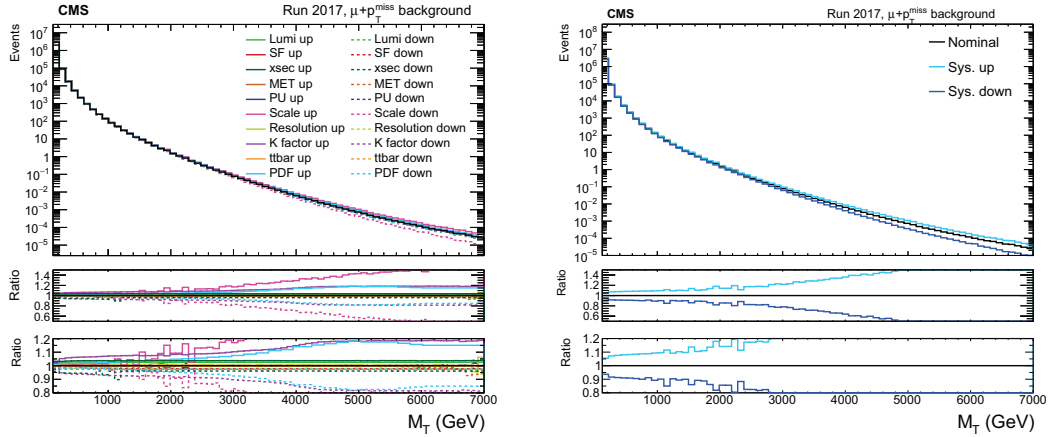
Figure 101: Background M_T distribution with the effect of each systematic sources shifted by $\pm 1\sigma$ (left), and the total effect of all the contributions (right). The two ratio plots only differ in the y-axis range.

5.7 Distributions after selection

The distribution of the main variables in the analysis after applying the complete selection process (Table 5.5) is shown in Figures 102, 103, and 104, for data and SM prediction for each year of data taking, 2016, 2017 and 2018 respectively. The final distributions for the three years together is shown in Figure 105. The gathered luminosity amounts to a total of $137\,\text{fb}^{-1}$. In each of these figures the kinematic variables, $p_T^\mu / p_T^{\text{miss}}$ and $\Delta\phi(\vec{p}_T^\mu, \vec{p}_T^{\text{miss}})$ are given in the top row; the muon variables η and p_T^μ in the middle one; and the event variables p_T^{miss} and M_T in the bottom row. The M_T distributions are shown above 120 GeV to avoid the resolution effect from the p_T threshold of 53 GeV. Each plot shows the data, the SM prediction, and the yields of two W' signals with mass $M_{W'} = 3.8$ TeV and 5.6 TeV. In all distributions there is a good agreement between data and MC background.
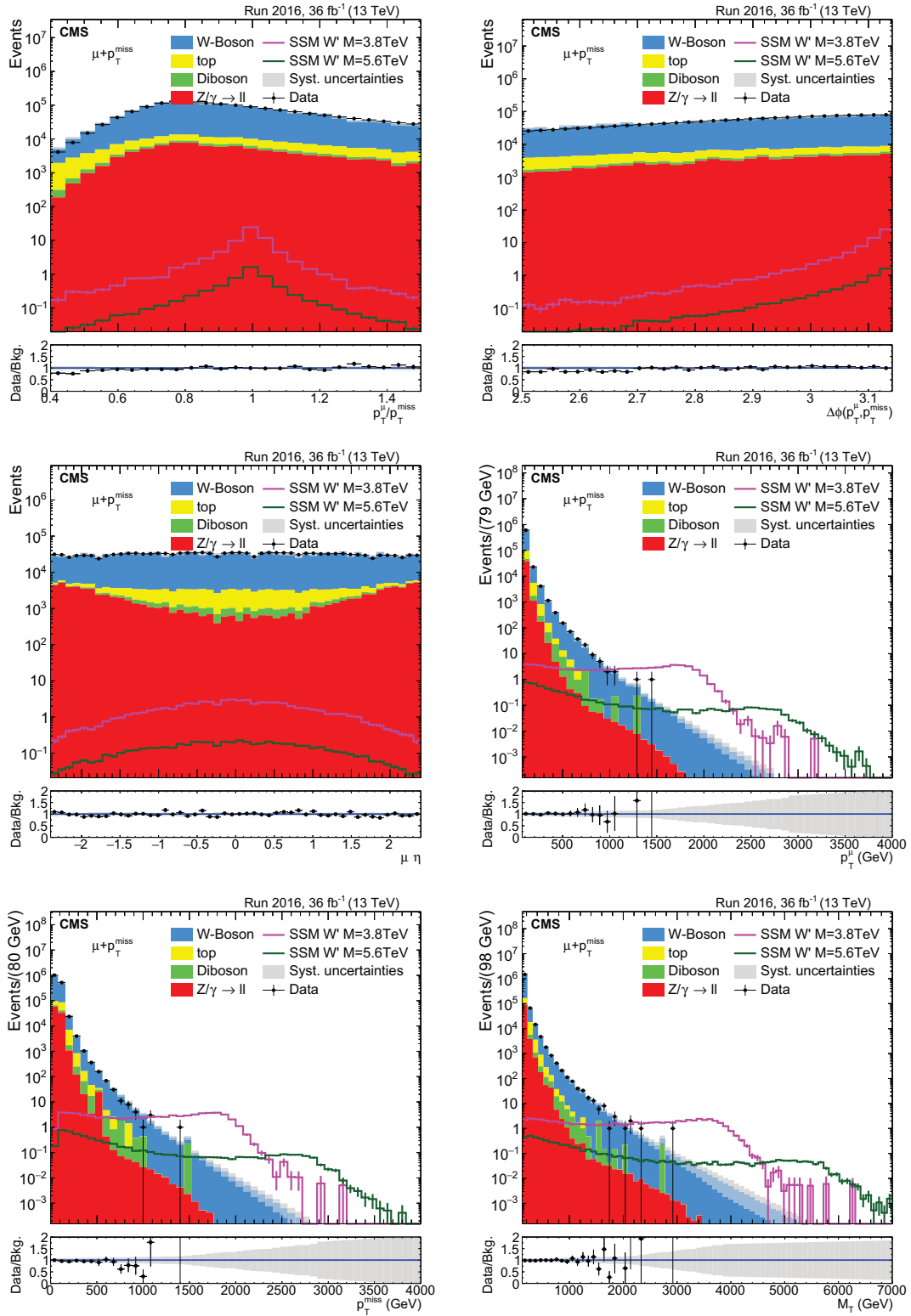
Figure 102: Distributions for p_T^μ/p_T^{miss} (top left), $\Delta\phi(\vec{p}_T^\mu, \vec{p}_T^{miss})$ (top right), muon η (middle left), muon p_T (middle right), p_T^{miss} (bottom left), and M_T (bottom right). Distributions after all selection for 2016 data ($36\,\text{fb}^{-1}$), SM prediction, and two W' signals with mass, $M_{W'} = 3.8$ TeV and 5.6 TeV.
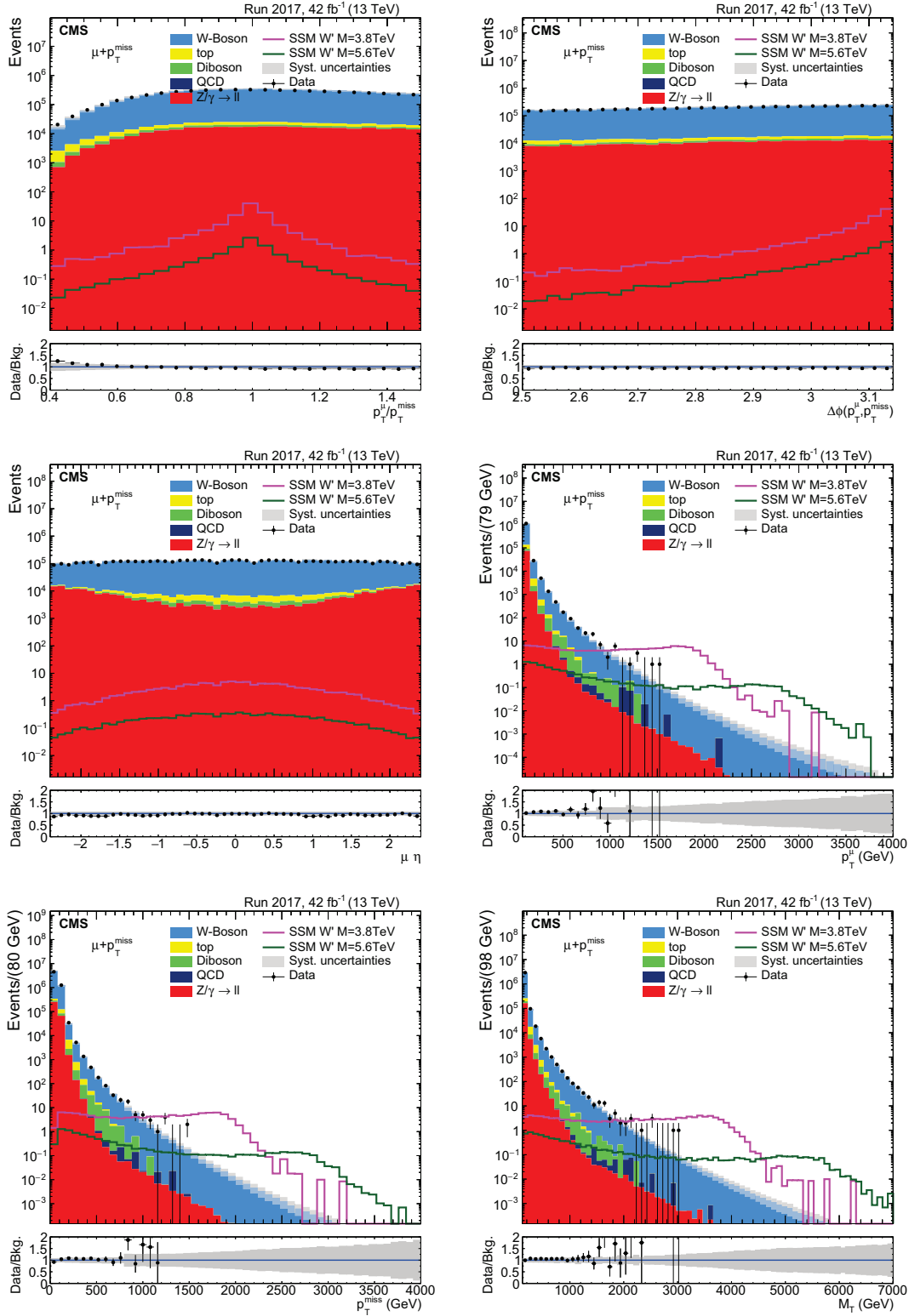
Figure 103: Distributions for p_T^μ/p_T^{miss} (top left), $\Delta\phi(\vec{p}_T^{\,\mu}, \vec{p}_T^{\,miss})$ (top right), muon η (middle left), muon p_T (middle right), p_T^{miss} (bottom left), and M_T (bottom right). Distributions after all selection for 2017 data ($42\,fb^{-1}$), SM prediction, and two W' signals with mass, $M_{W'} = 3.8$ TeV and 5.6 TeV.
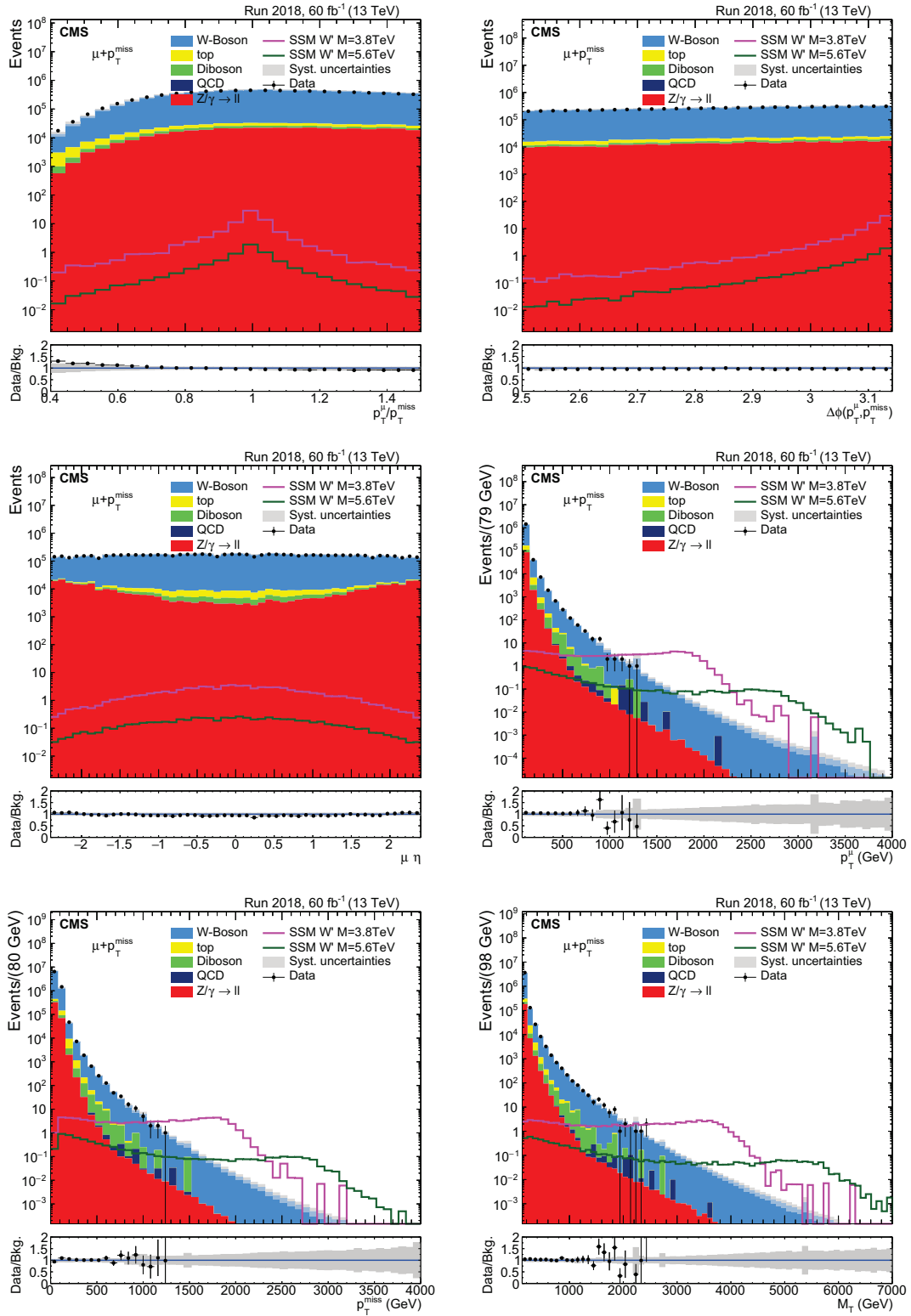
Figure 104: Distributions for p_T^{μ}/p_T^{miss} (top left), $\Delta\phi(\vec{p}_T^{\mu}, \vec{p}_T^{miss})$ (top right), muon η (middle left), muon p_T (middle right), p_T^{miss} (bottom left), and M_T (bottom right). Distributions after all selection for 2018 data ($60\,fb^{-1}$), SM prediction, and two W' signals with mass, $M_{W'} = 3.8$ TeV and 5.6 TeV.

Figure 105: Distributions for p_T^μ/p_T^{miss} (top left), $\Delta\phi(\vec{p}_T^\mu, \vec{p}_T^{miss})$ (top right), muon η (middle left), muon p_T (middle right), p_T^{miss} (bottom left), and M_T (bottom right). Distributions after all selection for full Run 2 data ($137\,\text{fb}^{-1}$), SM prediction, and two W' signals with mass, $M_{W'} = 3.8$ TeV and 5.6 TeV.
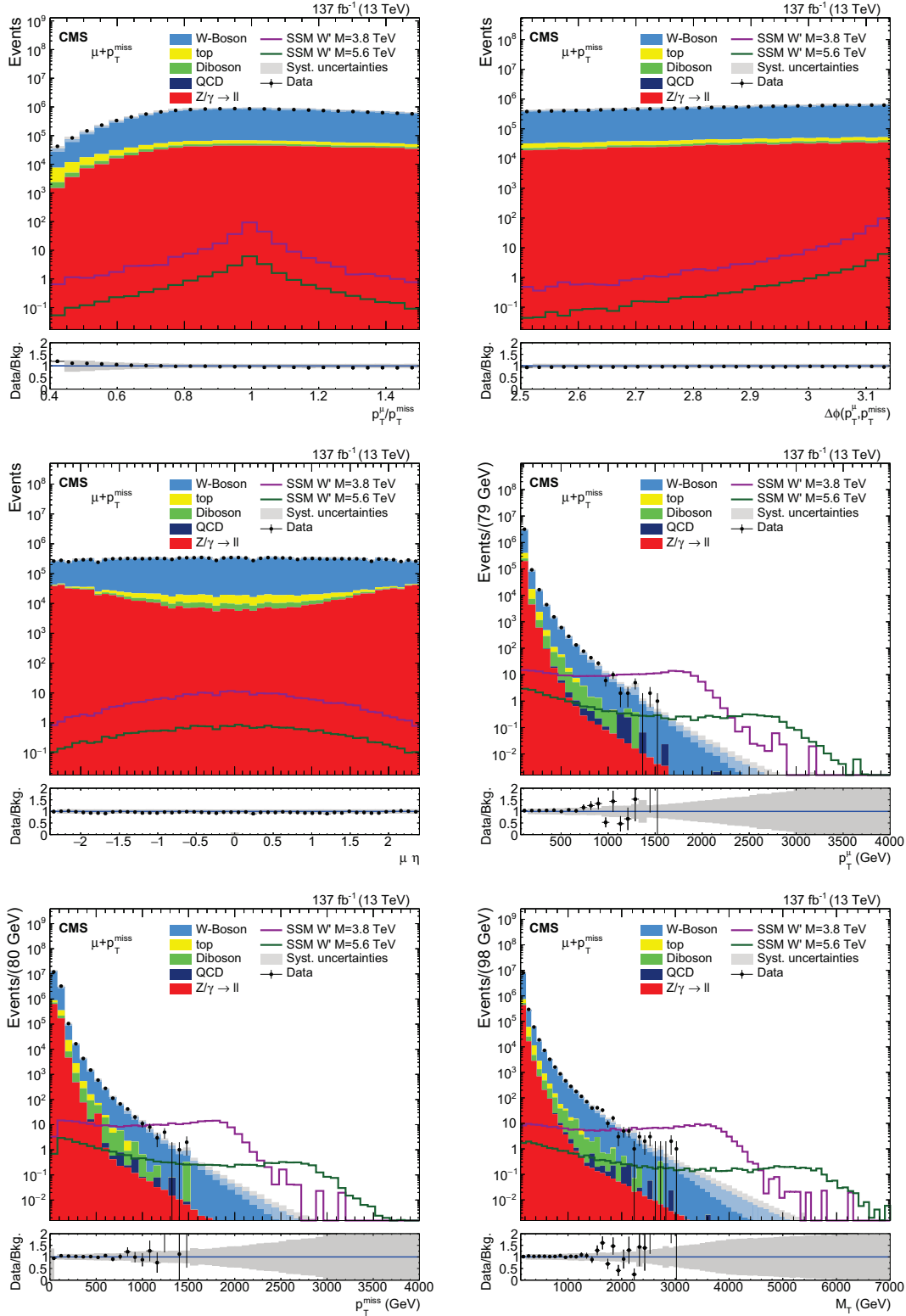
The final M_T distribution for the total integrated luminosity of $137\,\mathrm{fb}^{-1}$ is shown in Figure 106 in a cumulative way, where each bin corresponds to the integral between the M_T value in that bin to infinity.
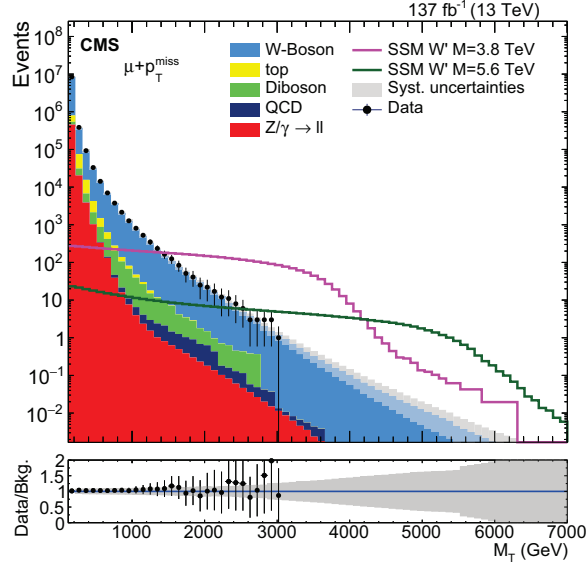
Figure 106: Cumulative M_T distribution after all selection. Each bin corresponds to the integral between the M_T value in that bin to infinity. Distribution presented for full Run 2 data $(137\,\mathrm{fb}^{-1})$, SM prediction, and two W' signals with mass, $M_{W'} = 3.8$ TeV and 5.6 TeV.

The final M_T yields for the total integrated luminosity of $137\,\mathrm{fb}^{-1}$, for data, SM background, and SSM W' $(M_{W'} = 5.6$ TeV) signal, are summarized in Table 5.7 after applying the complete selection, for four different M_T thresholds.

M_T threshold $(M_T >)$	0.4 TeV	1.0 TeV	2.0 TeV	3.0 TeV
Data	38143 ± 195	831 ± 29	21 ± 5	0 ± 0
Total SM bkg.	37170 ± 810	793 ± 17	21.0 ± 0.5	1.10 ± 0.02
W Boson	31923 ± 696	741 ± 16	19.6 ± 0.4	1.10 ± 0.02
Top quark	2602 ± 97	8.4 ± 0.6	0.0 ± 0.01	0.000 ± 0.001
Diboson	1389 ± 52	37.1 ± 2.6	0.73 ± 0.04	0.000 ± 0.001
DY (Z →)	1232 ± 46	4.10 ± 0.28	0.17 ± 0.01	0.000 ± 0.001
QCD	20.5 ± 0.7	2.55 ± 0.18	0.45 ± 0.03	0.000 ± 0.001
$M_{W'} = 5.6$ TeV	18.1 ± 0.1	11.4 ± 0.3	6.89 ± 0.21	4.88 ± 0.22

Table 5.7: Data, background and SSM W' signal $(M_{W'} = 5.6$ TeV) yields for the Run 2 M_T distributions after applying the complete selection. The uncertainties correspond to statistical and systematical uncertainties added in quadrature.

5.7.1 Highest transverse mass events

The number of events at the TeV scale are expected to be very low. The highest M_T events were scrutinized manually by inspecting their reconstruction parameters to avoid misreconstructed events that could end up with a high M_T value and create a fake signal.

The displays for the events with the highest M_T values among the selected $\mu + p_T^{miss}$ events, are shown in Figure 107 for 2017, and in Figure 108 for 2018. Their corresponding M_T values are (2.9 ± 0.1) TeV and (2.5 ± 0.1) TeV, respectively.
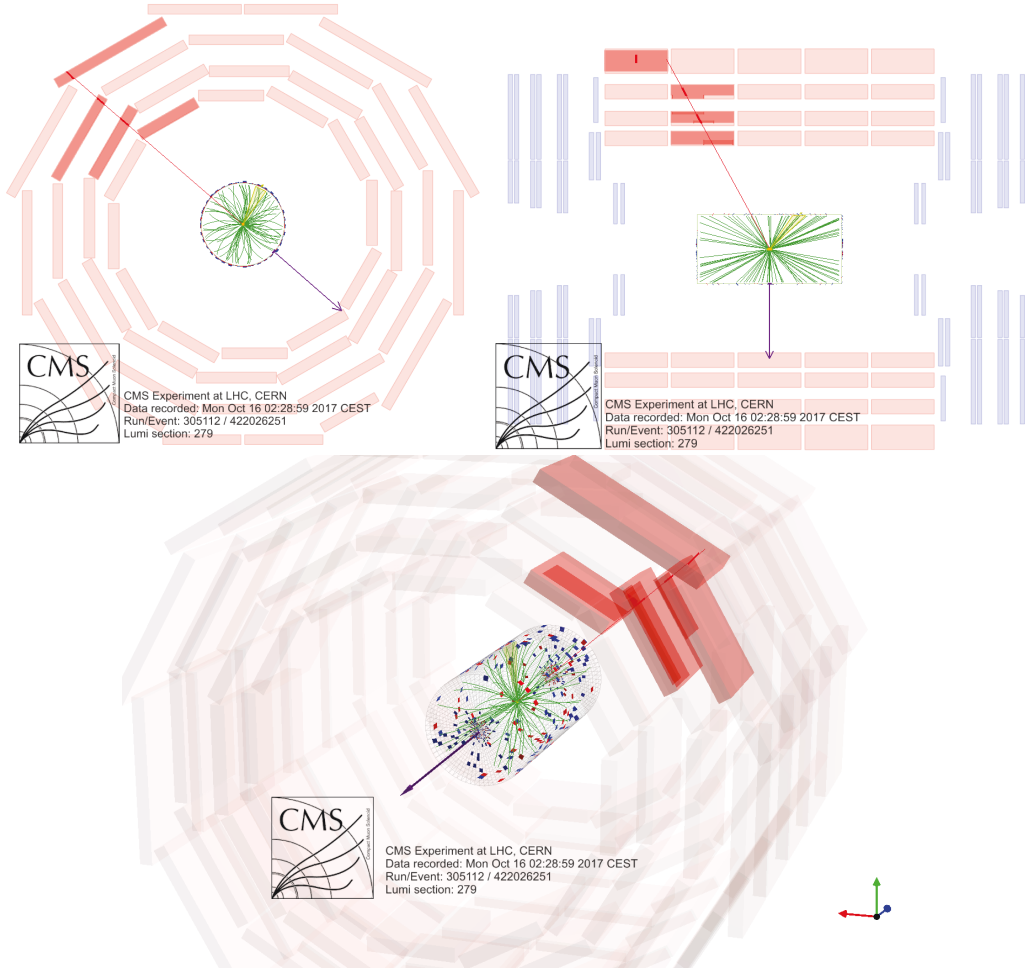
Figure 107: Event display for the event with the highest M_T value in 2017 data (M_T (2.9 ± 0.1) TeV, run 305112, lumi block 279, event 422026251).

The event displays shown in Figures 107 and 108 show three different views of the detector: the transverse plane $(r - \phi)$ (top–left), longitudinal plane $(r\text{-}z)$ (top–right), and a 3D view (bottom). Only particles (or jets) with a p_T above certain thresholds are displayed. The Tracker tracks are represented with green lines, the jets with yellow cones, the energy deposits in the calorimeters are shown as red and blue rectangles, the muon trajectory is a red line, the muon chambers with muon
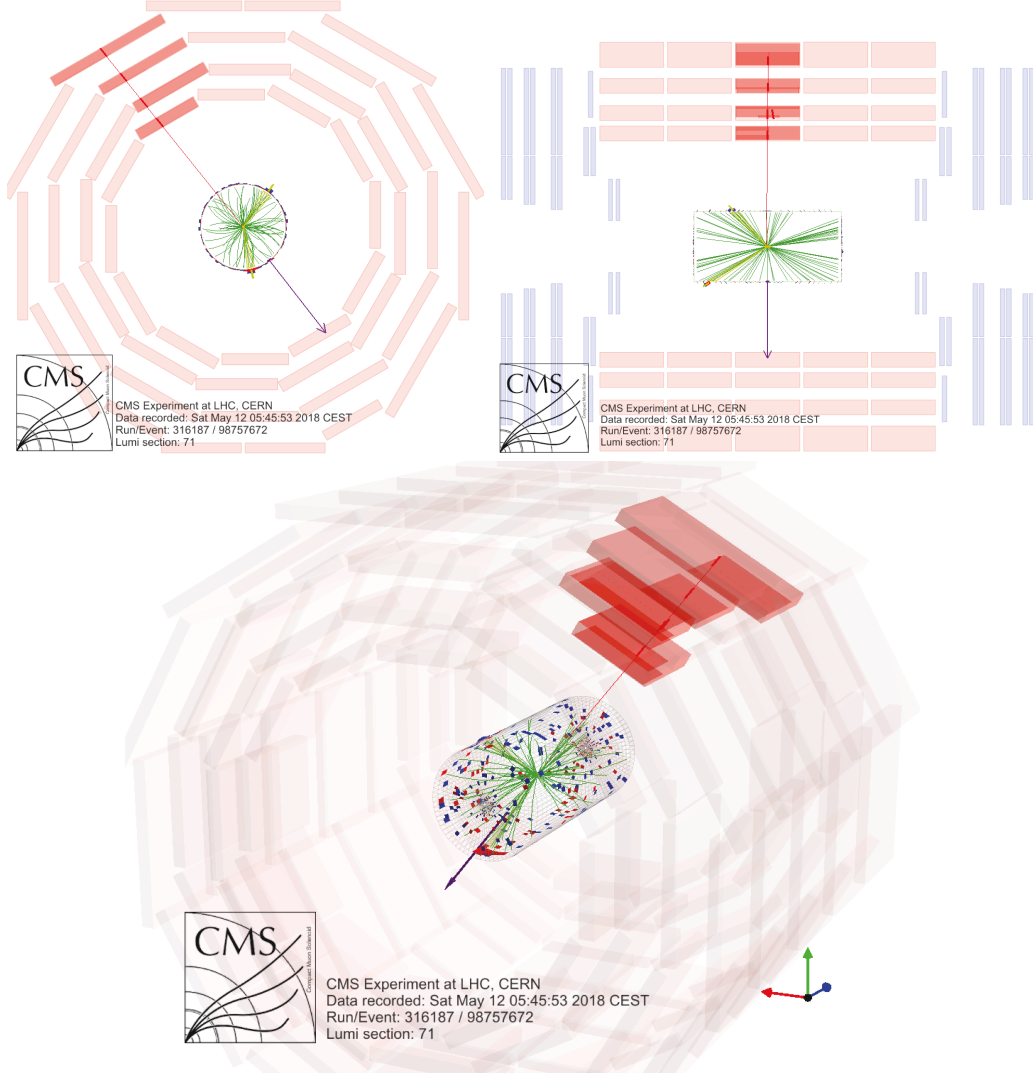
Figure 108: Event display for the event with the highest M_T value in 2018 data (M_T (2.5 ± 0.1) TeV, run 316187, lumi block 71, event 98757672).

signals are marked in a darker red than the rest of the chambers, and the p_T^{miss} is represented as a purple arrow proportional to its absolute value.

The highest M_T events in each year of data taking are summarized in Table 5.8. The events are tagged according to the CMS convention of run number, luminosity block number, and event number. The muon p_T, the event p_T^{miss}, and the reconstructed M_T values are also provided.

Year	run:lumiblock:event	M_T (TeV)	p_T^μ (TeV)	p_T^{miss} (TeV)
2016	276870:748:1302567662	2.9 ± 0.1	1.42 ± 0.08	1.51 ± 0.08
2017	305112:279:422026251	2.9 ± 0.1	1.49 ± 0.08	1.48 ± 0.08
2018	316187:71:98757672	2.5 ± 0.1	1.30 ± 0.07	1.18 ± 0.07

Table 5.8: Highest M_T events in each year.

5.7.2 W charge

It is important to measure the relative contribution of positive and negative W bosons in the selected sample. Even if the total observed yield in data is consistent with the SM prediction, new effects could be present if the proportion of positive W bosons and negative W bosons is not as expected.

Due to the evolution of the PDFs, the M_T distribution is also sensitive to the momentum fraction and nature of the partons involved in the interaction. The ratio $N(W^+)/N(W^-)$ measured experimentally at the scale of the W boson mass is $W^+/W^- = 1.3166 \pm 0.0019$ [155], while at higher mass this value is expected to increase.

In this analysis, the W boson charge is determined by the charge of the reconstructed muon from its decay. Figure 109 shows the M_T distributions separately for events with positive (left) and negative (right) muons after selection. Both distributions show good agreement data and SM prediction.
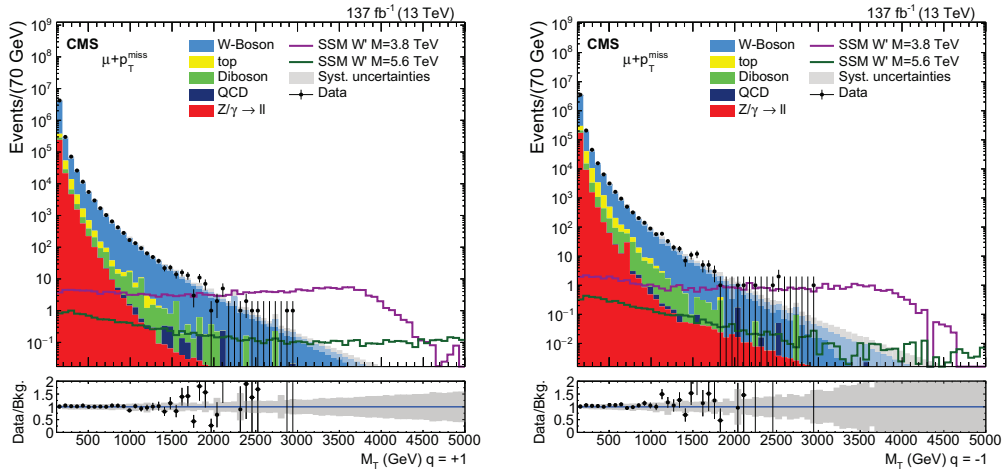
Figure 109: Distributions of M_T for events with positive (left) and negative (right) muons, after selection for Run 2 data ($137\,\mathrm{fb}^{-1}$), SM prediction, and two W' signals with mass, $M_{W'} = 3.8$ TeV and 5.6 TeV.

The contributions from other processes than W bosons are calculated from the MC simulation and subtracted from the data yields. The ratio $N(W^+)/N(W^-)$ measured in this analysis is $N(\mu^+ + p_T^{\mathrm{miss}})/N(\mu^- + p_T^{\mathrm{miss}}) = 1.205 \pm 0.001$, for data with $M_T > 120$ GeV, while, for higher mass thresholds the value of the ratio increases. A summary of the ratio of number of positive over negative W for different M_T thresholds for data and background is shown in Table 5.9. The background simulation uncertainties are calculated as explained in Section 5.6, while for this study should be calculated separately for each muon charge, therefore, this study should be taken as a first approach and not the complete measurement.

In Section 4.4 we discussed how the probability of charge mis–assignment in the process of SM W boson production and decay, was not independent of the W

Min. M_T		120 GeV	400 GeV	1000 GeV	2000 GeV
$N(W^+)/N(W^-)$	Data	1.205 ± 0.001	1.91 ± 0.03	2.06 ± 0.19	2.2 ± 1.4
	SM bkg.	1.208 ± 0.072	1.93 ± 0.27	2.47 ± 0.77	3.6 ± 2.2

Table 5.9: Ratio of $N(W^+)/N(W^-)$ for different M_T thresholds, for data and SM prediction. The uncertainties correspond to the statistical and systematic uncertainties. No split in charge has been taken into account in the corrections applied.

boson charge. Positive W bosons are more likely assigned a negative charge, than the opposite (see Figure 63), due to the kinematics and the geometry of the process. Therefore, the measured ratio, $N(W^+)/N(W^-)$, might be affected and result in a smaller ratio value than the real one, specially at high masses. The study was done with MC simulation, but this effect could be more pronounced in data. This should be taken into account for future precise measurements of the W boson charge.

5.7.3   Transverse mass resolution

Given that the muon p_T scale and resolution are significant systematic uncertainties it is important to evaluate the impact it may have in the M_T distribution, the discriminant variable. To evaluate the M_T resolution, the final selected events in the W MC simulated samples are divided in five M_T regions: [120, 200, 500, 1000, 3000, 6000] GeV. In each M_T region, the distribution of the difference between the real M_T (at generated level) and the reconstructed M_T values is fitted to gaussian function. The resulting σ of the fit is shown as function of the generated M_T in Figure 110.
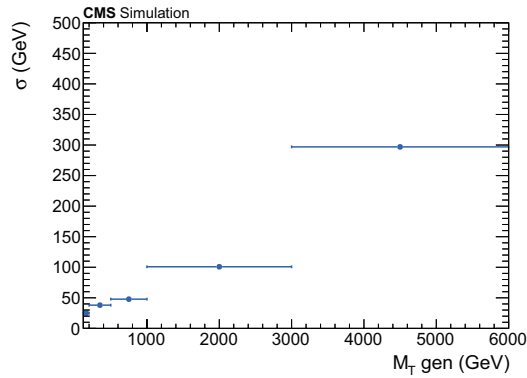
Figure 110: Resolution, σ, from the gaussian fit, as function of the generated M_T, evaluated in simulated samples.

The M_T resolution is ~ 30 GeV at $M_T < 200$ GeV, and it increases up to ~ 300 GeV at $M_T > 3000$ GeV. The σ of each M_T region is used as bin width of that region for the final M_T distribution shown in Figure 111.
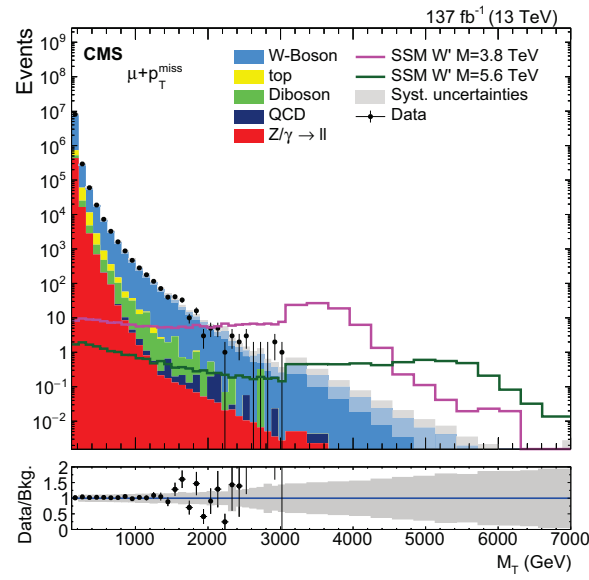
Figure 111: Distribution of M_T for Run 2 data ($137\,\text{fb}^{-1}$), SM prediction, and two W' signals with mass, $M_{W'} = 3.8$ TeV and 5.6 TeV.

Chapter 6

Results and interpretations

The differential M_T distribution (Figure 111) and its cumulative expression (Figure 106) gather our sensitivity to new physics processes in the muon $+ p_T^{miss}$ final state of the Run 2 data. The data show good agreement with the SM prediction for this channel, and no significant deviation appears. The observed and predicted M_T distributions, together with statistical analysis tools, are used in this chapter to interpret the data in terms of new physics scenarios and limit their parameters.

This same search in the electron channel, $e + p_T^{miss}$ final state, has been carried out in parallel by another CMS group. The Run 2 data scrutinized and the analysis strategy are essentially the same in both channels. In the following, results obtained in the muon channel are presented. For completeness from the scientific point of view, results from the electron channel are also added, together with their statistical combination, when possible. The M_T distribution used as input for the limit setting in the electron channel is shown in Figure 112 - right, next to the corresponding one in the muon channel (from Figure 111), for comparison.
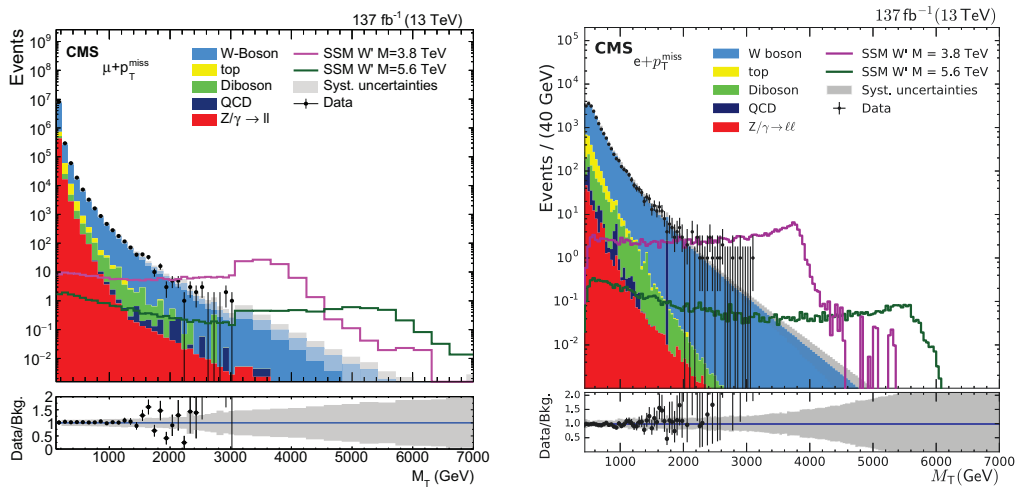
Figure 112: Distribution of M_T after selection of the lepton $+ p_T^{miss}$ system in the muon channel (left) and electron channel (right), for full Run 2 data ($137\,fb^{-1}$), SM prediction, and two W' signals with mass, $M_{W'} = 3.8$ TeV and 5.6 TeV.

Two of the main differences present in the electron channel with respect to the muon channel are the M_T threshold and the mass resolution. Figure 112 *x*–axis shows a higher mass threshold ($M_T > 500$ GeV) in the electron channel with respect to the muon channel ($M_T > 120$ GeV). This is due to the difference in the lepton p_T threshold of the electron trigger ($p_T > 200$ GeV), with respect to the muon one ($p_T > 50$ GeV). The size of the M_T bins in the electron channel is smaller than that in the muon channel, reflecting the better energy resolution for electrons shown in Figure 33, compared to muons, especially in the high mass region.

The observed data in the electron channel is also in agreement with the SM background expectations. A statistical analysis of the data is performed in the following, in two different scenarios, assuming the presence of a resonant or a non–resonant signal, as explained in Chapter 5.

In the first case, a BSM resonant signal, the search focuses on detecting a peak standing out of the SM predicted background, in the M_T distribution. In this scenario we set limits in two ways: model independent and model specific. And three specific models are studied: SSM, Split–UED model, and RPV SUSY model.

In the second case, a non–resonant signal, a deviation is looked for in the tail of the M_T. This is carried out by means of the measurement of the *W* and *Y* oblique electroweak parameters to constrain any deviation from the SM.

Finally, as a reinterpretation of both, resonant and non–resonant searches, a Higgs Composite model is explored by setting limits to a possible non–elementary Higgs.

6.1 Direct searches

We present in this section results of the search for a BSM resonance decaying into an energetic muon and an undetected particle, as schematically shown in Figure 73. We set limits in two ways: model independent, where the mass shape of the signal is not taken into account, and model specific, where different models and signal shapes are studied.

6.1.1 Signal efficiency

The signal efficiency times acceptance, $A \times \epsilon$, is defined as the ratio of signal events passing the analysis selection over the total SSM W' generated events. For simulated events passing all of the selection criteria, and for $M_T > 120$ GeV, the signal efficiency as a function of the SSM W' mass is shown in Figure 113 for each channel.

In the muon channel the signal efficiency is maximal at a value of 0.77, corresponding to a W' mass of 1800 GeV. This value decreases gradually to ~ 0.6 for larger and smaller masses. The value of ~ 0.4 of the first mass point ($M_{W'} = 200$ GeV) is due to the p_T and M_T thresholds applied. For masses above $M_{W'}$ 3000 GeV, the increasing off–shell production displaces events to lower M_T values (see M_T distribution of the SSM W' $M_{W'} = 5600$ GeV in Figure 75 - right).
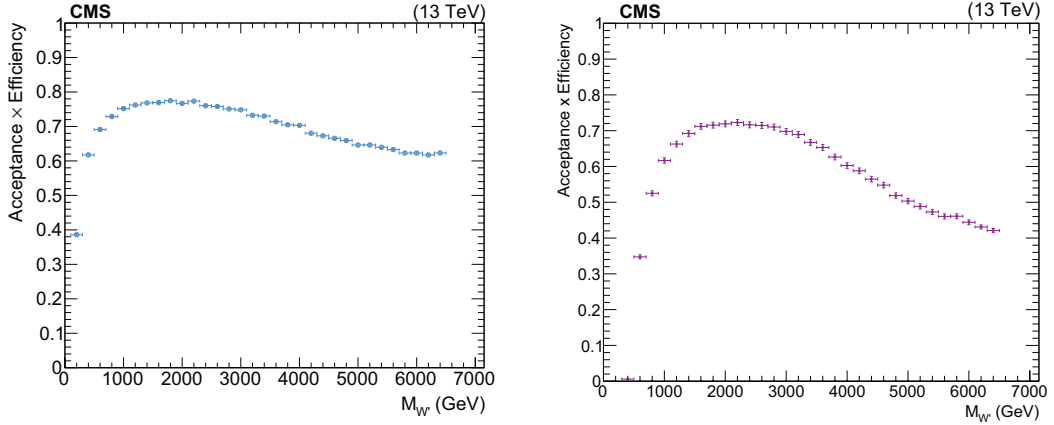
Figure 113: Signal Acceptance $\times$ Efficiency for the SSM W' as a function of the W' mass, for the muon channel (left) and electron channel (right).

In the electron channel the efficiency is maximal at a value of 0.73, corresponding to a W' mass of 2200 GeV. This value decreases gradually to ~ 0.4 for larger and smaller masses. The $A \times \epsilon$ values for low W' mass are lower in the electron channel than in the muon channel since the p_T threshold of the electron trigger is higher than the muon one. This effect is also reflected at high W' mass values because the increasing off–shell production displaces events to lower M_T values.

6.1.2 Statistical Procedure

The statistical analysis treatment applied is based on counting the number of data events above a given M_T threshold and compare it to the expected number of signal and background events, including the systematic uncertainties discussed in Section 5.6. The shape of the distribution is taken into account. In this way we quantify the level of agreement of the data with the sum of the background processes and the potential signal. The input used for the data, the background contribution, and the potential signal is given by the M_T distribution. The counting is done in each bin of the discriminant variable. In this way both, the information of the normalization and the shape of the M_T variable, contribute to the statistical treatment.

The probability of observing N_{ob} events in data is given by the Poisson distribution, as

$$P(N_{ob}) = \frac{d^{N_{ob}}}{N_{ob}!} e^{-d}, \tag{6.1}$$

where the number of expected events, d, is taken to be the Poisson mean. Background and signal contributions are taken into account by modeling d as

$$d = \mathcal{L} \prod_i \epsilon_s \, \nu_{i,s} \, \sigma_s + \prod_j \epsilon_b \, \nu_{j,b} \, \sigma_b \frac{N_{ob}}{\sigma_b} \tag{6.2}$$

where the following quantities represent:

- ϵ_s and ϵ_b are the signal and background efficiencies, respectively.

- σ_s and σ_b are the signal and background cross sections, being σ_s the parameter of interest.

- N_{ob} is the number of observed events.

- $v_{i,s}$ and $v_{j,b}$ are the nuisance parameters, for the signal and background respectively, based on the systematic uncertainties discussed in Section 5.6.

To determine the limits and confidence level (CL) on σ_s, the parameter of interest, the Bayesian method [6] is used. The posterior distribution used is

$$\underset{post}{\sigma|N_{ob}} = \int d\epsilon_s \, d\epsilon_b \, d\sigma_b \underset{ij}{\int} dv_{i,s} \, dv_{j,b} \frac{d^{N \, b}}{N_{ob}!} e^{-d} \pi(\epsilon_s, \epsilon_b, v_{i,s}, v_{j,b}, \sigma_b) \, \pi_{poi}(\sigma_s) \quad (6.3)$$

where the function $\pi()$ is the combined prior function relating the nuisance parameters. The distribution $\pi_{poi}(\sigma_s)$ is a prior function describing the parameter of interest. The prior probability function is chosen to be an uniform distribution for $\sigma_s > 0$. With this choice, all positive values for the signal cross section are assumed to be equally likely.

From this, a 95 % limit can be calculated with

$$0.95 = \underset{post}{\int} (\sigma_s | N_{ob}) d\sigma_s \quad (6.4)$$

For every result, two limits are calculated: the *observed* and the *expected* limits. The observed limit makes use of the measured M_T distribution of data as input for the statistical model. The expected limit instead, is computed taking as input pseudo–data from random experiments following expectations from SM simulations.

The Higgs Combine Tool (HCT) [156] is used to perform the analysis on the counting and shape experiment model and to calculate limits.

6.1.3 Model independent limits

A model independent limit is determined using a single–bin method integrating the M_T distribution from a given lower transverse mass threshold, M_T^{min}, to infinity. It uses the SSM W' production model as a guideline, taking into account its acceptance and efficiency, but it is independent on the actual shape of the M_T distribution. The limits obtained are valid for signals from several other theoretical models, with different mass distributions, as long as their acceptance (A) and efficiency (ϵ) are similar to those in the SSM.

The resulting model independent limits at 95 % CL on the cross section of new physics decaying to a muon and p_T^{miss} are shown for each year of the Run 2 data and the combination of them, in Figure 114. Notice the difference in the y–axis range between distributions for 2016 and other data years. The one and two standard

deviations from the expected excluded cross section are represented with green and yellow bands, respectively.
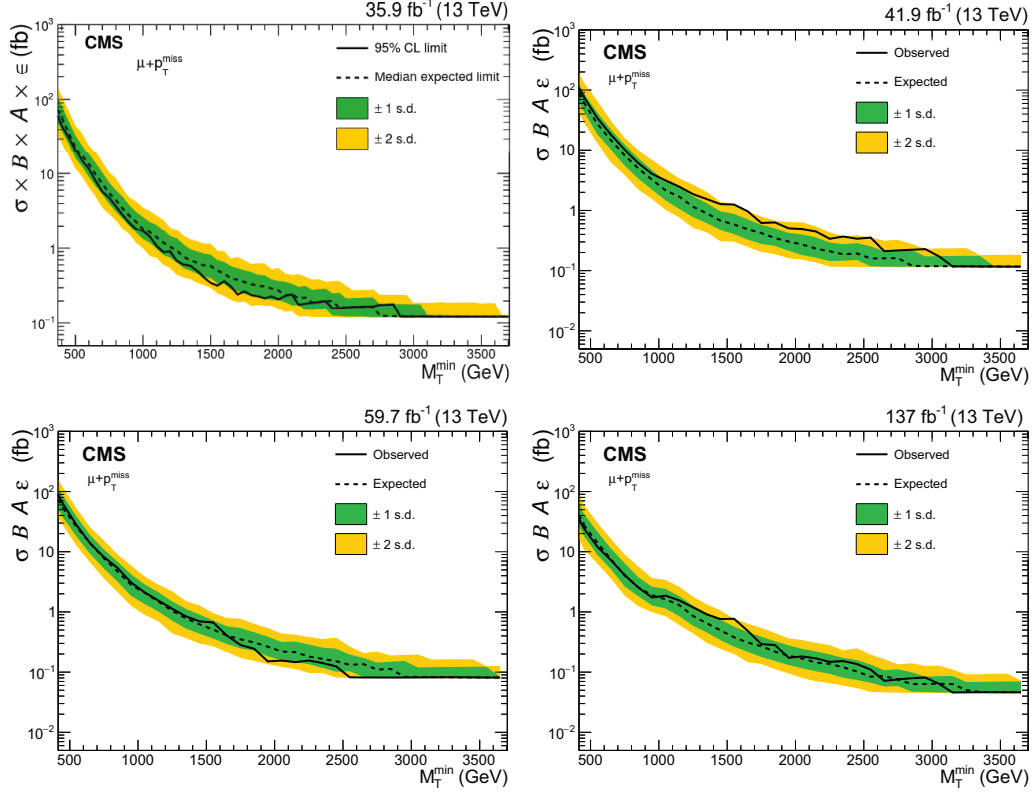
Figure 114: The model independent expected and observed 95 % CL limits on ($\sigma \times \mathcal{B} \times A \times \epsilon$) as a function of the lower cut on M_T, M_T^{min}, in 2016 [157] (top-left), 2017 (top-right), 2018 (bottom-left), and the combination of full Run 2 data ($137\,\text{fb}^{-1}$) (bottom-right), along with the one- and two-sigma uncertainty bands on the expected limit.

The observed limits are in agreement with the expected limits, within uncertainties. The best sensitivity is reached at the high M_T region ($M_T \geq 3$ TeV), where BSM processes with ($\sigma \times \mathcal{B} \times A \times \epsilon$) > 0.1 fb could be distinguished by the CMS detector.

In the lower M_T region ($M_T \leq 1$ TeV) the sensitivity worsens due to the larger ratio of background over signal. The mass region that has been explored was fixed by the reach of the experimental data ($M_T \sim 3$ TeV). The statistical combination of the three years of Run 2 data (Figure 114-bottom right) improves the limit down to ($\sigma \times \mathcal{B} \times A \times \epsilon$) ~ 0.05 fb.

By combining the model independent limits from the muon channel and the electron channel (Figure 115-top right), we obtain the limits in ($\sigma \times \mathcal{B} \times A \times \epsilon$)$_{\text{MI}}$ in Figure 115-bottom. For visual comparison, the limit from the muon channel is again shown in Figure 115-top left. This pattern will be used in the following limit results.

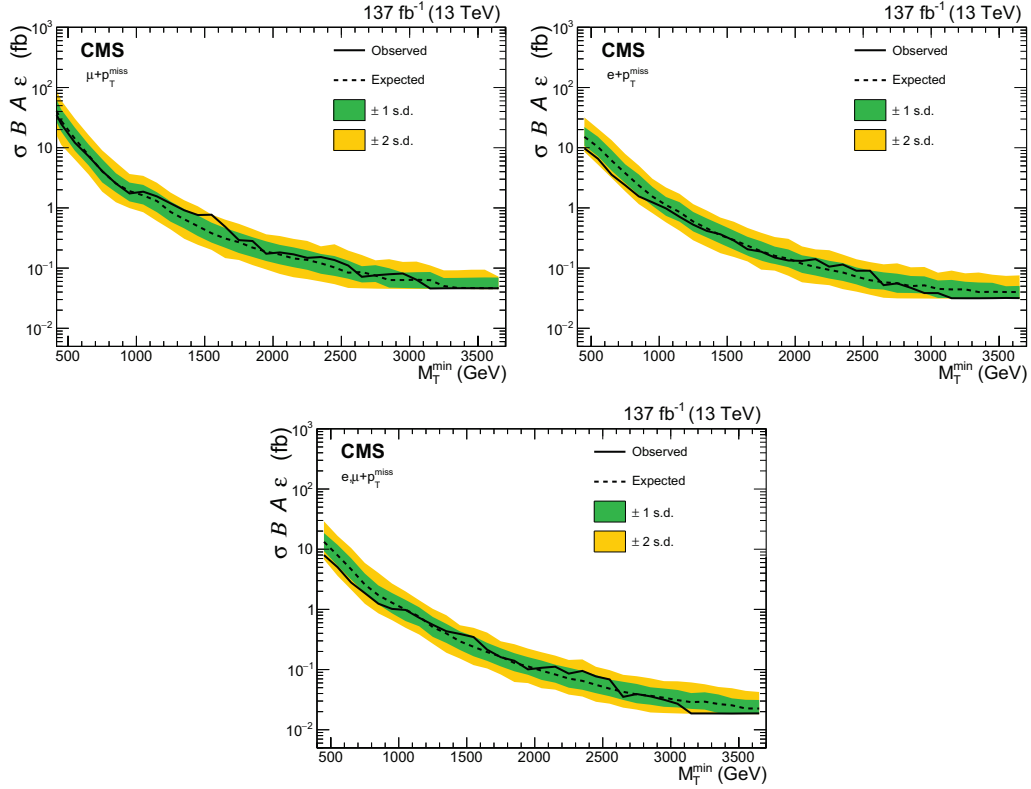**Figure 115:** The model independent expected and observed 95 % CL limits on $(\sigma \times \mathcal{B} \times A \times \epsilon)$, as a function of the lower cut on M_T, M_T^{min}, for the muon channel (top-left), electron channel (top-right), and the combination of muon and electron channels (bottom), for the full Run 2 data ($137\,\mathrm{fb}^{-1}$), along with the one- and two-sigma uncertainty bands on the expected limit.

The sensitivity in the electron channel in the high M_T region ($M_T \geq 3$ TeV) is $(\sigma \times \mathcal{B} \times A \times \epsilon) \sim 0.03\,\mathrm{fb}$, and in the muon channel is $(\sigma \times \mathcal{B} \times A \times \epsilon) \sim 0.05\,\mathrm{fb}$. This difference in the sensitivity is due to the better mass resolution in the electron channel relative to that in the muon channel (explained at the beginning of this Chapter 6). When combining both channels the limit reaches $(\sigma \times \mathcal{B} \times A \times \epsilon) \sim 0.02\,\mathrm{fb}$, for the same M_T region.

The limit for any specific model can be determined using the model independent limit in Figure 115-bottom. A limit on the production cross section times the branching fraction, $(\sigma \times \mathcal{B} \times A \times \epsilon)_{exc}$, can be obtained as follows:

$$(\sigma \times \mathcal{B} \times A \times \epsilon)_{exc} (M_T^{min}) = \frac{(\sigma \times \mathcal{B} \times A \times \epsilon)_{\mathrm{MI}}(M_T^{min})}{f_{M_T}(M_T^{min})} \tag{6.5}$$

where the effect of the threshold M_T^{min} on the signal is expressed as a factor f_{M_T}. This factor is determined in the model under study by counting the events with $M_T > M_T^{min}$ and dividing it by the number of generated events. The principle is

illustrated in Figure 116.
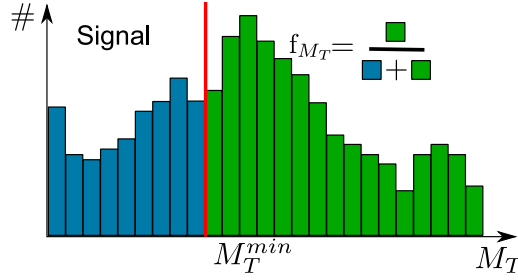
Figure 116: Scheme illustrating the determination of the f_{M_T} factor.

6.1.4 SSM W' model

The SSM, presented in Section 1.2.1 and Section 5.1.1, is the benchmark model in this analysis, used to establish the CMS sensitivity to the lepton $+ \, p_T^{miss}$ signature. The observed and expected excluded cross sections, $\sigma_{W'} \times \mathcal{B}(W' \rightarrow \mu\nu)$, at 95 % CL, are explored using the statistical method explained in Section 6.1.2 and the signal efficiency shown in Section 6.1.1.

The observed and expected excluded cross section values at the 95 % CL for each year and for the combination with full Run 2 data, in the muon channel, are shown in Figure 117. The one and two standard deviations from the expected excluded cross section are represented with green and yellow bands, respectively.

Each plot also shows the theoretical cross section prediction at NNLO precision for the SSM W' boson (W' $\rightarrow \mu\nu$) as a black line, and its corresponding systematic uncertainty as a gray band. These values correspond to those listed in Table 5.1. The mass region in which the observed cross section is below the SSM W' theory line, is excluded at 95 % CL. The intersection of the central value of the $\sigma \times \mathcal{B}$ curve and the limit curve gives the observed (expected) limit on the W' boson mass, $M_{W'} > 5.6\,(5.5)$ TeV at 95 % CL with the 137 fb^{-1} luminosity of the full Run 2 data.

Assuming that the SSM W' presents lepton flavour universality, the limits from the muon channel are combined with those from the electron channel, as if they were two independent measurements of the same SSM W' cross section and branching fraction, $\sigma \times \mathcal{B}$.

The expected and observed 95 % CL exclusion limits for the electron and muon channels individually (top) and combined (bottom), are shown in Figure 118 as a function of the W' mass.

The sensitivity is slightly better in the muon channel due to the higher SSM signal efficiency as presented in Section 6.1.1. Individual channel observed (expected) limits at 95 % CL in the SSM W' boson mass are $M_{W'} > 5.6\,(5.5)$ TeV and $M_{W'} > 5.4\,(5.3)$ TeV, for the muon and electron channel, respectively. With 137 fb^{-1} of combined electron and muon data during the Run 2, the observed (expected) limit in the W' mass is $M_{W'} > 5.7\,(5.6)$ TeV.
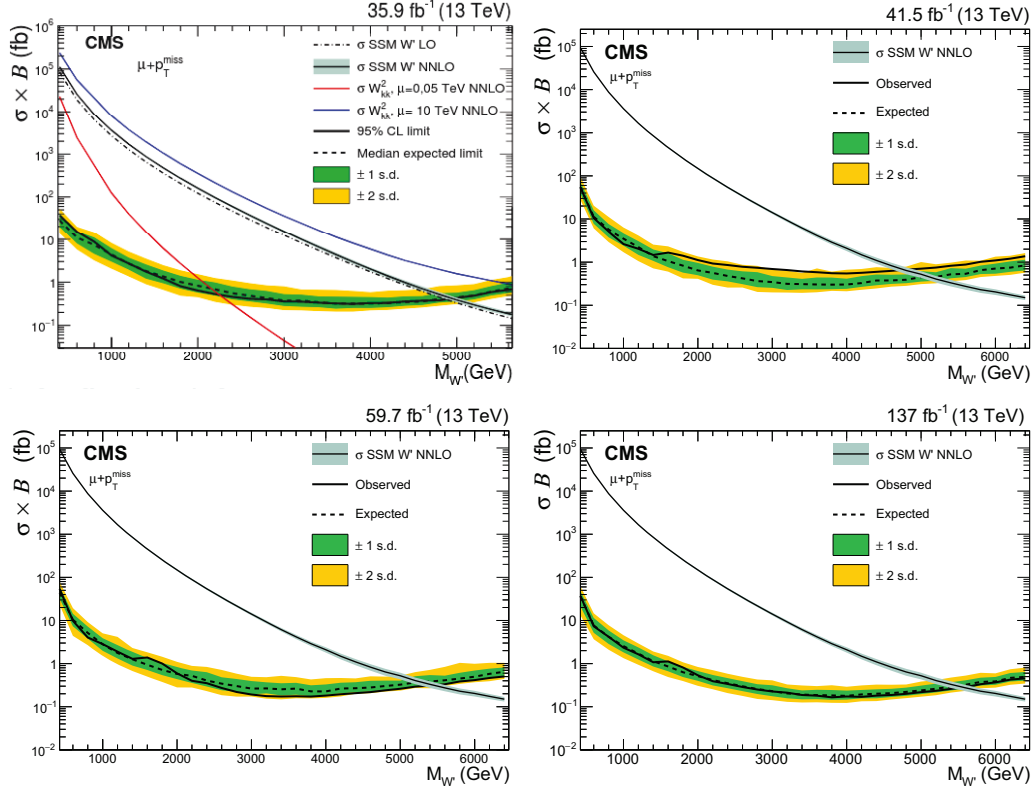
Figure 117: Expected and observed 95 % CL limits on $\sigma \times \mathcal{B}$, for the muon channel, as a function of the SSM W' mass, in 2016 [157] (top-left), 2017 (top-right), 2018 (bottom-left), and the combination of full Run 2 data ($137\,\text{fb}^{-1}$) (bottom-right), along with the one- and two-sigma uncertainty bands on the expected limits. Also shown, several theoretical cross section curves for different signals.

Table 6.1 shows the observed and expected exclusion mass limits for the SSM W' model split by year and channel, together with the combinations.

| Year | 2016 | 2017 | 2018 | Run 2 |
Luminosity	$(36\,\text{fb}^{-1})$	$(42\,\text{fb}^{-1})$	$(60\,\text{fb}^{-1})$	$(137\,\text{fb}^{-1})$
μ Obs. (Exp.) [TeV]	4.9 (4.9)	4.8 (5.1)	5.3 (5.3)	5.6 (5.5)
e Obs. (Exp.) [TeV]	4.9 (5.0)	4.7 (5.0)	5.3 (5.3)	5.4 (5.3)
$e + \mu$ Obs. (Exp.) [TeV]	5.2 (5.2)	5.0 (5.3)	5.7 (5.6)	5.7 (5.6)

Table 6.1: Observed and expected exclusion limits on SSM W' mass for the muon, electron, and combination of both channels, for each Run 2 year data and the combination.

The limits in the SSM W' mass presented here are the legacy from the Run 2 of LHC. These results will last years, until they are superseded by the obtained ones with Run 3 data.

142
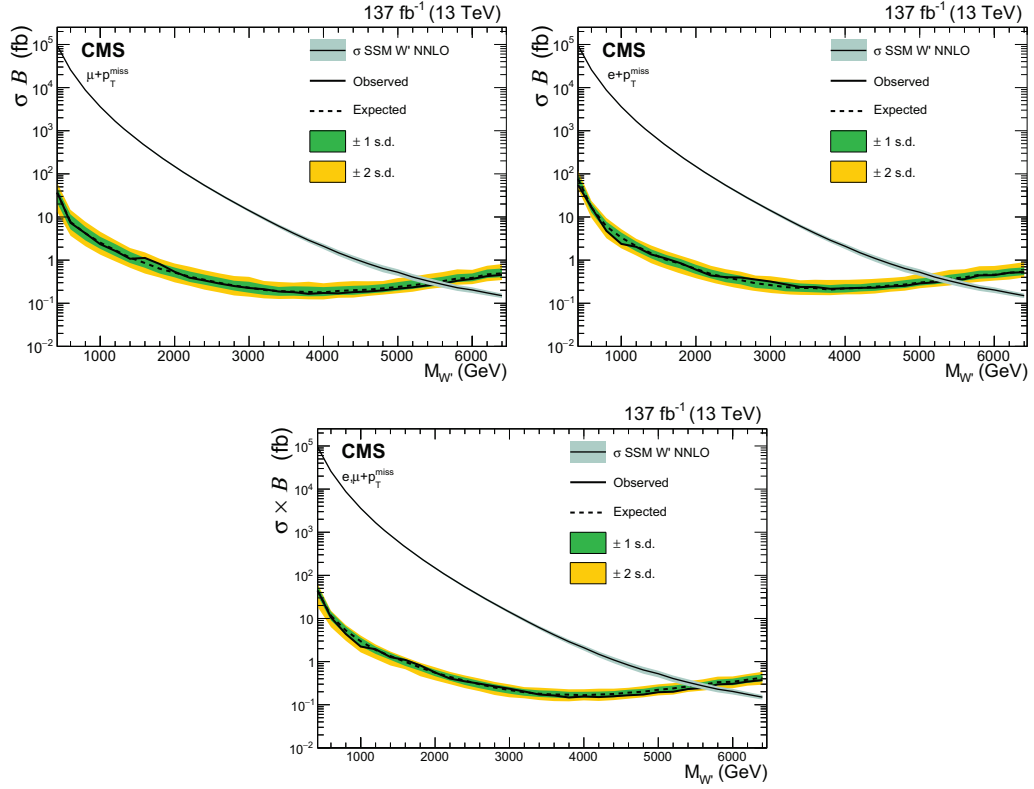
Figure 118: Expected and observed 95 % CL limits on $\sigma \times \mathcal{B}$, for the muon channel (top‑left), the electron channel (top‑right), and the combination of muon and electron channels (bottom), as a function of the SSM W' mass, for the full Run 2 data ($137\,\text{fb}^{-1}$), along with the one- and two-sigma uncertainty bands on the expected limit.

Experimental context

The results in the muon and electron decay channel, using 2016 data only corresponding to $36\,\text{fb}^{-1}$, are already published. The observed (expected) limits in the mass of the SSM W' were set to $M_{W'} > 5.2\,(5.2)$ TeV [157] by the CMS experiment, and to $M_{W'} > 5.1\,(5.2)$ TeV [158] by the ATLAS experiment, with the same 2016 data corresponding to $36\,\text{fb}^{-1}$.

The latest result, and most stringent limit up to date, is from the ATLAS experiment with full Run 2 statistics [159]. The observed (expected) limit in the mass of the W' in the muon channel is set to $M_{W'} > 5.1\,(5.1)$ TeV, and in the electron channel to $M_{W'} > 6.0\,(5.7)$ TeV. The combination of both channels gives a limit of $M_{W'} > 6.0\,(5.8)$ TeV.

The decay channel to the third lepton family ($W' \to \tau + \nu$) has the same cross section and branching fraction as the muon and electron decay channels, but the measurement is harder since the τ lepton needs to be reconstructed from its decay products. The observed (expected) limit for the W' mass in the $\tau \to$ hadrons channel with 2016 data, corresponding to $36\,\text{fb}^{-1}$, is $M_{W'} > 4.0\,(4.0)$ TeV [160] from the CMS

experiment and $M_{W'} > 3.7\,(3.8)$ TeV [161] from the ATLAS experiment.

The W' bosons that couple only to right–handed fermions may not have leptonic decay modes, depending on the mass of the right–handed neutrino. For these W' bosons, the decay to top + bottom quarks (tb) is important because in many models the W' boson is expected to have enhanced couplings to the third generation of quarks [162, 163, 164]. The decay channel $W' \to tb \to Wbb \to \ell\nu bb$ ($\ell = \mu, e$) is searched by the CMS experiment with $36\,\mathrm{fb}^{-1}$ of luminosity, and it set the observed (expected) limit in the right–handed W' mass to $M_{W'} > 3.6\,(3.5)$ TeV [165]. The search in the full hadronic decay channel, with $137\,\mathrm{fb}^{-1}$ of integrated luminosity, set an observed (expected) limit in the W' mass of $M_{W'} > 3.4\,(3.6)$ TeV [166].

The SSM also predicts the existence of a neutral boson, Z', as a heavy analog of the SM Z boson in the TeV scale. The SSM Z' boson has being experimentally searched in the dimuon and dielectron decay channels. The latest limit from the CMS Collaboration using Run 2 data, on the Z' mass, is $5.1\,(5.1)$ TeV [167], same limit value is set by the ATLAS Collaboration [168].

The Z' boson with Lepton Flavor Violating (LFV) [169] decay ($e + \mu$) is excluded for masses below 4.4 TeV [170], with 2016 data collected with the CMS experiment.

6.1.5 W' coupling strength

The exclusion limits derived in the previous section have assumed the same SSM W' couplings as the W SM boson, i.e. $g_{W'} = g_W$. The exclusion cross section limit depends on the width and the mass range of the potential signal. Because of the relation between the coupling of a particle to its width (Eq. 1.23), the limit on the cross section is used to set constraints on the coupling strength.

The simulation of SSM W' for different values of $g_{W'}/g_W$ from 1×10^{-2} to 3, is done with MADGRAPH (detail in Section 5.1.2). These signal samples at generator level have been used to weight the signal samples generated and reconstructed with PYTHIA, to account for different couplings values. The samples with $g_{W'}/g_W = 1$ are used as normalization validation. The weighted distributions of M_T are used as input to extract the limits in the coupling ratio, $g_{W'}/g_W$. One example of the M_T distribution at generator level for coupling ratio values, $g_{W'}/g_W = 3$ and 0.01 is shown in Figure 77 for an SSM W' of mass 2000 GeV.

We set a 95 % CL limit on $\sigma_{W'} \times \mathcal{B}(W' \to \mu\nu)$ as a function of the coupling strength for each W' mass point. Then the intersection point of the central value of the $\sigma_{W'} \times \mathcal{B}$ and the coupling limit is extracted. The procedure is repeated for every W' mass and the corresponding intersection points provide the input for the result. The resulting exclusion limit on the coupling strength, as a function of the W' boson mass, is shown in Figure 119 for each year separately and the combination of full Run 2 data. The area above the limit line is excluded.

The dotted line at $g_{W'}/g_W = 1$ corresponds to the SSM case studied in the previous Section 6.1.4. The intersection between the $g_{W'}/g_W = 1$ line and the coupling ratio limit corresponds to the SSM W' mass limits (summarized in Table 6.1).
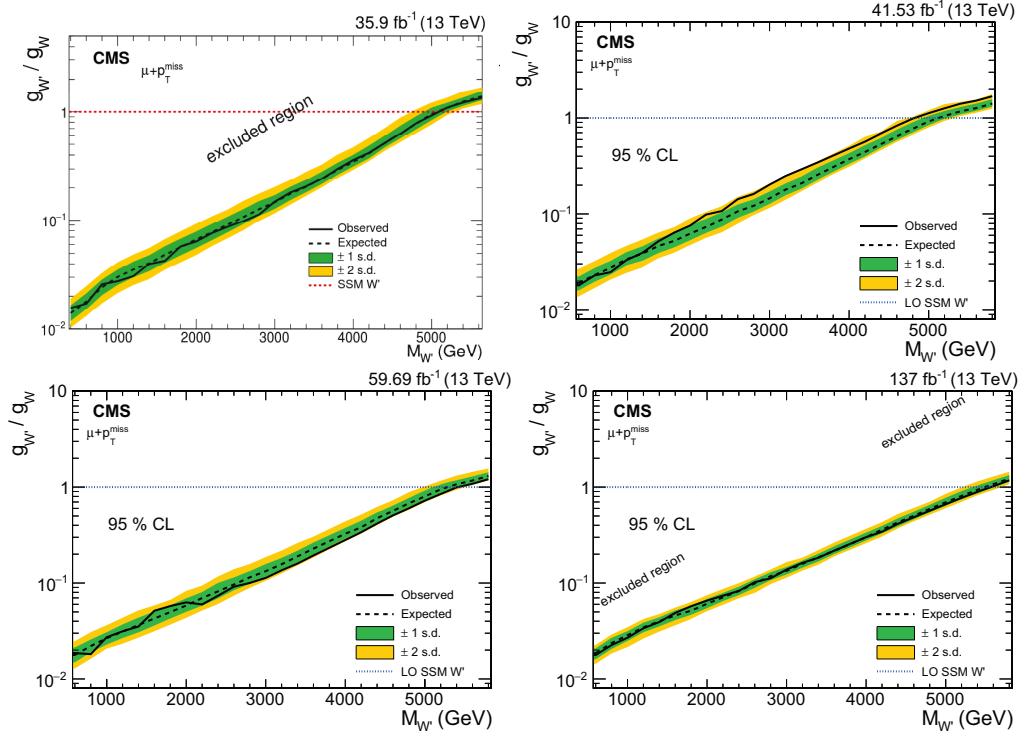
Figure 119: The expected and observed 95 % CL limits on the coupling ratio, $g_{W'}/g_W$, as a function of the W' mass in the muon channel, along with the one- and two-sigma uncertainty bands for in 2016 [157] (top-left), 2017 (top-right), 2018 (bottom-left), and the combination of full Run 2 data ($137\,\mathrm{fb}^{-1}$) (bottom-right).

The 95 % CL limits for the full Run 2 data, corresponding to $137\,\mathrm{fb}^{-1}$ of integrated luminosity, is shown in Figure 120 for each decay channel, $\mu + p_T^{\mathrm{miss}}$ (left) and $e + p_T^{\mathrm{miss}}$ (right). Both channels show a similar limit: for the low masses explored (~ 1000 GeV), very weak couplings are excluded, at $g_{W'}/g_W \sim 3 \times 10^{-2}$.
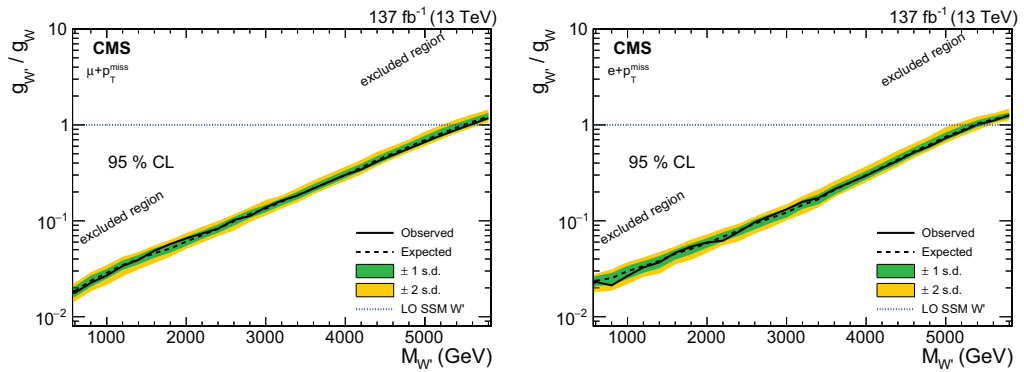
Figure 120: The expected and observed 95 % CL limits on the coupling ratio, $g_{W'}/g_W$, as a function of the W' mass in the muon channel (left) and electron channel (right), for full Run 2 data ($137\,\mathrm{fb}^{-1}$), along with the one- and two-sigma uncertainty bands on the expected limit.

Systematic uncertainties impact

The systematic uncertainties are included in the fit as nuisance parameters as explained in Section 6.1.2. To evaluate which uncertainties most affect the result of the signal strength, the *impact* is calculated as the $\pm 1\sigma$ of the post–fit value of each nuisance parameter, while the rest of the parameters are fixed to their best fitted value. Among the long list of uncertainties considered, the twenty that change the post–fit signal strength ($\mu = \sigma_{\text{obs}}/\sigma_{\text{theo}}$) the most are shown in Figure 121, in 2018 analysis and the SSM W' signal sample of mass $M_{W'} = 1000$ GeV, as an example.
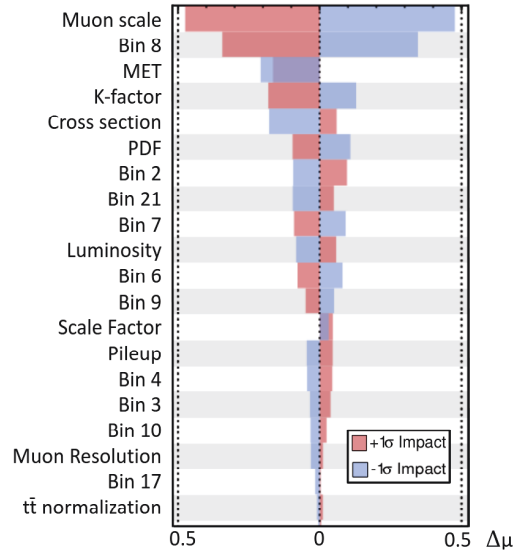
Figure 121: Variation at $+1\sigma$ (red) and -1σ (blue), of the signal strength for the 20 sources of uncertainty with highest impact.

The impact bars, $\Delta\mu$, represent the relative variation of the signal strength when a certain nuisance parameter shifts by one standard deviation. The sign of $\Delta\mu$ represents if the variation of the signal strength is correlated or anticorrelated with the variation in the nuisance parameter. The systematic uncertainty source with the highest impact is the one associated with the muon p_T scale. The sources labeled as "Bin i" correspond to the statistical uncertainties of the ith bin in the M_T distribution used as input.

Experimental context

In the framework of Heavy Vector Triplet (HVT) model [137] the W' decay to SM bosons is allowed. In this case the W' → WZ may come the dominant decay channel. The parameter $g_{W'}$ represents the typical strength of the new vector boson interaction, and, depending on this value it defines two kind of models. Model A ($0.65 \lesssim g_{W'} \lesssim 2$) is representative of a model of weakly coupled vector resonances in an extension of the SM gauge group where the HVT bosons have comparable decay branching ratios into SM fermions and vector bosons. Model B ($g_{W'}$ 3) is

representative of a composite model scenario where the HVT boson couplings to fermions are significantly reduced.

The search for heavy resonances in the HVT model has many possible decay channels. For example, the observed (expected) limits set in the semileptonic final state in which one vector boson decays leptonically while the other decays hadronically, by CMS, set limits at 95 % CL on the HVT W' boson mass of $M_{W'} > 2.3 \, (2.4)$ TeV for Model A, and $M_{W'} > 2.3 \, (2.6)$ TeV for Model B, with a luminosity of 36 fb^{-1} [171], and by ATLAS, of $M_{W'} > 3.9 \, (3.8)$ TeV for Model A, and $M_{W'} > 4.3 \, (4.0)$ TeV for Model B [172] with 139 fb^{-1} of integrated luminosity. And combining all the results from the different decay channels (to bosons and leptons), and all the final states (*qqqq, qqlν, qqbb, llqq*, etc.), CMS has set limits in the HVT W' mass to $M_{W'} > 5.0 \, (5.0)$ TeV for Model A, and $M_{W'} > 4.5 \, (4.2)$ TeV for Model B [173].

Prospects of W' boson search

At the time of this thesis work, LHC has provided the first two runs of collisions and it is upgrading during the Long Shutdown (LS2) period, in preparation for the next run: Run 3. After Run 3, during the LS3, it will be upgraded to the next generation of hadron collider: the High Luminosity LHC (HL–LHC) [174]. The HL–LHC program is planned until the year ~ 2040. Along this program there will be an increase in the collision energy until 14 TeV, and an increase in the instantaneous luminosity, with a consequently increase of integrated luminosity. With the Run 1 and Run 2 we have collected only the $\sim 5\,\%$ of the total integrated luminosity planned for the full LHC program: 3000 fb^{-1}.

With the increase in luminosity, the statistical uncertainties will be significantly reduced, and therefore, the sensitivity to rare processes such us the W' $\rightarrow \mu\nu$ presented in this work, will improve. With the upgrades of the detectors, the measurement of the collision products will improve and the systematic uncertainties will be reduced [175].

Taking into account all these changes, the exclusion limit in the W' mass is expected to reach 7.9 TeV [176], in muon and electron combined channels, with a total integrated luminosity of 3000 fb^{-1}, at a center of mass energy of 14 TeV. This W' mass limit prospect is ~ 2 TeV larger than the current limit.

6.1.6   Split–UED model

The analysis of data and the M_T distributions shown in Figure 112 are also interpreted in terms of the Split–UED model. This model (Section 1.2.2 and Section 5.1.3) assumes the existence of an additional spatial dimension and fermion fields. The model is parametrized by the radius of the extra dimension, *R*, and the bulk mass parameter of the fermion field in five dimensions, *μ*.

In this model SM particles have a corresponding Kaluza–Klein (KK) partner. For the mode *n* = 2, the KK partner of SM W boson, $W_{KK}^{(2)}$, decays to leptons

147

identically as the SSM W' boson. Figure 117-top left shows the $W_{KK}^{(2)}$ production cross section for $\mu = 0.05$ and 10 TeV. These cross sections, the M_T distributions of data, SM prediction, and SSM W' signal, that is kinematically identical to the $W_{KK}^{(2)}$, are used to set limits in the $W_{KK}^{(2)}$ mass. Lower limits on the $W_{KK}^{(2)}$ boson mass are translated into bounds on the Split–UED parameter space $(1/R, \mu)$ using Equations 1.24 and 1.25.

The Split–UED 95 % CL limits are displayed for the muon channel (top-left), electron channel (top-right), and the combination of electron and muon channels (bottom), for full Run 2 in Figure 122.
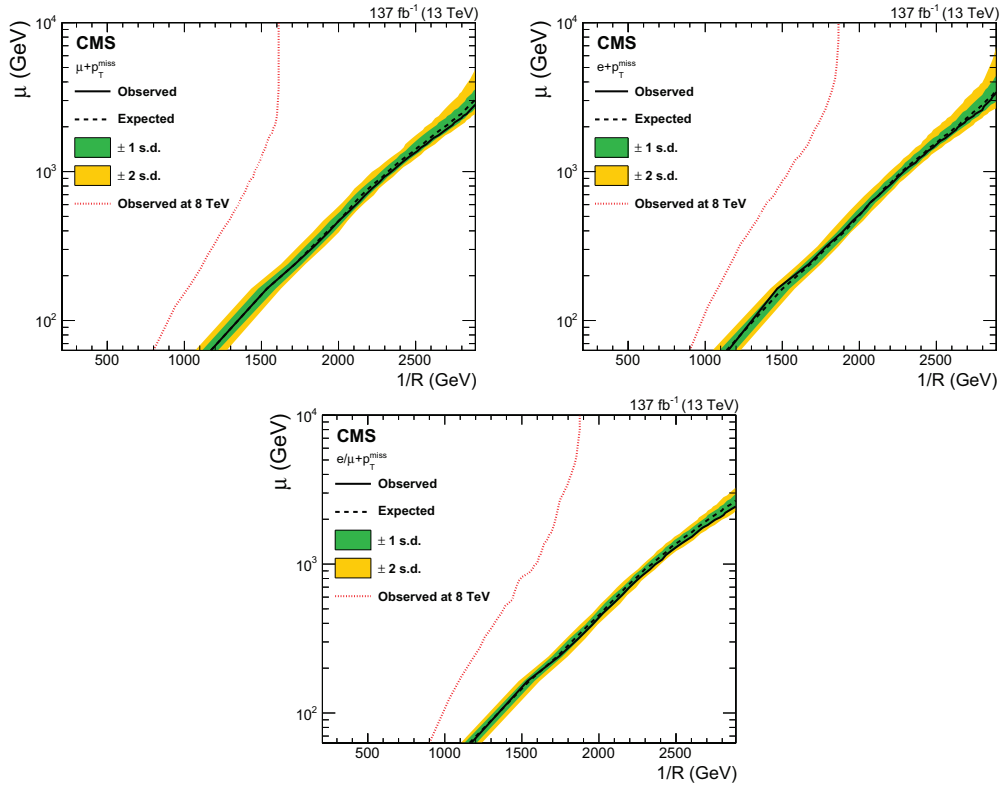
Figure 122: Expected and observed 95 % CL limits on the Split–UED parameter space $(1/R, \mu)$, in the muon channel (top-left), electron channel (top-right), and combining electron and muon channels (bottom), for full Run 2 data $(137\,\mathrm{fb}^{-1})$, along with the one- and two-sigma uncertainty bands on the expected limit. The area above the limit curve is excluded. For comparison, the previous result from Run 1 is shown as a red dotted line.

The observed (expected) lower limits on $1/R$ are 2.7 (2.7) TeV for muons, 2.7 (2.6) TeV for electrons, and 2.8 (2.7) TeV for the combination of the two channels at $\mu = 2$ TeV. For comparison, the previous Run 1 limit [25] is shown as a red, dotted line. It is appreciated how for the same $1/R$ value, i.e. 1.5 TeV, the limit in μ has decreased in ~ 0.7 TeV.

6.1.7 Stau in the RPV SUSY model

In a RPV SUSY model, the supersymmetric partner of the SM τ lepton is the scalar $\tilde{\tau}$, and decays to a charged lepton and a neutrino (details in Section 1.2.3). The decay of the stau $\tilde{\tau}$ to SM muon and neutrino has the same signature studied in this analysis, therefore, the model independent limit previously obtained (Figure 115) is applied to set limits in the mass of a $\tilde{\tau}$ in the RPV SUSY model.

The limit on the $\tilde{\tau}$ production cross section times the branching fraction is obtained by dividing the excluded cross section of the model independent limit by the fraction $f_{M_T}(M_T^{min})$, procedure explained in Section 6.1.3. The factor f_{M_T} is determined by counting the events with $M_T > M_T^{min}$, and dividing it by the number of $\tilde{\tau}$ generated events ($\tilde{\tau}$ signal generation explained in Section 5.1.4).

The RPV model is parametrized by the mass of the stau ($M_{\tilde{\tau}}$) mediator and its coupling to the muons and electrons, λ_{132} and λ_{231}, respectively. These two parameters provide the plane for the exclusion limit shown in Figure 123, for four values of the production coupling, λ'_{3ij}, for full Run 2 data.
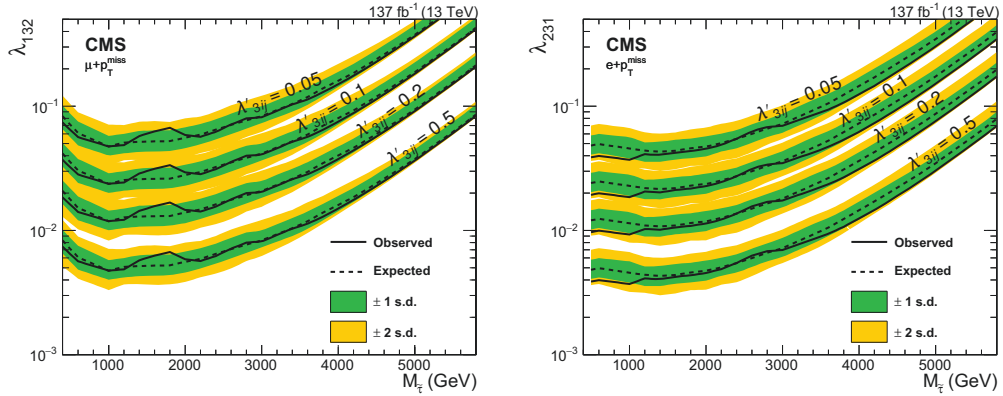
Figure 123: The observed (solid line) and expected (dashed line) upper limits at 95 % CL on the various couplings in the RPV SUSY model with a $\tilde{\tau}$ mediator, as a function of its mass, $M_{\tilde{\tau}}$. These are shown for the muon (left) and electron (right) channels. The couplings λ'_{3ij}, λ_{231}, and λ_{132} are defined in Section 1.2.3. The one (green) and two (yellow) standard deviation uncertainty bands for the expected limits are shown. The area above the limit curve is excluded.

Since the corresponding coupling for the $\tilde{\tau} \to \mu + \nu_e$ decay is λ_{132}, and for the $\tilde{\tau} \to e + \nu_\mu$ decay is λ_{231}, and they are not necessarily the same, the limits of each channel are not combined but presented separately instead. For $\lambda'_{3ij} = 0.5$, couplings values of λ_{132} 5×10^{-3} are excluded for $M_{\tilde{\tau}} \sim 1$ TeV.

RPV SUSY theories allow the slepton to be long–lived, and travel through the detector before decaying, leaving a displaced vertex from the collision point. Looking for this signature, CMS has set limits in the mass of the $\tilde{\tau}$ to be $M_{\tilde{\tau}} > 490$ GeV [177], and similarly the ATLAS experiment to $M_{\tilde{\tau}} > 430$ GeV [178], using Run 2 data.

6.2   *W* and *Y* oblique electroweak parameters

In previous sections we have assumed that the hypothetical new resonance is produced within the kinematic reach of the LHC, and the analyses presented have focused on a direct resonance search. In the current section the scenario is different, we assume that the new resonance is not accessible and lies beyond the experimental kinematic limit (see representation in Figure 74). Deviations from the SM predictions in the mass region between the SM W boson peak, and the hypothetical new resonance could, however, still be observed. By measuring the *W* and *Y* oblique electroweak parameters we are sensitive to such deviation.

With the final state of this analysis ($\mu + \mathrm{p_T^{miss}}$) (charged current) we measure the *W* oblique parameter, but we are not sensitive to the *Y* parameter. To determine the *Y* oblique parameter, the dimuon ($\mu^+ + \mu^-$) final state (neutral current), is also studied.

The statistical analysis is different from the one presented in Section 6.1.2. With the reweighting procedure explained in Section 1.2.4, the dilepton mass distribution ($\mathrm{M_T}$ for $+ \mathrm{p_T^{miss}}$ ($= \mu, e$), and invariant mass for dimuon final state) from the SM prediction is parametrized as a function of *W* and *Y* parameters. A binned maximum Likelihood fit is performed with MINUIT [179] comparing the experimental data to the parametrized prediction in *W* and *Y*, and obtaining the values that best reproduce the data, taking into account the nuisance parameters with a Log–Gaussian constraint.

6.2.1   Charged current, $l + p^{iss}$

The reweighing procedure for the charged current case is applied in the $\mu + \mathrm{p_T^{miss}}$ final state, to the predicted SM $\mathrm{M_T}$ distribution from the simulated samples of 2017 and 2018, after the analysis selection, and according to Equation 1.28. Figure 124 shows an example of the reweighting procedure. The $\mathrm{M_T}$ distribution is presented with no weight applied, $W = 0$ (top), and reweighted with large *W* oblique parameter values: $W = $ -0.001 (bottom - left), and $W = 0.001$ (bottom - right). The deviation affects mainly the tail and the middle $\mathrm{M_T}$ region of the distribution, while the low mass region is barely modified, as it was expected from the weight distribution presented in Figure 5.

The $\mathrm{M_T}$ distributions from Figure 124 also show the 2017 and 2018 data (black points) corresponding to $101 \, \mathrm{fb^{-1}}$, for comparison. The lower panels show the data to background prediction ratios. The gray bands reflect the systematic uncertainties. The selection criteria from Section 5.5 has been applied. The same process has been carried out in the electron channel.

With the background distribution as a function of the *W* oblique parameter, a negative Log–Likelihood function (–LogL) is defined, , assuming a Poisson distribution for the data, that considers appropriately the low statistics bins in the most signal significant region (the high $\mathrm{M_T}$ region) and Log–Gaussian constraints.
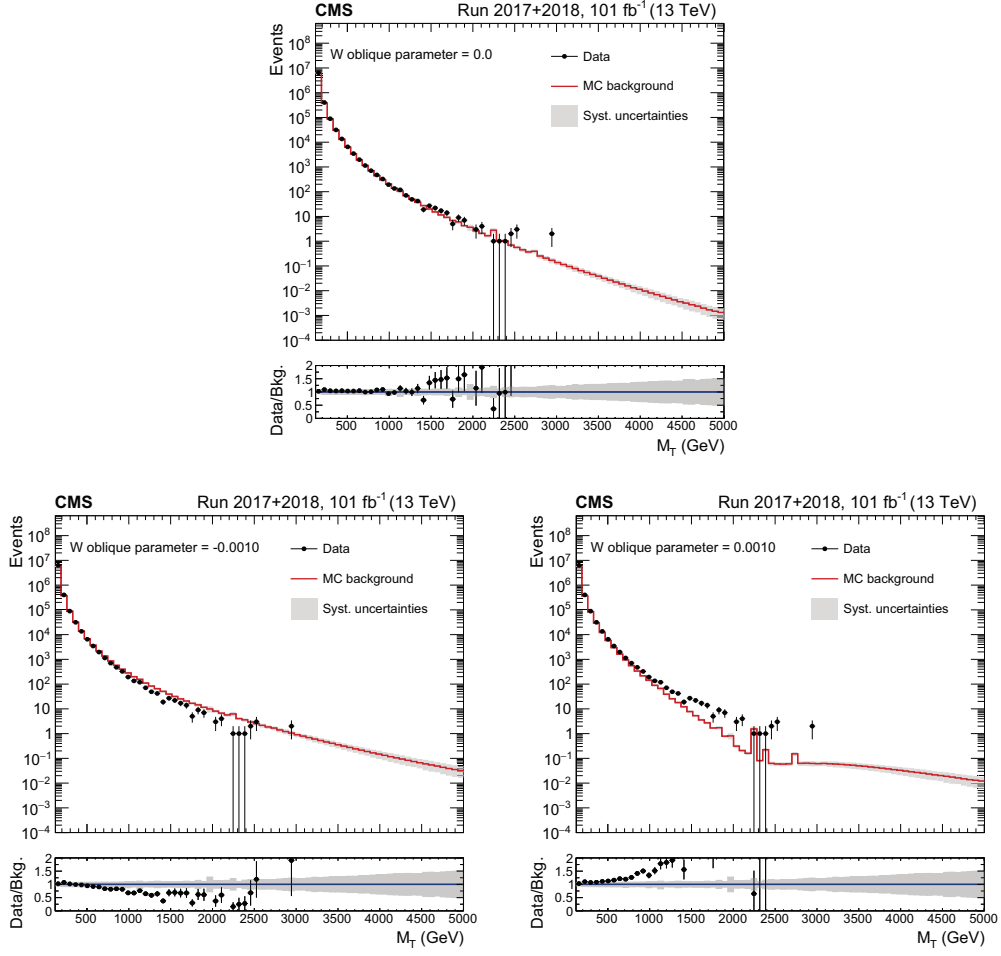
Figure 124: Distribution of M_T for the $\mu + p_T^{miss}$ final state, for 2017 and 2018 data and background, with $W = 0$ (top); and reweighted with large W oblique parameter values: -0.001 (bottom-left) and 0.001 (bottom-right).

A minimization of the –LogL function is performed with MINUIT to find the value of W that makes the background best reproduce the data.

To implement the systematic uncertainty (multiplicative factor σ) in the number of events, the parameter β is added via a Log–Gaussian constraint to the Likelihood function. Therefore, the expected number of events in a given bin i depends on both parameters W and β:

$$N_i(W, \beta) \equiv N_i(W) \cdot e^{\sigma_i \beta} \qquad (6.6)$$

and the corresponding –LogL function to be minimized as a function of parameters W and β, for number of observed events, n_i, is:

$$-\text{LogL}(W, \beta) \rightarrow \frac{\beta^2}{2} + \sum_{i=1}^{N} [N_i(W, \beta) - n_i \cdot \log[N_i(W, \beta)]] \qquad (6.7)$$

All the systematic uncertainties discussed in Section 5.6, are included as nuisance parameters, with a different β parameter for each uncorrelated source. The W parameter appears in the fit through the weight of each event in the SM W boson background sample.

As a test to validate the method and estimate the sensitivity, the study was first made using the SM prediction without the W parametrization instead of the data, the so–called, pseudodata. The –LogL post–fit function from the statistical analysis with pseudodata corresponding to 2017 luminosity, for the muon channel is shown in Figure 125 - left.
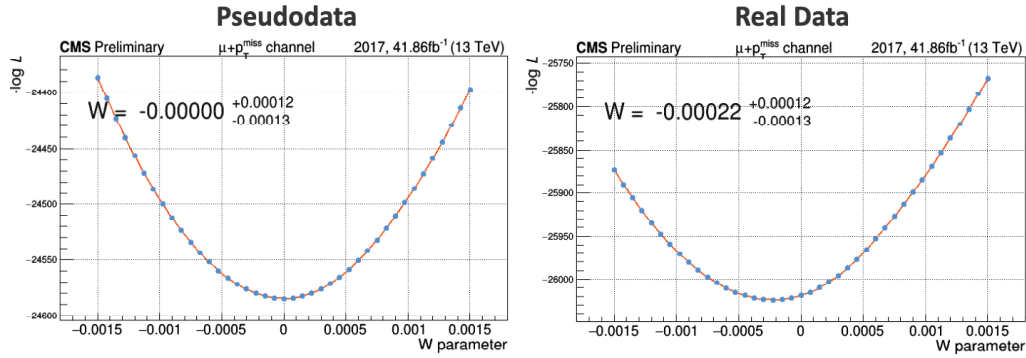
Figure 125: Scan of –Log–Likelihood function vs W oblique parameter for the muon channel, for pseudodata (left) scaled to 2017 luminosity, and for real 2017 data (right). The uncertainties quoted correspond to $\pm 1\sigma$ and include statistical and systematic components.

The result from the pseudodata test is quoted in Figure 125 - left at 68 % CL: $W = [0.0 \, ^{+1.2}_{-1.3}] \cdot 10^{-4}$, recovering the SM value ($W = 0$) and giving the sensitivity for one channel and one year of data: $\sim 1.2 \cdot 10^{-4}$ at 68 % CL.

Since the method is validated we now apply the same procedure using 2017 data instead of pseudodata and the scan of the –LogL function is shown in Figure 125 - right as a function of the W oblique parameter, and in Figure 126 - left as a function of the β parameter, where only one β parameter is considered for the total of all the systematic uncertainties as first approach, while for the final result each uncorrelated uncertainty is fitted with its corresponding nuisance parameter. The fitted values are $W = [-2.2 \, ^{+1.2}_{-1.3}] \cdot 10^{-4}$ and $\beta = [0.17 \, ^{+0.30}_{-0.31}]$, at 68 % CL. Figure 126 - right shows the 68 and 95 % CL contours of the fitted parameters in the W vs β plane.

The –Log–L distributions for each decay channel (muon and electron) and the combination are shown in Figure 127, for 2017 and 2018 data and MC simulation. And the fitted values are presented in Table 6.2.

We assume that only the SM W $\rightarrow$ ν process, the main contributing background, is modified by new physics at high energy scales, disregarding any potential effect on the Z $\rightarrow$ process. The contribution of this process is around 4 % of the selected $\mu + \mathrm{p_T^{miss}}$ events, while the SM W boson is the 86 % (see Table 5.7). In addi-
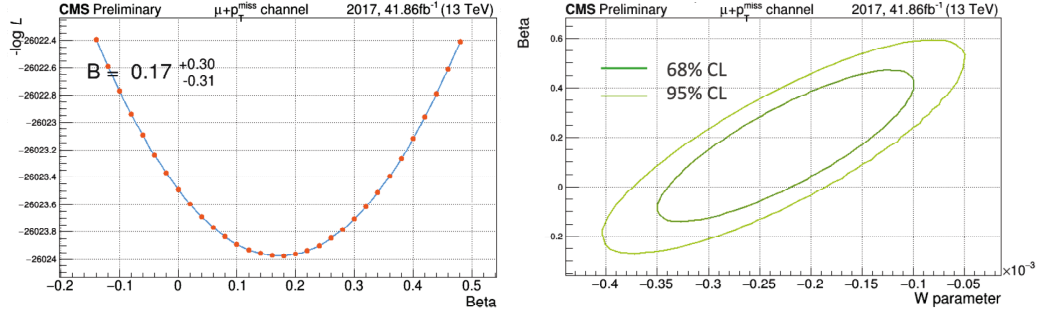
Figure 126: Scan of –Log–Likelihood function for 2017 data in the muon channel, as a function of β parameter (left), and contour β vs W oblique parameter at 68 % and 95 % CL (right).
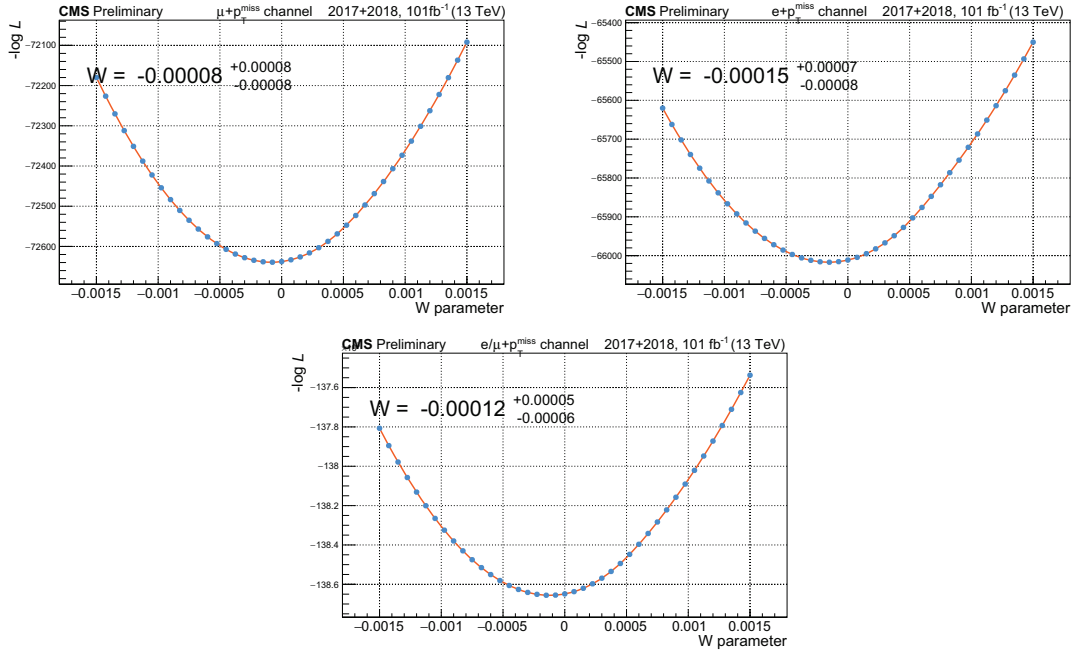
Figure 127: Scan of –Log–Likelihood function vs W oblique parameter for the muon channel (top-left), and the electron channel (top-right), and the combination of both channels (bottom), for 2017 and 2018 data ($101\,\text{fb}^{-1}$) and MC simulation. The values of W oblique parameter that minimize the –Log–Likelihood functions are labeled. The uncertainties quoted correspond to $\pm 1\sigma$ and include statistical and systematic components.

	W oblique parameter (95 % CL)
μ channel	$[-0.8\ ^{+1.6}_{-1.6}] \cdot 10^{-4}$
e channel	$[-1.5\ ^{+1.5}_{-1.6}] \cdot 10^{-4}$
$e + \mu$ channel	$[-1.2\ ^{+1.2}_{-1.2}] \cdot 10^{-4}$

Table 6.2: Fit values of W oblique parameter for each decay channel and the combination of both, for 2017 and 2018 data ($101\,\text{fb}^{-1}$). The uncertainties correspond to statistical and systematic components at 95 % CL.

tion, according to Ref. [48], the sensitivity of Z boson processes to the W parameter is much smaller than the one of W boson processes, for similar integrated luminosity and $\sqrt{s}$ values. The effect on the W oblique parameter determination from the Z→ process is estimated at the level of 1% and considered negligible in these results.

The combination of 2017 and 2018 years of Run 2 data, for both final state channels (electron and muon), yields a fitted value $W = [-1.2 \, ^{+1.2}_{-1.2}] \cdot 10^{-4}$, at 95% CL considering statistical and systematic uncertainties. The measured W oblique parameter is at 2σ from the SM prediction ($W = 0$). The measurement in the W oblique parameter from the $+ \mathrm{p}_{\mathrm{T}}^{\mathrm{miss}}$ ($= \mu, e$) analysis is shown in the Y vs W plane in Figure 128, where the coloured bands correspond to 68% and 95% CL uncertainties.
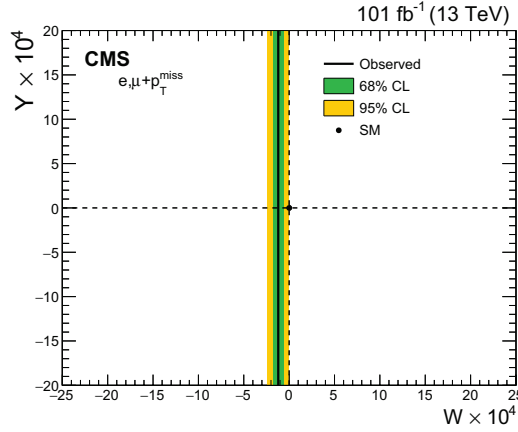
Figure 128: Measurement of the W oblique electroweak parameter (black line) from $+ \mathrm{p}_{\mathrm{T}}^{\mathrm{miss}}$ ($= \mu, e$) analysis, together with the 68% CL and 95% CL uncertainty bands shown in green and yellow respectively. The 2017 and 2018 datasets obtained at Run 2 are used with a corresponding luminosity of $101\,\mathrm{fb}^{-1}$.

6.2.2 Neutral current, $\mu^+ + \mu^-$

Using the dimuon selection (same one as that used for the $\mathrm{p_T}$ scale GE method, explained in Section 4.2.1) and following the same technique as in the previous subsection, with the reweighting procedure for neutral current case presented in Equation 1.36, we are sensitive to both W and Y oblique electroweak parameters. The input distribution for this analysis is the dimuon invariant mass shown in Figure 129, for 2017 and 2018 data and SM prediction from MC simulated samples.

Figure 130 shows an example of the reweighting procedure for the 2017 data and MC prediction. The $\mathrm{M_T}$ distribution is presented with no weight applied, $W = Y = 0$ (top); reweighted with large W oblique parameter values: $W = $-0.004 (middle-left), and $W = 0.004$ (middle-right), while fixing $Y = 0$; and reweighted with large Y oblique parameter values: $Y = $-0.004 (bottom-left), and $Y = 0.004$ (bottom-right), while fixing $W = 0$.
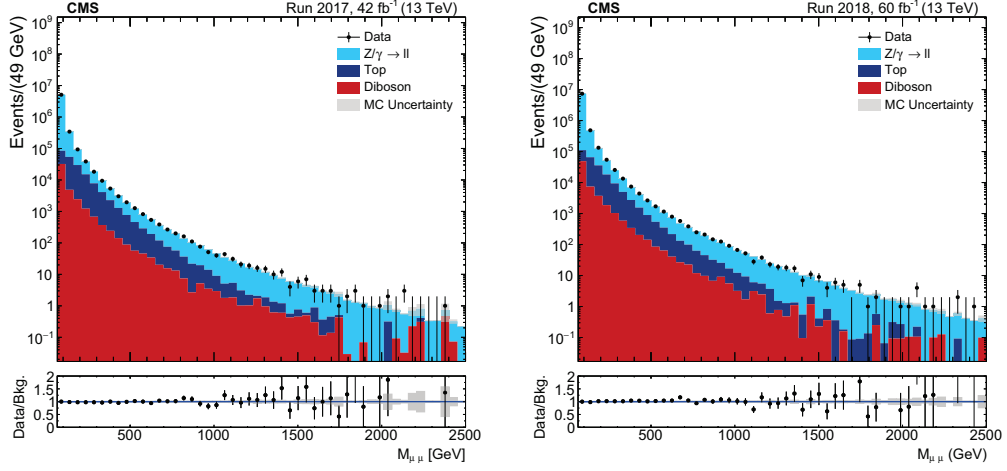
Figure 129: Invariant dimuon mass distribution of 2017 (left) and 2018 (right) data and SM background for the dimuon selection. Statistical uncertainties in the simulated samples are shown as a gray band.

With the background distribution as a function of both, the W and Y oblique parameters, a –Log–Likelihood minimization is performed to find the value of the parameters that makes the background best reproduce the data. As a test to validate the method, the study was first made using the SM prediction without the W and Y parametrization instead of the data, the so–called, pseudodata. The result from the statistical analysis with pseudodata corresponding to 2017 and 2018 luminosity ($101\,\mathrm{fb}^{-1}$), taking into account only statistical uncertainty, is $W = [0.0\ ^{+11.1}_{-10.0}] \cdot 10^{-4}$ and $Y = [0.0\ ^{+13.2}_{-8.9}] \cdot 10^{-4}$, at 95 % CL. Since the SM values ($W = Y = 0$) are recovered, the method is validated. The uncertainty on the W parameter ($\sim 11 \cdot 10^{-4}$) for a luminosity of $101\,\mathrm{fb}^{-1}$, and one decay channel, is larger than in the charged current case ($\sim 1.6 \cdot 10^{-4}$), where we were more sensitive to the W oblique parameter, but we had no sensitivity to the Y parameter. The result from the pseudodata test is shown in Figure 131.

Both, statistical and systematic uncertainties are taken into account for the analysis with real data. The systematic uncertainty estimation is taken from Ref. [167] and is included as a nuisance parameter in the fit with Log–Gaussian constraints. The combination of 2017 and 2018 years of Run 2 data yields a fitted value of $W = [-6.0\ ^{+19.6}_{-5.1}] \cdot 10^{-4}$ and $Y = [5.6\ ^{+7.5}_{-14.2}] \cdot 10^{-4}$, at 95 % CL, considering statistical and systematic uncertainties. The measurement of the W and Y oblique parameters from the dimuon analysis is shown in the Y vs W plane in Figure 132.

The measurement of the W oblique parameter coming from the channel $\ell + \mathrm{p}_\mathrm{T}^\mathrm{miss}$ ($\ell = \mu, e$) (black line), together with the measurement of W and Y oblique parameters from the dimuon analysis (violet) is presented in Figure 133. Previous W and Y oblique parameters estimations derived from results obtained by LEP experiments [48, 49] are shown (gray ellipsis) for comparison. The sensitivity is improved

155
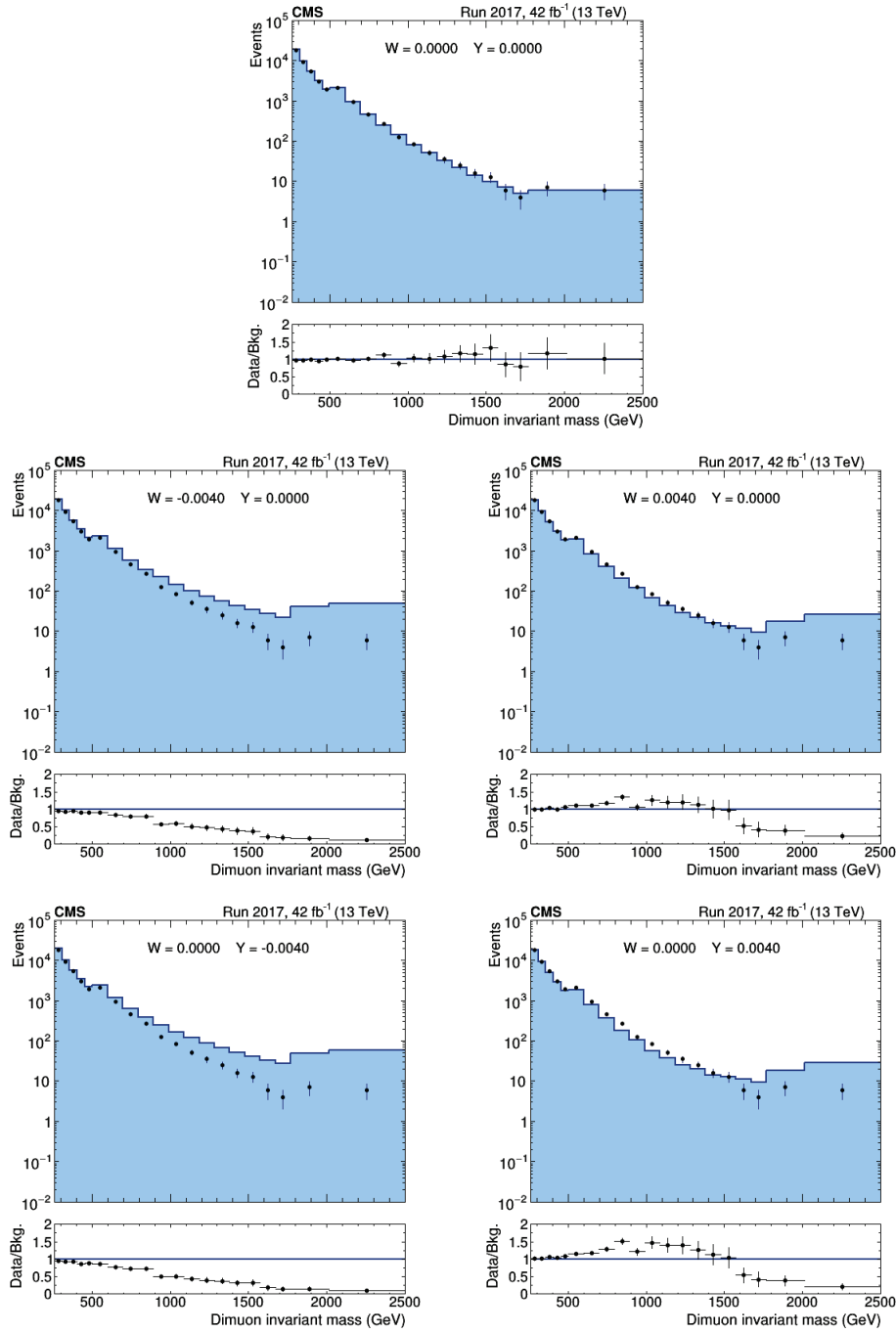
Figure 130: Invariant dimuon mass distribution of 2017, with no weight applied, ($W = 0$, $Y = 0$) (top); reweighted with large W oblique parameter values, ($W = -0.004$, $Y = 0$) (middle-left), and ($W = 0.004$, $Y = 0$) (middle-right); and reweighted with large Y oblique parameter values, ($W = 0$, $Y = -0.004$) (bottom-left), and ($W = 0$, $Y = 0.004$) (bottom-right).
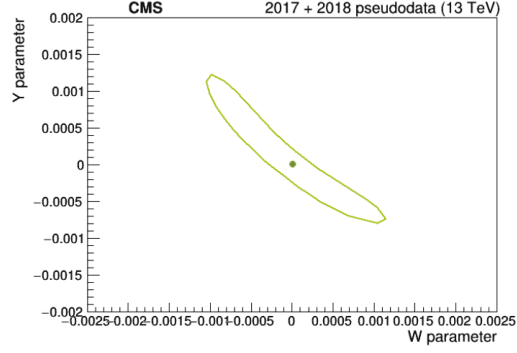
Figure 131: Oblique electroweak parameters, W vs Y, measured in the dimuon final state, at 95 % CL for pseudodata scaled to 2017 and 2018 luminosity $(101\,\text{fb}^{-1})$. Only statistical uncertainty is considered.
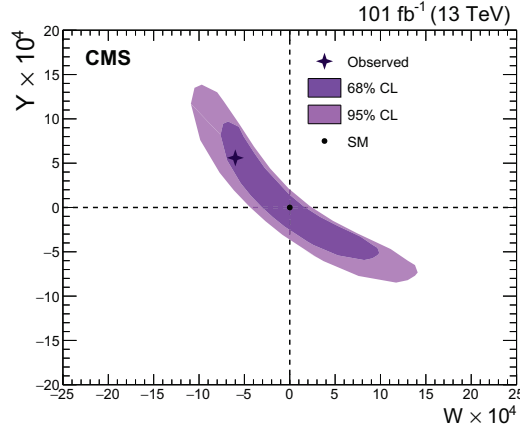
Figure 132: Measurement of the W and Y oblique electroweak parameters (cross) from the dimuon final state, together with the 68 % CL and 95 % CL uncertainty regions in dark violet and light violet, respectively, including statistical and systematic uncertainties. The 2017 and 2018 datasets obtained at Run 2 are used, with a corresponding luminosity of $101\,\text{fb}^{-1}$.

by a factor of ~ 1.5 in the Y oblique parameter, and by one order of magnitude in the W oblique parameter. The results from this work are the most precise up to date, and the first measurements of W and Y oblique parameters with LHC data.
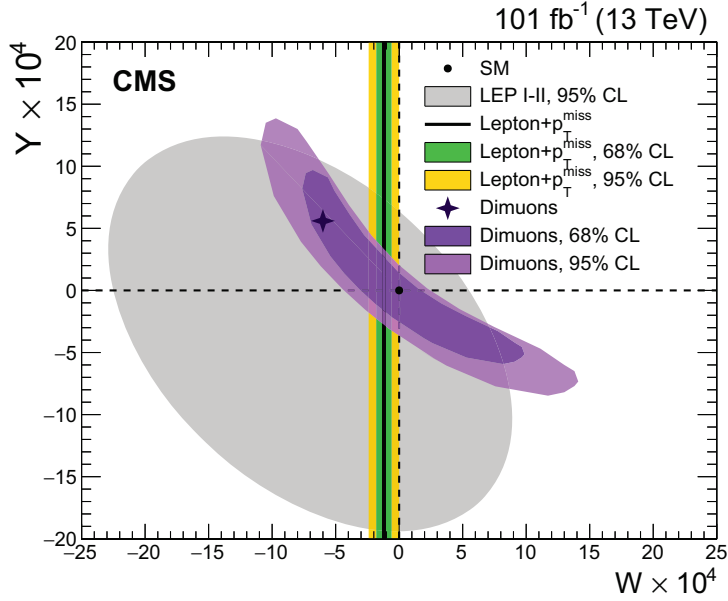
Figure 133: Measurement of the *W* oblique electroweak parameter (black line) from $\ell + p_T^{miss}$ ($\ell = \mu, e$) analysis, together with the 68 % CL and 95 % CL uncertainty bands shown in green and yellow, respectively. Measurement of the *W* and *Y* oblique electroweak parameters (cross) from the dimuon final state, together with the 68 % CL and 95 % CL uncertainty regions shown in dark violet and light violet, respectively. The 2017 and 2018 datasets obtained at Run 2 are used with a corresponding luminosity of $101\,fb^{-1}$. Previous estimation derived from results obtained by LEP experiments [48, 49] is shown as the gray ellipse.

6.3   Higgs Compositeness

Some of the results of the search in the $\mu + p_T^{miss}$ final state presented so far are used to set constraints on the Higgs compositeness sector, in particular on the $g_* - m_*$ plane, the coupling and mass scale for compositeness. As explained in Section 1.2.5, two different inputs are used to extract information about the potential new composite sector.

Indirect search

The measurement of the oblique *W* parameter provides already some information on constraints for the new physics scale. This is a first input to limit the $g_* - m_*$ plane. Equation 1.39 and the 95 % CL limit on *W* obtained in the previous subsection from the combination of the electron and muon channels, using 2017 and 2018 data, numerically implies $g_* < (4770\,GeV)\,/\,m_*$. Figure 134 presents the region in the $g_* - m_*$ plane excluded by these results at 95 % CL. This method is sensitive to the region of interference between the existing SM W boson and the new hypothetical resonance, out of the kinematic reach.
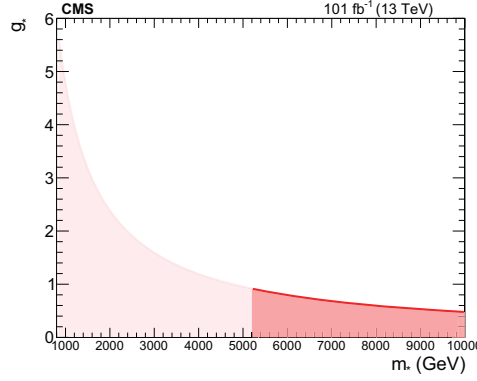
Figure 134: Excluded region in the g_* - m_* plane, using the *W* oblique electroweak parameter measurement at $95\,\%$ CL limit using the 2017 and 2018 datasets, for the electron and muon channel combination.

Direct search

The second input comes from the direct search for the W' resonance. Direct search for the W' resonance, in particular by making use of the constraints placed on its coupling strength, $g_{W'}$. In this case we consider two scenarios depending on the W' potential decay channels: SSM and HVT models.

  – SSM scenario: the model where the SSM W' boson only couples to fermions, as presented in Section 1.2.1. Using the combined coupling strength limit relative to the SM one, $g_{W'}/g_W$, for the muon and electron channel, for the complete Run 2 dataset from Figure 119, as input in Equation 1.40, limits are set in the g_* - m_* plane.

  Figure 135 - left presents the region in the g_* - m_* plane excluded with this method, which is kinematically limited by $\sqrt{s}$.
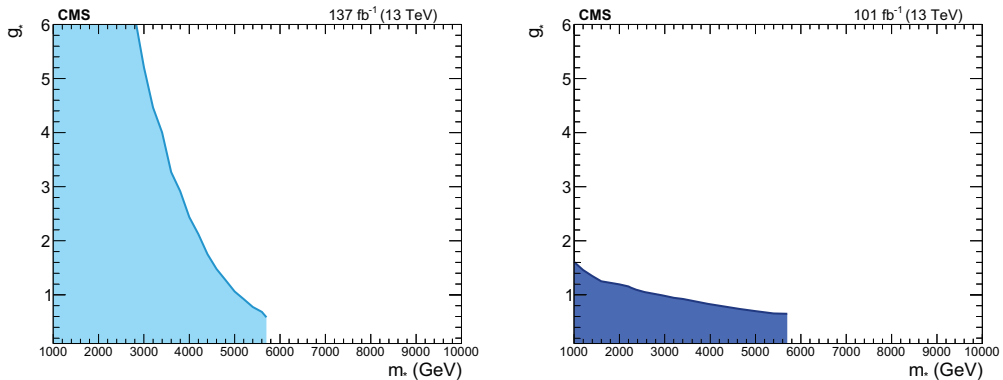
Figure 135: Excluded region in the g_* - m_* plane, using the relative W' coupling strength limit in the SSM model (left) and in the HVT model (right), using Run 2 dataset, for the electron and muon channel combination.

- HVT scenario: in a more general scope, and assuming that the new resonance couples to both, fermions and bosons, (HVT model [137]), the reweighting procedure, presented in Section 5.1, to the SSM signals has been applied.

The effect of the reweight to the HVT model for different coupling ratios was showed in Figure 80 for two samples of W' mass, $M_{W'} = 1000$ GeV (left), and 5000 GeV (right). For lower values of $g_{W'}/g_W$ the width increases, and the cross section is reduced. Therefore, the sensitivities to such signals are lower, and the limits are weaker.

When performing the analysis in the $\mu + p_T^{miss}$ decay channel, the exclusion for HVT W' is placed on the $g_* - m_*$ plane, shown in Figure 135 - right, carried out with datasets from 2017 and 2018, combining the muon and electron channels. Some of the samples for 2016 datasets were not accessible for this study.

As a third input, and an independent source from this work, there is the current CMS constraints on Higgs cross sections measurements [52]. Using the cross section value measured by CMS for the production of the Higgs boson, in a combination of decay channels, relative to the one predicted by the SM, signal strength μ, and taking into account its uncertainties, CMS obtains $\Delta\mu < 0.14$ at 95 % CL [52].

Equation 1.42 numerically implies $g_* < (1820 \text{ GeV}^{-1}) \times m_*$. Figure 136 shows the excluded region coming from the Higgs cross section constraint, together with the regions already presented. All in all, a composite Higgs is excluded for masses $m_* < 1000$ GeV if the HVT model is considered in the direct search, or $m_* < 3000$ GeV in the SSM model context.
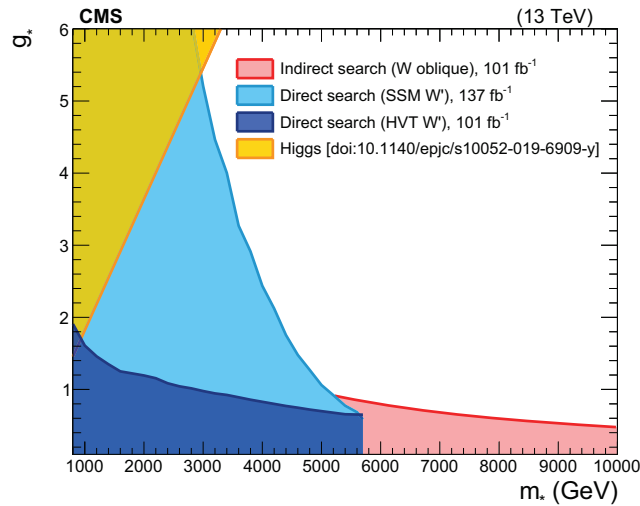
Figure 136: Regions in the $g_* - m_*$ plane excluded by the different methods: derived from *W* oblique electroweak measurement (red), from the current W' search in the SSM model (light blue), from the W' in the HVT model (dark blue), and those from the constraints on the Higgs boson cross section [52] (yellow).

Conclusions

Our goal as particle physicists is to understand which are the elementary components of matter and their behaviour. The powerful and beautiful theory of the Standard Model (SM) is able to describe with a high precision the elementary particles and their interactions. All the experimental results confirm its power of prediction and make the SM the most successful theory up to date. However, it does not explain all the observed phenomena of the Universe. With the aim of completing the Standard Model to accommodate the open questions, the big effort to find *Beyond Standard Model* (BMS) processes has started.

The particle physics community has explored up to unprecedented energy scales without finding clear deviations from the SM. Therefore, we can suspect that the *new physics* are hidden above the energy limit that we were able to study with the existing accelerators and available cosmic particles.

The world's most powerful particle accelerator, the Large Hadron Collider (LHC), is the exclusive place to explore the highest available laboratory energies with the largest collection of data. In fact, up to now, we have only collected a $\sim 5\%$ of the total integrated luminosity foreseen by the end of the LHC scientific program. This will enable us to carry out very precise measurements with the possibility of amplifying deviations from the SM, nowadays insignificant.

Muons leave a clean signature in the CMS detector at LHC, and $\mu + p_T^{miss}$ is an interesting channel open to many BSM interpretations. A search for deviation from the SM in events with a final state consisting of a muon and missing transverse momentum in proton–proton collisions at a center of mass energy of 13 TeV has been presented. This search used the complete data collected by the CMS detector between 2016 and 2018 years, with a corresponding integrated luminosity of $137 \, \mathrm{fb}^{-1}$.

This thesis work has presented two main fields of work. First, the studies of the reconstruction of muons, in particular the most energetic ones, in Chapters 3 and 4, and second, the Physics search using the reconstructed muons as main ingredient, in Chapters 5 and 6.

To ensure that the muon data has a good quality, I have followed it throughout the complete chain: from the data taking as muon detector shifter, to the reconstruction and validation of the muons, until the Physics interpretation. In particular, the high momentum muons, have special characteristics that demand the develop-

ment of innovative techniques for their proper reconstruction. The result in the muon momentum scale, is a bias compatible with zero within uncertainties, except at the forward endcaps for muons with $p_T > 2$ TeV, where the bias is -0.47 ± 0.12 (-0.13 ± 0.04), implying a maximum p_T shift of $10\,(5)\,\%$ in $2017\,(2018)$ data. The muon momentum resolution has been measured to be $0.4\,\%$ at $p_T \sim 100$ GeV, increasing until $20\,\%$ at p_T 1.5 TeV, in simulation. The value obtained on the ratio of charge misreconstruction for muons with $p_T \sim 1$ TeV is around $\sim 0.03\,\%$, in simulation. The results from these studies have demonstrated the excellent performance of the CMS detector at muon reconstruction, and they have been not only useful for our work, moreover they have been given as recommendations for other analysis using high p_T muons for the CMS Collaboration.

The analysis strategy followed using this experimental dataset has been to look for deviations from deviations from the SM prediction. The discriminant variable is the reconstructed transverse mass between the muon and the missing energy. No significant deviation from the SM has been observed when examining the transverse mass distributions. Therefore, these observations are interpreted as $95\,\%$ confidence limits on the parameters of several models, and when possible, combining the limit with the electron channel.

First of all, limits are provided in the cross section and branching fraction of the production of any process with the explored final state, without taking into account the shape of any possible resonance. These are model independent limits. This furnishes the tools to set limits in any other model with the same final state. We find that the cross section times branching fraction of production of a resonance that decays into lepton (muon or electron) and neutrino is below 1 fb for a resonance mass of 1 TeV, and 0.02 fb for a resonance mass of 3 TeV at $95\,\%$ CL.

The benchmark model for which the analysis was designed is the Sequential Standard Model (SSM). This model predicts the existence of the W' boson, a heavy analog of the SM W boson with equal couplings. The observed limit combining electron and muon channels, in the W' mass is $M_{W'} > 5.7$ TeV at $95\,\%$ CL. The variations in the coupling strength were also examined. Couplings above 10^{-2} are excluded at $95\,\%$ CL for low W' masses, $M_{W'} \approx 0.5$ TeV.

The split Universal Extra Dimension (Split–UED) model predicts the existence of a Kaluza–Klein partner of the W boson: the $W_{KK}^{(2)}$, with an identical decay than the SSM W' boson. We set limits on the radius of the extra dimension, R, and the bulk mass of the fermion field, μ. We constrained $1/R$ to 2.8 TeV for $\mu > 2$ TeV at $95\,\%$ CL, combining muon and electron channels.

The last resonance search presented is the context of the R–Parity violation SUSY model, that predicts a tau slepton, $\tilde{\tau}$, as mediator. Limits on the coupling strength at the decay vertex, λ'_{132}, have been derived as a function of the $\tilde{\tau}$ mass, for various values of the coupling at the production vertex λ'_{3ij}. For a λ'_{3ij} of 0.5, and a $\tilde{\tau}$ mass, $M_{\tilde{\tau}} > 1.6$ TeV, λ_{132} is excluded above 0.005 at $95\,\%$ CL.

162

After the direct resonance search, we can assume that the new resonance is above the experimental kinematic limit. The study of possible deviations from the SM predictions in the tail of the mass distribution is sensitive to the oblique electroweak W and Y parameters. From the lepton (muon and electron) and p_T^{miss} analysis, we have obtained $W = [-1.2^{+1.2}_{-1.2}] \cdot 10^{-4}$ at $95\,\%$ CL. Since this channel is not sensitive to the Y parameter, a dimuon analysis has been carried out, giving the following results: $W = [-6.0^{+19.6}_{-5.1}] \cdot 10^{-4}$, and $Y = [5.6^{+7.5}_{-14.2}] \cdot 10^{-4}$ at $95\,\%$ CL.

The final result presented refers to the composite Higgs scenario. If the Higgs boson is not an elementary particle but formed by other elementary particles instead, we could expect discrepancies with respect to the SM predictions. This effect depends on the energy scale of the potential new composite scenario. If this energy is accessible in the experimental setup, the resonance coupling would be affected. However, if the energy is above the kinematic limit, it could create a deviation in the tail of the mass distribution. As a reinterpretation of the coupling limit and the W oblique parameter measurement, regions in the $g_* - m_*$ plane of Higgs composite model are excluded. We set a lower limit of $3\,(1)$ TeV for the mass scale of the Higgs Composite scenario, m_*, assuming the SSM (HVT) model for a W' resonant production.

Table 6.3 summarizes all the limits on the search for BSM processes in the muon and missing energy final state with Run 2 data recorded by the CMS experiment.

Model	Parameter	Channel	Observed (Expected) limit
SSM	$M_{W'}$	$e + p_T^{miss}$	$M_{W'} < 5.4\ (< 5.3)$ TeV
		$\mu + p_T^{miss}$	$M_{W'} < 5.6\ (< 5.5)$ TeV
		$e/\mu + p_T^{miss}$	$M_{W'} < 5.7\ (< 5.6)$ TeV
SSM $g_{W'}/g_W \neq 1$	$g_{W'}/g_W$ ($M_{W'} = 1$ TeV)	$e + p_T^{miss}$	$g_{W'}/g_W \geq 1.6\ (\geq 2) \times 10^{-2}$
		$\mu + p_T^{miss}$	$g_{W'}/g_W \geq 1.6\ (\geq 2) \times 10^{-2}$
Split–UED	$1/R$ ($\mu = 2$ TeV)	$e + p_T^{miss}$	$1/R \leq 2.7\ (\leq 2.6)$ TeV
		$\mu + p_T^{miss}$	$1/R \leq 2.7\ (\leq 2.7)$ TeV
		$e/\mu + p_T^{miss}$	$1/R \leq 2.8\ (\leq 2.7)$ TeV
RPV SUSY	$\lambda_{231}, \lambda_{132}$ ($\lambda'_{3ij} = 0.5$, $M_{\tilde{\tau}} = 1$ TeV)	$e + p_T^{miss}$	$\lambda_{231} \geq 5\ (\geq 5) \times 10^{-3}$
		$\mu + p_T^{miss}$	$\lambda_{132} \geq 5\ (\geq 5) \times 10^{-3}$
EFT	W, Y oblique	$e/\mu + p_T^{miss}$	$W = -1.2 \times 10^{-4}$
		$\mu + \mu$	$W = -6.0 \times 10^{-4}$
		$\mu + \mu$	$Y = 5.6 \times 10^{-4}$
Composite Higgs	m_*	$e/\mu + p_T^{miss}$	$m_* \geq 3.0$ TeV

Table 6.3: Summary of all exclusion limit results with various theoretical model interpretations in the electron and muon channels, and the combination of both channels.

This manuscript summarizes my doctoral research carried out at Centro de Investigaciones Energéticas Medioambientales y Tecnológicas (CIEMAT), in Madrid, Spain, as a member of the CMS Collaboration. This work was financially supported by the Formación de Personal Investigador (FPI) contract, granted by the Ministerio de Ciencia e Innovación of the Spanish Government.

This thesis is the result of four years of intense research where I had the chance to learn from experts on the field, and to contribute with my knowledge and ideas. The result is a small, although significant, step ahead in the frame of the huge humankind effort to understand Nature.

Irene Bachiller Perea

Conclusiones

El objetivo de la física de particulas es entender cuáles son los componentes elementales de la materia y cómo interaccionan. La teoría del Modelo Estándar (ME) es capaz de describir con muy buena precisión las partículas elementales y sus interacciones. Todos los resultados experimentales confirman su poder de predicción y hacen del ME la teoría con más éxito hasta la fecha. Sin embargo, no explica todos los fenómenos observados en el universo. Con el fin de completar el ME para acomodar las preguntas pendientes, se está llevando a cabo un gran esfuerzo para encontrar procesos *más allá del Modelo Estándar*.

La comunidad de física de partículas ha explorado hasta una cierta escala de energías sin encontrar desviaciones claras del ME. Por lo tanto, podemos sospechar que los nuevos procesos físicos están ocultos por encima del límite de energía que hemos podido estudiar con los aceleradores existentes y las astropartículas. Para seguir explorando, se ha construido el acelerador de partículas más potente del mundo: el LHC. El LHC es la herramienta ideal para explorar las altas energías y recopilar suficiente estadística para un posible descubrimiento.

Los muones dejan una señal muy clara en el detector CMS del LHC, y el canal muon + momento faltante es un canal especialmente interesante, abierto a muchas interpretaciones más allá del ME. Se ha presentado una búsqueda de desviaciones del ME en eventos con un estado final de un muon y un momento transverso faltante en las colisiones protón–protón con una energía de centro de masas de 13 TeV. En esta búsqueda se han utilizado los datos recogidos por el detector CMS entre los años 2016 y 2018, con una luminosidad integrada de $137\,\mathrm{fb}^{-1}$.

Este trabajo de tesis ha presentado dos campos de trabajo principales. Primero, los estudios de reconstrucción de muones, en particular de muones energéticos, en los capítulos 3 y 4, y segundo, el análisis y la interpretación física utilizando los muones reconstruidos como ingrediente principal, en los capítulos 5 y 6.

Para verificar de que los datos de muones tienen buena calidad, los he seguido a lo largo de toda la cadena: desde la toma de datos con los detectores de muones, pasando por la reconstrucción y validación de los muones y sus variables, hasta la interpretación física. En particular, los muones de alto momento, tienen características especiales que exigen el desarrollo de técnicas innovadoras para su adecuada reconstrucción. El resultado en la escala de momento es un sesgo compatible con

cero dentro de las incertidumbres, excepto en las zonas de alta η para los muones con $p_T > 2$ TeV, donde el sesgo en la escala es $-0{,}47 \pm 0{,}12\,(-0{,}13 \pm 0{,}04)$, lo que implica un desplazamiento máximo de $10\,(5)\,\%$ en la medida del p_T del muon en datos de 2017 (2018). Se ha medido que la resolución del momento del muon es del $0{,}4\,\%$ a $p_T \sim 100$ GeV, aumentando hasta el 20% para $p_T \quad 1{,}5$ TeV, en simulación. El valor obtenido en simulación para el cociente de confusión de carga para los muones con $p_T \sim 1$ TeV es de $\sim 0{,}03\%$. Los resultados de estos estudios han demostrado el excelente funcionamiento del detector CMS en la reconstrucción de muones, y no sólo se han utilizado en su para nuestro trabajo, además se han dado como recomendaciones para los análisis con muones de la Colaboración CMS.

La estrategia de análisis ha sido la búsqueda en este conjunto de datos experimentales posibles desviaciones de las predicciones del ME. La variable discriminante es la masa transversa reconstruida del muon y el momento faltante. No se ha observado una desviación significativa del ME al examinar la distribución de masa transversa, por lo que estas observaciones se interpretan como límites de confianza del 95 % en los parámetros de varios modelos y, cuando es posible, combinando el límite con el canal de electrones.

En primer lugar, se proporcionan límites en la sección eficaz de producción de cualquier proceso con el estado final explorado, independientemente de la forma de la posible resonancia. Esto proporciona las herramientas para establecer límites en cualquier modelo con el mismo estado final. Encontramos que la sección eficaz multiplicada por la proporción del canal leptónico para la producción de una resonancia es inferior a 1 fb para una masa de resonancia de 1 TeV y 0.02 fb para una resonancia de masa 3 TeV.

El modelo de referencia para el que se diseñó el análisis es el modelo estándar secuencial (SSM). Este modelo predice la existencia del bosón W', un análogo pesado del bosón W del ME, con los mismos acoplos. El límite observado en la masa del W', que combina los canales de electrones y muones, es $M_{W'} > 5{,}7$ TeV al 95 % NC. También se han estudiado variaciones en la constante de acoplamiento. Los acoplamientos por encima de 10^{-2} están excluidos al 95 % NC para masas de W', $M_{W'} \sim 0{,}5$ TeV.

El modelo Split–UED predice la existencia de una dimensión espacial extra, y un bosón de Kaluza–Klein asociado al bosón W del ME: el $W_{KK}^{(2)}$, con una desintegración idéntica al del bosón W' del SSM. Establecemos límites al 95 % NC en el radio de la dimensión extra, R, y la masa aparente del campo de fermiones, μ. Restringimos $1/R$ a 2.8 TeV para $\mu > 2$ TeV, combinando los canales de muones y electrones.

La última búsqueda de resonancia presentada es en el contexto del modelo de SUSY con violación de paridad, que predice la existencia de un lepton supersimétrico, $\tilde{\tau}$, como mediador. El límite de la constante de acoplamiento en el vértice de desintegración, λ'_{132}, se ha calculado en función de la masa del $\tilde{\tau}$ para varios valores del acoplamiento en el vértice de producción λ'_{3ij}. Para un λ'_{3ij} de 0,5 y una

masa del $\tilde{\tau}$ de 1,6 TeV, λ'_{132} se excluye por encima de 0,005.

Después de la búsqueda directa de una resonancia, podemos asumir que la nueva resonancia estaría por encima del límite cinemático experimental. El estudio de las posibles desviaciones de las predicciones del ME en la cola de la distribución de masa es sensible a los parámetros electrodébiles oblicuos, W e Y. A partir del análisis de leptones (muones y electrones) y de energía faltante, hemos obtenido $W = [-1.2^{+1.2}_{-1.2}] \cdot 10^{-4}$ al 95 % NC. Dado que este canal no es sensible al parámetro Y, se ha realizado un análisis de eventos de dimuones, dando los siguientes resultados: $W = [-6.0^{+19.6}_{-5.1}] \cdot 10^{-4}$, e $Y = [5.6^{+7.5}_{-14.2}] \cdot 10^{-4}$, al 95 % NC.

El último resultado presentado es en el escenario de un bosón de Higgs compuesto. Si el bosón de Higgs no es una partícula elemental sino que está formada por otras partículas elementales, esperaríamos discrepancias con respecto a las predicciones del ME. Este efecto depende de la escala de energía de la potencial nueva resonancia. Si esta energía es accesible experimentalmente, el acoplamiento de la resonancia se vería afectado. Sin embargo, si la energía está por encima del límite cinemático, podría crear una desviación en la cola de la distribución de masa. Como una reinterpretación del límite del acoplamiento y de la medida del parámetro oblicuo W, se excluyen las regiones en el plano g_* - m_* del modelo de Higgs compuesto. Establecimos un límite inferior de 3 TeV para la masa del hipotético bosón de Higgs compuesto, asumiendo el escenario SSM para la producción de W'.

La tabla 6.3 resume todos los límites en la búsqueda de procesos más allá del modelo estándar con el estado final de un muon y energía faltante, con los datos del Run 2 recogidos por el experimento CMS.

Esta tesis es el resultado de cuatro años de intensa investigación donde tuve la oportunidad de aprender de personas expertas en la materia, y de aportar mis conocimientos e ideas. El resultado es un pequeño, aunque significativo, paso adelante en el marco del enorme esfuerzo de la humanidad para entender los fundamentos de la naturaleza.

Irene Bachiller Perea

Bibliography

[1] S. Weinberg. A Model of Leptons. *Phys. Rev. Lett.*, 19:1264–1266, 1967. doi: 10.1103/PhysRevLett.19.1264.

[2] S.L. Glashow. Partial–symmetries of weak interactions. *Nuclear Physics*, 22 (4):579–588, 1961. doi: 10.1016/0029-5582(61)90469-2.

[3] A. Salam. Weak and Electromagnetic Interactions. *Conf. Proc. C*, 680519: 367–377, 1968. doi: 10.1142/9789812795915_0034.

[4] S. L. Glashow, J. Iliopoulos, and L. Maiani. Weak Interactions with Lepton–Hadron Symmetry. *Phys. Rev. D*, 2(7):1285, 1970. doi: 10.1103/PhysRevD. 2.1285.

[5] G. 't Hooft. Renormalization of massless Yang–Mills fields. *Nuclear Physics B*, 33(1):173–199, 1971. doi: 10.1016/0550-3213(71)90395-6.

[6] Particle Data Group. Review of Particle Physics. *Progress of Theoretical and Experimental Physics*, 2020(8), 2020. doi: 10.1093/ptep/ptaa104.

[7] F. Englert and R. Brout. Broken Symmetry and the Mass of Gauge Vector Mesons. *Phys. Rev. Lett.*, 13:321–323, 1964. doi: 10.1103/PhysRevLett.13.321.

[8] P.W. Higgs. Broken symmetries, massless particles and gauge fields. *Phys. Lett.*, 12(2):132–133, 1964. doi: 10.1016/0031-9163(64)91136-9.

[9] P.W. Higgs. Broken Symmetries and the Masses of Gauge Bosons. *Phys. Rev. Lett.*, 13(16):508–509, 1964. doi: 10.1103/PhysRevLett.13.508.

[10] G. S. Guralnik, C. R. Hagen, and T. W. B. Kibble. Global Conservation Laws and Massless Particles. *Phys. Rev. Lett.*, 13:585–587, 1964. doi: 10.1103/ PhysRevLett.13.585.

[11] P.W. Higgs. Spontaneous Symmetry Breakdown without Massless Bosons. *Phys. Rev.*, 145(4):1156–1163, 1966. doi: 10.1103/PhysRev.145.1156.

[12] D.W. Hertzog et al. Measurement of the Positive Muon Lifetime and Determination of the Fermi Constant to Part–per–Million Precision. *Phys.Rev.Lett*, 106:041803, 2011. doi: 10.1103/PhysRevLett.106.041803. arXiv:1010.0991.

[13] CMS Collaboration. Observation of a new boson at a mass of 125 GeV with the CMS experiment at the LHC. *Physics Letters B*, 716(1):30–61, 2012. doi: 10.1016/j.physletb.2012.08.021.

[14] ATLAS Collaboration. Observation of a new particle in the search for the

Standard Model Higgs boson with the ATLAS detector at the LHC. *Physics Letters B*, 716(1):1–29, 2012. doi: 10.1016/j.physletb.2012.08.020.

[15] N. Cabibbo. Unitary Symmetry and Leptonic Decays. *Phys. Rev. Lett.*, 10 (12):531–533, 1963. doi: 10.1103/PhysRevLett.10.531.

[16] M. Kobayashi and T. Maskawa. CP–Violation in the Renormalizable Theory of Weak Interaction. *Progress of Theoretical Physics*, 49(2):652–657, 1973. doi: 10.1143/PTP.49.652.

[17] G. Altarelli, B. Mele, and M. Ruiz-Altaba. Searching for new heavy vector bosons in pp colliders. *Z. Phys. C*, 45:109, 1989. doi: 10.1007/BF01556677. [Erratum: doi:10.1007/BF01552335].

[18] M. Tanabashi et al. Review of Particle Physics. *Phys. Rev.*, D98(3):030001, 2018. doi: 10.1103/PhysRevD.98.030001.

[19] E. Accomando, D. Becciolini, S. De Curtis, D. Dominici, L. Fedeli, and C. Shepherd-Themistocleous. Interference effects in heavy W' boson searches at the LHC. *Physical Review D*, 85(11), 2012. doi: 10.1103/PhysRevD.85. 115017. arXiv:1110.0713.

[20] T.G. Rizzo. The determination of the helicity of W' boson couplings at the LHC. *Journal of High Energy Physics*, 2007(05):037–037, 2007. doi: 10.1088/ 1126-6708/2007/05/037. URL `10.1088/1126-6708/2007/05/037`.

[21] E. Boos, V. Bunichev, L. Dudko, and M. Perfilov. Interference between W' and W in single–top quark production processes. *Physics Letters B*, 655(5): 245–250, 2007. doi: 10.1016/j.physletb.2007.03.064. arXiv:hep-ph/0610080.

[22] D0 Collaboration. Search for W' Bosons Decaying to an Electron and a Neutrino with the D0 Detector. *Phys. Rev. Letters*, 100(3), 2008. doi: 10.1103/PhysRevLett.100.031804. arXiv:0710.2966.

[23] CDF Collaboration. Search for a new heavy gauge boson W' with event signature electron + missing transverse energy in pp collisions at $\sqrt{s} = 1.96$ TeV. *Phys. Rev. D*, 83(3), 2011. doi: 10.1103/PhysRevD.83.031102. arXiv:1012.5145.

[24] CMS Collaboration. Search for new physics in final states with a lepton and missing transverse energy in pp collisions at the LHC. *Phys. Rev. D*, 87(7), 2013. doi: 10.1103/PhysRevD.87.072005. arXiv:1302.2812.

[25] CMS Collaboration. Search for physics beyond the standard model in final states with a lepton and missing transverse energy in proton–proton collisions at $\sqrt{s} = 8$ TeV. *Phys. Rev. D*, 91(9):092005, 2015. doi: 10.1103/PhysRevD.91. 092005. arXiv:1408.2745.

[26] CMS Collaboration. Search for heavy gauge W' boson in events with an energetic lepton and large missing transverse momentum at $\sqrt{s} = 13$ TeV. *Phys. Lett. B*, 770:278–301, 2017. doi: 10.1016/j.physletb.2017.04.043.

arXiv:1612.09274.

[27] I. Cholis, G. Dobler, D.P. Finkbeiner, L. Goodenough, and N. Weiner. Case for a 700 + GeV WIMP: Cosmic ray spectra from PAMELA, Fermi, and ATIC. *Physical Review D*, 80(12), 2009. doi: 10.1103/PhysRevD.80.123518.

[28] AMS Collaboration. The Alpha Magnetic Spectrometer (AMS) on the international space station: Part II – Results from the first seven years. *Physics Reports*, 894:1–116, 2021. doi: 10.1016/j.physrep.2020.09.003.

[29] T. Appelquist, H. Cheng, and B.A. Dobrescu. Bounds on universal extra dimensions. *Phys. Rev. D*, 64:035002, 2001. doi: 10.1103/PhysRevD.64.035002. arXiv:hep-ph/0012100.

[30] D. Hooper and K.M. Zurek. PAMELA and ATIC signals from Kaluza–Klein dark matter. *Physical Review D*, 79(10), 2009. doi: 10.1103/PhysRevD.79. 103529. arXiv:0902.0593.

[31] S.C. Park and J. Shu. Split–UED and Dark Matter. *Physical Review D*, 79 (9), 2009. doi: 10.1103/PhysRevD.79.091702. arXiv:0901.0720.

[32] C. Chen, M.M. Nojiri, S.C. Park, J. Shu, and M. Takeuchi. Dark matter and collider phenomenology of split-UED. *JHEP*, 09:078, 2009. doi: 10.1088/ 1126-6708/2009/09/078. arXiv:0903.1971.

[33] K. Kong, S.C. Park, and T.G. Rizzo. Collider phenomenology with Split-UED. *JHEP*, 04:081, 2010. doi: 10.1007/JHEP04(2010)081. arXiv:1002.0602.

[34] CMS Collaboration. Search for heavy resonances that decay into a vector boson and a Higgs boson in hadronic final states at $\sqrt{s} = 13\,\text{TeV}$. *The European Physical Journal C*, 77(9), 2017. doi: 10.1140/epjc/s10052-017-5192-z. arXiv:1707.01303.

[35] ATLAS Collaboration. Search for heavy resonances decaying to a W or Z boson and a Higgs boson in the $\text{qq}^{(')}\text{bb}$ final state in pp collisions at $\sqrt{s} = 13\,\text{TeV}$ with the ATLAS detector. *Physics Letters B*, 774:494–515, 2017. doi: 10.1016/j. physletb.2017.09.066. arXiv:1707.06958.

[36] J. Beuria, A. Datta, D. Debnath, and K.T. Matchev. LHC collider phenomenology of minimal universal extra dimensions. *Computer Physics Communications*, 226:187–205, 2018. doi: 10.1016/j.cpc.2017.12.021. arXiv:1702.00413.

[37] N. Deutschmann, T. Flacke, and J.S. Kim. Current LHC constraints on minimal universal extra dimensions. *Physics Letters B*, 771:515–520, 2017. doi: 10.1016/j.physletb.2017.06.004. arXiv:1702.00410.

[38] A. Salam and J. Strathdee. Super–symmetry and non–Abelian gauges. *Physics Letters B*, 51(4):353–355, 1974. doi: 10.1016/0370-2693(74)90226-3.

[39] Yu. A. Golfand and E. P. Likhtman. Extension of the Algebra of Poincare Group Generators and Violation of P–Invariance. *JETP Lett.*, 13:323–326,

1971.

[40] R. Barbier, C. Bérat, M. Besançon, M. Chemtob, A. Deandrea, E. Dudas, P. Fayet, S. Lavignac, G. Moreau, E. Perez, and et al. R–Parity–violating supersymmetry. *Physics Reports*, 420(1-6):1–195, 2005. doi: 10.1016/j.physrep. 2005.08.006. arXiv:hep-ph/0406039.

[41] G.R. Farrar and P. Fayet. Phenomenology of the Production, Decay, and Detection of New Hadronic States Associated with Supersymmetry. *Phys. Lett. B*, 76:575, 1978. doi: 10.1016/0370-2693(78)90858-4.

[42] H. K. Dreiner and T. Stefaniak. Bounds on R–Parity violation from resonant slepton production at the LHC. *Phys. Rev. D*, 86(5):055010, 2012. doi: 10. 1103/PhysRevD.86.055010. arXiv:1201.5014.

[43] ATLAS Collaboration. Search for direct stau production in events with two hadronic tau–leptons in $\sqrt{s} = 13$ TeV pp collisions with the ATLAS detector. *Physical Review D*, 101(3), 2020. doi: 10.1103/PhysRevD.101.032009. arXiv:1911.06660.

[44] DELPHI Collaboration. Search for supersymmetry with R–Parity violation at $\sqrt{s} = 192$ to 208 GeV. Technical Report 4, CERN, 2002. URL `http://cds.cern.ch/record/993933`.

[45] L3 Collaboration. Search for R–Parity violating decays of supersymmetric particles in e^+e^- collisions at $\sqrt{s} = 189$ GeV. *The European Physical Journal C - Particles and Fields*, 19(1-2):397–141, 2001. doi: 10.1007/s100520100608.

[46] M.E. Peskin and T. Takeuchi. Estimation of oblique electroweak corrections. *Phys. Rev. D*, 46:381–409, 1992. doi: 10.1103/PhysRevD.46.381.

[47] R. Barbieri, A. Pomarol, R. Rattazzi, and A. Strumia. Electroweak symmetry breaking after LEP–1 and LEP–2. *Nucl. Phys.*, B703:127–146, 2004. doi: 10.1016/j.nuclphysb.2004.10.014. arXiv:hep-ph/0405040.

[48] M. Farina, G. Panico, D. Pappadopulo, J.T. Ruderman, R. Torre, and A. Wulzer. Energy helps accuracy: Electroweak precision tests at hadron colliders. *Phys. Lett.*, B772:210–215, 2017. doi: 10.1016/j.physletb.2017.06.043. arXiv:1609.08157.

[49] A. Falkowski and K. Mimouni. Model independent constraints on four–lepton operators. *JHEP*, 02:086, 2016. doi: 10.1007/JHEP02(2016)086. arXiv:1511.07434.

[50] J.L. Hewett and T.G. Rizzo. Low–Energy Phenomenology of Superstring Inspired E(6) Models. *Phys. Rept.*, 183:193, 1989. doi: 10.1016/0370-1573(89) 90071-9.

[51] G.F. Giudicea, C. Grojeana, A. Pomarolc, and R. Rattazzi. The Strongly–Interacting Light Higgs. *JHEP*, 0706:045:45, 2007. doi: 10.1088/1126-6708/ 2007/06/045. arXiv:hep-ph/0703164.

[52] CMS Collaboration. Combined measurements of Higgs boson couplings in proton–proton collisions at $\sqrt{s} = 13$ TeV. *The European Physical Journal C*, 79(5):079, 2019. doi: 10.1140/epjc/s10052-019-6909-y. arXiv:1809.10733.

[53] O. Bruning et al. LHC Design Report. *CERN-2004-003-v1*, 2004. doi: CERN-2004-003-v1. URL `https://cds.cern.ch/record/782076`.

[54] LEP Injector Study Group. LEP Design Report Vol.1: The LEP Injector Chain. *CERN-LEP-83-01*, 1, 1983. URL `https://cds.cern.ch/record/98881`.

[55] LEP. LEP Design Report Vol.2: The LEP main ring. *CERN-LEP-84-01*, 2, 1984. URL `https://cds.cern.ch/record/102083`.

[56] M. Benedikt, P. Collier, V. Mertens, J. Poole, and K. Schindl. LHC Design Report: the LHC Injector Chain. *CERN Yellow Reports: Monographs*, 2004. doi: 10.5170/CERN-2004-003-V-3. URL `http://cds.cern.ch/record/823808`.

[57] E. Mobs. The CERN accelerator complex. *Complexe des accélérateurs du CERN*, 2019. URL `https://cds.cern.ch/record/2684277`.

[58] ATLAS Collaboration. The ATLAS experiment at the CERN LHC. *JINST*, 3:S08003, 2008.

[59] CMS Collaboration. The CMS experiment at the CERN LHC. *JINST*, 3: S08004, 2008. URL `https://cds.cern.ch/record/1129810`.

[60] ALICE Collaboration. The ALICE experiment at the CERN LHC. *JINST*, 3:S08002, 2008.

[61] LHCb Collaboration. The LHCb experiment at the CERN LHC. *JINST*, 3: S08005, 2008.

[62] L. Evans and P. Bryant. LHC Machine. *JINST*, 3(08):S08001, 2008. doi: 10.1088/1748-0221/3/08/s08001. URL `https://cds.cern.ch/record/1129806`.

[63] S. Van der Meer. Calibration of the effective beam height in the ISR. Technical Report CERN-ISR-PO-68-31, CERN, 1968. URL `https://cds.cern.ch/record/296752`.

[64] CMS Luminosity, Public Results. URL `https://twiki.cern.ch/twiki/bin/view/CMSPublic/LumiPublicResults`.

[65] A. H. Mueller. *Perturbative QCD*. Advanced Series on Directions in High Energy Physics, Volume 5, 1989. ISBN 978-981-4503-26-6. doi: 10.1142/0494.

[66] S. Bailey, T. Cridge, L. A. Harland-Lang, A. D. Martin, and R. S. Thorne. Parton distributions from LHC, HERA, Tevatron and fixed target data: MSHT20 PDFs. *The European Physical Journal C*, 81(4), 2021. doi: 10.1140/epjc/s10052-021-09057-0. arXiv:2012.04684.

[67] R.D. Ball et al. Parton distributions with LHC data. *Nucl. Phys. B*, 867:244, 2013. doi: 10.1016/j.nuclphysb.2012.10.003. arXiv:1207.1303.

[68] R.D. Ball et al. Parton distributions from high–precision collider data. *Eur. Phys. J. C*, 77(10):663, 2017. doi: 10.1140/epjc/s10052-017-5199-5. arXiv:1706.00428.

[69] CMS Collaboration. Event generator tunes obtained from underlying event and multiparton scattering measurements. *Eur. Phys. J. C*, 76(3):155, 2016. doi: 10.1140/epjc/s10052-016-3988-x. arXiv:1512.00815.

[70] CMS Collaboration. Extraction and validation of a new set of CMS PYTHIA8 tunes from underlying–event measurements. *The European Physical Journal C*, 80(1), 2020. doi: 10.1140/epjc/s10052-019-7499-4. arXiv:1903.12179.

[71] T. Sjöstrand, S. Ask, J.R. Christiansen, R. Corke, N. Desai, P. Ilten, S. Mrenna, S. Prestel, C.O. Rasmussen, and P.Z. Skands. An introduction to PYTHIA8.2. *Comp. Phys. Comm.*, 191:159, 2015. doi: 10.1016/j.cpc.2015. 01.024. arXiv:1410.3012.

[72] S. Alioli, P. Nason, C. Oleari, and E. Re. A general framework for implementing NLO calculations in shower Monte Carlo programs: the POWHEG BOX. *JHEP*, 06:043, 2010. doi: 10.1007/JHEP06(2010)043. arXiv:1002.2581.

[73] S. Frixione, P. Nason, and C. Oleari. Matching NLO QCD computations with Parton Shower simulations: the POWHEG method. *JHEP*, 11:070, 2007. doi: 10.1088/1126-6708/2007/11/070. arXiv:0709.2092.

[74] P. Nason. A new method for combining NLO QCD with shower Monte Carlo algorithms. *JHEP*, 11:040, 2004. doi: 10.1088/1126-6708/2004/11/040. arXiv:hep-ph/0409146.

[75] J. Alwall, M. Herquet, F. Maltoni, O. Mattelaer, and T. Stelzer. MAD-GRAPH5: going beyond. *JHEP*, 06:128, 2011. doi: 10.1007/JHEP06(2011)128. arXiv:1106.0522.

[76] J. Alwall, R. Frederix, S. Frixione, V. Hirschi, F. Maltoni, O. Mattelaer, H. S. Shao, T. Stelzer, P. Torrielli, and M. Zaro. The automated computation of tree–level and next–to–leading order differential cross sections, and their matching to parton shower simulations. *JHEP*, 07:079, 2014. doi: 10.1007/ JHEP07(2014)079. arXiv:1405.0301.

[77] R. Frederix and S. Frixione. Merging meets matching in MC@NLO. *JHEP*, 12:061, 2012. doi: 10.1007/JHEP12(2012)061. arXiv:1209.6215.

[78] CMS Collaboration. CMS Physics: Technical Design Report Volume 1: Detector Performance and Software . *CERN-LHCC-2006-001*, 2006. URL https://cds.cern.ch/record/922757.

[79] V.I. Klyukhin, N. Amapane, V. Andreev, A. Ball, B. Cure, A. Herve, A. Gaddi, H. Gerwig, V. Karimaki, R. Loveless, et al. The CMS Magnetic Field Map Performance. *IEEE Transactions on Applied Superconductivity*, 20(3):152–155, 2010. doi: 10.1109/tasc.2010.2041200. arXiv:1110.0607.

[80] CMS Collaboration. Description and performance of track and primary–vertex reconstruction with the CMS tracker. *JINST*, 9, 2014. doi: 10.1088/1748-0221/9/10/P10009. arXiv:1405.6569.

[81] R. Fruhwirth. Application of Kalman filtering to track and vertex fitting. *Nucl. Instrum. Methods Phys. Res., A*, 262(HEPHY-PUB-503):444, 1987. doi: 10.1016/0168-9002(87)90887-4. URL `https://cds.cern.ch/record/178627`.

[82] CMS Collaboration. CMS Technical Design Report for the Pixel Detector Upgrade. *CERN-LHCC-2012-016, CMS-TDR-11*, 2012. doi: 10.2172/1151650. URL `https://cds.cern.ch/record/1481838`.

[83] CMS Collaboration. Performance of electron reconstruction and selection with the CMS detector in proton–proton collisions at $\sqrt{s} = 8$ TeV. *JINST*, 10:P06005, 2015. doi: 10.1088/1748-0221/10/06/P06005. arXiv:1502.02701.

[84] A. Benaglia. The CMS ECAL performance with examples. *JINST*, 9(02):C02008, 2014. doi: 10.1088/1748-0221/9/02/c02008. URL `htts://cds.cern.ch/record/1632384`.

[85] CMS Collaboration. Energy calibration and resolution of the CMS electromagnetic calorimeter in pp collisions at $\sqrt{s} = 7$ TeV. *JINST*, 8(09):P09009, 2013. doi: 10.1088/1748-0221/8/09/P09009. arXiv:1306.2016.

[86] CMS Collaboration. The CMS electromagnetic calorimeter project. *Technical Design Report*, 1997. URL `https://cds.cern.ch/record/349375`.

[87] CMS Collaboration. The CMS hadron calorimeter project: Technical Design Report. *Technical Design Report*, 1997. URL `http://cds.cern.ch/record/357153`.

[88] CMS Collaboration. Performance of the CMS hadron calorimeter with cosmic ray muons and LHC beam data. *JINST*, 5:T03012, 2010. doi: 10.1088/1748-0221/5/03/T03012. arXiv:0911.4991.

[89] CMS Collaboration. Design, Performance, and Calibration of CMS Hadron-Barrel Calorimeter Wedges. *The European Physical Journal C*, 55(1):159–171, 2008. doi: 10.1140/epjc/s10052-008-0573-y. URL `https://cds.cern.ch/record/1049915`.

[90] CMS Collaboration. Design, performance, and calibration of CMS forward calorimeter wedges. *European Physical Journal C*, 53:139–166, 2008. doi: 10.1140/epjc/s10052-007-0459-4. URL `https://cds.cern.ch/record/951395`.

[91] CMS Collaboration. Design, Performance, and Calibration of the CMS Hadron-Outer Calorimeter. *Eur. Phys. J. C*, 57:653–663, 2008. doi: 10.1140/epjc/s10052-008-0756-6. URL `http://cds.cern.ch/record/1127569`.

[92] CMS Collaboration. The CMS Muon Project: Technical Design Report. *CMS-TDR-003*, 1997. URL `https://cds.cern.ch/record/343814`.

[93] CMS Collaboration. Performance of the CMS muon detector and muon re-

construction with proton–proton collisions at $\sqrt{s} = 13$ TeV. *JINST*, 13(06): P06015, 2018. doi: 10.1088/1748-0221/13/06/P06015. arXiv:1804.04528.

[94] CMS Collaboration. Calibration of the CMS Drift Tube Chambers and Measurement of the Drift Velocity with Cosmic Rays. *JINST*, 5:T03016, 2010. doi: 10.1088/1748-0221/5/03/T03016. arXiv:0911.4895.

[95] CMS Collaboration. The performance of the CMS muon detector in proton–proton collisions at $\sqrt{s} = 7$ TeV at the LHC. *JINST*, 8(11):P11002–P11002, 2013. doi: 10.1088/1748-0221/8/11/P11002. arXiv:1306.6905.

[96] CMS Collaboration. Performance of the CMS drift–tube chamber local trigger with cosmic rays. *JINST*, 5:T03003. 31, 2009. doi: 10.1088/1748-0221/5/03/T03003. arXiv:0911.4893.

[97] CMS Collaboration. Performance of the CMS Cathode Strip Chambers with Cosmic Rays. *JINST*, 5:T0301, 2010. doi: 10.1088/1748-0221/5/03/T03018. arXiv:0911.4992.

[98] CMS Collaboration. The CMS trigger system. *JINST*, 12(01):P01020, 2017. doi: 10.1088/1748-0221/12/01/P01020. arXiv:1609.02366.

[99] CMS Collaboration. CMS Level–1 Trigger. *Nuclear Instruments and Methods in Physics Research Section A: Accelerators, Spectrometers, Detectors and Associated Equipment*, 384(1):143, 1996. doi: 10.1016/S0168-9002(96)01068-6.

[100] CMS Collaboration. CMS Technical Design Report for the Level–1 Trigger Upgrade. *CERN-LHCC-2013-011,CMS-TDR-012*, 2013. URL `https://cds.cern.ch/record/1556311`.

[101] CMS Collaboration. Performance of the CMS Level–1 trigger in proton–proton collisions at $\sqrt{s} = 13$ TeV. *JINST*, 15(10):P10017–P10017, 2020. doi: 10.1088/1748-0221/15/10/p10017. arXiv:2006.10165.

[102] W. Adam et al. The CMS High Level trigger. *Eur. Phys. J. C*, 46:605–667, 2006. doi: 10.1140/epjc/s2006-02495-8. arXiv:hep-ex/0512077.

[103] K. Bos, N. Brook, D. Duellmann, C. Eck, I. Fisk, D. Foster, B. Gibbard, C. Grandi, F. Grey, J. Harvey, A. Heiss, F. Hemmer, S. Jarp, R. Jones, D. Kelsey, J. Knobloch, M. Lamanna, H. Marten, P. Mato Vila, F. Ould-Saada, B. Panzer-Steindel, L. Perini, L. Robertson, Y. Schutz, U. Schwickerath, J. Shiers, and T. Wenaus. LHC Computing Grid. *Technical Design Report. LCG*, 2005. URL `https://cds.cern.ch/record/840543`.

[104] I. Bird, P. Buncic, F. Carminati, M. Cattaneo, P. Clarke, I. Fisk, M. Girone, J. Harvey, B. Kersevan, P. Mato, R. Mount, and B. Panzer-Steindel. Update of the Computing Models of the WLCG and the LHC Experiments. *Technical Design Report. LCG*, 2014. URL `http://cds.cern.ch/record/1695401`.

[105] CMS Collaboration. CMS The Computing Project. *Technical Design Report*, 23:1–137, 07 2005.

[106] R. Brun and F. Rademakers. ROOT – An object oriented data analysis framework. *Nuclear Instruments and Methods in Physics Research Section A: Accelerators, Spectrometers, Detectors and Associated Equipment*, 389(1):81 – 86, 1997. doi: 10.1016/S0168-9002(97)00048-X. New Computing Techniques in Physics Research V.

[107] CMS Data Quality Information, 2018. URL `https://twiki.cern.ch/twiki/bin/view/CMSPublic/DataQuality`.

[108] CMS Collaboration. CMS Technical Design Report for the Phase 1 Upgrade of the Hadron Calorimeter. *CERN-LHCC-2012-015, CMS-TDR-10*, 2012. doi: 10.2172/1151651. URL `https://cds.cern.ch/record/1481837`.

[109] CMS Collaboration. CMS Technical Design Report for the Muon Endcap GEM Upgrade. *CERN-LHCC-2015-012, CMS-TDR-013*, 2015. URL `https://cds.cern.ch/record/2021453`.

[110] I. Shvetsov. Operational experience with the Silicon Strip Tracker at the CMS experiment. *CMS-CR-2019-012*, 2019. doi: 10.22323/1.348.0003. URL `http://cds.cern.ch/record/2689274`.

[111] Siddireddy P.K. The CMS ECAL Trigger and DAQ system: electronics auto–recovery and monitoring. *CMS CR-2018/084*, 2018. arXiv:1806.09136.

[112] A. Navarro Tobar, A. Triossi, I. Redondo-Fernández, D. Francia-Ferrero, C. Fernández Bedoya, J. Sastre, J.M. Cela Ruiz, D. Redondo-Ferrero, J. Fernandez Menendez, and J.F. de Troconiz. CMS Drift Tubes Readout Phase–1 Upgrade. *PoS TWEPP2018*, 2019. doi: 10.22323/1.343.0039.

[113] D. Barney. CMS Slice. *CMS-OUTREACH-2018-017*, 2015. URL `https://cds.cern.ch/record/2628641`.

[114] CMS Collaboration. Particle–Flow reconstruction and global event description with the CMS detector. *JINST*, 12(10):P10003, 2017. doi: 10.1088/1748-0221/12/10/P10003. arXiv:1706.04965.

[115] S. Agostinelli et al. GEANT4: A Simulation toolkit. *Nucl. Instrum. Meth. A*, 506:250–303, 2003. doi: 10.1016/S0168-9002(03)01368-8.

[116] P. Billoir. Progressive track recognition with a Kalman–like fitting procedure. *Computer Physics Communications*, 57(1):390–394, 1989. ISSN 0010-4655. doi: 10.1016/0010-4655(89)90249-X. URL `https://www.sciencedirect.com/science/article/pii/001046558990249X`.

[117] R. Mankel. A concurrent track evolution algorithm for pattern recognition in the HERA-B main tracking system. *Nuclear Instruments and Methods in Physics Research Section A*, 395(2):169–184, 1997. ISSN 0168-9002. doi: 10.1016/S0168-9002(97)00705-5.

[118] CMS Collaboration and T. Mc Cauley. Collision events recorded by CMS in 2016, 2017. URL `https://cds.cern.ch/record/2241144`. CMS Collection.

[119] W. Adam, R. Fruhwirth, A. Strandlie, and T. Todor. Reconstruction of electrons with the Gaussian–sum filter in the CMS tracker at LHC. *J.Phys. G*, 31:9, 2005. doi: 10.1088/0954-3899/31/9/N01. arXiv:physics/0306087.

[120] CMS Collaboration. Electron and photon reconstruction and identification with the CMS experiment at the CERN LHC. *JINST*, 16(05), 2021. doi: 10.1088/1748-0221/16/05/P05014. arXiv:2012.06888.

[121] M. Cacciari, G.P. Salam, and G. Soyez. The anti–k_t jet clustering algorithm. *JHEP*, 04:063, 2008. doi: 10.1088/1126-6708/2008/04/063. arXiv:0802.1189.

[122] Q. Ingram. Energy resolution of the barrel of the CMS Electromagnetic Calorimeter. *JINST*, 2(04):P04004, 2007. doi: 10.1088/1748-0221/2/04/P04004. URL http://cds.cern.ch/record/1009081.

[123] CMS Collaboration. Calibration of the CMS hadron calorimeters using proton–proton collision data at $\sqrt{s} = 13$ TeV. *JINST*, 15(05):P05002, 2020. doi: 10.1088/1748-0221/15/05/P05002. arXiv:1910.00079.

[124] CMS Collaboration. Determination of Jet Energy Calibration and Transverse Momentum Resolution in CMS. *JINST*, 6(11):P11002–P11002, 2011. doi: 10.1088/1748-0221/6/11/P11002. arXiv:1107.4277.

[125] D. Guest, J. Collado, P. Baldi, S. Hsu, G. Urban, and D. Whiteson. Jet flavor classification in high–energy physics with deep neural networks. *Physical Review D*, 94(11), 2016. doi: 10.1103/PhysRevD.94.112002. arXiv:1607.08633.

[126] CMS Collaboration. Identification of heavy–flavour jets with the CMS detector in pp collisions at 13 TeV. *JINST*, 13(05):P05011, 2018. doi: 10.1088/1748-0221/13/05/P05011. arXiv:1712.07158.

[127] CMS Collaboration. Performance of missing transverse momentum reconstruction in proton–proton collisions at $\sqrt{s} = 13$ TeV using the CMS detector. *JINST*, 14(07):P07004, 2019. doi: 10.1088/1748-0221/14/07/P07004. arXiv:1903.06078.

[128] CMS Collaboration. Performance of MET reconstruction and pileup mitigation techniques in CMS. *Nucl. Part. Phys. Proc.*, pages 2512–2514, 2015. arXiv:1502.05207.

[129] CMS Collaboration. Performance of the reconstruction and identification of high–momentum muons in proton–proton collisions at $\sqrt{s} = 13$ TeV. *JINST*, 15(02):P02027, 2020. doi: 10.1088/1748-0221/15/02/P02027. arXiv:1912.03516.

[130] CMS Collaboration. Performance of CMS muon reconstruction in pp collision events at $\sqrt{s} = 7$ TeV. *JINST*, 7(10):P10002, JINST. doi: 10.1088/1748-0221/7/10/P10002. arXiv:1206.4071.

[131] CMS Collaboration. Aligning the CMS muon chambers with the muon alignment system during an extended cosmic ray run. *JINST*, 5(03):T03019, 2010. doi: 10.1088/1748-0221/5/03/t03019. arXiv:0911.4770.

[132] CMS Collaboration. Performance of muon reconstruction including alignment position errors for 2016 collision data. *CMS Detector Performance Summary*, 2016. URL `https://cds.cern.ch/record/2229697`. CMS-DP-2016-067.

[133] A. Bodek, A. Van Dyne, J. Y. Han, W. Sakumoto, and A. Strelnikov. Extracting muon momentum scale corrections for hadron collider experiments. *The European Physical Journal C*, 72(10), 2012. doi: 10.1140/epjc/s10052-012-2194-8. arXiv:1208.3710.

[134] CMS Collaboration. Muon Reconstruction and Identification Performance with Run 2 data. *Detector Performance Summary*, 2020. URL `http://cds.cern.ch/record/2727091`.

[135] CMS Collaboration. Muon identification and isolation efficiencies with 2017 and 2018 data. *Detector Performance Summary*, 2018. URL `https://cds.cern.ch/record/2629364`.

[136] Y. Li and F. Petriello. Combining QCD and electroweak corrections to dilepton production in FEWZ. *Phys. Rev. D*, 86:094034, 2012. doi: 10.1103/PhysRevD.86.094034. arXiv:1208.5967.

[137] D. Pappadopulo, A. Thamm, R. Torre, and A. Wulzer. Heavy vector triplets: bridging theory and data. *JHEP*, 09:060, 2014. doi: 10.1007/jhep09(2014)060. arXiv:1402.4431.

[138] M.L. Mangano, M. Moretti, F. Piccinini, and M. Treccani. Matching matrix elements and shower evolution for top–pair production in hadronic collisions. *JHEP*, 1:13, 2007. doi: 10.1088/1126-6708/2007/01/013. arXiv:hep-ph/0611129.

[139] A. Arbuzov, D. Bardin, S. Bondarenko, P. Christova, L. Kalinovskaya, U. Klein, V. Kolesnikov, L. Rumyantsev, R. Sadykov, and A. Sapronov. Update of the MCSANC Monte Carlo integrator, v.1.20. *JETP Lett.*, 103(2): 131–136, 2016. doi: 10.1134/S0021364016020041. arXiv:1509.03052.

[140] S. Alioli et al. Precision studies of observables in $pp \rightarrow W \rightarrow \ell\nu$ and $pp \rightarrow \gamma, Z \rightarrow \ell^+\ell^-$ processes at the LHC. *Eur. Phys. J. C*, 77(5):280, 2017. doi: 10.1140/epjc/s10052-017-4832-7. arXiv:1606.02330.

[141] J. Butterworth, S. Carrazza, A. Cooper-Sarkar, A. Roeck, J. Rojo, J. Feltesse, S. Forte, J. Gao, S. Glazov, and et al. PDF4LHC recommendations for LHC Run 2. *Journal of Physics G: Nuclear and Particle Physics*, 43:023001, 2016. doi: 10.1088/0954-3899/43/2/023001. arXiv:1510.03865.

[142] CMS Collaboration. Measurement of the inelastic proton–proton cross section at $\sqrt{s} = 13$ TeV. *JHEP*, 07:161, 2018. doi: 10.1007/JHEP07(2018)161. arXiv:1802.02613.

[143] CMS Collaboration. Measurements of differential Z boson production cross sections in proton–proton collisions at $\sqrt{s} = 13$ TeV. *Journal of High Energy*

Physics, 2019(12), 2019. doi: 10.1007/jhep12(2019)061. arXiv:1909.04133.

[144] J. M. Campbell, R. K. Ellis, and C. Williams. Vector boson pair production at the LHC. *JHEP*, 07:018, 2011. doi: 10.1007/JHEP07(2011)018. arXiv:1105.0020.

[145] CMS Collaboration. Measurement of differential cross sections for top quark pair production using the lepton + jets final state in proton–proton collisions at 13 TeV. *Phys. Rev. D*, 95:092001, 2017. doi: 10.1103/PhysRevD.95.092001. arXiv:1610.04191.

[146] Michal Czakon, Paul Fiedler, and Alexander Mitov. Total Top–Quark Pair–Production Cross Section at Hadron Colliders Through $\mathcal{O}(\alpha_S^4)$. *Phys. Rev. Lett.*, 110(25):252004, 2013. doi: 10.1103/PhysRevLett.110.252004. arXiv:1303.6254.

[147] M. Czakon, D. Heymes, A. Mitov, D. Pagani, I. Tsinikos, and M. Zaro. Top–pair production at the LHC through NNLO QCD and NLO EW. *JHEP*, 10:186, 2017. doi: 10.1007/JHEP10(2017)186. arXiv:1705.04105.

[148] T. Gehrmann and others. W^+W^- Production at Hadron Colliders in Next-to-Next-to-Leading Order QCD. *Phys. Rev. Lett.*, 113:212001, 2014. doi: 10.1103/PhysRevLett.113.212001. arXiv:1408.5243.

[149] J. M. Campbell, R. K. Ellis, and C. Williams. Vector boson pair production at the LHC. *JHEP*, 07:018, 2011. doi: 10.1007/jhep07(2011)018. arXiv:1105.0020.

[150] F. Cascioli et al. ZZ production at hadron colliders in NNLO QCD. *Phys. Lett. B*, 735:311, 2014. doi: 10.1016/j.physletb.2014.06.056. arXiv:1405.2219.

[151] CMS Collaboration. Jet energy scale and resolution in the CMS experiment in pp collisions at 8 TeV. *JINST*, 12(02):P02014, 2017. doi: 10.1088/1748-0221/12/02/P02014. arXiv:1607.03663.

[152] CMS Collaboration. Precision luminosity measurement in proton–proton collisions at $\sqrt{s} = 13$ TeV in 2015 and 2016 at CMS. *EPJC*, 2021. arXiv:2104.01927.

[153] CMS Collaboration. CMS luminosity measurement for the 2017 data-taking period at $\sqrt{s} = 13$ TeV, 2017. URL `https://cds.cern.ch/record/2621960`.

[154] CMS Collaboration. CMS luminosity measurement for the 2018 data-taking period at $\sqrt{s} = 13$ TeV, 2018. URL `https://cds.cern.ch/record/2676164`.

[155] CMS Collaboration. Measurements of the W boson rapidity, helicity, double-differential cross sections, and charge asymmetry in pp collisions at $\sqrt{s} = 13$ TeV. *Physical Review D*, 102(9), 2020. doi: 10.1103/physrevd.102.092012. arXiv:2008.04174.

[156] ATLAS and CMS Collaborations and The LHC Higgs Combination Group. Procedure for the LHC Higgs boson search combination in Summer 2011. Technical Report CMS-NOTE-2011-005. ATL-PHYS-PUB-2011-11, CERN, 2011.

URL `http://cds.cern.ch/record/1379837`.

[157] CMS Collaboration. Search for high–mass resonances in final states with a lepton and missing transverse momentum at $\sqrt{s} = 13$ TeV. *JHEP*, 06:128, 2018. doi: 10.1007/JHEP06(2018)128. arXiv:1803.11133.

[158] ATLAS Collaboration. Search for a new heavy gauge boson resonance decaying into a lepton and missing transverse momentum in $36\,\text{fb}^{-1}$ of pp collisions at $\sqrt{s} = 13$ TeV with the ATLAS experiment. *Eur. Phys. J. C*, 78(5):401, 2018. doi: 10.1140/epjc/s10052-018-5877-y. arXiv:1706.04786.

[159] ATLAS Collaboration. Search for a heavy charged boson in events with a charged lepton and missing transverse momentum from pp collisions at $\sqrt{s} = 13$ TeV with the ATLAS detector. *Phys. Rev. D*, 100(5):052013, 2019. doi: 10.1103/PhysRevD.100.052013. arXiv:1906.05609.

[160] CMS Collaboration. Search for a W' boson decaying to a τ lepton and a neutrino in proton–proton collisions at $\sqrt{s} = 13$ TeV. *Physics Letters B*, 792: 107–131, 2019. doi: 10.1016/j.physletb.2019.01.069. arXiv:1807.11421.

[161] ATLAS Collaboration. Search for high–mass resonances decaying to $\tau\nu$ in pp collisions at $\sqrt{s} = 13$ TeV with the ATLAS Detector. *Physical Review Letters*, 120(16), 2018. doi: 10.1103/physrevlett.120.161802. arXiv:1801.06992.

[162] D.J. Muller and S. Nandi. Topflavor: a separate SU(2) for the third family. *Physics Letters B*, 383(3):345–350, 1996. doi: 10.1016/0370-2693(96)00745-9. arXiv:hep-ph/9602390.

[163] C.T. Hill. Topcolor assisted technicolor. *Physics Letters B*, 345(4):483–489, Feb 1995. doi: 10.1016/0370-2693(94)01660-5. arXiv:hep-ph/9411426.

[164] M. Abdullah, J. Calle, B. Dutta, A. Flórez, and D. Restrepo. Probing a simplified W' model of R(D(*)) anomalies using b–tags, τ leptons, and missing energy. *Physical Review D*, 98(5), 2018. doi: 10.1103/PhysRevD.98.055016. arXiv:1805.01869.

[165] CMS Collaboration. Search for heavy resonances decaying to a top quark and a bottom quark in the lepton + jets final state in proton–proton collisions at $\sqrt{s} = 13$ TeV. *Physics Letters B*, 777:39–63, 2018. doi: 10.1016/j.physletb. 2017.12.006. arXiv:1708.08539.

[166] CMS Collaboration. Search for W' bosons decaying to a top and a bottom quark at $\sqrt{s} = 13$ TeV in the hadronic final state. *Phys. Lett. B*, 820:136535, 2021. doi: 10.1016/j.physletb.2021.136535. arXiv:2104.04831.

[167] CMS Collaboration. Search for resonant and nonresonant new phenomena in high–mass dilepton final states at $\sqrt{s} = 13$ TeV. *JHEP*, 2021. doi: 10.1007/ jhep07(2021)208. arXiv:2103.02708.

[168] ATLAS Collaboration. Search for high–mass dilepton resonances using $139\,\text{fb}^{-1}$ of pp collision data collected at $\sqrt{s} = 13$ TeV with the ATLAS detec-

tor. *Physics Letters B*, 796:68–87, 2019. doi: 10.1016/j.physletb.2019.07.016. arXiv:1903.06248.

[169] J.M. Frère, M. Libanov, S. Mollet, and S. Troitsky. Flavour changing Z' signals in a 6D inspired model. *Journal of High Energy Physics*, 6, 2016. doi: 10.1007/jhep06(2016)063. arXiv:1505.08017.

[170] CMS Collaboration. Search for lepton–flavor violating decays of heavy resonances and quantum black holes to $e\mu$ final states in proton–proton collisions at $\sqrt{s} = 13$ TeV. *Journal of High Energy Physics*, 4, 2018. doi: 10.1007/JHEP04(2018)073. arXiv:1802.01122.

[171] CMS Collaboration. Search for a heavy resonance decaying into a Z boson and a Z or W boson in 2l2q final states at $\sqrt{s} = 13$ TeV. *Journal of High Energy Physics*, 101(9), 2018. doi: 10.1007/jhep09(2018)101. arXiv:1803.10093.

[172] ATLAS Collaboration. Search for heavy diboson resonances in semileptonic final states in pp collisions at $\sqrt{s} = 13$ TeV with the ATLAS detector. *The European Physical Journal C*, 80:1165, 2020. doi: 10.1140/epjc/s10052-020-08554-y. arXiv:2004.14636.

[173] CMS Collaboration. Combination of CMS searches for heavy resonances decaying to pairs of bosons or leptons. *Physics Letters B*, 798:134952, 2019. doi: 10.1016/j.physletb.2019.134952. arXiv:1906.00057.

[174] I. Béjar Alonso et al. High–Luminosity Large Hadron Collider (HL–LHC): Technical design report. *CERN Yellow Report*, 2020. doi: 10.23731/CYRM-2020-0010. URL https://e-publishing.cern.ch/index.php/CYRM/issue/view/127.

[175] CMS Collaboration. Expected performance of the physics objects with the upgraded CMS detector at the HL–LHC. Technical report, CERN, 2018. URL https://cds.cern.ch/record/2650976.

[176] ATLAS Collaboration. Prospects for searches for heavy Z' and W' bosons in fermionic final states with the ATLAS experiment at the HL–LHC. *ATL-PHYS-PUB-2018-044*, 2018. URL http://cds.cern.ch/record/2650549.

[177] CMS Collaboration. Search for long–lived charged particles in proton–proton collisions at $\sqrt{s} = 13$ TeV. *Phys. Rev. D*, 94(11):112004, 2016. doi: 10.1103/PhysRevD.94.112004. arXiv:1609.08382.

[178] ATLAS Collaboration. Search for heavy charged long–lived particles in the ATLAS detector in $36.1\,\text{fb}^{-1}$ of proton–proton collision data at $\sqrt{s} = 7$ TeV. *Phys. Rev. D*, 99(9), 2019. doi: 10.1103/PhysRevD.99.092007. arXiv:1902.01636.

[179] F. James. MINUIT: Function Minimization and Error Analysis Reference Manual. Technical Report CERN-D-506, CERN Computing and Networks Division, 1998. URL http://cds.cern.ch/record/2296388.